A segmented interior permanent magnet synchronous machine with wide field-weakening range

Author:
Dutta, Rukmi

Publication Date:
2007

DOI:
https://doi.org/10.26190/unsworks/17300

A Segmented Interior Permanent Magnet Synchronous Machine with Wide Field-Weakening Range

Rukmi Dutta

A thesis submitted to
The University of New South Wales for the degree of
Doctor of Philosophy

School of Electrical Engineering and Telecommunications
August, 2007

ACKNOWLEDGEMENTS

I wish to express my sincere gratitude to Professor M.F Rahman for his support and guidance throughout my study. Your timely and constructive suggestion has made it possible for me to accomplish this goal. It would not have been possible without your financial support. I gratefully acknowledge the help and input from CSIRO during the construction of the prototype segmented rotor. I would also like to thank my colleagues Huu To Phuc and Dr. Baburaj Karnayil for their helps and suggestions during experimental set up. A special thank to Richard Tuck from the workshop.

Last but not least, a grateful acknowledgement to my husband Dr. Dushmanta Dutta for his support during the whole tenure.

ABSTRACT

Many high performance drive applications require wide Constant Power Speed Range (CPSR) for efficient use of energy. The examples of such applications are the starter-alternator system of automobiles proposed for the 42V PowerNet, traction in the hybrid/electric vehicle, wind power generator etc. The Permanent Magnet (PM) machine is the natural choice of such niche applications because of their higher efficiency and compact size. However, the Surface Permanent Magnet (SPM) machine with sine distributed winding and radially-laminated Interior Permanent Magnet (IPM) machine with conventional structure has very limited or zero flux-weakening capability.

The flux-weakening capability of the SPM machine can be improved by using concentrated, fractional-slot stator but here well-known advantages of the sine distributed winding are needed to be compromised. In the IPM machine, flux-weakening was improved using axial lamination and more than two magnet layers per pole. However, the construction of such IPM machine is complicated and expensive.

This thesis presents design and analysis of a new type of the Interior Permanent Magnet (IPM) machine that have a very wide Constant Power Speed Range (CPSR) without compromising simplicity of construction and advantages of the distribution winding.

In the new IPM machine, the magnet poles were segmented in the radially direction and the iron bridges between magnet segments provide for additional paths of flux-canalization to give the rotor an inherent capability of flux-weakening. Consequently, a very wide constant power speed range can be

achieved in such machines. The proposed IPM machine of this work was referred as the Segmented IPM machine.

The thesis focuses on the optimization of the Segmented IPM machine in a 42V environment of the automobile. First, for the conceptual evaluation a 4 pole, 550W Segmented Magnet IPM machine was optimized using finite element analysis. The parameters were calculated for prediction of the steady-state and transient performances. The torque- and power-speed capability were estimated using time-step, circuit-coupled finite element analysis. The cogging torque and variation of iron loss with frequency were also investigated during the design process.

A prototype machine was constructed on the basis of the optimized design. The steady-state and transient performances of the prototype machine were measured and compared with the predicted results for experimental verification. The measured performance analysis was found to match very well with the predicted results. The measured torque- and power-speed capability of the Segmented IPM machine was also compared to those of a conventional, non-segmented IPM machine of similar rating and size.

The thesis also presents the optimized design of a 6kW, 12 pole Segmented Magnet IPM machine for application in the Integrated Starter Alternator (ISA) of the electric/hybrid vehicle. It can be concluded from the predicted steady-state analysis of the 6 kW, 12 pole Segmented Magnet IPM machine that it should be able to satisfy most of the required criteria of an ISA with appropriate design optimization.

TABLE OF CONTENTS

LIST OF FIGURES

LIST OF TABLE

LIST OF SYMBOLS

a	No. of parallel path
$\vec{A}$	Magnetic vector potential
A_g	Cross-sectional area of the air gap
A_{PM}	Cross-sectional area of the magnet
$\vec{B}$	Magnetic flux density vector
B	Magnitude of magnetic flux density
B_{g1}	Fundamental Air-gap flux density
B_r	Remanance
$\vec{E}$	Electric flux density vector
D	Stator bore diameter
E_0	Normalized induced back EMF
E	Back EMF
f_s	Switching frequency
F	Energy functional
F_{pk}	Peak of the fundamental mmF
g	Air-gap length
h_{PM}	Height of the magnet
$\vec{H}$	Magnetic field intensity vector
H	Magnitude of magnetic field intensity
H_c	Coercivety
i_d , i_q	d- and q- axes currents
I_{ch}	Characteristic current
I_m	Peak value of phase current

I_{pu}	pu current
I_{rated}	Rated current
I_s	Current space vector
I_{Si}	Current in the ith stator slot
I_{sm}	System current limit
$\vec{J}$	Current intensity vector
k_{eddy}	Eddy current loss constant
k_{exe}	Excess loss coefficient
k_{hys}	Hysteresis loss constant
K_{d1}	Distribution factor
K_e	Back EMF constant
K_{p1}	Short pitch factor
K_{s1}	Skew factor
K_{w1}	Winding factor
l	Active machine core length
l_{avg}	Average length of the one turn of the winding
l_{PM}	Length of the magnet in the magnetization direction
L_d	d-axis inductance
L_{end}	End-turn leakage inductance of winding
L_q	q-axis inductance
L_{ld}, L_{lq}	d- and q-axes leakage inductance
L_{md}, L_{mq}	d- and q-axes magnetizing inductance
m	No. of phases
M	Magnetization
N	No. of conductors per slot per pole

N_{ph}	No. of series turns per phase
p	Number of pole pair
p_{core}	Core loss density
p_{eddy}	Eddy current loss density
p_{exe}	Excess loss density
p_g	Mesh grid potential
p_{hys}	Hysteresis loss density
P_c	Permeance co-efficient
P_o	Output power
P_{pu}	pu power
q	No. of slot per pole per phase
R_s	Stator winding resistance
S	Cross-sectional area
T	Torque
T_{cog}	Cogging torque
T_s	Switching time period
v_d, v_q	d- and q-axes voltages
V_{dc}	DC bus voltage
V_{pu}	pu voltage
V_{sm}	System voltage limit
w_{PM}	Width of the magnet
X_d,X_q	d- and q-axis reactances at base frequency
β	Angle where peak of mmf wave occurs [Elec. Deg]
γ	Current angle
δ	Torque angle

Δ	Operator del
ε	Short pitch angle
σ	Conductivity
λ	Slot pitch angle
ξ	Ratio of q-axis to d-axis inductance
ζ	Steinmetz constant
ψ_d, ψ_q	d- and q-axes stator flux linkage
ψ_{end}	End-turn leakage flux linkage
ψ_{PM}	Magnet flux-linkage
μ	Magnetic permeability
μ_0	Permeability of air
μ_r	Recoil permeability
μ_{rrec}	Relative recoil permeability
θ_r	Rotor position
θ_0	Initial angle
θ_i	Angle from the d-axis to the ith stator tooth
ν	Reluctivity
ν_0	Reluctivity of air
ν_r	Recoil reluctivity
φ	Phase angle
ϕ	Magnetic flux
$\Re$	Reluctance
τ	Pole pitch
ω_e	Electrical speed in rad/s

ω_{pu}	pu speed
ω_r	Rotor angular speed
ω_b	Base speed
ω_c	Critical speed
$\omega_{cross\text{-}over}$	Cross-over speed

Superscripts

*	Reference or command value

Subscripts

0	Initial value
Capital letters	Steady state values

Abbreviations

EMF	Electro Motive Force
FEM	Finite Element Method
ISA	Integrated Starter Alternator
MMF	Magneto Motive Force
NdFeB	Nyobdium Iron Boron
PM	Permanent Magnet
PMSM	Permanent Magnet Synchronous Machine
PWM	Pulse Width Modulation
VSI	Voltage Source Inverter

CHAPTER 1

1. Introduction

1.1. General Background

The recent advancement in the field of high energy permanent magnet materials and power electronics has broadened the field of application for Permanent Magnet (PM) machines greatly. It has been adopted for many high performance applications such as robotics, aerospace, power tools, generation with renewable energy source, various medical equipments and electric/hybrid vehicles etc. Because of its many advantages, the permanent magnet machines are preferred over other traditional machines such as brush commutated DC motor, synchronous motor and induction motor especially for highly efficient servo and variable speed drive applications. Some of the advantages offered by the permanent magnet machine are listed as:

- The rotor copper loss is zero which results in higher efficiency.
- High torque and output power per volume results in compact design.
- Elimination of slip ring, commutator and carbon brush etc. which simplifies construction and maintenance.
- Air-gap flux density is relatively high; hence, dynamic performance is better.

Additionally, the PM machine is capable of operating with high power factor, precise and fast torque/speed/position control is possible with the simple six-switch Voltage Source Inverter (VSI).

In a Permanent Magnet (PM) machine, the field excitation comes from the permanent magnet pole pieces. Depending on working principles, the PM machine can be categorized broadly into three main groups: - (a) Brush commutated PMDC machines, (b) Brushless PMDC machine and (c) Brushless PMAC or PM Synchronous Machine (PMSM). The **Error! Reference source not found.** shows the configuration of the three types of PM machines.

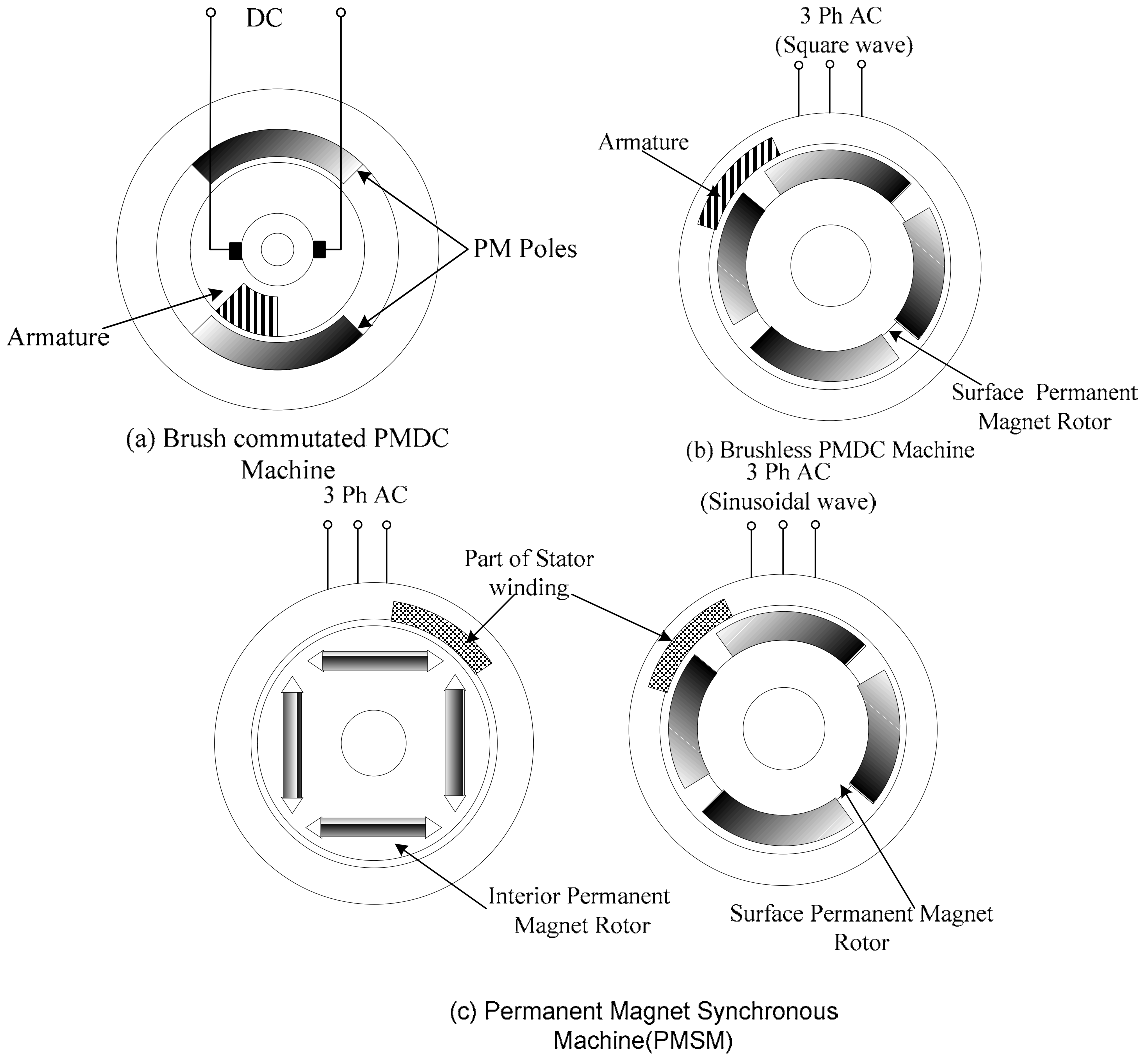

Fig.1.1 Configuration of three types of PM Machines

The brush-commutated PMDC machine is the DC machine in which electromagnetic field has been replaced by the permanent magnet field. As a result, field copper loss is eliminated but the machine is no longer field controllable; hence, usages of such machines are restricted to low power and high dynamic applications that require no field-weakening.

The advances in the semiconductor switch technology have led to the development of another kind of PMDC machines where carbon brush commutation is replaced by the electronic commutation. In such machines, permanent magnet poles are situated on the rotating part and the stator consists of three-phase windings that are fed with square waveforms from three-leg converters. The switching of the converter is controlled in such a way that at one time only two phases conduct. This electronic commutation scheme is functionally equivalent to the mechanical brush commutation of the DC machine. Hence, this type of PM DC machines is known as brushless PMDC machine or square-wave PMDC machine. The brushless PM DC machine is preferred for many applications because of its low maintenance, high efficiency and relatively simple switching scheme.

The brushless PM AC machine also has permanent magnet poles in the rotating part and the stator or armature consists of the three-phase, sine-distributed windings. The machine operates with the principle of synchronous rotating magnetic field, hence, they are also known as PM Synchronous Machine (PMSM).

In most of the high performance drive applications, an inverter interface is needed for variable voltage and variable frequency output. The block diagram of a commonly used PMSM drive system is shown in the Error! Reference source not found.. The rotor field of the PMSM can be held in synchronism with the inverter from zero to maximum speed without requiring any rotor cage winding.

However, for both the brushless PMDC and PMSM machines, information of rotor position is essential in the drive operations. Hence, in such machines the physical interface with an encoder or a resolver is unavoidable. The mechanical sensor-less position estimation techniques are being developed for the both types of machines to eliminate this constraint.

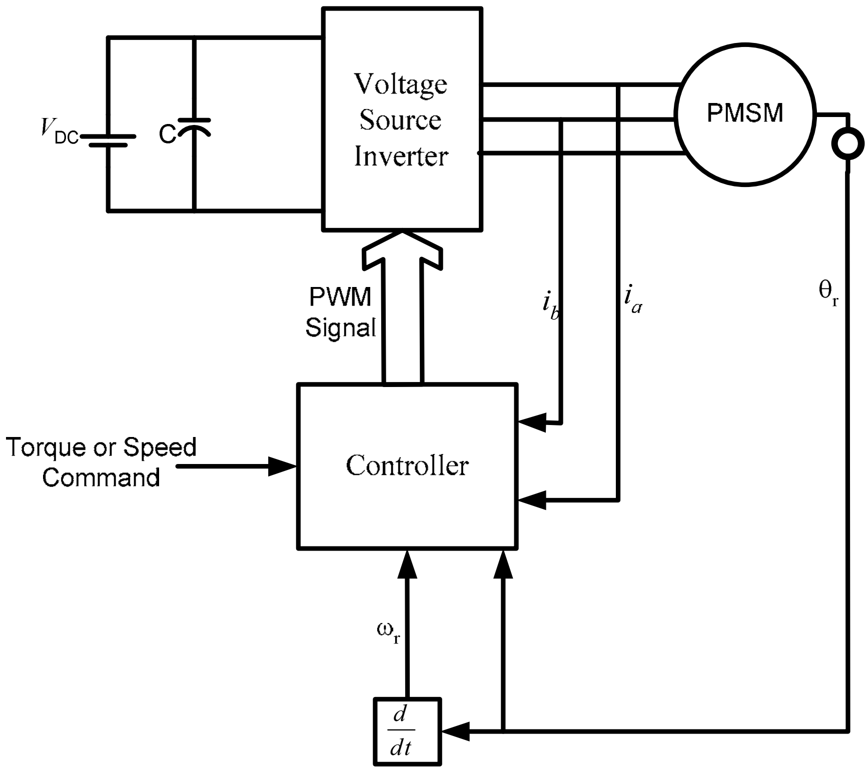

Fig.1.2 Block diagram of a PMSM drive systems

The PM synchronous machines are built with a number of rotor configurations. Among them, interior and surface magnet rotors are the two most commonly used configurations. In the interior magnet structure, magnet poles are buried inside the rotor where as in the surface magnet rotor, the magnet poles are glued to the rotor surface as shown in the Fig1.3(a) and (b).

The air-gap of the interior magnet rotor structure is very small. Hence, the air-gap flux can be weakened effectively by negative armature reaction. Another important feature of the Interior Permanent Magnet (IPM) rotor is its inverse saliency i.e. the q-axis inductance L_q is larger than the d-axis inductance L_d. Consequently, it has an additive reluctance torque component which can be exploited to extend constant power operation during flux-weakening. Additionally, in the IPM rotor, the effect of centrifugal force over the pole magnet during very high speed application is minimal; hence, it is mechanically robust compared to surface magnet rotor structure.

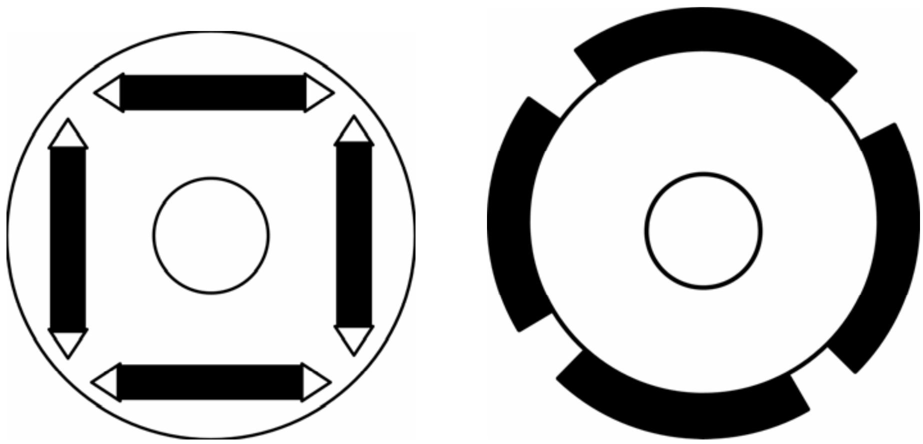

(a) (b)

Fig. 1.3 Cross-section of the (a) IPM rotor (b) Surface Permanent Magnet rotor

In the surface magnet rotor, magnet poles are also part of the air-gap and since, the permeability of the rare-earth magnet is close to air, the effective air-gap of the machine becomes relatively large. Therefore, in the Surface Permanent Magnet (SPM) machine with sine distributed stator winding the effect of negative armature reaction during flux-weakening is marginal. Moreover, the SPM machine is magnetically non-salient; hence, there is no reluctance torque contribution.

As a result, the interior magnet structure is preferred over surface magnet structure in many applications, especially, where the machine needs to operate above base speed with constant power. The design of IPM machine with wide Constant Power Speed Range (CPSR) has received much attention from the research community in the last couple of decades.

1.2. Numerical Techniques in Design and Analysis of Electric machines

The Numerical techniques such as Finite Element Method (FEM) play a vital role during designing of the electric machine with complex geometry and magnetic property. The analysis and prediction of the performance by FEM during design stage are necessary not only to avoid any design misjudgment but also to optimize the performance criteria.

The functioning of an electric machine is dictated mostly by the electromagnetic field which in turn can be expressed in numerical form by the Maxwell's equations of electromagnetics and by solving these equations, the performance of an electric machine and its magnetic characteristics can be estimated accurately.

The Maxwell's equations express problems of electromagnetic field in the form of partial differential equations which can be subjected to specific boundary conditions. Analytical solutions of these equations are possible for simple cases but complex problems of the electric machine demands for numerical solutions. In the most of numerical solutions, the differential or integral forms of electromagnetic field problems are converted to matrix equations which simplifies the process to a great extent [2].

There are a number of numerical methods exist for solving magnetic field problems such as finite difference method, boundary element method, moment method and finite element method (FEM) etc. Among them, the FEM is widely used because of its flexibility. It can solve both linear and non-linear problems, static and dynamic problems, 2D and 3D plane problems with equal accuracy.

The electrical machine can be evaluated in FEM either in frequency or time domain. In the frequency domain, performances of the machine are determined by the distribution of the magnetic field and current density. The influence of eddy current and skin-effect over the performances can be studied very accurately. However, the accuracy of the solution greatly depends on the correct formation of an equivalent circuit. It is also incapable to take account of the effect of rotating air-gap and non-sinusoidal excitation.

The time domain FEM solution of the electric machine can overcome many of the limitations of the frequency domain. Both the steady state and dynamic performances of an electric machine can be studied in the time domain FE analysis. Due to the recent development in the field of time-stepping FEM, an external electric circuit depicting the electrical characteristic can be directly coupled to the electro-magnetic model of the electric machine. The simulation of rotating air-gap is also possible in the time-stepping FEM [3-5].

In this work, the time-stepping, 2D finite element method was extensively used for design optimization and performance prediction of the studied IPM machines. A two-dimensional model was considered to be sufficient for this study because in the IPM machine the air-gap between stator and rotor is very small and hence, the magnetic field is virtually two dimensional in the whole area except in the end-turn regions [6]. Moreover, the 2D FEM requires far less computing time, memory and power compared to 3D analysis.

1.3. Designing of IPM Synchronous Machine for wide Constant Power Speed Range Applications

Many high performance drive applications such as traction and Integrated Starter Alternator (ISA) of electric/hybrid vehicle requires a highly efficient and robust electric machine that have a very wide constant power speed range [7-9]. Some of these applications demand for a constant power speed ratio as high as 1:10. Achieving such a wide CPSR in any electric machine is a challenge for the design engineers.

Once, the potential of flux-weakening in the IPM machine was realized in the [10], there is enormous interest in the research community to design IPM machines with wide constant power speed range. The detailed analysis of power and voltage equations of the IPM machine in [11] and [12] has lead to the condition of optimum flux-weakening which is given as,

$$I_{rated} = \left| \frac{\psi_{PM}}{L_d} \right| \tag{1.1}$$

where, ψ_{PM} is the magnet flux-linkage and I_{rated} is the rated current of the machine. However, the machine parameters such as ψ_{PM} and L_d can vary with operating conditions. Therefore, maintaining the condition of (1.1) in a practical machine may not always be possible. Moreover, the optimum condition of (1.1) can not be achieved in some of the applications due to other electrical and magnetic constraints. On the other hand, the reluctance torque component of the IPM machine provides useful torque during flux-weakening and it can be exploited to extend the flux-weakening range. A high ratio of L_q to L_d ensures a large reluctance torque.

A number of attempts have been made to modify the rotor and stator structures to achieve high ratio of L_q to L_d in bid of achieving wide constant power speed range. The axially laminated structure of [13] and double magnet layer structure of [14] are example of such motors. However, the constructions of such machines are far more complex than that of commercially available IPM machine. Moreover, the q-axis saturation in these machines is very prominent; hence, a constant ratio of L_q to L_d can not be maintained at all operating conditions. Increase in stator current, reduces L_q which leads to deterioration of performance at high load condition.

Additionally, a reasonably large L_q to L_d ratio alone can not guarantee wide range of constant power speed range. For example, the 4-pole, 1kW Kollmorgen gold-line IPM motor has a saliency ratio of $\frac{L_q}{L_d} = \frac{0.1024}{.0448} = 2.3$; however, the CPSR in the motor is insignificant. The characteristic current of this particular machine is $I_{ch} = \frac{\psi_{PM}}{L_d} = 11.9$ A which is almost 4 times larger than its rated current (3 A). In other words, the machine requires a negative d-axis current 4 times larger than its rated current to offset the magnet field for optimum flux-weakening. Consequently, the effective flux-weakening is very small.

The SPM rotor with fractional-slot concentrated winding described in the [15] and [16] shows a very wide CPSR characteristic. However, some of the well-known problems associated with concentrated winding such as torque ripple due to high space harmonics and other problems associated with SPM rotor can not be avoided in such machines. A study conducted in the [17] concluded that concentrated winding is not effective in the IPM machine to expand the constant power speed range. In the concentrated winding IPM machine, the ratio of the q-axis to d-axis can not be increased sufficiently to produce useful reluctance torque during flux-weakening. Besides, the machines with concentrated winding will not be able to utilize the well-known advantages of the sine-distributed winding.

Reference [18] describes the CRSR characteristics of a circumferentially magnetized segmented rotor IPM machine in which the magnets are in the form of spokes in the rotor and the rotor iron is segmented using flux barriers. In this machine, the d-axis inductance (L_d) is higher than the q-axis inductance (L_q). Because of this reversal of inductance values, the reluctance torque does not enhance the torque contributed by the magnets, as it does in a conventional IPM machine. There are also problems of high cogging torque and non-sinusoidal back emf associated with the circumferentially magnetized design of IPM machines.

Ŝtumberger et al. has proposed a design concept of the IPM rotor in [19] where the magnet pole of the rotor is segmented to provide additional path of flux-canalization so that the rotor can have an inherent flux-weakening capability . The segmented magnet pole design is simple and similar to the commercially-available, radially-laminated IPM machine. Since the segmentation provides physical reduction of the air-gap magnet flux during flux-weakening, a very high ratio of L_q to L_d is not crucial to extend the flux-weakening range. By proper optimization, a very wide constant power speed range is possible in the Segmented IPM machine. The cross-section of a prototype Segmented IPM machine and its torque- and power-speed characteristics are shown in the Fig1.4 (a) and (b) respectively.

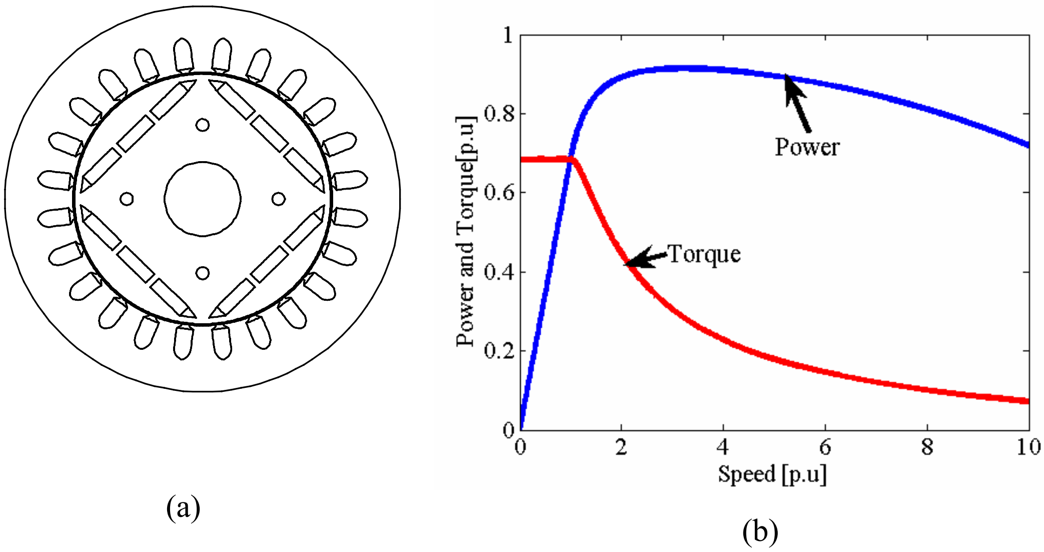

Fig. 1.4 (a) Segmented Magnet IPM Machine and (b) its torque- and power-speed characteristics

The work presented in this thesis, a Segmented IPM machine was first analysed in the 2D FEM. The dimension of the machine, width of the magnet segments and iron bridges etc. were optimized for a wide CPSR. The constraints of the 42V environment of the automobile were imposed on the design during optimization. The circuit-coupled, time-stepping finite element method was used to predict and analyse the performance of the proposed machine. A proto-type machine was built on the basis of the optimized design and all the predicted performances were verified with experimental results.

1.4. Scope of the Project

The primary objective of this work is to design an IPM machine with wide constant power speed range. The configuration of the machine should have an easy-to-construct and cost-effective structure.

In order to achieve the objectives, first the electro-magnetic properties of IPM machines were studied in the FE analysis. The concept of the segmented magnet pole is introduced to the rotor to give it an inherent capability of flux-weakening. The design is then optimized for wide constant power speed range under voltage limit constraint of 42V environment of the automobile. The machine parameters such as d- and q-axis inductances are calculated from the finite element. The time-stepping finite element analysis is used to predict and analyse the steady state performance of the proposed machine. The model of the segmented IPM machine drive is also developed in the Matlab-Simulink environment to investigate the transient and steady-state performances of the machine under current control. During the optimization process, the above mentioned procedure is repeated until an optimum solution is achieved.

A proto-type Segmented IPM machine is constructed based on the optimized design. The drive system of the prototype machine is implemented in hardware through DS1104 microcontroller board. The steady-state and transient performances are measured to verify the predicted result. The core losses for various frequencies, cogging torque at low speed, torque-speed envelope during motoring and power-speed characteristic during generation are measured and compared with the predicted results obtained from the finite element analysis of the same machine. The performance of the proposed machine is also compared with a conventional non-segmented IPM machine of same ratings. The same stator is used in both the machines for direct comparison.

In the last part of the work, an investigation is initiated for a 12-pole, 6-kW Segmented IPM machine which is suitable for applications such as integrated starter alternator of automobile.

1.5. Outline of the Thesis

The contents of the thesis are organized in the following manner:

The chapter 1 introduces the background of this work along with the scope and outline of the work.

The chapter 2 begins with the review of the Interior Permanent Magnet machine technology. It also looks into the property of the rare-earth magnets and electric steel. The basic configurations and characteristics of the IPM machine are discussed in depth. This chapter also introduces concept of the segmented IPM machine. The theory of flux-weakening in the conventional IPM machine was re-examined to understand the inherent flux-weakening of the segmented IPM machine.

The numerical techniques such as time-stepping finite element method are extensively used for design optimization of the proposed segmented IPM machine. These techniques and their relevance to this work are discussed in chapter 3.

The chapter 4 presents the design and optimization process of the prototype Segmented IPM machine. The estimated machine parameters and their characteristics are also presented in this chapter. The calculation of cogging torque and core loss of the Segmented IPM machine from the finite element analysis are also discussed in this chapter.

The current vector control of the IPM machine drive is simple but robust. Hence, it is selected to study the steady state and transient performance of the segmented IPM machine. The chapter 5 discusses the current vector control of the IPM machine. The responses of current and speed controllers for the Segmented IPM machine under step changes are also examined in this chapter.

The experimental verifications of the predicted performances of the segmented IPM machine are presented in the chapter 6.

Chapter 7 investigates the application of the Segmented IPM machine as Integrated Starter Alternator of automobile.

Finally, the conclusion and suggestion for the future work are presented in the chapter 8.

CHAPTER 2

1. Review of Interior Permanent Magnet Machine Drive Technology

1.1. Introduction

The permanent magnet machine with three-phase sinusoidal, distributed winding is categorized as Permanent Magnet Synchronous Machine (PMSM) because of their working principle which resembles closely to that of the traditional synchronous machine. The PMSM with buried or interior magnet structure is known as the Interior Permanent Magnet Synchronous Machine (IPMSM). The Interior Permanent Magnet Machine has number of useful properties such as-

- The developed torque is combination of magnet alignment and reluctance torque.
- Flux-weakening capability
- High speed capability
- Relatively higher inductances
- Under excited operation in the most of load conditions
- Magnets are well protected from centrifugal force by the buried structure.
- The machine can be run easily with a standard induction motor stator.

The IPM machine with a cage winding in the rotor can be run from the three-phase AC supply without any electronic converter. The IPM machine, when interfaced with power electronic inverter is capable of running at the synchronous speed from zero to the maximum speed. In such case, the rotor cage winding of line start becomes redundant and can be eliminated.

1.2. Magnetic Materials

The magnetic characteristics of the PM machine depend on the properties of the magnetic material used for rotor and stator. Therefore, the basic knowledge of the various magnetic materials and their properties is essential in design optimization. The two main magnetic materials used in construction of the IPM machine are: the permanent magnet for the rotor poles and the electrical steel for the rotor and stator cores.

1.2.1. Permanent Magnet Material

The permanent magnet (PM) material requires no external energy to produce and maintain a magnetic field in the air-gap. Like any other ferromagnetic material, magnetic characteristic of PM can be described by its B-H loop. The B-H loop of a typical PM material is shown in the Fig. 2.1. The characteristic of a permanent magnet is evaluated using three main properties: remanance, coercivety and recoil permeability. The remanance B_r of a magnet is defined as the value of magnetic flux density B retained by it when the magnetic field H is zero. On the other hand, the negative field that brings the flux density to zero is called coercivety (H_c) of the PM. If an applied negative field is switched off at operating point ‘S’ of Fig. 2.1 then the magnet will recoil back to ‘R’ along a minor loop. This loop can be approximated as a straight line and is known as recoil line. The gradient of this line is defined as the recoil permeability of the magnet [20]. The PM reaches saturation when all the magnetic moments of the domain align in the direction of the applied field [21].

All of the above mentioned quantities (except for saturation) are defined in the third quadrant of the BH loop. The third quadrant part of the BH loop of the PM is known as the demagnetizing curve. The characteristic of various permanent magnet materials are normally described by the demagnetizing curve instead of the B-H loop.

Both the B_r and H_c of magnet materials depend on temperature. The demagnetization of a permanent magnet is influenced by the temperature rise and duration of exposure to the high temperature condition. The temperature at which magnetization of PM reduces to zero is know as Curie temperature.

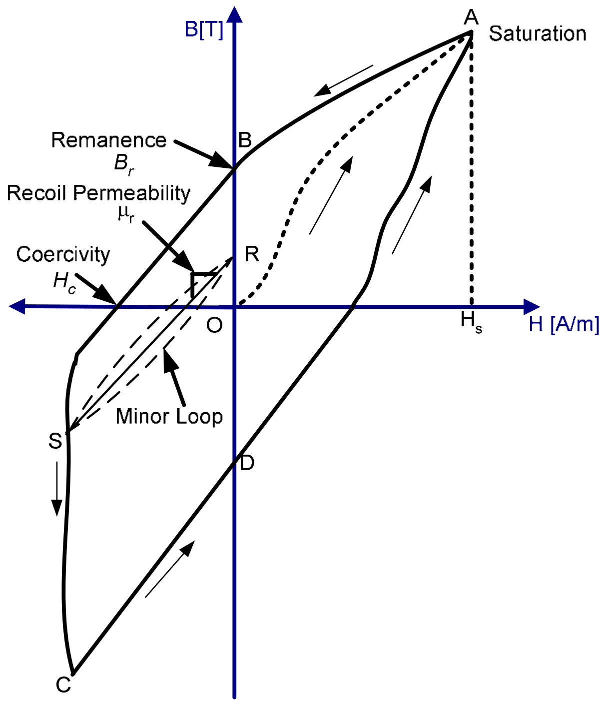

Fig. 1.1 B-H loop of Permanent magnet material

The operating point of a magnet depends on the permeability of the surrounding magnetic circuit. If permeance is low, operating point lies at the lower side of the demagnetizing curve, close to the coercivety. In such a case, the possibility of irreversible demagnetization is high. The position of the operating point in the demagnetizing curve is determined from the coefficient of permeance. It can be defined as,

$$P_c = \frac{A_g l_{PM}}{A_{PM} g} \tag{2.1}$$

where,

A_g : the area of air gap [m^2]

l_{PM} : the length of the magnet [m]

A_{PM} : the area of the magnet [m^2]

g : the length of the air gap [m]

Another important parameter of a magnet is its maximum stored energy which is defined as $(BH)_{max}$. The product of B and H is a hyperbola in the B-H plane as shown in Fig. 2.2. The $(BH)_{max}$ of a given magnet occurs at the point where BH hyperbola is tangent to the demagnetizing curve.

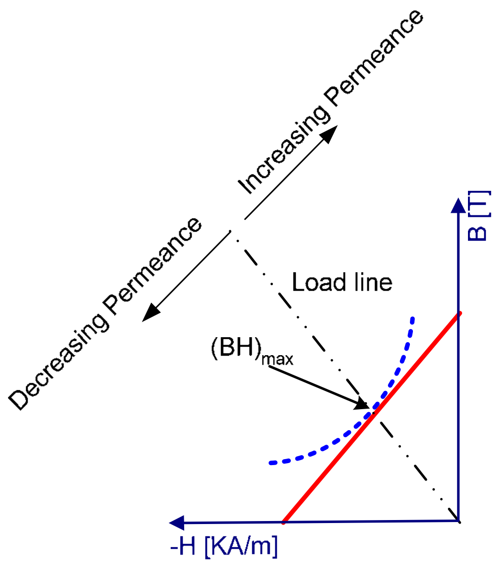

Fig. 1.2 Definition of Permeance Coefficient and $(BH)_{max}$

Depending on demagnetizing characteristics, the permanent magnet can be divided into a number of groups. The three main groups of PM are:

- Alinco (grades: Alinco5, Alinco5-7, Alinco 9 etc.)
- Ferrites (grades: Barium Ferrite, Strontium ferrite etc.)
- Rare-earth (grades: SmCo and NdFeB)

The demagnetizing curves of these materials are presented in Fig. 2.3. It can be seen from this figure that Alinco has the highest remanance flux density but very small coercivety and non-linear demagnetization curve. It can be magnetized and demagnetized very easily. Alinco was widely used in the PMDC brush-commutated motor until the ferrites magnets became commercially available.

The ferrites are better than Alinco in terms of coercivety but its remanance is lower. The Ferrites are the cheapest PM available in the market at present and are commonly used for fractional horsepower PM machines.

The rare-earth PM materials both Smco and NdFeB have linear demagnetizing characteristics. They have high remanance and coercivety. The maximum allowable operating temperature of SmCo is around 350^0, whereas that of NdFeB is 250^0. NdFeB is susceptible to corrosion. However, cost of SmCo is much higher than any other PM material. Therefore, NdFeB is normally preferred over SmCo. Although, cost of NdFeB is higher than ferrites, it is more suitable for high performance PM machines, because of its superior magnetic properties. At present, NdFeB is exclusively used for construction of almost all high performance PM machines.

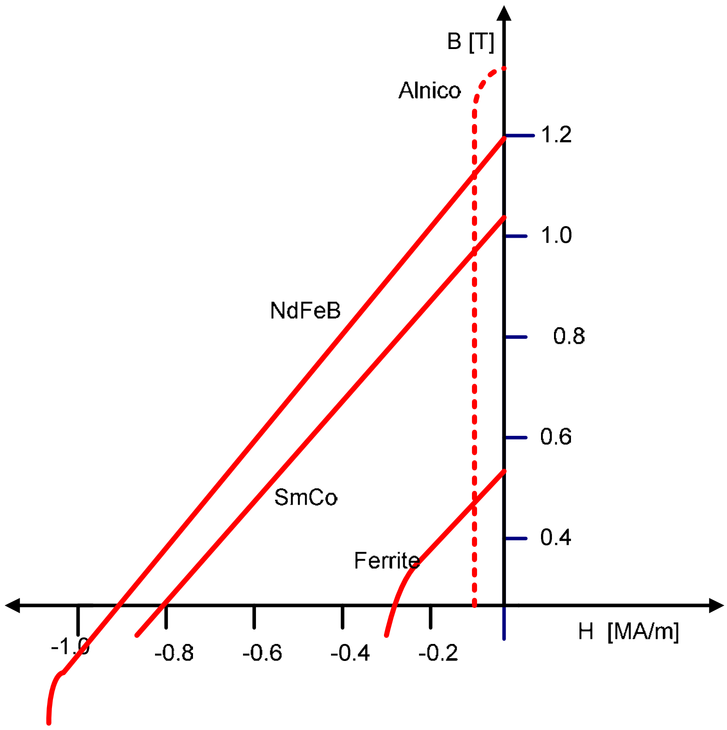

Fig. 1.3 The demagnetizing curves various permanent magnet materials

1.2.2. Electrical Steel

The magnetic flux produced by a current carrying coil is higher in an iron core because of the ferromagnetism. However, the solid iron cores has two main disadvantages: skin-effect and loss due to the induced eddy current. A large potion of the magnetic fluxes is forced to the outer surface of the core by the skin-effect which results in under-utilization of the material. On the other hand, the phenomenon of eddy current causes ^{I2R} loss in the core. The influence of the skin-effect and eddy current on the performance of iron core can be minimized by increasing the resistivity and also by using a stack of thin laminated sheets. The laminated steels sheets were specially developed for the electrical equipments. The core of an electric machine is made with the stack of laminated sheets. Each lamination sheet of the core is insulated from each other. As a result, loss due to eddy current at the operating frequency can be minimized. The laminated steel sheets are also known as electrical steel or silicon steel. Silicon, phosphorous, manganese, etc., are added to the normal steel and Carbon, Sulphur, N_2 ,O_2 etc. are removed as much as practicable from it to fabricate the electrical steel. Thus, the magnetic, electrical and mechanical properties of the electrical steel is enhanced [22]. The B-H curve of the electrical steel compared to cast iron and normal steel is shown in Fig. 2.4. It is obvious from this figure that the electric steel has superior magnetic property than other two. Depending on the lamination-thickness and core loss, many different grades of electrical steel are available in the market. The grades are selected for the electric machine design on basis of the minimum loss at the operating frequency.

Normally, the rotor cores of the PM machines are laminated in the radial direction. In the reference [13], an axially laminated machine was proposed to improve some performance criteria. However, the construction of such rotor is complex and expensive.

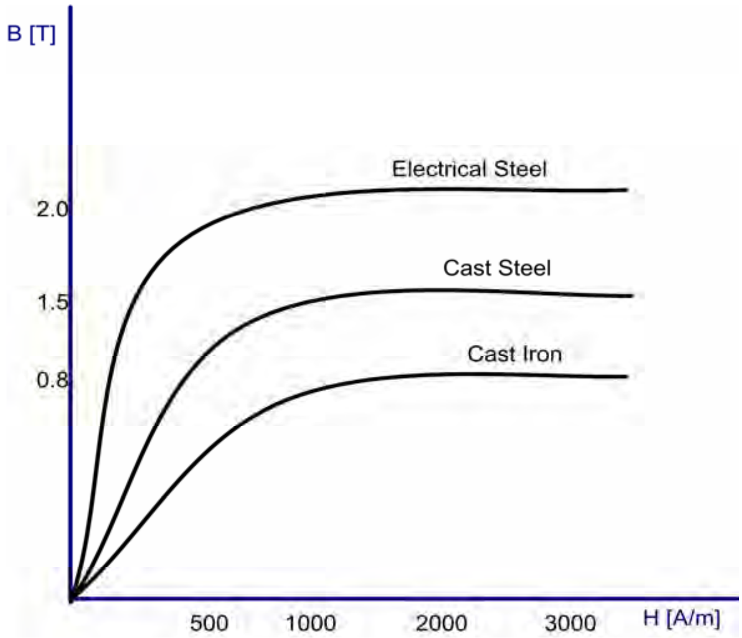

Fig. 1.4 The B-H curve of electrical steel compared to cast steel and cast iron

1.3. Rotor Configurations of the IPM Machine

There exist several different rotor configurations of the Interior Permanent magnet machines. Depending on the direction of flux crossing in the air gap, the IPM machine can be broadly categorized as radial flux, transversal flux and axial flux types. The configuration of rotor pole and stator winding may vary from one construction to other. Since, it is a new emerging technology, none of the configurations yet has been standardized. Nevertheless, the most common construction is the radial flux type rotor with distributed windings stator. This work concentrates mainly on the radial flux type IPM machine. Hence, discussions about the transversal and axial flux IPM machine are not included.

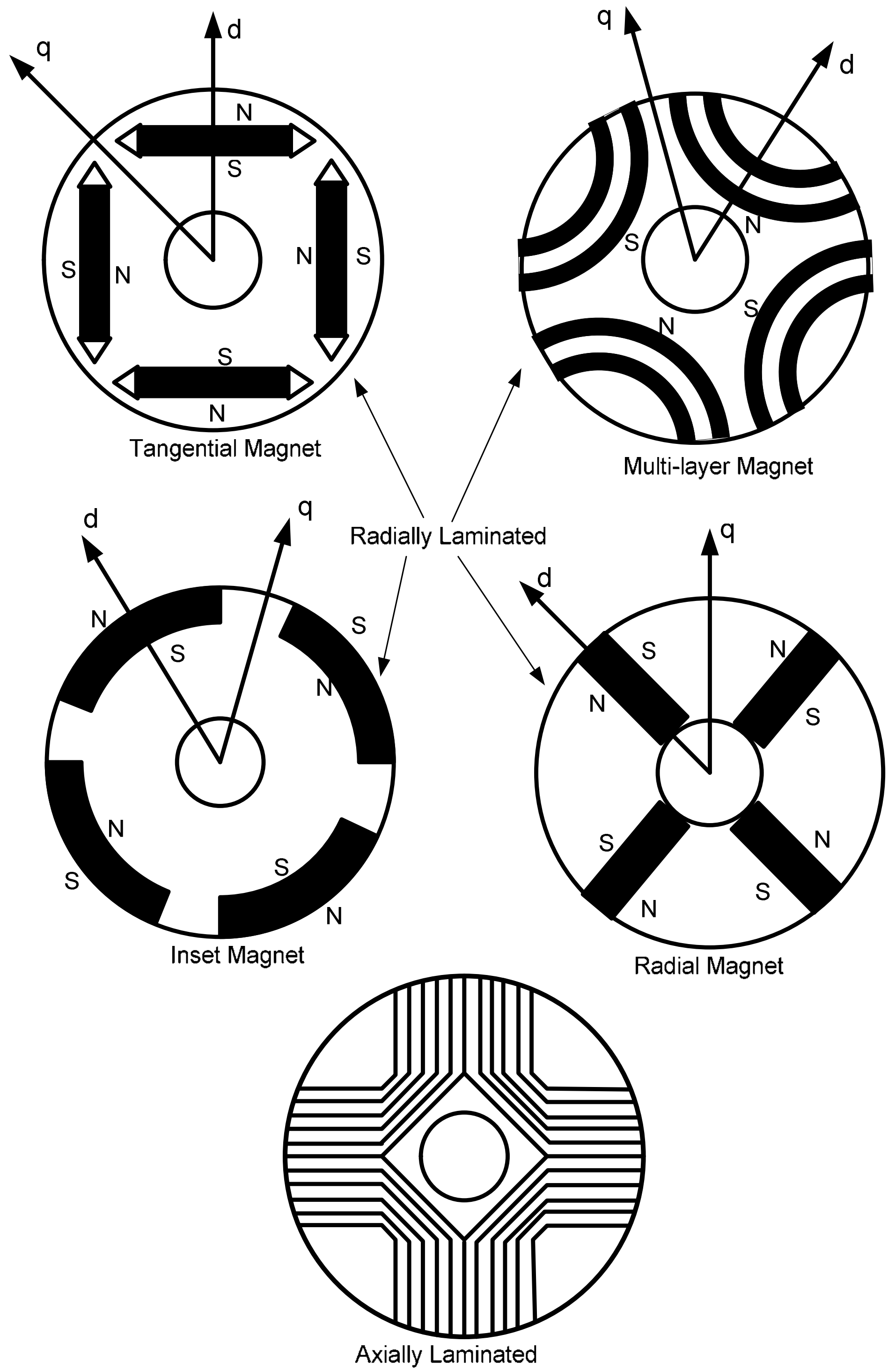

Fig. 1.5 Various rotor configurations of IPM machines

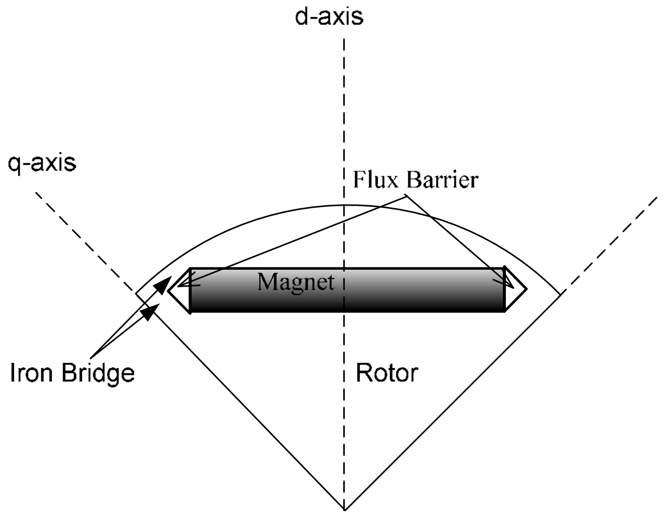

Fig. 1.6 Sketch of one quarter of a conventional IPM rotor

There exist a number of different radial flux rotor configurations of the IPM machine. Some of the well-known rotor structures are: tangential magnet, multi-layered, inset magnet, and radial magnet IPM machine. The Fig. 2.5 shows the cross-sections of some of these rotor structures.

Since the magnets are buried inside the rotor core of the IPM machine, there exist iron bridges on the either side of the magnet poles. The bridges are made as small as physically possible and usually are deeply saturated by the leakage flux. The flux barriers/guards made of non-magnetic material are provided to prevent magnetic short circuit of the adjacent opposite poles. The flux barriers also aid in the flux concentration at the individual pole shoe. The Fig. 2.6 shows the flux barriers and iron bridges in the one pole pitch of a typical IPM machine.

1.4. Characteristics of the IPM Machine

The open circuit air-gap flux density of the IPM machine is less than the magnet flux density. Therefore, it is inherently under-excited and the total air-gap flux is summation of the magnet flux and armature reaction [20]. Since the air-gap between rotor and stator in such machine is relatively small, the negative armature reaction can effectively reduce air-gap flux during flux-weakening.

The buried magnet structure also gives the IPM machine a unique feature of inverse saliency i.e. q-axis inductance is larger than the d-axis inductance. Since, the magnet of which the permeability is close to air, lies on the path of the d-axis flux, the magnetic reluctivity of the d-axis flux path is higher than that of the q-axis. Consequently, the d-axis flux-linkage or inductance is lower than the q-axis. The inverse saliency contributes an additive reluctance torque [10]. Thus, the electro-magnetic torque of the IPM machine is of hybrid nature. It is summation of two torque components: one is due to the interaction of the magnet with stator MMF and the other one is the reluctance torque due to the inverse saliency.

1.4.1. Two axes theory of the IPM machine

Like any other salient pole electric machine, the IPMSM is also analysed by two axes theory. The voltage and current equations are derived for the rotor reference frame. As indicated in the Fig. 2.7, the d-axis aligns with the permanent magnet flux linkage ψ_{PM} so that orthogonal q-axis lies along the induced EMF E. The relation between EMF and magnet flux linkage is given as,

$$E = \omega_e \psi_{PM} \tag{2.2}$$

where, ω_e is the electrical speed of rotor in rad/s.

Using Park's transformation, any three-phase quantities can be converted to d- and q-axes quantities. The instantaneous voltages and flux linkages in the d-q-axes are,

$$v_d = R_s i_d + \frac{d\psi_d}{dt} - \omega_e \psi_q \tag{2.3}$$

$$v_q = R_s i_q + \frac{d\psi_q}{dt} - \omega_e \psi_d \tag{2.4}$$

and

$$\psi_d = (L_{ld} + L_{md}) i_d + \psi_{PM} = L_d i_d + \psi_{PM} \tag{2.5}$$

$$\psi_q = (L_{lq} + L_{mq}) i_q = L_q i_q \tag{2.6}$$

where,

R_s : Stator winding resistance [Ω]

i_d, i_q: d and q axes currents [A]

v_d, v_q: d and q axes voltages [V]

ψ_d, ψ_q: d and q axes stator flux linkage [Wb]

L_{ld},L_{lq}:d and q axes leakage inductance[H]

L_{md},L_{mq}:d and q axes stator inductance [H]

L_d , L_q : d and q axis total stator inductances [H]

In the steady-state, the equations are given as,

$$V_d = V_s \sin\delta = R_s I_d - \omega_e L_q I_q \tag{2.7}$$

$$V_q = V_s \cos\delta = R_s I_q + \omega_e (\Psi_{PM} + L_d I_d) \tag{2.8}$$

$$I_d = -I_s \sin\gamma \tag{2.9}$$

$$I_q = I_s \cos\gamma \tag{2.10}$$

The upper case letters indicate steady state voltages and currents. The basic vector diagram of the IPM shown in the Fig. 2.7is obtained from these equations. The Fig. 2.8 shows the d-q axes equivalent circuit of the machine in the synchronously rotating reference frame. Since the d-axis magnet flux-linkage ψ_{PM} (ignoring any variation due to temperature and cross coupling saturation) is constant, it is represented as the constant current source. The rotor equivalent circuit is open and can be omitted when there is no damping effect [23].

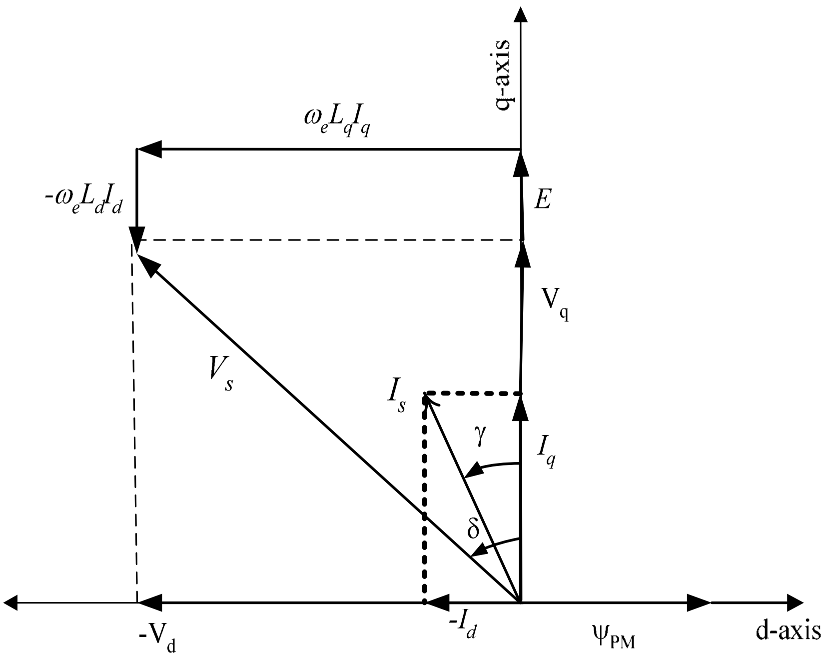

Fig. 1.7 Basic Phasor diagram of the IPM machine

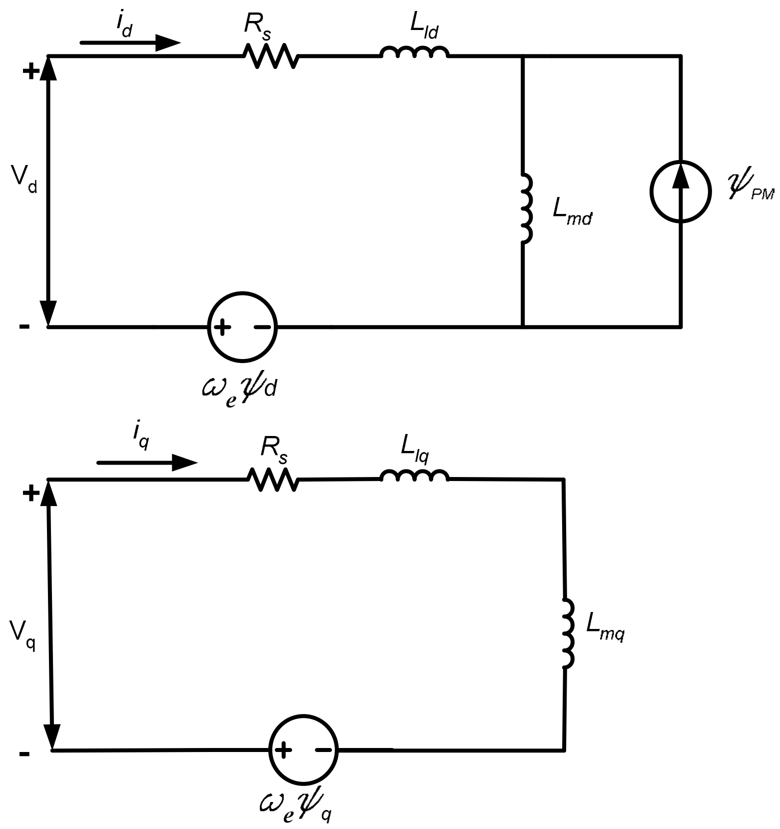

Fig. 1.8 d- and q-axes equivalent circuits of the IPM machine

The well-known electro-magnetic torque equation of the electric machine in the d-q synchronous reference frame is $T = \frac{3}{2} p(\psi_d I_q - \psi_q I_d)$. This equation can be expressed in terms of machine parameters of the IPM machine as,

$$T = \frac{3}{2} p[\psi_{PM} I_q + (L_d - L_q) I_d I_q] \tag{2.11}$$

The first term in the above equation (2.11) of torque, comes from the alignment of magnet with the stator MMF and the second term is due to the reluctance of the flux path. Since, $L_d < L_q$ and current phasor lies in the third quadrant of d-q plane in the IPM machine, the reluctance torque component of the above equation is additive.

1.4.2. Configuration of the Drive System for an IPM machine

In the variable speed applications, the stator terminal voltage and frequency of the IPM machines are varied through the inverter.

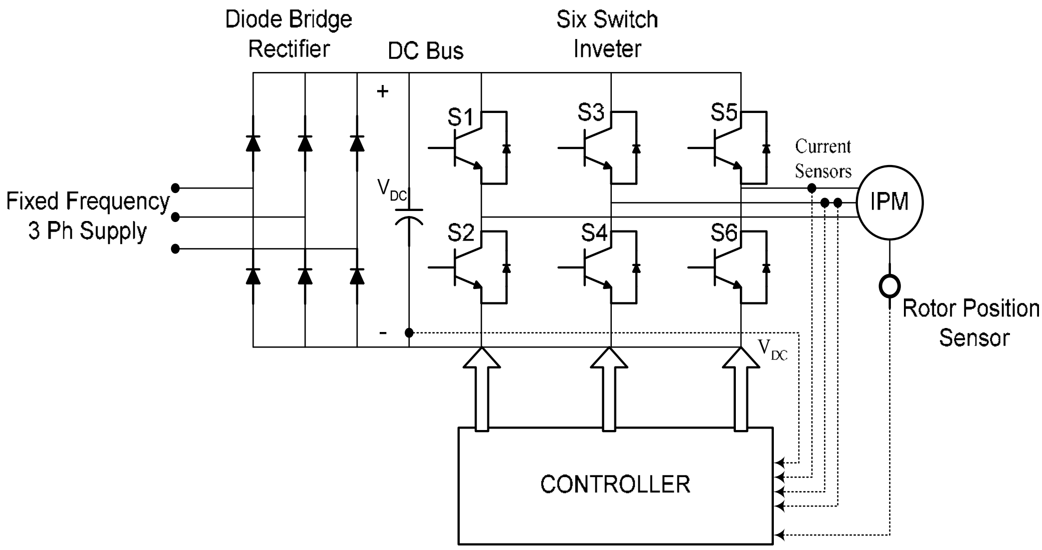

Fig. 1.9 A typical IPM machine Drive System

The pulse width modulated (PWM) scheme is usually used to control the switching signals of the inverter legs. A commonly used arrangement of the IPM machine drive system is shown in the Fig. 2.9. It consists of an uncontrolled rectifier, a DC bus, inverter, the IPM machine, rotor position sensor and the controller. The rectifier is needed when the main supply is from fixed frequency AC source. Otherwise, a DC source such as battery can be used. The six-switch, three-phase inverter changes the DC bus voltage to the variable voltage and variable frequency supply. The semiconductor devices such as IGBT, MOSFET, bipolar transistor and GTO, etc., can be used in the inverter.

There are several different switching schemes for these semiconductor devices. Some of the commonly used schemes are: sub-oscillation method, synchronized carrier modulation and Space Vector Modulation (SVM), etc. In the modern microprocessor based systems, the SVM scheme is preferred because it requires fewer hardware and the modulation ratio can be extended up to 0.907 compared to 0.785 of the SPWM scheme [24].

Space Vector Modulation: In a six switch inverter shown in Fig. 2.9, there exist eight permissible switching states. Voltages are applied to the machine terminals in the first six states (V_1-V_6) whereas the machine terminals are shorted through the upper or lower switches in the remaining two states (V_0 and V_7). It is useful to express these states as voltage vectors which in turn can represent three 120^0 spatially separated voltages V_{an}, V_{bn} and V_{cn} as a space vector V. The Fig. 2.10 shows all these vectors in a voltage plane which is divided in to six sectors. The Table 2-1 summarizes the 8 switching states and magnitudes of their vectors. In order to produce a sinusoidal voltage at motor terminal certain switching rules are followed so that the voltage vector V_x rotate continuously with a smooth transition from one sector to other. The switching time intervals are calculated using (2.17), (2.18) and (2.19).

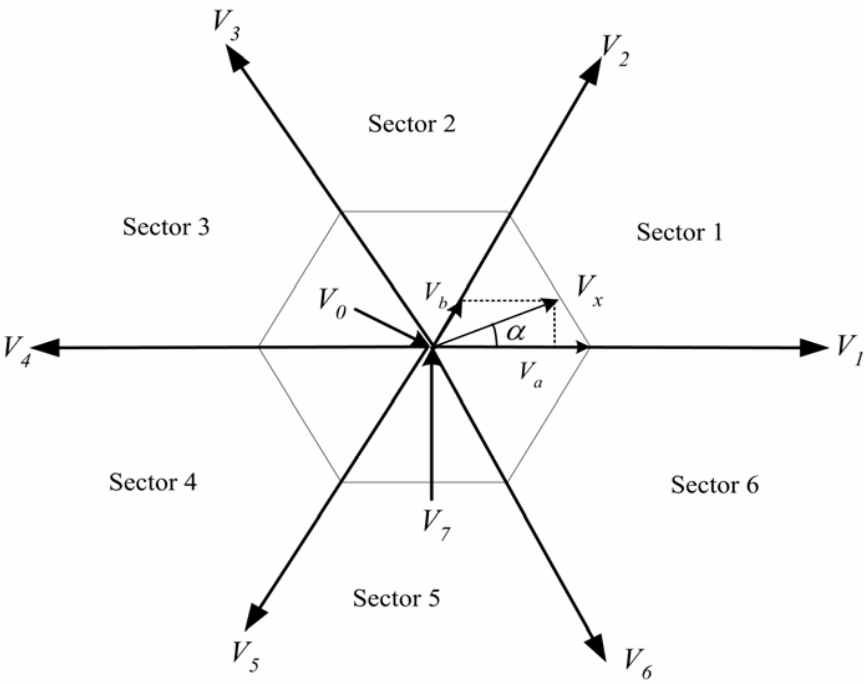

Fig. 1.10 The space vectors of the inverter voltage

Table 1-1 Switching States of the Inverter

State	On Device	V_{an}	V_{bn}	V_{cn}	Space Vector
0	S2,S4,S6	0	0	0	V_0(000)
1	S1,S4,S6	$\frac{2V_{dc}}{3}$	$-\frac{V_{dc}}{3}$	$-\frac{V_{dc}}{3}$	V_1(100)
2	S1,S3,S6	$\frac{V_{dc}}{3}$	$\frac{V_{dc}}{3}$	$-\frac{2V_{dc}}{3}$	V_2(110)
3	S3,S2,S6	$-\frac{V_{dc}}{3}$	$\frac{2V_{dc}}{3}$	$-\frac{V_{dc}}{3}$	V_3(010)
4	S2,S3,S5	$-\frac{2V_{dc}}{3}$	$\frac{V_{dc}}{3}$	$\frac{V_{dc}}{3}$	V_4(011)
5	S2,S4,S5	$-\frac{V_{dc}}{3}$	$-\frac{V_{dc}}{3}$	$\frac{2V_{dc}}{3}$	V_5(001)
6	S1,S4,S5	$\frac{V_{dc}}{3}$	$-\frac{2V_{dc}}{3}$	$\frac{V_{dc}}{3}$	V_6(101)
7	S1,S3,S5	0	0	0	V_7(111)

The relationship between V_x and its components can be found from the Fig. 2.10 and given as:

$$V_x \sin(\frac{\pi}{3} - \alpha) = V_a \sin\frac{\pi}{3} \tag{2.12}$$

$$V_x \sin\alpha = V_b \sin\frac{\pi}{3} \tag{2.13}$$

Therefore,

$$V_a = \frac{2}{\sqrt{3}} V_x \sin(\frac{\pi}{3} - \alpha) \tag{2.14}$$

$$V_b = \frac{2}{\sqrt{3}} V_x \sin\alpha \tag{2.15}$$

where, V_a and V_b are the component of V_x aligned in the direction of V_1 and V_2 respectively. Any voltage V_x can be approximated by switching V_1 for a percentage of time t_a and V_2 for percentage of time t_b over a period of T_0. Thus, V_x can be expressed in terms switching time t_a and t_b for vector addition as,

$$V_x = V_a + V_b = V_1 \frac{t_a}{T_0} + V_2 \frac{t_b}{T_0} + (V_0 \text{ or } \mathrm{V}_7)\frac{\mathrm{t}_0}{\mathrm{T}_0} \tag{2.16}$$

where,

$$t_a = \frac{V_a}{V_1} T_0 \tag{2.17}$$

$$t_b = \frac{V_b}{V_2} T_0 \tag{2.18}$$

$$t_0 = T_0(1 - t_a - t_b) \tag{2.19}$$

This process is repeated in each sector. With the knowledge of t_a and t_b, a switching pattern such as shown in the Fig. 2.11 can be constructed for a time period of $T_s = 1/f_s$, where f_s is the switching frequency. The reference voltage signal of PWM generation comes from the controllers. Thus, the voltage and frequency of the machine terminal can be varied in accordance with the operating requirements.

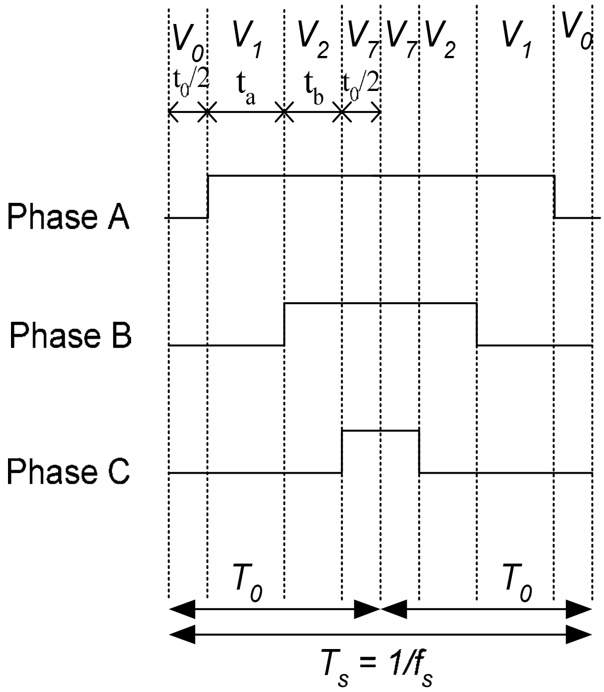

Fig. 1.11 The generated switching pulse from the SVM scheme

1.4.3. Basic Control of the IPM Drive

The reference voltage signals of the PWM generation can be derived from various control schemes such as open/close loop current vector control [23, 25, 26] and direct torque control (DTC) [27]. Since the average torque can be produced only when the stator excitation is precisely synchronized with rotor frequency and instantaneous position, the information of rotor position sensor is essential in these schemes. The Hall-effect transducer, optical encoder and resolver, etc., are used as rotor position sensor in the PM machine drive. The rotor position sensor causes additional cost and requires special mounting arrangement in the rotor shaft. Hence, it is sometime cited as limitation of the PM machine drive. In recent years position sensors-less schemes are also being developed [28-31]. However, in this work, the current vector control technique with position sensor has been exclusively used. The discussion about sensor-less techniques is out of scope of this work.

In the vector control, actual phase currents are measured and compared to the reference currents that are derived from either torque or speed command. The current controllers can be hysteresis or PI controller. The hysteresis controllers are simple and provide good current amplitude control, but the major disadvantage of such controller is the variable PWM switching rate and presence of lower frequency harmonics in the output waveform. On the other hand, PI controllers are robust and can provide constant switching frequency PWM.

The phase current of the IPM motor is controlled in the rotating dq-reference frame. For a balanced 3-phase system, only two current controllers are necessary. The third phase current is computed from the summation of the two measured currents. By this way, the problem of unwanted zero sequence component caused by errors in the current sensors can be eliminated effectively. The measured phase currents are transformed into the rotor reference frame quantities by Park's transformation. In the steady-state, dq-axes quantities become DC signals. Consequently, it is possible to achieve fast response time and zero steady-state error using simple PI controllers. The block diagram of basic vector control is shown in Fig. 2.12. Some of the well-known control schemes are: unity power factor control, maximum efficiency control, Maximum Torque per Ampere (MTPA) control and flux or field- weakening control. The high performance drives require maximum torque per ampere and many applications also need the machines to run above their base speed which requires flux-weakening control.

In the basic vector control scheme, the reference current i^* and current angle γ comes from a speed, position or torque controller. It is then compared to the measured quantity and the error signal is used in PI controller to generate the reference voltage vector for PWM switching.

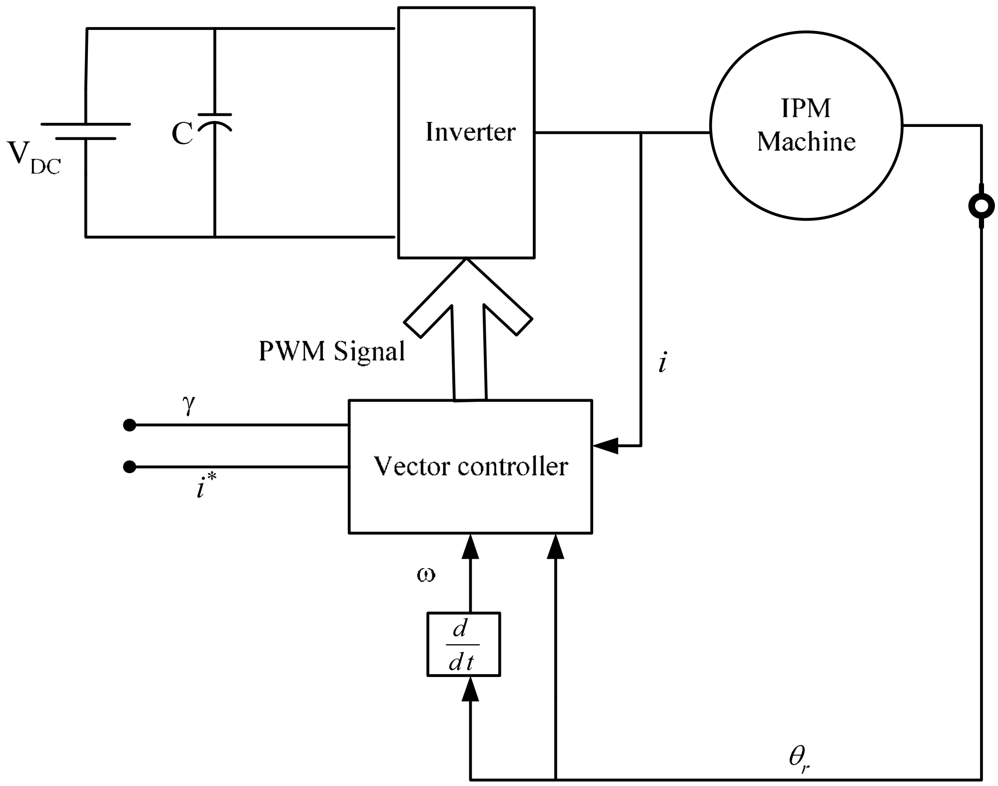

Fig. 1.12 Block diagram of basic vector control of the IPM machine

The control scheme must operate within the voltage and current limit of the system for the satisfactory performance of the drive system. The current limit in the drive system comes from the rating of the machine and inverter switches. On the other hand, voltage is limited by the available DC link voltage of the system which overcomes the back EMF, reactance and resistance drops of the machine [25, 32].

The locus of the current limit in the d-q plan forms a circle and it is described as,

$$I_s = \sqrt{I_d^2 + I_q^2} \le I_{sm} \qquad (2.20)$$

The voltage limit is expressed as,

$$V_s = \sqrt{V_d^2 + V_q^2} \leq V_{sm} \tag{2.21}$$

The equation (2.21) can also be expressed in terms of machine parameters as,

$$\sqrt{(\omega\psi_{PM} + \omega L_d I_d)^2 + (\omega L_q I_q)^2} \leq V_{sm} \tag{2.22}$$

The loci of voltage limits for various speeds in I_d and I_q plane gives a series of concentric ellipses, centre of which lies at $(-\frac{\psi_{PM}}{L_d}, 0)$. Since, machine terminal voltage grows toward the limit value with increasing speed, the voltage limit ellipses shrinks. The current control of the IPM machine will be discussed further in chapter 5.

The maximum torque per ampere algorithm is applied until the terminal voltage of the machine becomes equal to the voltage limit of the system. The maximum speed up to which the constant maximum torque is available is known as base speed of the machine. The terminal voltage of the machine will be higher than the system limit voltage above this speed without flux-weakening. The flux-weakening, in the wound rotor synchronous machine or in the DC machine, is achieved by reducing the field current. However, in a PM machine, the field is constant which comes from the rotor magnet; hence, the direct reduction of the rotor magnet field is not possible. The principle behind the flux-weakening of the PM machine is discussed in the following section.

1.5. Flux-weakening and Constant Power Operation

The flux-weakening of the electric machine is synonymous to its constant power operation. Ideally, a constant torque is available in the electric machine from zero to the rated speed. In this speed range, the power increases steadily and reaches the rated value at the base speed. Above the base speed, power remains constant till the maximum speed of the machine. The ideal torque- and power-speed characteristics of an electric machine are shown in Fig. 2.13. However, a real machine does not have an ideal flat power against speed characteristic. Due to the less than unity inverter utilization factor, mechanical/electrical losses and less than unity power factor, a real machine operates somewhat lower than its ideal power rating. The power remains constant only up to a certain speed above which power falls sharply and becomes zero at maximum speed. The power-speed characteristic of a real machine is shown in Fig. 2.14. The speed range over which constant rated power can be maintained is known as Constant Power Speed Range (CPSR). Some of the high performance applications such as traction in the hybrid vehicle, Integrated Starter Alternator (ISA), etc., favour a highly efficient electric machine with a very wide CPSR, so that required rating of the electric machine can be lowered for energy saving [8, 33, 34] .

The permanent magnet machines are considered to be one of the most efficient ones. A PM machine drive with wide CPSR should be ideal for the above mentioned applications. However, the constant power and flux-weakening operation are not direct in the PM machines due the permanent magnet excitation. The air-gap flux of the PM machine can be effectively reduced by the negative armature reaction.

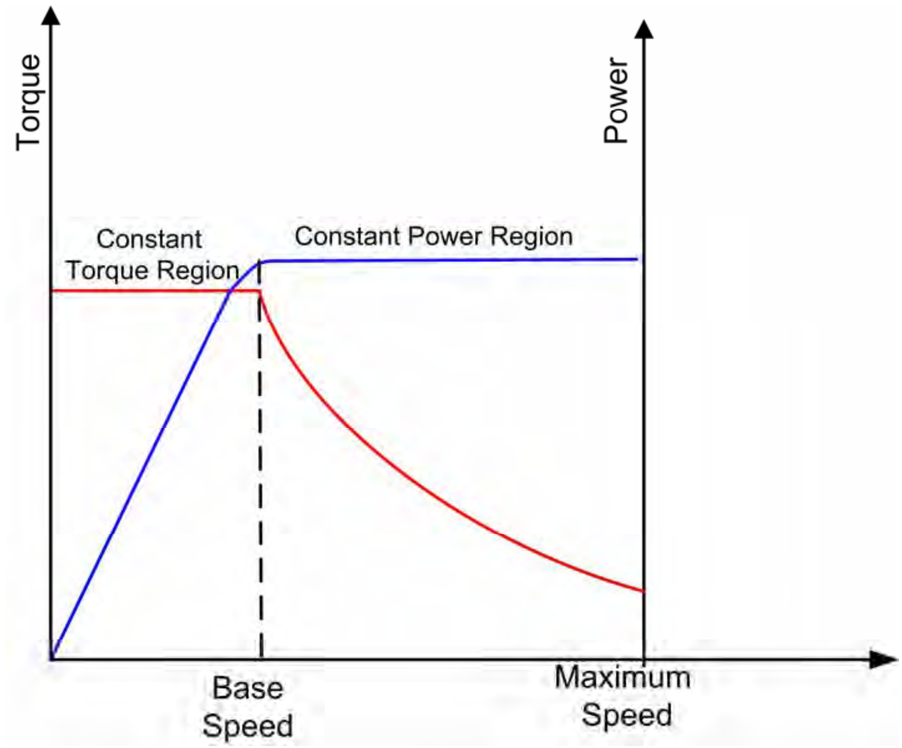

Fig. 1.13 Ideal torque- and power-speed characteristic of an electric machine

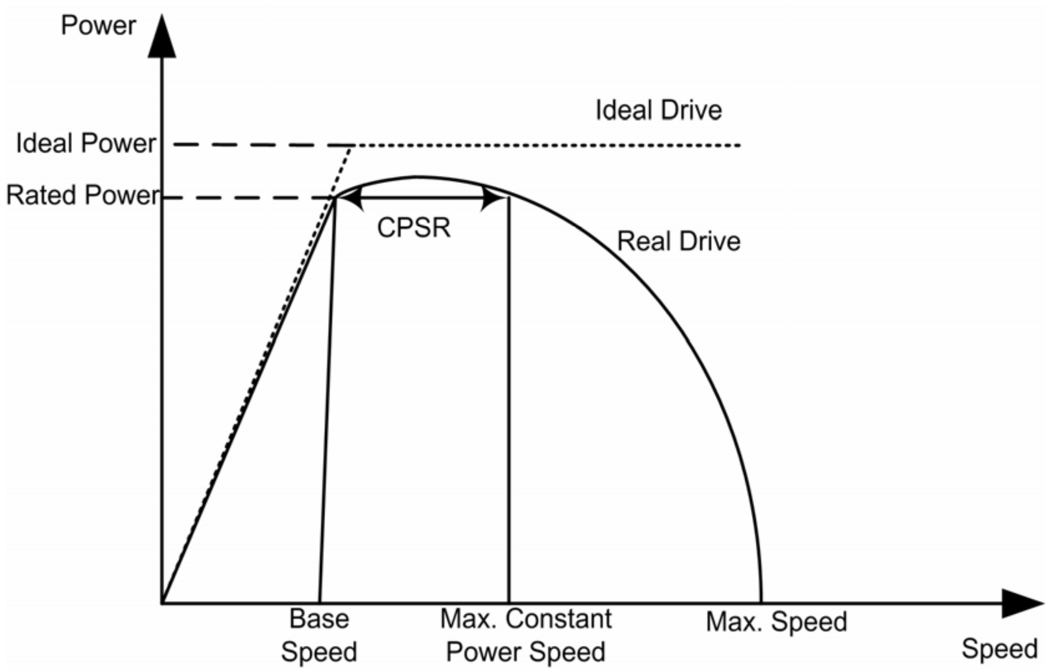

Fig. 1.14 Power Speed characteristic of a real electric machine

1.5.1. Principle of flux weakening in the IPM machine

The concept of flux-weakening in the electric machine has come from the separately excited DC machine which has decoupled torque and flux components of current. By reducing the field current at high speed, magnetic flux in the DC machine is reduced so that terminal voltage can be maintained at the rated value for higher than rated speed. In the PM machine, the rotor field is produced by the permanent magnet; hence, the field can not be reduced directly. However, by imposing a negative d-axis armature reaction, resultant air-gap flux of a PM synchronous machine can be weakened effectively. The concept can be explained with help of the Fig. 2.15. The d-axis of the PM machine is defined in such a way that the magnet flux linkage ψ_{PM} aligns with it and the phasor of induced EMF lies 90^0 ahead of it on the q-axis. In the motoring operation, the current phasor lies in the third quadrant of the d-q-plane. Hence, the current has a positive q-component and a negative d-component. The negative flux contribution of the d-axis current offsets the constant magnet flux. By increasing the negative d-axis current, the magnet flux-linkage can be reduced further.

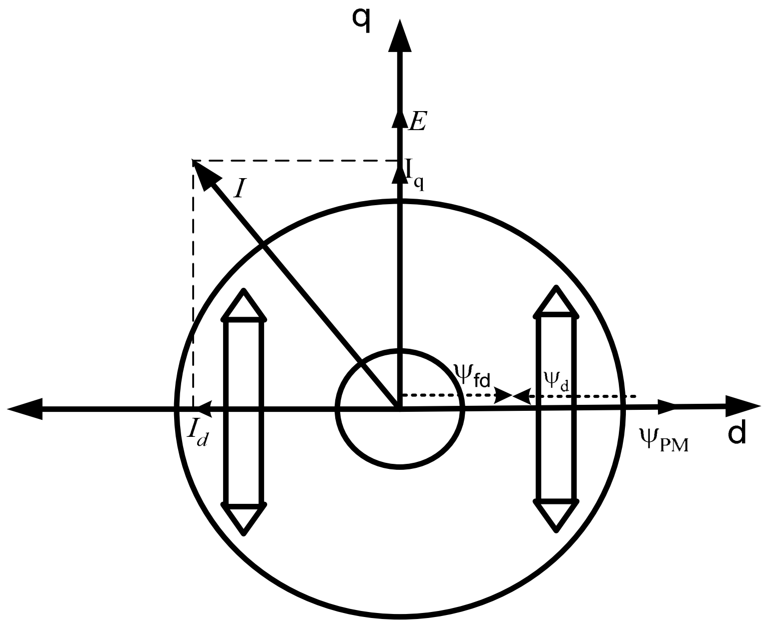

Fig. 1.15 Flux-weakening of the PM machine

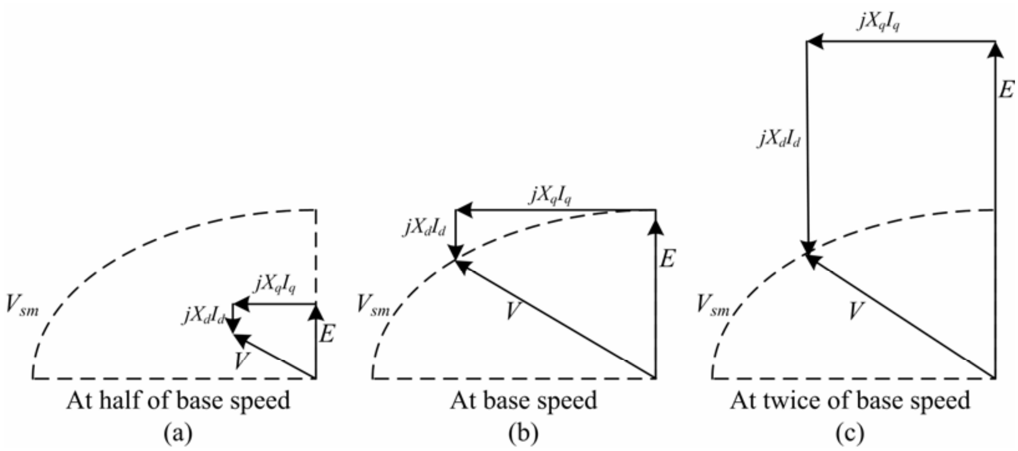

Fig. 1.16 Voltage phasor of an IPM machine at three different speed conditions

The effective flux-weakening can also be explained with help of the voltage vector diagram of Fig. 2.16. The amplitude of terminal voltage of an IPM machine when the resistive drop is ignored is given by (2.23). This terminal voltage must be less than equal to the system voltage limit V_{sm} at all operating speed.

$$|V| = \omega_e \sqrt{(L_q I_q)^2 + (\psi_{PM} - L_d I_d)^2} \leq V_{sm} \tag{2.23}$$

It is obvious from (2.23) that the terminal voltage V is directly proportional to speed ω_e. Hence, the terminal voltage starts to grow with rising speeds. Below base speed as shown in the Fig. 2.16(a), the terminal voltage is lower than the limit value. At the base speed the terminal voltage attains the limit value as shown in the Fig. 2. 16(b). Once the terminal voltage reaches its limit, speed can be increased further only if the negative d-axis reactive drop is big enough (as shown in the Fig. 2.16(c)) to keep the terminal voltage constant at the limit value. In other words, the negative d-axis current needs to increase for the effective flux-weakening. The flux-weakening control algorithm calculates the required increase in the negative d-axis current and rotates the current vector. The flux-weakening control technique for the vector controlled IPM machine is discussed further in chapter 5.

1.5.2. Optimal Flux weakening conditions

An electric machine said to have optimum flux-weakening when it has a CPSR that spreads out to the infinity. The condition of such an operation for the IPM machine can be derived from the per unit (pu) voltage and power equations when losses and saturations are neglected [11].

$$V_{p.u} = \omega_{pu}\sqrt{(E_0 - X_d I_{p.u}\sin\gamma)^2 + (X_q I_{p.u}\cos\gamma)^2} \tag{2.24}$$

$$P_{p.u} = \omega_{pu}[E_0 I_{p.u}\cos\gamma + \frac{(X_q - X_d)}{2} I_{p.u}^2 \sin\gamma] \tag{2.25}$$

where, V_{pu}, I_{pu} and P_{pu} are the pu terminal voltage, line current and shaft power respectively, X_d and X_q are the normalized d- and q-axis reactances, ω_{pu} is the pu speed and E_0 is the normalized induced back EMF. Here, the rated voltage and current are taken as the base quantities.

In a real machine, the output shaft power is zero at its maximum speed. In other words, the machine is unable to provide any output power above this speed without raising its terminal voltage. This situation occurs when current phasor angle γ becomes 90^0. Therefore, for any IPM machine the maximum pu speed for 1 pu voltage can be derived from (2.24) by substituting $\gamma = 90^0$.

$$\omega_{pu(\max)} = \frac{1}{\left|E_0 - X_{ds} I_{pu}\right|} \tag{2.26}$$

Thus, for infinite CPSR,

$$E_0 = X_d I_{pu}$$
or, (2.27)
$$\psi_{PM} = L_d I_{sm}$$

where, I_{sm} is the rated current of the machine. The power capability curve of an IPM machine with optimum flux-weakening condition is shown in Fig. 2.17.

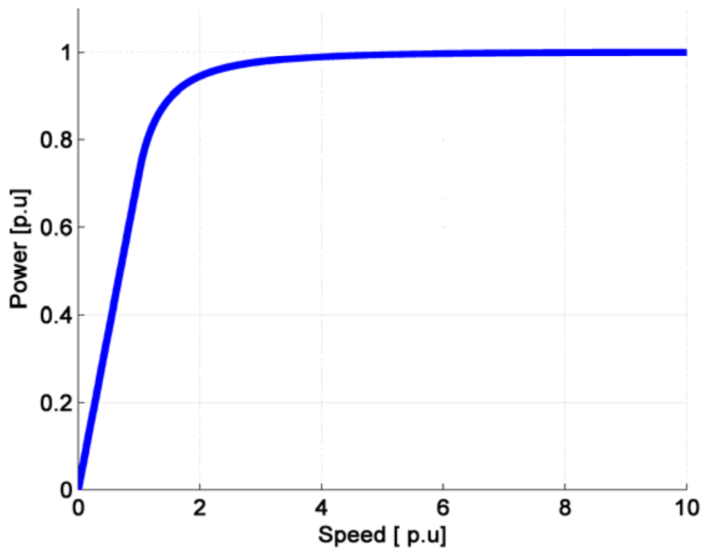

Fig. 1.17 Optimal Power Capability of an IPM machine

The torque equation of the IPM motor in terms of saliency ratio $\xi = \dfrac{L_q}{L_d}$ is given by,

$$T = \frac{3}{2} p \left[\psi_{PM} I_q - L_d (1-\xi) I_d I_q \right] \tag{2.28}$$

The higher is the ratio ξ, better is the contribution of the reluctance torque in the machine. In the flux-weakening mode, the air-gap flux reduces and the available torque decreases proportionally. Since the reluctance torque of the IPM machine is additive, it can provide useful shaft torque in the extended speed range during flux-weakening. A torque- and power-speed characteristic of the IPM machine with and without reluctance torque components are shown in Fig. 2.18.

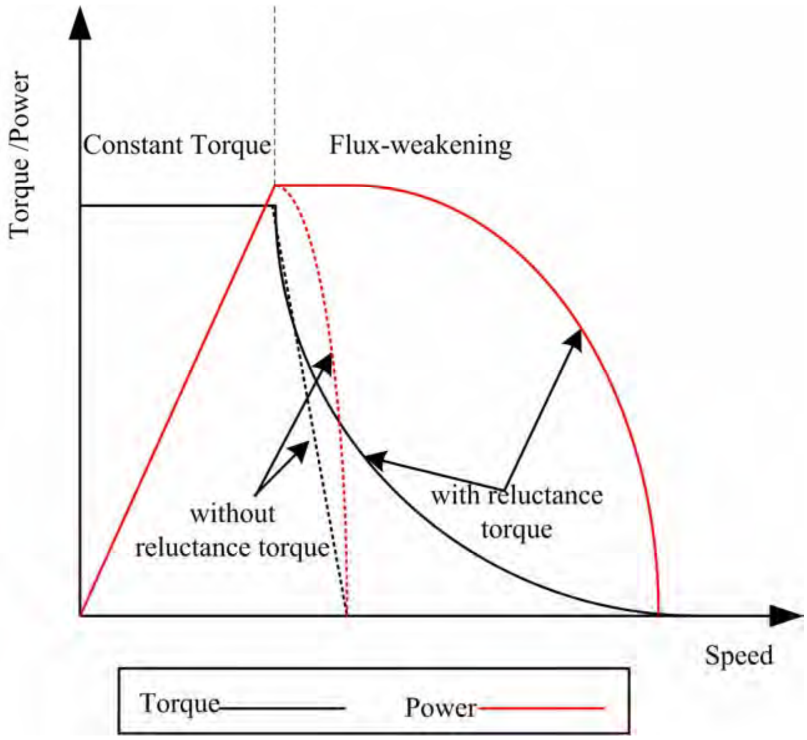

Fig. 1.18 Effect of reluctance torque during flux-weakening

1.5.3. Practical limitations and factors

A number of assumptions have been made while deriving the optimal flux-weakening condition above. For example, the stator copper and core losses were assumed negligibly small, magnet flux-linkage is assumed to be constant in all operating conditions, and the effect of saturation and d-q axes cross-coupling are neglected. However, in a real machine these assumptions are not always correct. The presence of losses in the practical machine reduces the output power but does not have any first order effect on CPSR. The magnetic saturation and cross-coupling affects the value of d- and q-axis inductances. Saliency ratio reduces at high current due to q-axis saturation which in turn decreases the output torque. The saturation also causes premature increase in the current angle γ. As a result, it can approach to 90^0 earlier than anticipated. This leads to a reduced CPSR in the IPM machine [35]. Thus, the infinite CPSR is not possible for any IPM machine in reality. In fact, achieving a reasonably high CPSR ratio is a challenge for the IPM machine designers.

1.6. Segmented IPM Machine

Most of the commercially available IPM machines from Kollmorgen and Yaskawa Corporation offer very small CPSR. These IPM machines have tangential magnets in the rotor configuration with radial lamination as shown in Fig. 2.5. Although, it is a cost-effective and easy-to-construct design, the performance of the machine deteriorates quickly above base speed. Therefore, this type of IPM machine is not suitable for applications that require constant power for a wide speed range.

In order to extend the CPSR operation in the IPM machine, a number of different rotor configurations have been investigated in the last couple of decades. Among them, the axially laminated IPM machine and double magnet layer IPM machine show promising results of wider CPSR [13, 36]. In these two IPM machines (cross-sections are shown in Fig. 2.5), the saliency ratio ξ is improved by providing additional path to q-axis flux. As a result, higher reluctance torque contribution was achieved during flux-weakening which in turn has extended the CPSR in these IPM machines. However, the construction of axially laminated IPM machine is complicated and expensive [13]. On the other hand, the double magnet layer IPM machines are heavily saturated in q-axis which leads to reduction of saliency ratio at high speed and high current operation [14, 37].

The search for an IPM machine with wide flux-weakening capability has led B. Ŝtumberger et al. to propose a new IPM machine design concept in [19]. In the proposed machine, magnet of each pole is segmented and between each segment there exists a rotor iron bridge. Because of its segmented magnet poles structure, we will call this type of IPM machine as '**Segmented IPM (SIPM) Machine**' in this work. The cross-section of such an IPM machine is shown in Fig. 2.19. This type of IPM machine is capable of a very wide flux-weakening range. Since the lamination structure is very close to the commercially available IPM machine, the segmented IPM machine has an easy-to-construct configuration. Moreover, the high saturation of q-axis seen in the double magnet layer configuration can be avoided to some extent by careful positioning of the magnets. Although, the total q-axis flux path is enhanced in the double magnet-layer IPM machines, the cross-sectional area of individual path is relatively smaller than that of the segmented IPM machine. Hence, the saturation of q-axis in the double magnet-layer IPM machine will be relatively higher than that of the segmented IPM machine. The following section analyses the flux-weakening capability of the segmented IPM machine.

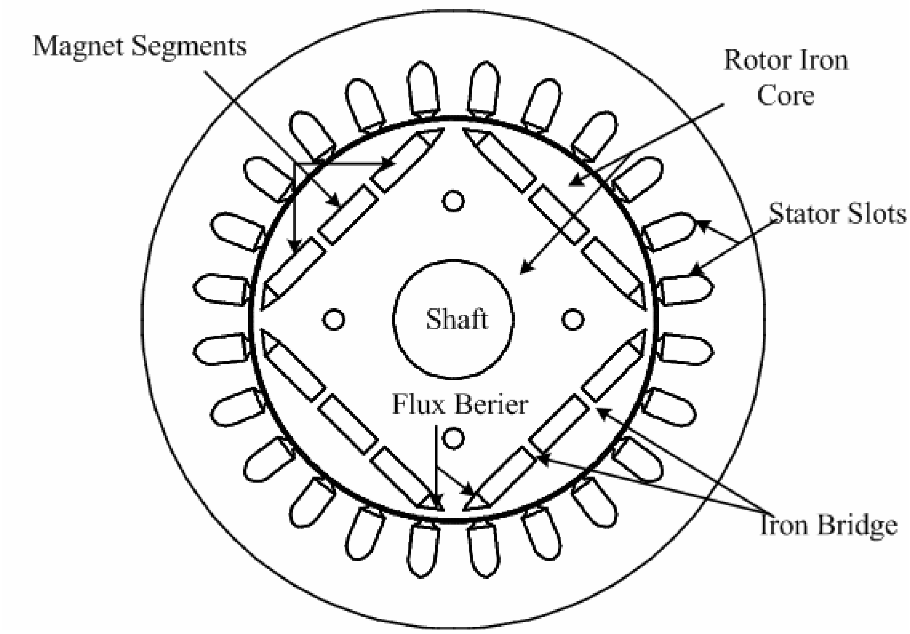

Fig. 1.19 Detailed cross-sectional view of a segmented IPM machine

1.6.1. Flux-weakening in the segmented IPM machine

Due to its segmented poles and iron bridges, the segmented IPM machine has an inherent flux-weakening capability. Like any other IPM machine, here too the negative d-axis armature reaction is used to weaken the air-gap fluxes, but at the same time it also assists to alter the path of some magnet fluxes. As a result, higher flux-weakening is possible in the segmented IPM machine for the same amount of negative d-axis current compared to a conventional, non-segmented, one-magnet-layer, radially-laminated IPM machine [38]. The magnet leakage fluxes canalize in the iron bridges which exist between the magnet segments and is shown in the Fig. 2. 20(a). The flux produced by the negative d-axis armature reaction crossing the iron bridges in absence of the magnet leakage flux is shown in the Fig. 2. 20(b).The armature reaction of the negative d-axis current tries to inhibits the magnet flux to cross the air-gap and thus encourages more magnet flux to canalize at the iron bridges.

Consequently, magnet flux crossing the air-gap reduces, resulting in a reduced air-gap flux density.

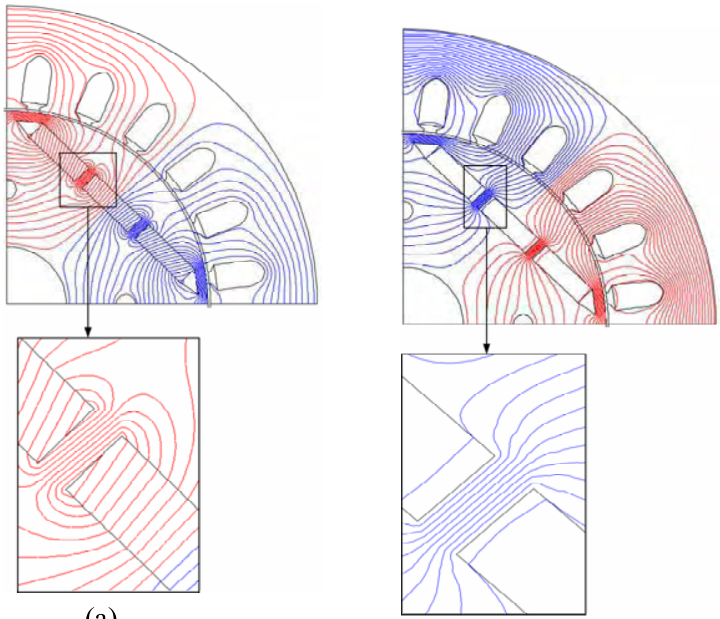

(a) (b)

Fig. 1.20 (a) Magnet flux path in the iron bridge between segments (b) d-axis

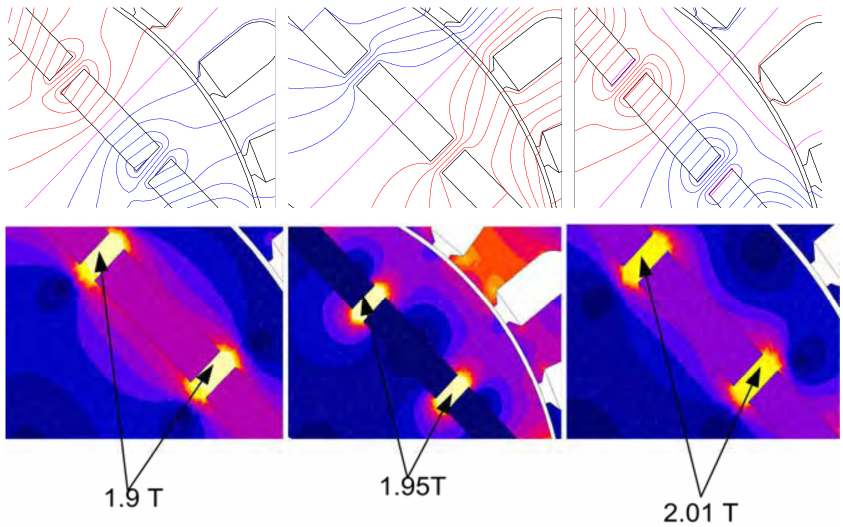

(a) (b) (c)

Fig.2.21 (a)Magnet leakage flux in the iron bridges (b)Negative d-axis current flux in the bridges (c) Magnet and negative d-axis fluxes in the bridges

The flux-density in the bridges increase with negative d-axis current by the additional magnet flux leaked in to the bridges. The figure above shows the flux path and flux-density at the bridges for three conditions- a) when only magnet flux is present b) when only negative d-axis current is present and c) when both magnet and the negative d-axis current field are present.

In order to show that the segmentation of the rotor pole magnet provides for an inherent flux-weakening capability the reduction of the air gap flux density by the negative d-axis current were calculated for both a non-segmented IPM machine and segmented IPM machine. The non-segmented IPM machine of the fig.2.22(b) is identical in all aspects to the segmented IPM machine of the fig.2.22(a) except iron bridges in the pole magnet.

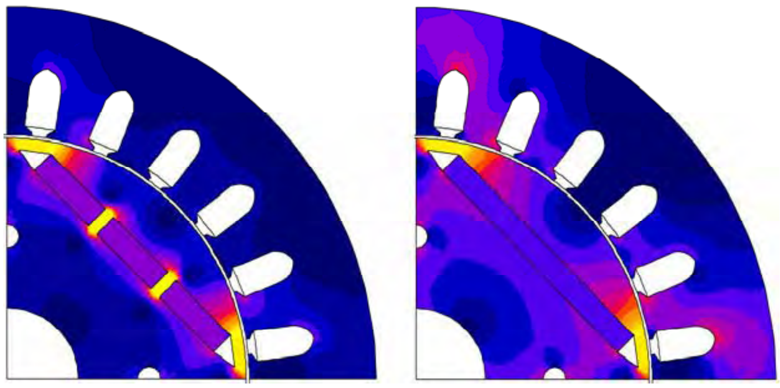

(a) (b)

Fig. 2.22 Flux density colour plot(a) Segmented IPM rotor (b) Non segmented IPM rotor

The fig.2.23 shows the air gap flux density of the segmented and non-segmented IPM machine with d-axis current I_d =-14A and -4A. The peak fundamental values of the air gap flux density at open circuit condition for both the rotor structures are also calculated. The table 2-2 compares peak fundamental flux-density of the segmented and non-segmented IPM machine for open circuit condition, and also for flux-weakening condition with rated d-axis current.

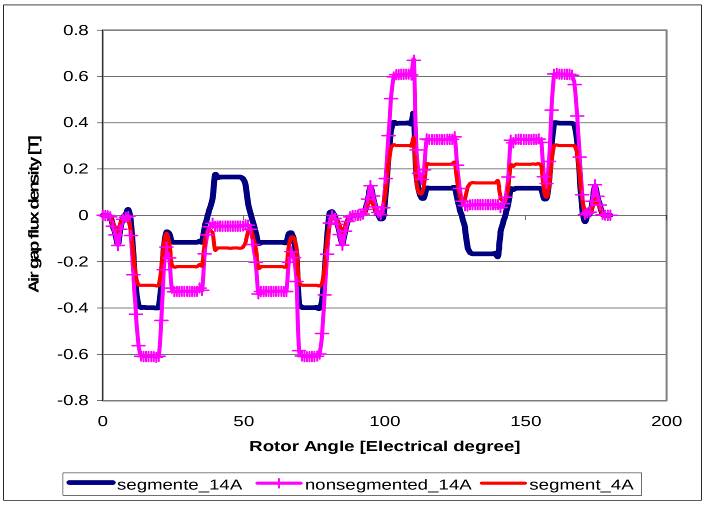

Fig.2.23 The air gap flux density of the segmented and non-segmented IPM

Table 2-2 Comparison of the peak fundamental air gap flux densities

	Non-segmented IPM Machine	Segmented IPM machine
With Magnet alone	0.494 T	0.227 T
With magnet and Id=-14A	0.329 T	0.111 T
Reduction	33%	51%,
With magnet and Id=-4A	-	0.229 T

Due to the leakage in the additional iron bridges and reduced magnet length the air gap flux density of the segmented IPM machine is lower than that of the non-segmented IPM machine. The percentage reductions of the peak fundamental air gap flux density by negative d-axis current I_d = -14 are also compared in the table 2-2 and it is seen that a higher reduction can be achieved in the segmented structure than that of the non-segmented IPM machine with the same negative d-axis current.

Fig.2.23 The air gap flux density of the segmented and non-

This comparison clearly shows that higher reduction of the air-gap flux density in the segmented IPM machine is possible because of the iron –bridge between two adjacent magnet segments.

The optimum condition of flux-weakening is satisfied when the ratio of magnet flux linkage to d-axis inductance is equal to the system limit current i.e. $\frac{\psi_{PM}}{L_d} = I_{sm}$.

In the segmented rotor structure, due to the iron bridges the ψ_{PM} is lower whereas value of L_d is relatively higher because of the addition d-axis paths provided by the iron bridges. This indicates a reduced characteristic current (the ratio $\frac{\psi_{PM}}{L_d}$ is also known as characteristic current). If the characteristic current is lower than the system limit current, theoretically the constant power speed range can be extended to infinity. Moreover, by varying the width of the iron bridges the ratio $\frac{\psi_{PM}}{L_d}$ can be adjusted which provides an additional flexibility to the designer of the high flux-weakening IPM machine.

Quantitively, the flux-weakening in the segmented IPM machine can be explained with help of the voltage equation of the IPM machine.

$$V = \sqrt{V_d^2 + V_q^2} = \omega_e \sqrt{(L_q I_q)^2 + (\psi_{PM} - L_d I_d)^2} \tag{2.29}$$

During flux-weakening of the segmented IPM machine, when the negative d-axis current increases, $L_d I_d$ increases and the magnet flux-linkage ψ_{PM} reduces since more magnet fluxes canalize in the iron bridges. This results in a larger reduction of the second term in (2.29). Thus, higher level of flux-weakening can be achieved in the segmented IPM machine for the same amount of negative d-axis current.

The power capability curve of the IPM machine can be estimated from machine parameters using a procedure described by Schiferl et al. in the [11]. The rated voltage and current of the machines are considered as the base quantities for the p.u system. The speed at which the back EMF of the machine becomes 1 pu, is taken as the base speed. This process will be discussed in detail in chapter 4. The calculated power capabilities of a prototype segmented IPM machine compared with two other conventional non-segmented IPM machines (IPM machine-I and commercially available Kollmorgen IPM machine) of similar rating are shown in the Fig. 2.24. The figure shows clearly that among the three machines the proposed Segmented IPM machine has the widest constant power operation range.

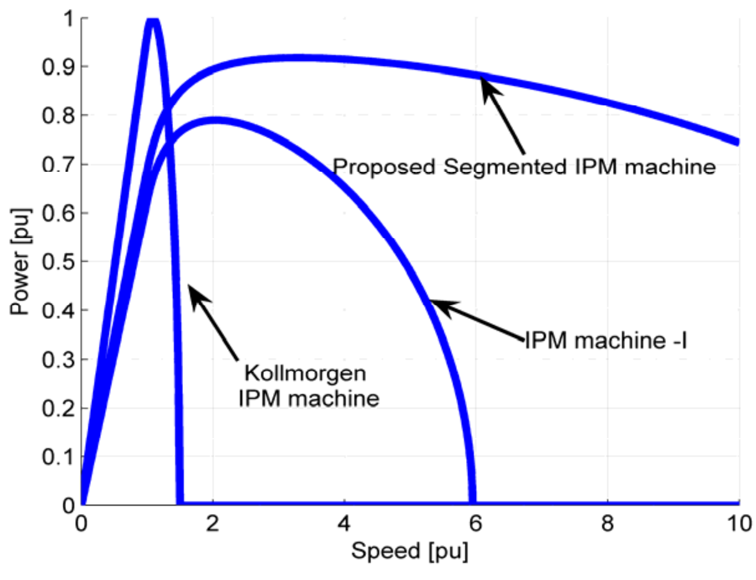

Fig. 1.21 Comparison of theoretical Power capability of Segmented Magnet

1.7. Conclusion

In this chapter, the Interior Permanent Magnet machine technology was reviewed in detail. The dynamic model of the IPM machine, its voltage and torque equations are also discussed. The basic IPM drive system and its control techniques are also discussed. The theory and limitations related with the flux-weakening of the conventional IPM machine are reviewed. A new design concept of segmented IPM machine for improving the flux-weakening capability of the radially laminated IPM machine was introduced. In chapter 4 the evolution of this concept for a prototype Segmented IPM machine is presented.

CHAPTER 3

3. Numerical Techniques used for Performance Prediction and Analysis of the Interior Permanent Magnet Machine

3.1. Introduction

Accurate prediction and detailed electro-magnetic analysis are necessary during development of a prototype design so that any kind of oversight that could prove costly after actual construction can be avoided beforehand.

The working principles of electrical machines can be described as the interaction of electromagnetic fields. On the other hand, an electromagnetic phenomenon can be expressed in mathematical form by Maxwell's electromagnetic equations. These equations are solved by various methods. These methods can be grouped into analytical and numerical methods. The example of the analytical methods includes lumped parameter model and equivalent circuit method whereas the numerical methods consist of the finite differential and finite element methods etc.

The analytical methods are considered to be inadequate when the problem involves magnetic saturation and complex geometry. The numerical methods are better equipped to handle such difficult problems. Among the various numerical methods, the finite element method (FEM) is widely used because of its flexibility and reliability.

The FEM can estimate the effect of armature reaction, winding inductances, core losses and cogging torque of the permanent magnet (PM) machine quite accurately [21]. The effect of rotating air-gap over the electromagnetic field can also be assessed when time-stepping FEM is used. The developed torque and power at various speeds can be calculated from FEM with fair accuracy.

This chapter discusses the theory behind the finite element analysis of two-dimensional electromagnetic field which was used to evaluate the proposed prototype IPM machines.

3.2. Finite Element Method (FEM)

In the finite element method, complexity of a problem is minimized by dividing the study domain into finite elements of simpler geometric shapes and then the partial differential equations related to these elements are solved by the numerical techniques. The finite element analysis of a physical event consists of following general steps:-

- Representation of the physical event in mathematical model
- Construction of the geometry and its discretization to finite elements (also known as 'Mesh Formation' of the study domain)
- Assignment of material properties to various regions
- Assignment sources of excitation (if present)
- Assignment of boundary conditions
- Derivation and assembling of the element matrix equations
- Solution of the equations for unknown variables
- Post processing or analysis of results obtained

Some these procedures are discussed in detail in subsequent sections. The basis of following sections are derived from [6, 39-41].

3.2.1. Basic Principle

In the finite element method, unknown parameters are determined from minimization of energy functional of the system. The energy functional consists of various physical energies associated with a particular event. According to the law of conservation of energy, unless atomic energy is involved, the summation of total energies of a device or system is zero. On basis of this universal law, the energy functional of the finite element model can be minimized to zero. The minimum of energy functional is found by equating the derivative of the functional with respect to unknown grid potential to zero i.e if F is the functional and p is the unknown grid potential then the unknown potential p is found from the equation $\frac{\partial F}{\partial p} = 0$. The solutions of various differential equations of physical models including electro-magnetic system are obtained using this basic principle.

3.2.2. Maxwell's equations

The governing laws of electromagnetic field problems can be expressed with well-known Maxwell's equation in differential form. These are given as,

$$\nabla \times \vec{H} = \vec{J} + \frac{\partial \vec{D}}{\partial t} \tag{3.1}$$

$$\nabla \vec{B} = 0 \tag{3.2}$$

where, $\vec{H}$ is magnetic field intensity [A/m], $\vec{B}$ is magnetic flux density [T], $\vec{D}$ is Electric flux density [coulomb/m^2] $\vec{J}$ is electric current intensity [A/m^2] and $\nabla = \vec{1}_x \frac{\partial}{\partial x} + \vec{1}_y \frac{\partial}{\partial y} + \vec{1}_z \frac{\partial}{\partial z}$ is the operator del.

Each of the above electro-magnetic quantities can be a function of three space coordinates *x*, *y*, *z* and time *t* but in steady state condition $\frac{\partial}{\partial t}$ part is zero and for such condition Maxwell's equation can simply be expressed as,

$$\nabla \times \vec{H} = \vec{J} \tag{3.3}$$

A field problem is greatly simplified when solved for the field potentials rather than the field itself [41]. In order to take the advantage of this simplification, the magnetic potential A is introduced from the vector identity of (3.4) in electromagnetics.

$$\nabla . \nabla \times \vec{A} = 0 \tag{3.4}$$

It is true for any vector A and ascertains that (3.2) will always be satisfied when flux density $\vec{B}$ is expressed in terms of vector potential A as,

$$\vec{B} = \nabla \times \vec{A} \tag{3.5}$$

The magnetic materials can be represented as function of $\vec{B}$ and $\vec{H}$,

$$\vec{B} = \mu \vec{H} \quad \text{or,} \quad \vec{H} = \nu \vec{B} \tag{3.6}$$

where, μ and ν are permeability and reluctivity of magnetic materials respectively. In case of ferromagnetic material, the *B-H* relationship is nonlinear whereas for rare earth permanent magnet material, the relationship is linear as shown in the Fig. 3.1. The equation (3.6) can also be expressed in terms of relative permeability and reluctivity [42]. It is given as,

$$\vec{B} = \mu_r \mu_0 \vec{H} \text{ and with permanent magnet } \vec{B} = \mu_r \mu_0 \vec{H} + \vec{B}_r \quad \text{or,} \quad \vec{H} = \nu_r \nu_0 \vec{B} \text{ and with permanent magnet } \vec{H} = \nu_r \nu_0 \vec{B} - \vec{H}_c \tag{3.7}$$

Substituting (3.7) and (3.5) to (3.3), Mexwell's *curl* equation for permanent magnet machine can be obtained as,

$$\nabla \times \left[\nu_0 \nu_r \left(\nabla \times \vec{A} \right) - \vec{H}_c \right] = \vec{J} \tag{3.8}$$

The three components of vector B in Cartesian coordinate system from (3.5) are,

$$\begin{aligned} B_x &= \frac{\partial A_z}{\partial y} - \frac{\partial A_y}{\partial z} \\ B_y &= \frac{\partial A_x}{\partial z} - \frac{\partial A_z}{\partial x} \\ B_z &= \frac{\partial A_y}{\partial x} - \frac{\partial A_x}{\partial y} \end{aligned} \tag{3.9}$$

In the electric machine, the air-gap between stator and rotor is very small over the entire axial length except at the end-turn region. In other words, the magnetic field is virtually two-dimensional at the study domain provided the effect of end-turn region is negligible. Therefore, use of 2D finite element analysis for most of the electric machines is justifiable [6]. Additionally, 2D FEM requires less computing memory, power and time compared to 3D FEM.

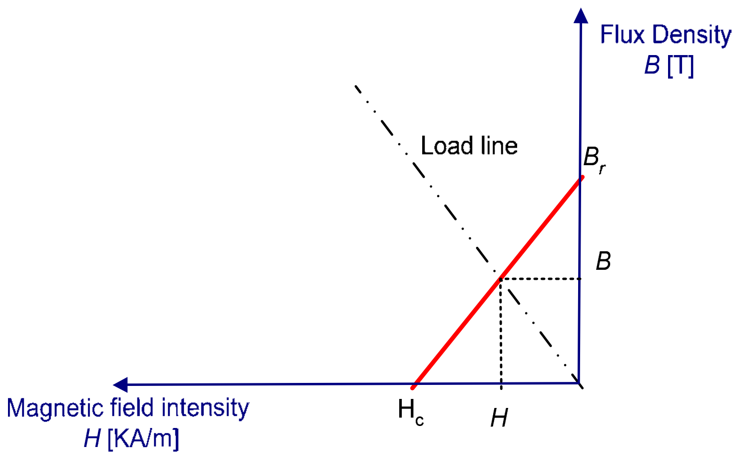

Fig. 3.1 *B-H* characteristic of rare-earth magnet

In two-dimensional problems the magnetic vector potential $\vec{A}$ is normal to the studied plane; hence, z component is non-zero. Consequently, components of magnetic flux density $\vec{B}$ in 2D plane are given as,

$$B_x = \frac{\partial A_z}{\partial y};\ B_y = -\frac{\partial A_z}{\partial x};\ B_z = 0; \tag{3.10}$$

Therefore, the equation of the permanent magnet machine given in (3.8) is simplified as,

$$\frac{\partial}{\partial x}(\nu \frac{\partial A_z}{\partial x}) + \frac{\partial}{\partial y}(\nu \frac{\partial A_z}{\partial y}) = -J_z + J_m \tag{3.11}$$

where $J_m = \nabla \times H_c$ is the equivalent current density of permanent magnet and J_z is the density of the excitation current source. In case of time varying field of linear domain, (3.11) can be expressed as,

$$\frac{\partial}{\partial x}(\nu \frac{\partial A_z}{\partial x}) + \frac{\partial}{\partial y}(\nu \frac{\partial A_z}{\partial y}) = -J_0 + j\omega\sigma A_z + J_m \tag{3.12}$$

where J_0 is the current density of source, ω is the angular velocity and σ is the conductivity of the material.

3.2.3. Mesh Formation

After the mathematical formulation of a physical model, the second important step in the FEM is to discretize the study domain. The process of discretization of the study domain is also known as mesh formation. The accuracy of the solution greatly depends on the fineness of mesh. On the other hand, finer mesh requires larger computing time and memory of the computer. Therefore, better understanding of the domain regions and their fields is necessary to distribute the mesh in the most optimum way. The thumb rule of mesh distribution is that mesh should be as fine as possible where field changes rapidly.

There exist various types of elements which can be one, two and three-dimensional. Some of the most commonly used elements are shown in the Fig.3. 2. The triangle element in 2D FEM and tetrahedron in 3D FEM are widely used since any polygon of 2D plane, no matter how irregular can be represented by the combinations of triangles and any polyhedron of the 3D plane as a combination of tetrahedrons.

The corner point of a finite element is called grid point or node. The main task of the FEM computation is to solve for all unknown node potentials. Each element has a material property that may or may not be different from the surrounding elements. Excitation may also present within the element or at the nodes.

After the mesh formation, a polynomial shape function or interpolation is derived for the unknown variables. In a typical triangular element as shown in the Fig. 3.3, it is assumed that the unknown potential '*A*' can sufficiently be represented by the polynomial expression of (3.13).

$$A = a + bx + cy \tag{3.13}$$

where, *a*, *b* and *c* are some constants that will be determined in the process. Thus, the real solution of the potential is replaced by the discretized function in the *xy* plane of the problem. Although a potential function is discretized, its distribution in the region remains continuous through out. Therefore, the approximate of (3.13) is discrete but continuous everywhere and can be differentiated anywhere [41].

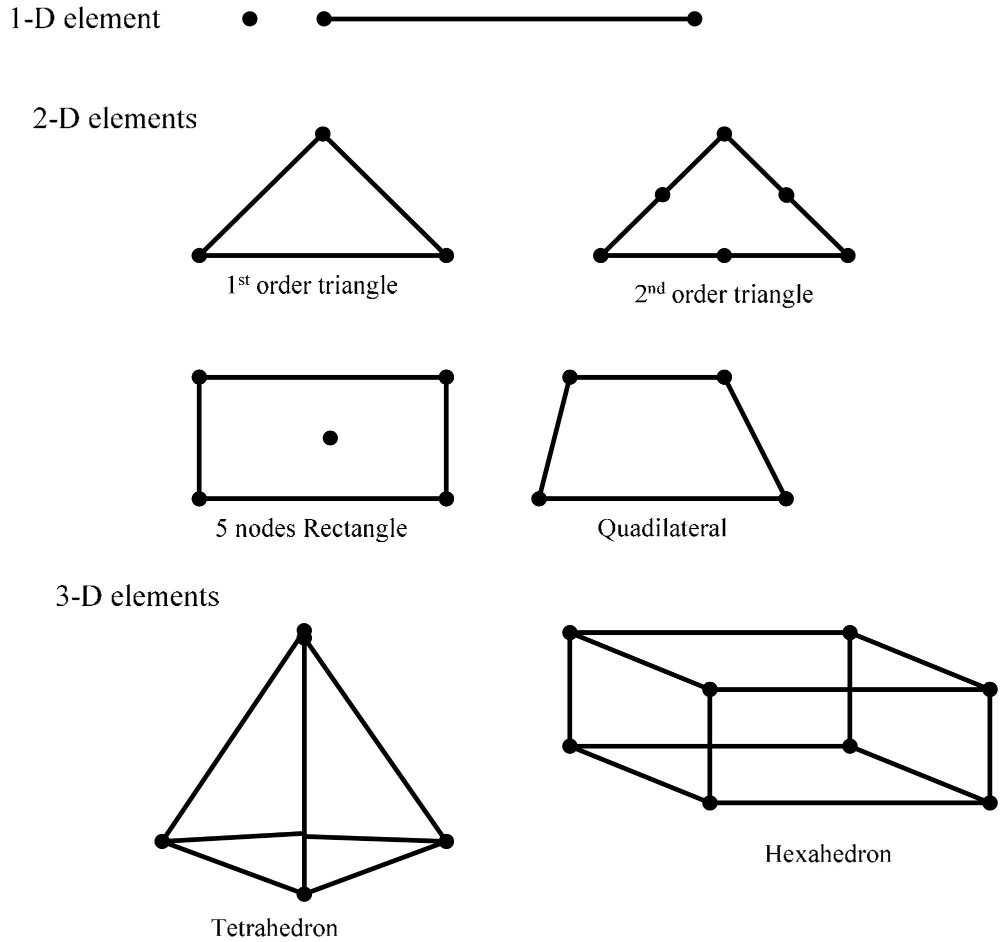

Fig. 3.2 Some basic elements use for mesh formation in a finite element study

The constants *a*, *b* and *c* are estimated from the three independent simultaneous equations of potentials that can be derived for three vertices of the triangle which are given as,

$$a + bx_i + cy_i = A_i \tag{3.14}$$

$$a + bx_j + cy_j = A_j \tag{3.15}$$

$$a + bx_k + cy_k = A_k \tag{3.16}$$

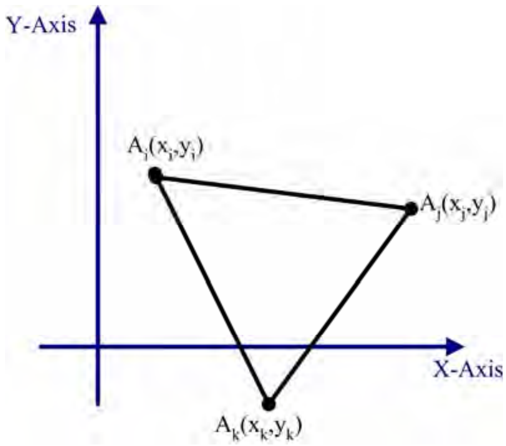

Fig. 3.3 The magnetic vector potential at the node of a typical triangular- element

These equations can also be represented in a matrix form. The matrix of co-efficient can be derived from these equations as,

$$\begin{bmatrix} a \\ b \\ c \end{bmatrix} = \begin{bmatrix} 1\, x_i\;\, y_i \\ 1\, x_j\;\, y_j \\ 1\, x_k\;\, y_k \end{bmatrix}^{-1} \begin{bmatrix} A_i \\ A_j \\ A_k \end{bmatrix} \tag{3.17}$$

Substituting these constants in (3.13) and after some simplifications, the magnetic vector potential *A* can be express as,

$$A = \sum_{i=1}^{m} A_i \alpha_i (x, y) \tag{3.18}$$

where, *m* is the number of nodes in the element and $\alpha_i\,(x,y)$ is the position function. The position function α (*x*,*y*) for nodes *i,j,k* are given as,

$$\alpha_i = \frac{1}{2\Delta}\{(x_j y_k - x_k y_j) + (y_j - y_k)x + (x_k - x_j)y\} \tag{3.19}$$

$$\alpha_j = \frac{1}{2\Delta}\{(x_k y_i - x_i y_k) + (y_k - y_i)x + (x_i - x_k)y\} \tag{3.20}$$

$$\alpha_k = \frac{1}{2\Delta}\{(x_i y_j - x_j y_i) + (y_i - y_j)x + (x_j - x_i)y\} \tag{3.21}$$

where, Δ is the area of triangle. It can be shown that because of interpolatory nature of position functions,

$$\begin{aligned} \alpha_i(x_j, y_j) &= 0 \quad i \neq j \\ &= 1 \quad i = j \end{aligned} \tag{3.22}$$

Depending on complexity of the problem, higher order elements and polynomials are also used to define shape functions. The above discussion is valid for first order elements.

The following section discusses how matrix equations of elements are used to solve a complicated electromagnetic problem in the FEM.

3.2.4. Matrix Equations of Elements

In order to solve a field problem, the matrix equations of elements need to be derived and assembled. The two main methods to derive the matrix equations of elements are:

(1) The weighted residual method and

(2) Variational method.

In both the methods, the error between real and approximate solution is minimized to zero. The most commonly used technique to minimize this error is known as *Galerkin's method*. It is closely related to both the variational formulation and weighted residual approach. In fact, *Galerkin's method* is a special case of the very general weight residual method. In *Galerkin's method* residual weight and shape functions become same.

In general, any electromagnetic field problem of region *Ω* with boundary condition of '*C*' can be expressed by an operator equation such as,

$$F(u) = v \tag{3.23}$$

The equation (3.23) can be also be rewritten as,

$$F(u) - v = R \tag{3.24}$$

where, *R* is the residue that needs to be minimized. For this purpose, an appropriate weighing function *W* is chosen and a double integration is applied to the product of *W* and *R* over the region *Ω*.

The Galerkin's formulation of a permanent magnet machine can be obtained from (3.12) and is expressed as,

$$\iint_{\Omega} W(\nu \frac{\partial^2 \hat{A}}{\partial x^2} + \nu \frac{\partial^2 \hat{A}}{\partial y^2}) dxdy + j\omega\sigma \iint_{\Omega} W\hat{A} dxdy - \iint_{\Omega} WJ_0 dxdy = \iint_{\Omega} WJ_m dxdy \tag{3.25}$$

After some simplifications, the (3.25) can be expressed in matrix form and is given as,

$$[S][\hat{A}] = [I] + [PM] \tag{3.26}$$

where, [*S*] is the global coefficient matrix that is expressed in terms of magnetic properties and coefficients *b* , *c*.

$$[S] = \frac{\nu}{4\Delta} \begin{bmatrix} b_i^2 + c_i^2 & b_i b_j + c_i c_j & b_i b_k + c_i c_k \\ b_i b_j + c_i c_j & b_j^2 + c_j^2 & b_j b_k + c_j c_k \\ b_i b_k + c_i c_k & b_j b_k + c_j c_k & b_k^2 + c_k^2 \end{bmatrix} + j\frac{\omega\sigma}{12} \begin{bmatrix} 2 & 1 & 1 \\ 1 & 2 & 1 \\ 1 & 1 & 2 \end{bmatrix} \tag{3.27}$$

The matrix of nodal magnetic vector potentials is given as,

$$[\hat{A}] = \begin{bmatrix} \hat{A}_i \\ \hat{A}_j \\ \hat{A}_k \end{bmatrix} \tag{3.28}$$

The matrix of nodal currents is given as,

$$[I] = J_0 \frac{\Delta}{3} \begin{bmatrix} 1 \\ 1 \\ 1 \end{bmatrix} \tag{3.29}$$

The contribution of permanent magnet [*PM*] in (3.26) can be expressed in terms of magnetization '*M*' as,

$$[PM] = \frac{\nu \mu_0}{2\Delta} \left(M_x \begin{pmatrix} c_i \\ c_j \\ c_k \end{pmatrix} - M_y \begin{pmatrix} b_i \\ b_j \\ b_k \end{pmatrix} \right)$$

(3.30)

The equation (3.26) is solved for vector potential $\vec{A}$ in a region Ω that contains triangular elements with nodes *i*, *j* and *k*. Generally, the study domain consists of finite number of elements. The matrix equation of (3.26) is determined for each element. Thus, the size of total matrix equations is determined by the number of finite elements present in the study domain. However, nodes can be common to various adjacent elements in a region. This results in a number of zero elements in the main matrix. Consequently, the resultant matrix is sparse, symmetric and definite and it can be solved using a standard processor.

3.2.5. Boundary Conditions

The boundary conditions are imposed on the study domains of the electromagnetic field problems. It restricts the study domain to certain extent which in turns reduces the computational burden. Hence, the accuracy and efficiency of a FEM solution greatly depends on appropriate boundary conditions.

The boundary due to symmetry reduces the size of an element matrix considerably. For example, most of the rotating electric machines have identical full or half pole pitch. In such case, the modeling of one or half pole pitch is sufficient to represent the field problem adequately. Thus, the size of the element matrix for an electric machine can be reduced significantly.

In general, boundary conditions are categorized in to three main groups [43]. They are:

Dirichlet boundary condition

Neumann boundary condition

Interconnection boundary condition

In the Dirichlet boundary condition, a specified value is assigned to the magnetic vector potential of a particular point. It forces the flux lines to be parallel to the boundary edge. In a rotating machine, the outer stator yoke may have Dirichlet boundary condition of $\vec{A} = 0$. It is valid as long as the leakage flux beyond the stator yoke is negligible. High permeability of the stator core material normally ensures that the majority of the fluxes are contained in the stator yoke. Therefore, assumption of Dirichlet boundary condition at the edge of the stator yoke is a reasonable simplification.

The requirement in a Neumann boundary condition is that normal derivative of magnetic vector potential in the boundary must be zero. Neumann boundary condition is also known as natural boundary of a finite element domain. Hence, they are not required to be specified explicitly. The flux lines cross Neumann boundary orthogonally. Neuman boundary is normally imposed to a region that has symmetry. The flux lines are orthogonal to the plane in Neumann boundary.

Interconnection boundary is also known as cyclic or periodic boundary. It sets a constraint between two nodes which could be geometrically adjacent or at a particular interval. In the rotating electric machine, the interconnection boundary condition relates two nodes that are one or multiple pole pitches apart.

3.2.6. Methods of Solving System Equations

The linear algebraic equations are generally solved by either direct method or iterative method. From theoretical point of view, the direct method should be capable of giving an exact solution of the linear algebraic equations. However, in reality due to the rounding off errors, the solution is actually an approximation. On the other hand, the iterative methods are not affected by the rounding off errors. The iterative methods can also take advantage of the sparseness of the coefficient matrix of the linear algebraic equations.

It is mentioned earlier that the global matrix of the finite element model is large but sparse and positive definite. Hence, the global matrix equation of the finite element model can be efficiently solved by the iterative methods. One of the most efficient methods to solve such matrix equations is Incomplete Choleski Conjugate Gradient (ICCG) iterative method. It is a preconditioned conjugate gradient method. The simultaneous equation given in (3.31) can be solved by the ICCG method.

$$Ax = b \tag{3.31}$$

In this method, first an arbitrary initial solution x_0 is estimated, and then the associated residual r_0 is computed. The initial search direction p_0 for the final solution is chosen in such a way that it coincides with r_0.

$$r_0 = Ax_0 - b \tag{3.32}$$

$$p_0 = r_0 \tag{3.33}$$

Afterward, a succession of residuals and search directions are computed in recursive steps as shown below:

$$x_{k+1} = x_k + \alpha_k p_k \tag{3.34}$$

$$r_{k+1} = r_k + \alpha_k A p_k \tag{3.35}$$

where,

$$\alpha_k = \frac{p_k^T r_k}{r_k^T A p_k} \tag{3.36}$$

In order to determine the preconditioned conjugate gradient, the matrix A is modified by a positive definite and symmetric preconditioning matrix B as BAB^T. The (3.31) can be rewritten as,

$$(BAB^T)(B^{-T}x) = Bb \tag{3.37}$$

From the equation (3.37), $y = B^T x$ is solved using modified right hand side and the coefficient matrix. Later the convergence x is recovered from y. The search direction of successive steps are expressed as,

$$p_{k+1} = Br_{k+1} + \beta_k p_k \tag{3.38}$$

where scaling factor β_k is calculated as,

$$\beta_k = -\frac{p_k^T ABr_{k+1}}{p_k^T A p_k} \tag{3.39}$$

Any symmetric, positive definite matrix 'A' can be represented in the form of :

$$A = LL^T \quad (3.40)$$

where, L is a lower triangular matrix that has only zero elements above and to the right of its principal diagonal and L^T is its transposition. The process of computing L

is known as triangular factorization and labeled as triangular factor of '*A*'. If the matrix '*A*' is sparse, Incomplete Choleski Factorization is the best way to construct a sparse, lower triangular preconditioning matrix *L*. In this type of factorization, many elements of the Choleski factors are forced to zero so that the computing time and memory space can be saved. The resultant factorization is an approximation only, but accuracy can be improved with additional conjugate gradient steps. The incomplete Choleski factorization of the modified matrix BAB^T produces most of its Eigen values close to unity and all others remaining values are very close to each other. As a result, residual components corresponding to them can be eliminated with fewer conjugate gradient steps [41].

3.2.7. Iterative Method for Nonlinear Problems

It is well known that the most of the electromagnetic problems have nonlinear characteristics. In case of permanent magnet machines, the ferromagnetic property of the core material, demagnetizing characteristics of some of the permanent magnet materials and relationship between voltage and flux are non-linear. Hence, the mathematical model of the electric machine consists of a set of nonlinear equations which can not be solved directly in closed form. These types of equations are solved using numerical iterative methods. Among various iterative schemes, Newton Raphson method is widely used for solving nonlinear finite element equations. The popularity of this method lies in the fact that it converges rapidly and has an unconditional stability. Here, the error in a given step decreases as the square of the error in the previous step. The formulation of Newton Raphson iteration method for FEM solution can be described in brief as follows:

Let us consider the energy functional given in (3.13). Here *A* is the correct solution to be found and A' be the reasonably close estimate of *A* so that,

$$A' = A - \partial A' \tag{3.41}$$

The multidimensional Taylor's series gives the gradient of function F(A') as,

$$\frac{\partial F}{\partial A'_m} = \left.\frac{\partial F}{\partial A'_m}\right|_{A'} + \sum_n \left.\frac{\partial^2 F}{\partial A'_m \partial A'_n}\right|_{A'} \partial A' + ... \tag{3.42}$$

However, when $A = A'$, all components of gradient vanishes. Thus, neglecting the higher terms of Taylor's series,

$$\partial A' = -P^{-1} \left.\frac{\partial F}{\partial A'_m}\right|_{A'} \tag{3.43}$$

where, *P* is the Jacobian matrix of Newton Raphson iteration and the element *mn* is given as,

$$P_{mn} = \left.\frac{\partial^2 F}{\partial A'_m \partial A'_n}\right|_{A'} \tag{3.44}$$

The difference $\partial A'$ is estimated and added to the initial approximation of A' until it converges to *A*. Thus, an iterative process is established and for any step *k* it is expressed as,

$$A'^{(k+1)} = A'^{(k)} - (P^{(k)})^{-1} \left.\frac{\partial F}{\partial A'}\right|_{A'}^{(k)} \tag{3.45}$$

The precision of Newton Raphson method depends mainly on derivation of $\frac{\partial F}{\partial A'_m}$ and

$\frac{\partial^2 F}{\partial A'_m \partial A'_n}$.

Following section examines how Newton Raphson method can be applied to a non-linear finite element model of permanent magnet machine.

Let us consider the simplified version of (3.26) for this purpose,

$$\frac{\nu}{4\Delta}\begin{bmatrix} s_{ii} & s_{ij} & s_{ik} \\ s_{ji} & s_{jj} & s_{jk} \\ s_{ki} & s_{kj} & s_{kk} \end{bmatrix}\begin{bmatrix} A_i \\ A_j \\ A_k \end{bmatrix} = \frac{\Delta}{3} J \begin{bmatrix} 1 \\ 1 \\ 1 \end{bmatrix} \tag{3.46}$$

In the permanent magnet machine, the *B-H* characteristics of the stator and rotor core materials are non-linear. In such a case, solution of (3.46) in one single iteration step is not possible. For simplicity, we will derive Newton Raphson form only for the first row of (3.46). The procedure is repetitive for other rows and will not be considered here. Let us assume,

$$F = \frac{\nu}{4\Delta}\begin{bmatrix} s_{ii} & s_{ij} & s_{ik} \end{bmatrix}\begin{bmatrix} A_i \\ A_j \\ A_k \end{bmatrix} - \frac{J\Delta}{3} \tag{3.47}$$

Taking derivation with respect to A gives,

$$\frac{\partial F}{\partial A_i} = \frac{\nu}{4\Delta} s_{ii} z + \frac{1}{4\Delta}[s_{ii}A_i + s_{ij}A_j + s_{ik}A_k]\frac{\partial \nu}{\partial A_i} \tag{3.48}$$

$$\frac{\partial F}{\partial A_j} = \frac{\nu}{4\Delta} s_{ij} + \frac{1}{4\Delta}[s_{ii}A_i + s_{ij}A_j + s_{ik}A_k]\frac{\partial \nu}{\partial A_j} \tag{3.49}$$

$$\frac{\partial F}{\partial A_k} = \frac{\nu}{4\Delta} s_{ik} + \frac{1}{4\Delta}[s_{ii}A_i + s_{ij}A_j + s_{ik}A_k]\frac{\partial \nu}{\partial A_k} \tag{3.50}$$

The term $\frac{\partial \nu}{\partial A}$ can be represented by using chain rule,

$$\frac{\partial \nu}{\partial A} = \frac{\partial \nu}{\partial B^2}\frac{\partial B^2}{\partial A} \tag{3.51}$$

In the equation (3.51), the term $\frac{\partial B^2}{\partial A}$ is derived as follows:

We know from the earlier analysis that,

$$A = \frac{a_i + b_i x + c_i y}{2\Delta} A_i + \frac{a_j + b_j x + c_j y}{2\Delta} A_j + \frac{a_k + b_k x + c_k y}{2\Delta} A_k \tag{3.52}$$

and $B = \sqrt{B_x^{\ 2} + B_y^{\ 2}}$ (3.53)

where,

$$B_y = \frac{\partial A}{\partial y} = \frac{A_i c_i + A_j c_j + A_k c_k}{2\Delta} \tag{3.54}$$

$$B_x = \frac{\partial A}{\partial x} = \frac{A_i b_i + A_j b_j + A_k b_k}{2\Delta} \tag{3.55}$$

Therefore,

$$B^2 = \left(\frac{\partial A}{\partial x}\right)^2 + \left(\frac{\partial A}{\partial y}\right)^2 = \frac{(A_i b_i + A_j b_j + A_k b_k)^2 + (A_i c_i + A_j c_j + A_k c_k)^2}{4\Delta^2} \tag{3.56}$$

and

$$\frac{\partial B^2}{\partial A_i} = \frac{2b_i(A_i b_i + A_j b_j + A_k B_k) + 2c_i(A_i c_i + A_j c_j + A_k c_k)}{4\Delta^2} \tag{3.57}$$

$\frac{\partial B^2}{\partial A_j}$ and $\frac{\partial B^2}{\partial A_k}$ can also be calculated similar way. The second term of (3.51), $\frac{\partial \nu}{\partial B^2}$ comes from the nonlinear magnetizing curve of the core material which can be represented in a number of ways for the computation purpose.

Representation of non-linear BH curve for FEM computation: Normally, the magnetizing curve of a core material is represented by a set of discrete points in the computer. However, in iterative methods like Newton Raphson, continuous representation of data is necessary. Hence, for such cases, interpolation methods are used for data representation. There exists a number of models to describe the physical property of the ferromagnetic material for this purpose. Some of them are:

Simple analytical saturation curve: It defines BH curve very quickly by combining a straight line and an arc tangent. In this model, the BH curve closely follows the approximate asymptote of the saturation. However, the difference between experimental curve and the model can be large in the saturation band region.

Analytical saturation curve with bend adjustment: This model is more accurate then the simple analytical saturation curve. In this model bend of the saturation is adjusted with the help of a co-efficient so that curve resembles closely to the curve obtained from measured data points. The smaller is the coefficient the sharper will be the bend in the *BH* curve.

Spline saturation curve: This model is based on the cubic spline functions. It defines the *BH* curves from the measured data. Computation wise it takes longer time but fits the experimental curve very well. It comprise of three main parts, first of which is a homographic function that passes through the origin and describes the bend, the second part is a connecting function that is tangent to the first and last parts of the curve and the third part is a straight line of slope μ_0, of which ordinates at the origin is the saturated magnetization.

The construction of *BH* curve to use in the FE analysis by utilizing the above mentioned models is shown in the Fig. 3.4. Usually, the spline model is chosen for the best accuracy when data of *BH* curves comes from actual measurements. The analytical model serves best when quicker computation is necessary.

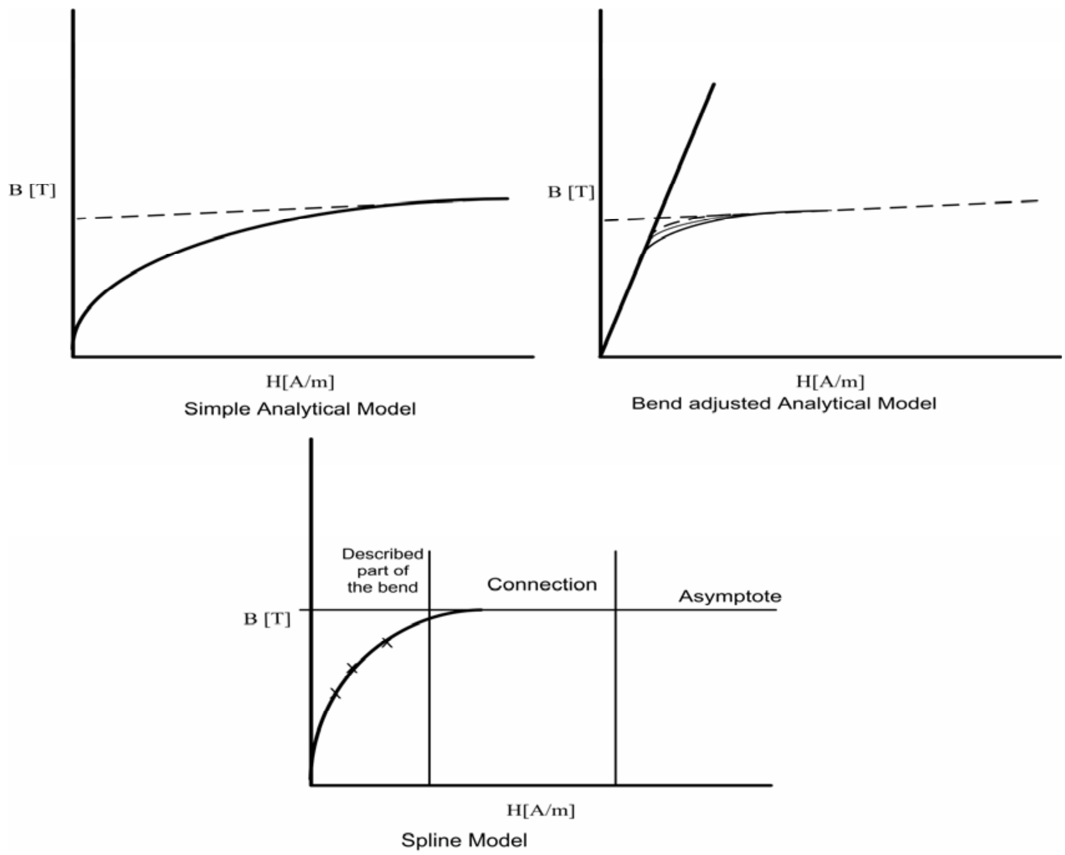

Fig. 3.4 BH models to represent non linear characteristic

3.3. Time stepping Finite Element Method (Transient Magnetics)

The time stepping finite element method can be used to study the phenomena created by time varying magnetic field. In such cases, the time derivative parts of the system differential equations are no longer zero. The time varying field induces voltage and current. The induced eddy current due to the variation of field may also affect the performance of a system considerably. The time varying magnetic field can be modeled either in time domain or in frequency domain. For a sinusoidally varying field, frequency domain model are used whereas the transient behaviour of magnetic devices that are excited by time varying current and voltage source are studied in the time domain FE model.

All electromagnetic devices are associated with some sorts of electric circuit. The corresponding circuit equations can be coupled to the transient finite element field equations. In addition to this, electromagnetic devices such as motors, generators, actuators, etc., have moving parts and also associated with electromechanical equations. These equations also can be coupled to the transient FE model.

In the coupled system, the known input is terminal voltage (or current) and terminal current (or voltage) is computed as unknown quantity. In case of the electric motor, the Mexwell's equations of electromagnetic are coupled with the stator circuit equations and rotor motion equations. These equations are solved simultaneously at each time step. The solution of each step is not independent; each solution is linked to the previous one by the temporal equation. The inputs to the system are stator phase voltage (or current), rotor position, geometry of the machine and characteristics of materials. The stator current (or voltage), back emf, developed torque and speed, etc. are the unknown quantities which can be computed from the time-step finite element analysis.

3.3.1. Electromagnetic field equation in time domain

The Mexwell's equations for time dependent field is expressed as,

$$\nabla \times (\nu \nabla \times A_z) = -J_z + \sigma \frac{\partial A_z}{\partial t} \tag{3.58}$$

The current density J_z is due to the applied source and $\frac{\partial A_z}{\partial t}$ is due to the induced eddy current by a time varying magnetic field.

In a thin conductor such as stator winding, the skin-effect is minimal. Hence, the field equation in such a region is given as,

$$\nabla \times (\nu \nabla \times A_z) = -J_z = -i_s / S \tag{3.59}$$

Where, i_s is the applied stator current and S is the cross-sectional area of the coil. In case of stator and rotor cores, the skin-effect can not be neglected. Hence, the field equation becomes,

$$\nabla \times (\nu \nabla \times A_z) = \sigma \frac{\partial A_z}{\partial t} \tag{3.60}$$

In case of permanent magnet, the field equation includes the remanance of the material which is given as,

$$\nabla \times (\nu \nabla \times A_z) = \nabla \times (\nu B_r) \tag{3.61}$$

In the air-gap region of an electric machine, J_z and $\frac{\partial A_z}{\partial t}$ both are zero; hence, the field equation in this region is given as,

$$\nabla \times (\nu \nabla \times A_z) = 0 \tag{3.62}$$

3.3.2. Coupling of the Electric Circuits

The numerical analysis of the electric device can be hampered by associated complexity of the electrical circuit. It may be difficult to estimate values of excitation current and/or voltage of various components while solving the field equations. This difficulty can be eliminated by coupling the circuit equations to the field equations by an external circuit. The principle of coupling depends on the formulation of the magnetic field equations and the analysis of the related electric circuit [44].

The space distribution of the magnetic field is not affected by the induced current. Hence, the magnetic and electric field equations of a system can be decoupled easily. The components that are common to both the field and circuit are defined twice: first as a component of the circuit and second, as a region in the finite element domain. The electrical circuit consists of various components, nodes and branches. These components are defined by their electrical behaviour. The generic components are defined by their voltage–current relationship and specific components are defined by the differential equations that relate the magnetic potential, current and voltage. The electric circuits coupled to the field equations obey Kirchoff's laws.

The terminal voltage of an electric circuit associated with an electrical motor can be expressed as,

$$V = Ri + L\frac{di}{dt} + \frac{d\phi}{dt} \tag{3.63}$$

The flux ϕ in (3.63) can also be expressed in terms of magnetic vector potential and by expressing (3.63) in the matrix form, it can be combined to the system matrix equation of the FEM. Thus, a coupled system matrix is obtained, which is solved by the time-stepping method.

3.3.3. Rotating Air-gap

In the rotating electric machine, the movement of rotor is associated with the time variation of the magnetic field. The accuracy of the field solution depends on proper representation of the rotor movement in the air-gap.

In a finite element model, the rotating air-gap is a circular surface. It can be defined by either the two circles or arcs placed in the air-gap of the machine which are the outlines of the rotor and stator. The mesh of the stator and rotor are generated independently. During the rotor movement, the mesh of the rotor rotates without any change in the shape. The Fig. 3.6 shows the mesh of the rotor and stator after the rotation of the rotor for a few time-steps.

For each time step, the co-ordinate of the rotor mesh and its periodic boundary condition related to the stator-interface changes according to the rotor position. In other word, the rotor slide in the circular surface of the air-gap region. The air-gap region is meshed in such a way that all its nodes lie inside the region. The Fig. 3.6 shows the mesh in a rotating air gap of a permanent magnet electric machine.

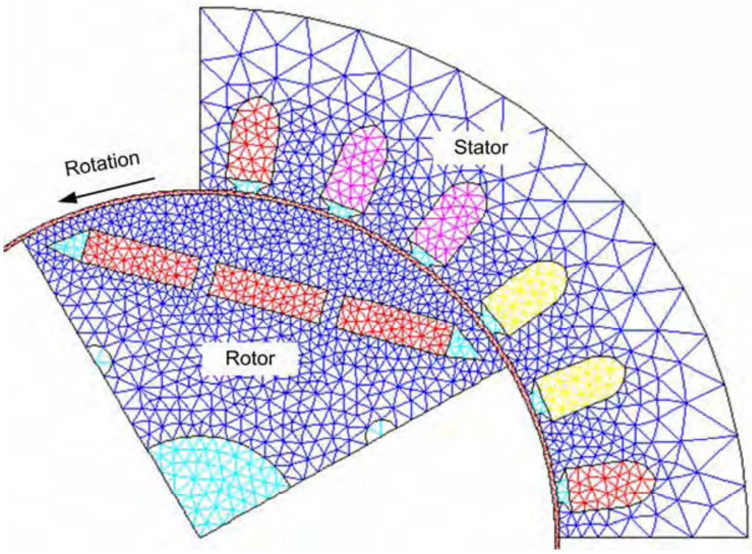

Fig. 3.5 The FEM mesh of the rotor and stator after rotation of a few time-steps

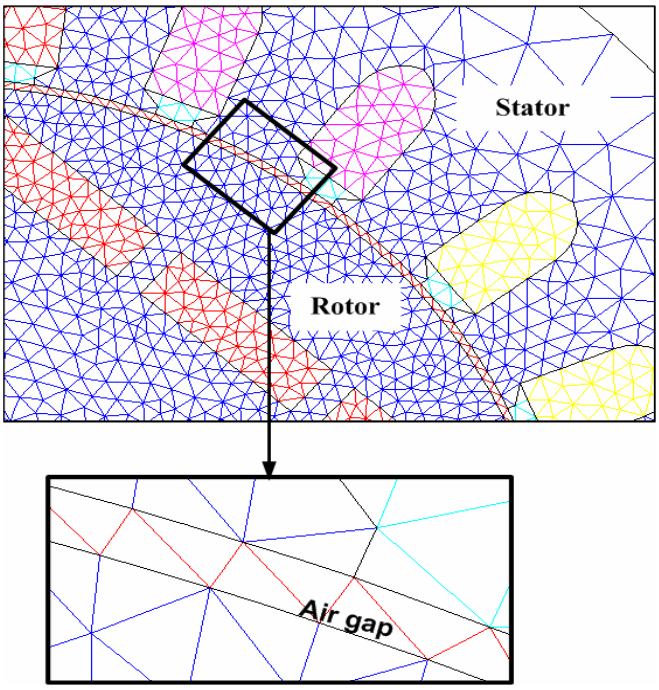

Fig. 3.6 The mesh of the rotating air gap in the segmented IPM machine

3.3.4. Solving of Global Equations in Time-stepping FEM

The global system equations of time-stepping FEM are solved by Newton-Raphson iteration with ICCG algorithm. The general form of the global equation for time domain can be expressed as,

$$AX + B\frac{\partial X}{\partial t} = P \tag{3.64}$$

where, X is the unknown vector such as magnetic potential, stator current (or voltage) etc., A and B are sparse coefficient matrices and P is the input voltage (or current). The equation (3.64) can be expressed in time-discretize form by backward Euler's method as,

$$[A^k + \frac{B^k}{(\Delta t)^k}]X^k = P^k + \frac{B^k}{(\Delta t)^k}X^{(k-1)} \tag{3.65}$$

The iterative steps of Newton-Raphson method stop when error becomes smaller than the specified tolerance value. The ICCG algorithm is applied in each cycle of Newton-Raphson to reduce memory usages and computation time. The flow chart of the process is given in the Fig. 3.7.

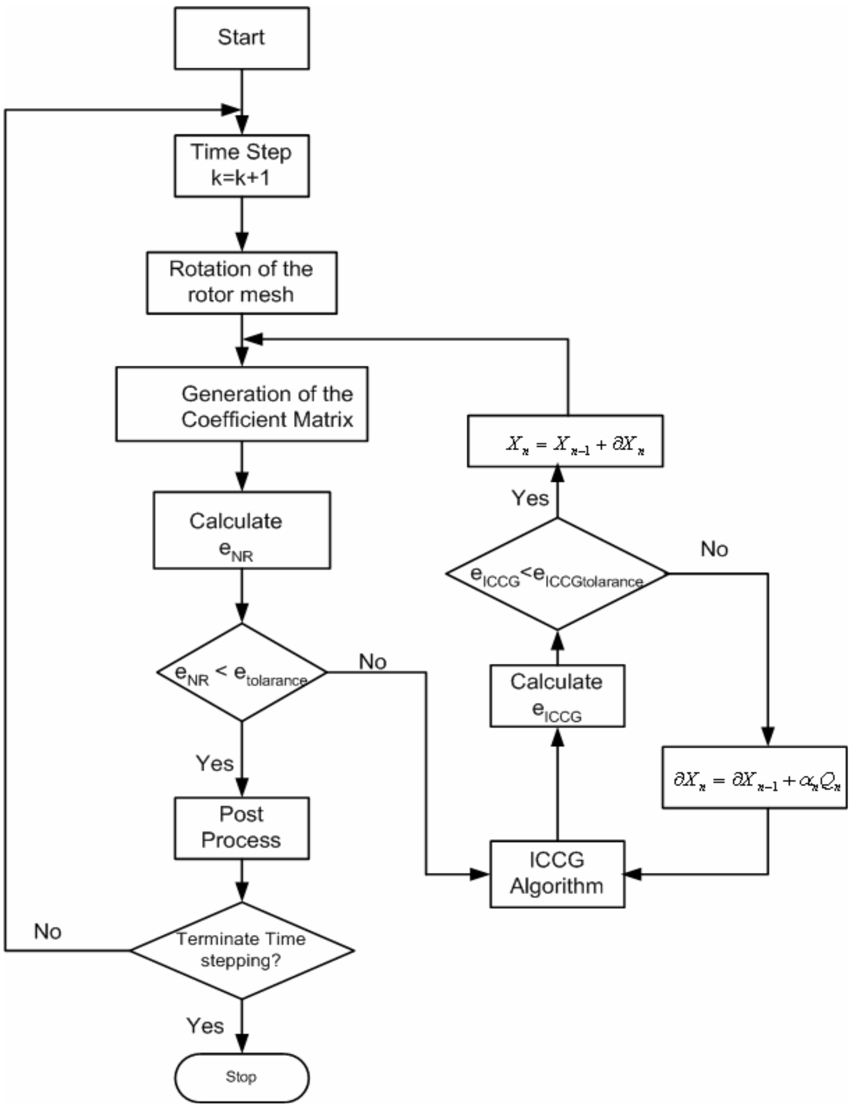

Fig. 3.7 Flow chart of time-step iteration in the FEM

3.3.5. Data Storage

In a finite element problem, number of unknowns can vary from couple of thousand to hundreds of thousand. The size of the global matrix is huge. Therefore, the efficiency of a finite element solving process depends greatly on the effective storage schemes. In most of the cases, the global matrix is symmetric and non-zero terms clustered around the main diagonal. For such matrix, the most suitable storage method is the *non-zero index storage method*. It works very well with ICCG algorithm. In this method, only the non-zero elements of the triangle matrix are stored. The non-zero elements are arranged column by column in a matrix (say [A]), the corresponding row numbers of each elements are stored in a separate matrix and the position of each diagonal element in matrix [A] is stored in a third matrix. In ICGG, non-zero element positions are retrieved from the second and third matries and the elements themselves are retrieved from the first matrix. This storage scheme is widely used in the FEM to save both the computation time and memory space.

3.4. Construction of the FEM Models of the Two Prototype IPM Machines

In this work, the two prototype Interior Permanent Magnet (IPM) machines are analysed in FEM. One of them is an existing four pole machine (IPM Machine-I) with the rotor configuration given in the Fig. 3.8(a) and the second one is the proposed Segmented IPM machine whose rotor configuration is shown in the Fig. 3.8 (b). The stator constructions of the both machines are same which has 24 slots and double layer distributed winding. The full geometries of both machines indicating different regions in one pole pitch are shown in the Fig. 3.9 and Fig. 3.10. The main geometrical dimensions of the Segmented IPM machine and the IPM machine-I are provided in the Tables B-1 and B-2 of the appendix B respectively. Most of the finite element software packages provide a CAD environment to draw the geometry of the studied domain. In this work, the software package used was CEDRAT's Flux2D. Because of the periodicity and symmetry, 1/4th of the machine i.e., one pole pitch was considered as the study domain. The geometry of one pole of each IPM machine was constructed in CAD environment of the Flux2D. After completion of the geometry, the surface regions were built. The next step in this process is to form mesh of various densities for various regions.

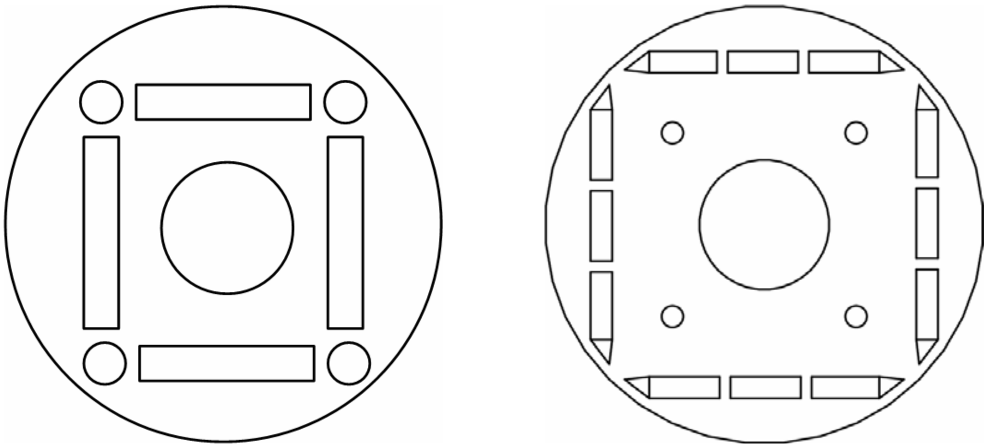

(a) (b)

Fig. 3.8 Rotor configurations of (a) IPM machines-I and (b) the proposed Segmented IPM machine

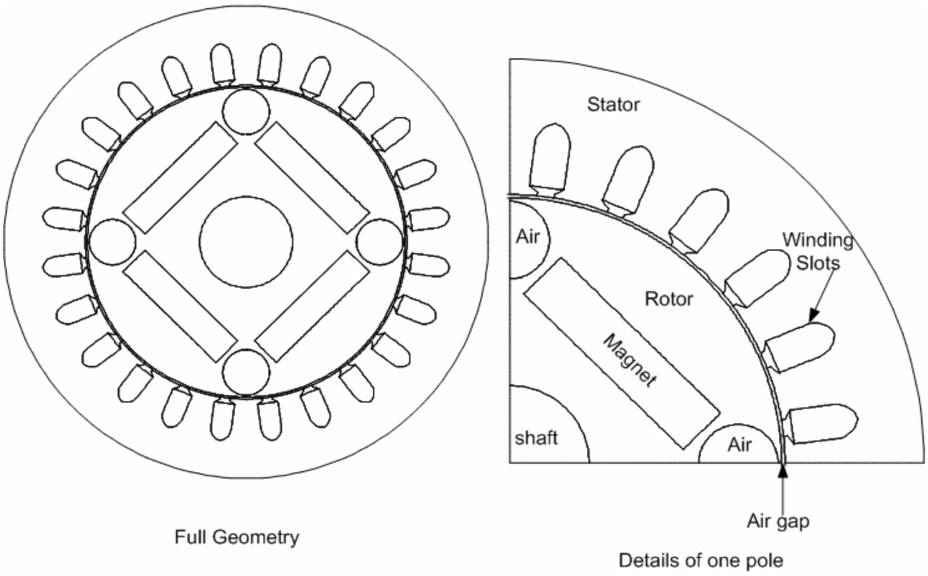

Fig. 3.9 Detailed geometry of the conventional, non-segmented IPM Machine-I

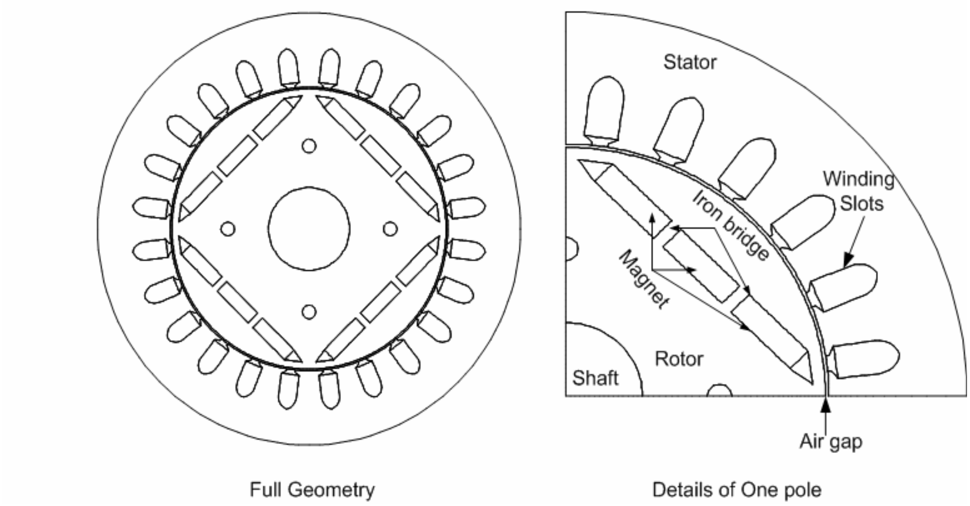

Fig. 3.10 Detailed geometry of the proposed segmented IPM machine

As mentioned earlier, finer mesh around rapidly changing field improves accuracy. In case of the studied IPM machines, the rapid change of fields occurs in the air-gap and regions near it. Therefore, the mesh of these regions was of fine quality. Moreover, the stator teeth and the iron bridges of the studied IPM machines are subjected to magnetic saturation and they too need to have fine quality mesh.

The FE software packages usually provide the automatic mesh generation, which depends on the weight of mesh at the associated regions. Consequently, a perfect mesh may not be produced in every case. However, quality of elements can be improved by adjusting the mesh density of a region manually. The model of the IPM machine-I and the Segmented IPM machine after the formation of mesh are shown in the Fig. 3.11.

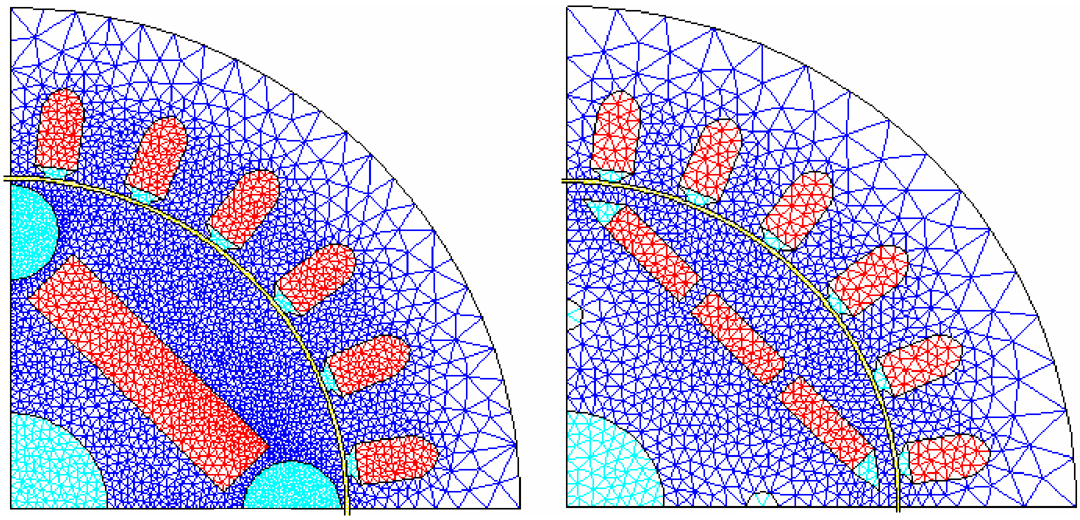

(a) (b)

Fig. 3.11 The FEM model of the (a) IPM Machine-I and (b) the segmented magnet IPM machine after formation of mesh

After the mesh generation, the physical properties are assigned to the various regions. The stator and rotor are assigned with appropriate electrical steel grades whereas the permanent magnet regions are assigned with NdFeB. The rotor of the prototype Segmented IPM machine was constructed from the electrical steel grade Lycore 140.

The *BH* curve of Lycore 140 was represented for finite element calculation using spline model and measured data. The hysteresis loop and the *BH* curve of Lycore 140 are shown in Fig. 3.12 (a) and (b) respectively. These data are measured by applying appropriate AC field to the sampled lamination material. The spline model of the same constructed for the FEM calculation is shown in the Fig.3.13.

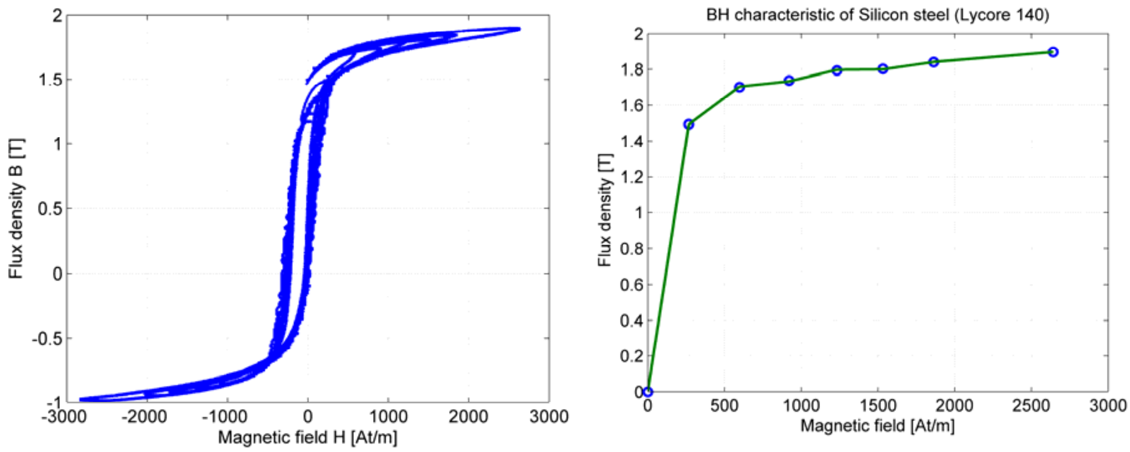

Fig. 3.12 (a) The hysteresis loop and (b) *BH* curve of the electrical steel (Grade Lycore 140) obtained from measurements

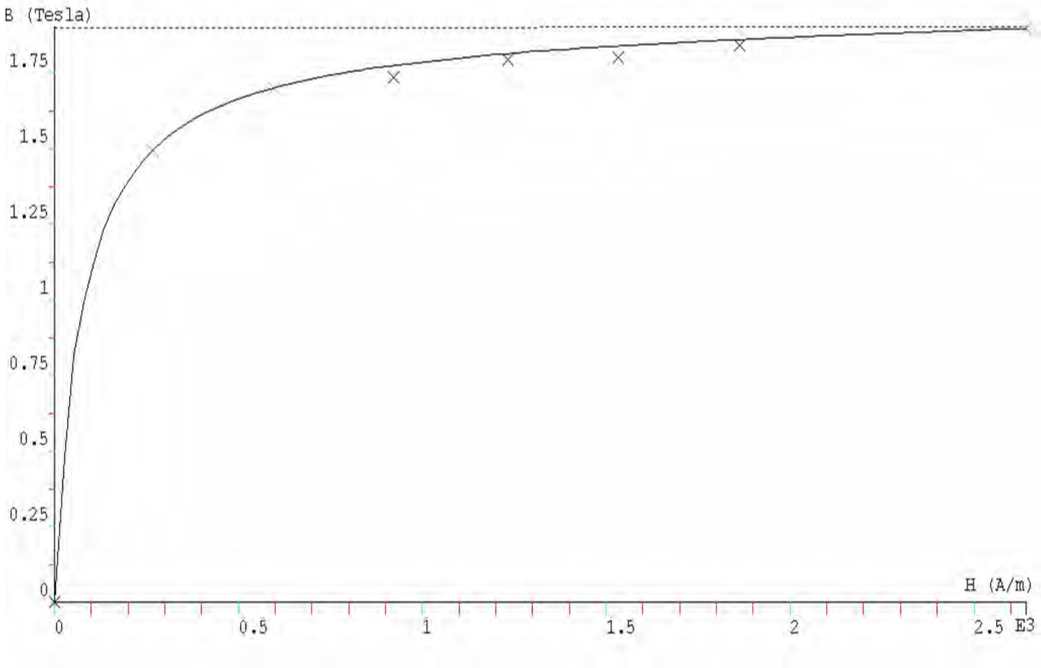

Fig. 3.13 The spline model of the BH-characteristic of Lycore 140 in Flux2D

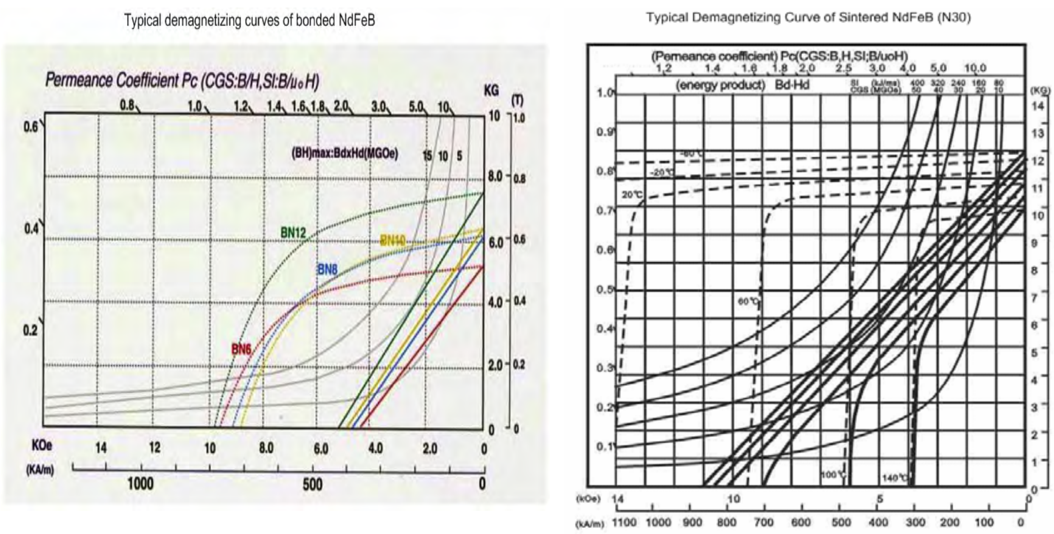

Fig. 3.14 Demagnetizing curve of rare earth permanent magnet- NdFeB

The rare earth magnet-NdFeB has linear demagnetizing characteristic as shown in the Fig. 3.1. The typical demagnetizing characteristics of different grades of the NdFeB are shown in Fig.3.14. The finite element model of the NdFeB is defined by its remnant flux density B_r and relative permeability μ_r. The magnet segments of each pole have parallel magnetization i.e. direction of magnetization of each segments makes 45 degree with horizontal axis.

The current/voltage sources related to the stator winding can be assigned either directly in the slot regions or through external electric circuit coupled to the regions. In a real drive system, the IPM machine is fed through the three-phase inviter, the six semiconductor switches of which are turned on or off by the PWM signals. The reference signal of the PWM generation is derived from a control algorithm. In case of vector current control, the amplitude of the current and the angle γ between the current phasor and synchronous reference frame q-axis are maintained at certain value depending on the operating conditions. At any instant, the stator MMF (Magneto Motive Force) aligns with the phase axis that carries maximum current. The concept of space current vector is related to the MMF. The space vector $\vec{i}_s$ can be expressed in synchronous rotating frame as:

$$\vec{i}_s = I_m \cos(\varphi - \theta_{e0}) + jI_m \sin(\varphi - \theta_{e0}) \tag{3.66}$$

where, I_m is the peak value of the phase current, φ is the phase angle and θ_{e0} is the initial angle between synchronous frame q-axis and phase-a axis which carries maximum current at that instant [45].

If the initial angle θ_{e0} is zero i.e., q-axis aligns with the a-phase axis then the current angle γ and the phase angle φ becomes same. Moreover, the stator current of the current controlled IPM machine is nearly sinusoidal. Therefore, the per phase stator excitation of such IPM machines can be represented in the FEM simply by sinusoidal current source. The amplitude and phase angle of the current sources can be varied to simulate various operating conditions [46]. The external circuit with sinusoidal current sources for the star-connected IPM machine is shown in Fig. 3.15. In case of star connection and balance supply, the third phase current $i_c(t)$ is calculated from the other two given sources so that any small zero sequence current caused by computation errors can be avoided completely. The coils *a*, *b* and *c* of the circuit in the Fig. 3.15 represent stator phase windings which are defined by the coil resistance and number of turns. Since the 2D FEM can not represent effect of end-turn, the inductance related with it needs to be calculated separately by some empirical formula and the value is included in the electric circuit as a series inductance L_{end}.

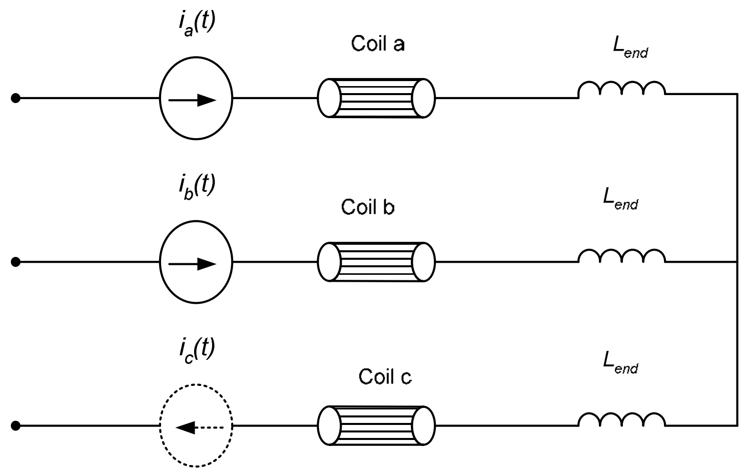

Fig. 3.15 Coupled external circuit for the IPM machine

After allocation of the physical properties and excitation sources, the boundary conditions are imposed on the study domain so that solving process can be simplified to some extent. Assuming negligible leakage flux from the stator yoke to the surrounding air, Dirichlet boundary is assigned to the stator outer diameter as shown in the Fig. 3.16. The center point of the geometry is also assigned with the same boundary as it represents the magnetic symmetry. Because of the periodicity, only one pole geometries of the two studied machines are described. Hence, the interconnection boundary condition is assigned to the both sides of the pole pitches. The Fig. 3.16 shows the boundary conditions of the IPM machine-I. In the segmented IPM machine also same boundary conditions are used.

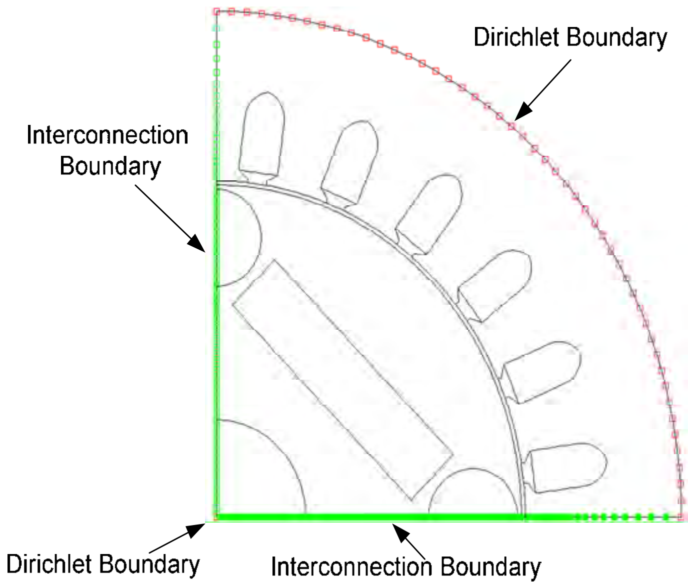

Fig. 3.16 Boundary conditions defined in one pole pitch of the IPM machine-I

In the final step, the global matrices of the study domains are constructed and iterative solutions are initiated. The solution process finishes when the error between the steps approaches predefined minimum value.

After solving the field problems the flux path and flux-density in the machine can be analysed. The flux-path of the prototype Segmented IPM machine for three different conditions: magnet field alone, stator MMF alone and both stator MMF and magnet field are shown in the fig. 3. 17 (a), (b) and (c) respectively. The flux density color plot are also shown for these three conditions in the fig. 3.18 (a), (b) and (c) respectively. The flux path for magnet filed alone and flux density for both stator MMF and magnet field of the prototype IPM machine-I is presented in the fig. 3.19

(a) and (b) respectively. Many other important machine parameters such as d- and q-axes inductances, induced back EMF, core losses, cogging torque, and developed electromagnetic torque can also be analysed in the post-processing. For calculation of the air gap flux density and d- and q-axes inductances magnetostatics solution is sufficient whereas for dynamic performances circuit-coupled, time-stepping FEM are used. The design optimization and performance analysis of the Segmented IPM machine using finite element method are presented in the next chapter.

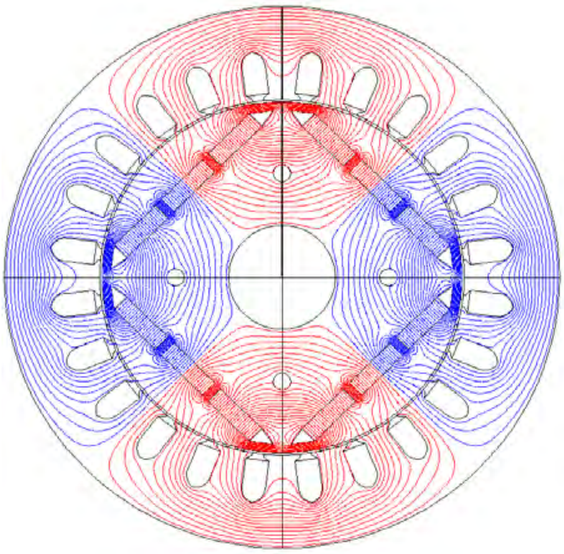

(a)

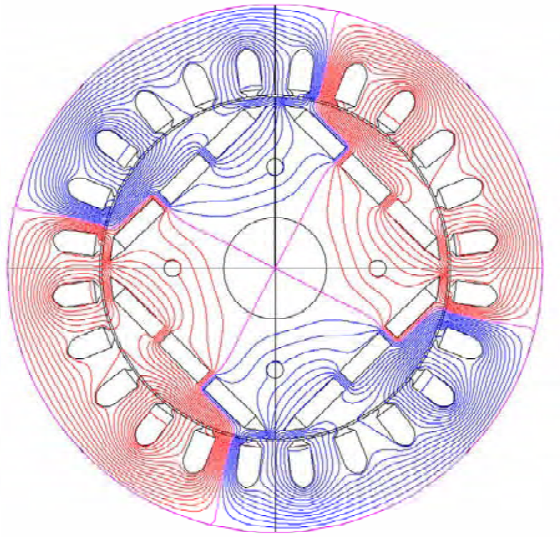

(b)

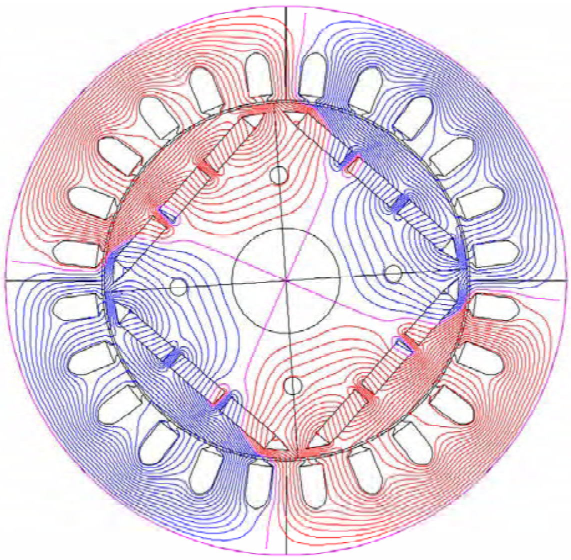

(c)

Fig. 3.17 The flux paths of the prototype Segmented IPM machine for conditions of (a) the magnet field alone[parallel magnetization in the magnet segments of each pole] (b) the stator MMF alone and (c) both stator MMF and magnet field present

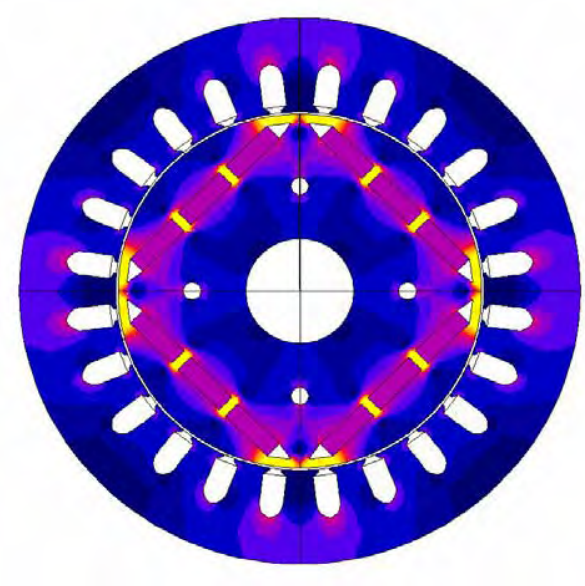

(a)

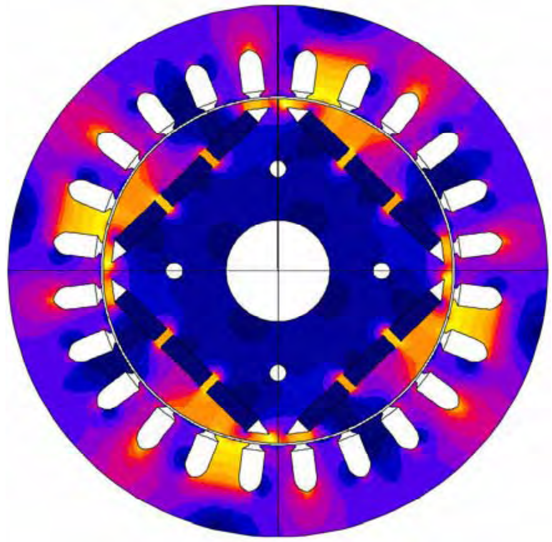

(b)

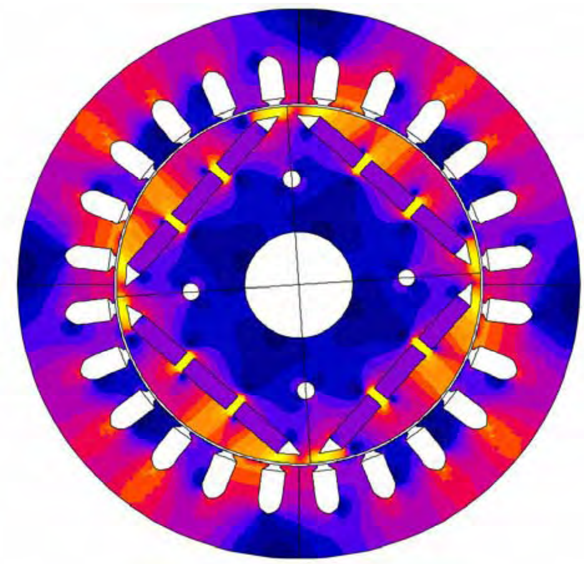

(c)

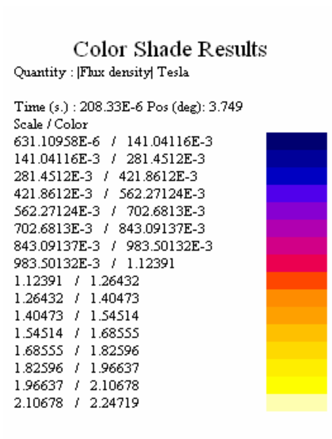

Fig. 3.18 The flux-density distribution of the proto type Segmented IPM machine for conditions of (a) the magnet field alone (b) the stator MMF alone and (c) both magnet field and stator MMF present.

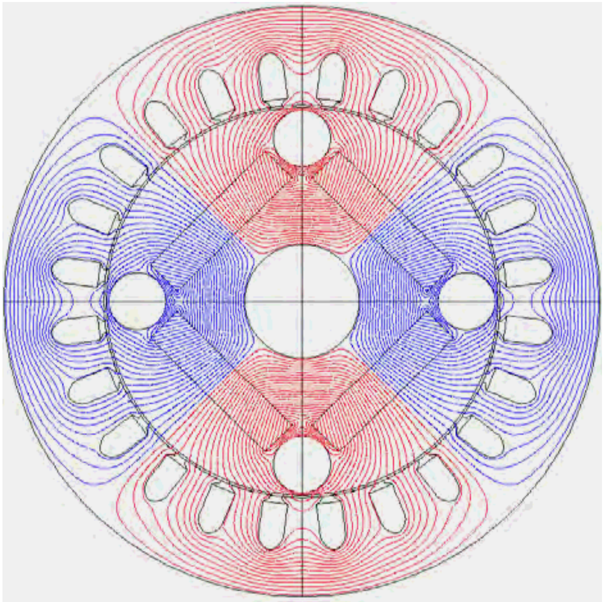

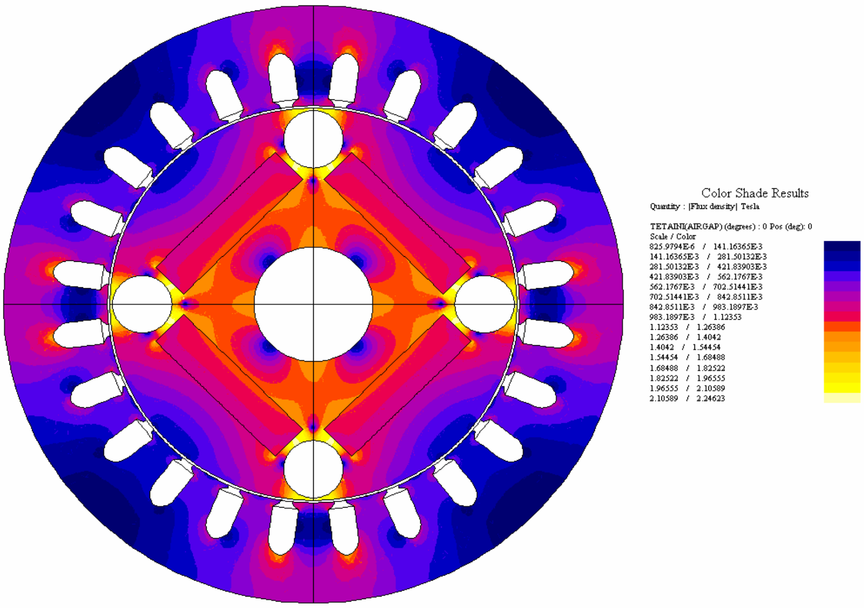

Fig. 3.19 (a) The flux paths for condition of magnet field alone and (b) the flux density color plot for the condition of both stator-MMF and magnet filed present in the prototype IPM machine-I respectively.

3.5. Conclusion

This chapter has reviewed the 2D finite element method of the Interior Permanent Magnet machine in general. The main steps involved in the finite element analysis of the electric machine are discussed in detail. The time- stepping FEM and external circuit coupling with the FE model are also discussed.

The process of developing the FEM models for the two studied machines-the IPM machine-I and the Segmented IPM machine are described. The FE models of the proposed segmented IPM machine are used in the chapter 4 for the design optimization and steady-state performance analysis. The FE model of the IPM machine-I was used to estimate the various performance indicators such as the cogging torque and iron loss, etc. They were compared with those of the proposed segmented IPM machine to evaluate the performance of the new design.

CHAPTER 4

4. Design and Analysis of the Prototype Segmented IPM Machine

4.1. Introduction

This chapter describes the design methodology of the prototype Segmented IPM machine. The chapter presents the optimization process of the Segmented IPM machine design to achieve the performances in terms of high CPSR as explained in chapter 1 and 2.

As a part of design process, prediction of the performance and estimation of parameters are essential so that any kind of misjudgments can be rectified prior to actual construction. The analytical and finite element methods are widely used to predict the performance of an electric machine during design process. However, the accuracy of the analytical method suffers when saturation and non-linearity are involved. For such cases, the finite element method is preferred over others.

In this work, the prototype IPM machine is optimized and analysed using finite element method exclusively. The magneto-static FEM was used to calculate the air-gap flux, and variation of *dq*-axis flux linkages with currents. On the other hand, the back EMF, cogging torque, iron losses and electromagnetic torque are estimated using time-stepping and external circuit-coupled finite element method. Since the proposed machine is symmetrical in the axial direction, the two-dimensional finite element method was considered to be accurate enough for various estimations. These estimations are verified for the prototype segmented IPM machine by the experimental measurements later in this chapter and steady-state performances are verified in the chapter 6.

4.2. Magnetic Design

The following sections focus on the magnetic design of the prototype Segmented Interior Permanent Magnet machine. There are several essential criteria that must be considered while designing a PM machine such as choice of the magnet and their arrangements, choice of iron core material, protection against demagnetization due to overloading and thermal capability. The design process starts with specific targets depending on the applications. Since, the machine will operate within the boundary of the system imposed constraints; they need to be defined beforehand.

4.2.1. Design Specification and Constraints of the prototype Segmented IPM machine

The targeted design objectives for the prototype IPM machine were:

- To design a three-phase PM synchronous generator/motor, capable of providing a constant output power from its base speed to the maximum speed of 6000~8000r/min in a 42V PowerNet environment of automobile. In other word the Constant Power Speed Range (CPSR) should cover the speed range of the automobiles i.e. up to 8000r/min.
- The machine should also be capable of producing maximum torque from zero speed to its base speed.

- The rotor should have easy-to-construct and cost-effective configuration with radial lamination. The stator should have standard three-phase sine distributed winding.

Considering above objectives, the rotor configuration of the Segmented IPM machine with a standard stator was considered to be the ideal choice. The purpose of this work is also to verify the flux-weakening capability of the segmented rotor structure in 42V ISA environment. As a basic design step, 4-pole, 550W IPM machine was considered.

The constraints on the design of the proposed machine are:-

1) In the six-switch inverter, the peak phase voltage is related to the DC bus voltage by (4.1).

$$V_{sm} = m\frac{2V_{dc}}{\pi} \tag{4.1}$$

where, m is the modulation index, V_{dc} is the DC bus voltage and V_{sm} is the peak of the phase voltage. In the 42V PowerNet system, the allowable maximum DC bus voltage including transient is no greater than 52V. Considering space vector modulation for the inverter, it can be shown from (4.1) that required phase voltage rating of the machine is 21.2V (rms).

2) For ease of construction as well as to have a direct comparison of performances to those of an existing IPM machine-I which has a conventional, non-segmented rotor configuration, it was decided to keep the stator and frame size of the prototype Segmented IPM machine same as the IPM machine-I. The outer dimensions of the Segmented IPM rotor are thus restricted to fit inside the existing stator so that an air gap length

of 0.5mm can be maintained. The outer rotor diameter is kept at 81mm and the effective axial length of the machine is limited to 55 mm.

3) The prototype Segmented IPM machine was expected to run both as generator and motor in a 42V PowerNet ISA environment. The output voltage of the machine was to be controlled by the flux-weakening operation when the speed rises above the base speed. In the event of control failure during generation at very high speed, power flow will be through the 6 flywheel diodes shown in the Fig. 4.1. Assuming diode voltage drop as V_{diode}, the generated DC link voltage at the maximum speed will be,

$$V_{dc} = \sqrt{3}\psi_{PM}\omega_{e\_\max} - 2 \times V_{diode} \tag{4.2}$$

where, ψ_{PM} is magnet flux-linkage, $\omega_{e\_\max}$ is the maximum electrical speed and V_{diode} is the diode drops per switch. However, according to the standard of 42V PowerNet, maximum allowable DC bus voltage should not exceed above 52V at any time. This condition leads to a design constraint over maximum magnet flux-linkage which can be given as,

$$\psi_{PM} \leq \frac{0.05}{p} = \psi_{\max} \tag{4.3}$$

Here maximum speed is 6000r/min, diode voltage drops are assumed to be 0.8 V per switch and p is the number of pole pair in the machine [47].

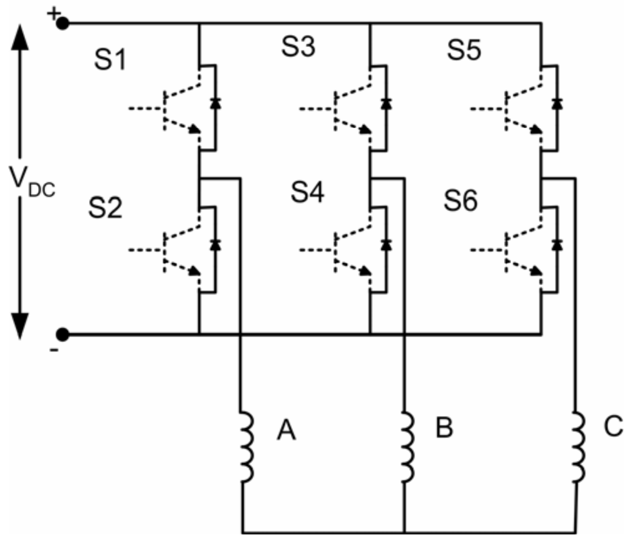

Fig. 4.1 Rectifier Circuit composed of flywheel diode without inverter control

However, it should be noted here that this constraint imposed by the standard of the 42 V is unique to the ISA system of the automobile. In case of traction or any other wide CPSR applications where DC bus voltage is as high 550~600V, in general this constraint can be expressed as,

$$\frac{V_{DC} + 2V_{diode}}{\sqrt{3}\omega_{e\_max}} \leq \psi_{max} \tag{4.4}$$

For example, the traction system with a 550V DC bus, this constraint can be given as,

$$\psi_{PM} \leq \frac{0.8768}{p} \tag{4.5}$$

4) One of the targeted objectives is to achieve a wide CPSR in the IPM machine. Ideally, the parameters of the proposed machine should be such that the condition of optimum flux-weakening given in (2.26) can be

maintained. The equation (2.26) can be expressed in terms of machine parameter as,

$$\psi_{optimum} = L_d I_{sm} \qquad (4.6)$$

where, $\psi_{optimum}$ is the optimum magnet flux-linkage, L_d is the d-axis inductance and I_{sm} is the system current limit. However, the electric machine used in the 42V ISA environment is a low-voltage and high-current machine. It has relatively large d-axis inductance L_d and system current limit I_{sm}. Consequently, the optimum flux-linkage of (4.6) is larger than the allowable maximum flux linkage $\psi_{\max}$ given in the(4.3). Therefore, in the proposed machine magnet flux-linkage is chosen to satisfy (4.3) instead of (4.6). The value of d-axis inductance can be optimized to satisfy the condition (4.6) by changing thickness of the flux-barrier. It has not been attempted in this work.

4.2.2. Brief description of the stator

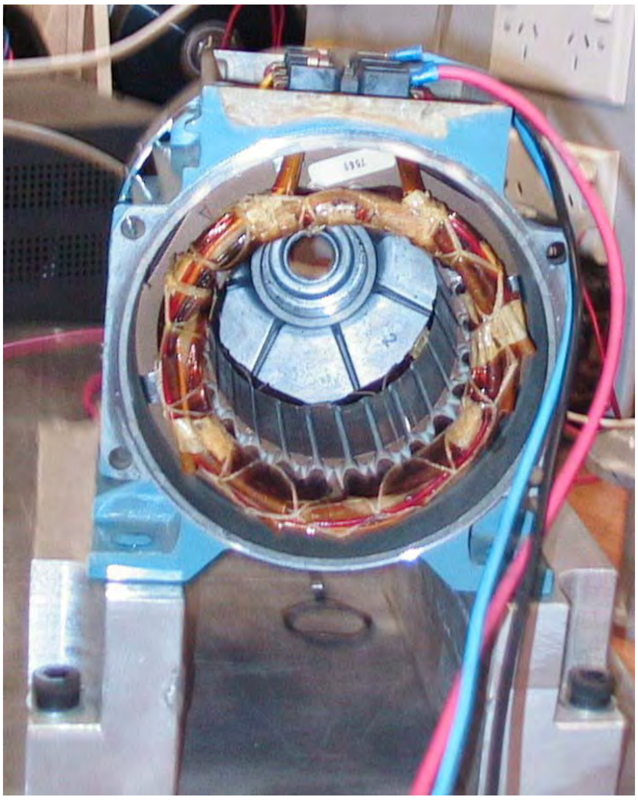

Fig. 4.2 Three-Phase distributed winding Stator

As mentioned earlier, an existing stator (shown in the Fig. 4.2) with standard distributed winding was used with the prototype Segmented IPM machine. In this section, the stator configuration is described briefly so that rotor design process can be understood. The stator consists of the core made of standard grade of electrical steel and sine-distributed, double-layer and short pitch windings. The windings are housed in 24 slots and each coil consists of 23 turns. The lay-out of the double layer winding distribution for the stator of Fig. 4.2 is shown in Fig. 4.2.

Slt	1	2	3	4	5	6	7	8	9	10	11	12	13	14	15	16	17	18	19	20	21	22	23	24
L1	A+	C-	C-	B+	B+	A-	A-	C+	C+	B-	B-	A+	A+	C-	C-	B+	B+	A-	A-	C+	C+	B-	B-	A+
L2	A+	A+	C-	C-	B+	B+	A-	A-	C+	C+	B-	B-	A+	A+	C-	C-	B+	B+	A-	A-	C+	C+	B-	B-
Pole	N						S						N						S					

Fig. 4.3 Laid out diagram of the winding

The actual number of series turns per phase is,

$$N_{ph} = 2pN = 46 \tag{4.7}$$

where, p is number of pole pairs and N is the number of conductors per slot per pole. The distribution factor k_{d1}, pitch factor k_{p1} of the machine are defined as follows,

$$k_{d1} = \frac{\sin\frac{q\gamma}{2}}{q\sin\frac{\gamma}{2}} = 0.9659 \tag{4.8}$$

where, q = 2 is number of slots per pole per phase and $\gamma = \frac{\pi}{3q} = 30^{\circ}$ is slot pitch in electrical degree.

$$k_{p1} = \cos\frac{\varepsilon}{2} = 0.9659 \tag{4.9}$$

The coil is short pitch by one slot; hence, the short pitch angle is $\varepsilon = \frac{\pi}{6}$.

In this particular stator, the slots are not skewed; hence, the windings skew factor k_{s1} is 1. Therefore, the total winding factor of the stator is,

$$k_{w1} = k_{d1}k_{p1}k_{s1} = 0.933 \tag{4.10}$$

It should also be noted here that this same stator was also used with the conventional non-segmented IPM machine-I. As a result, the direct comparison of performances of the proposed segmented IPM rotor with the non-segmented conventional rotor is possible.

The stator lamination and slot dimensions are shown in the Fig. 4.4 below. Other main dimensions are provided in the appendix B.

This same stator is also used with the conventional, non-segmented prototype IPM machine-I. Thus a direct comparison of performance of the segmented IPM machine with that of the non-segmented IPM machine-I is realized.

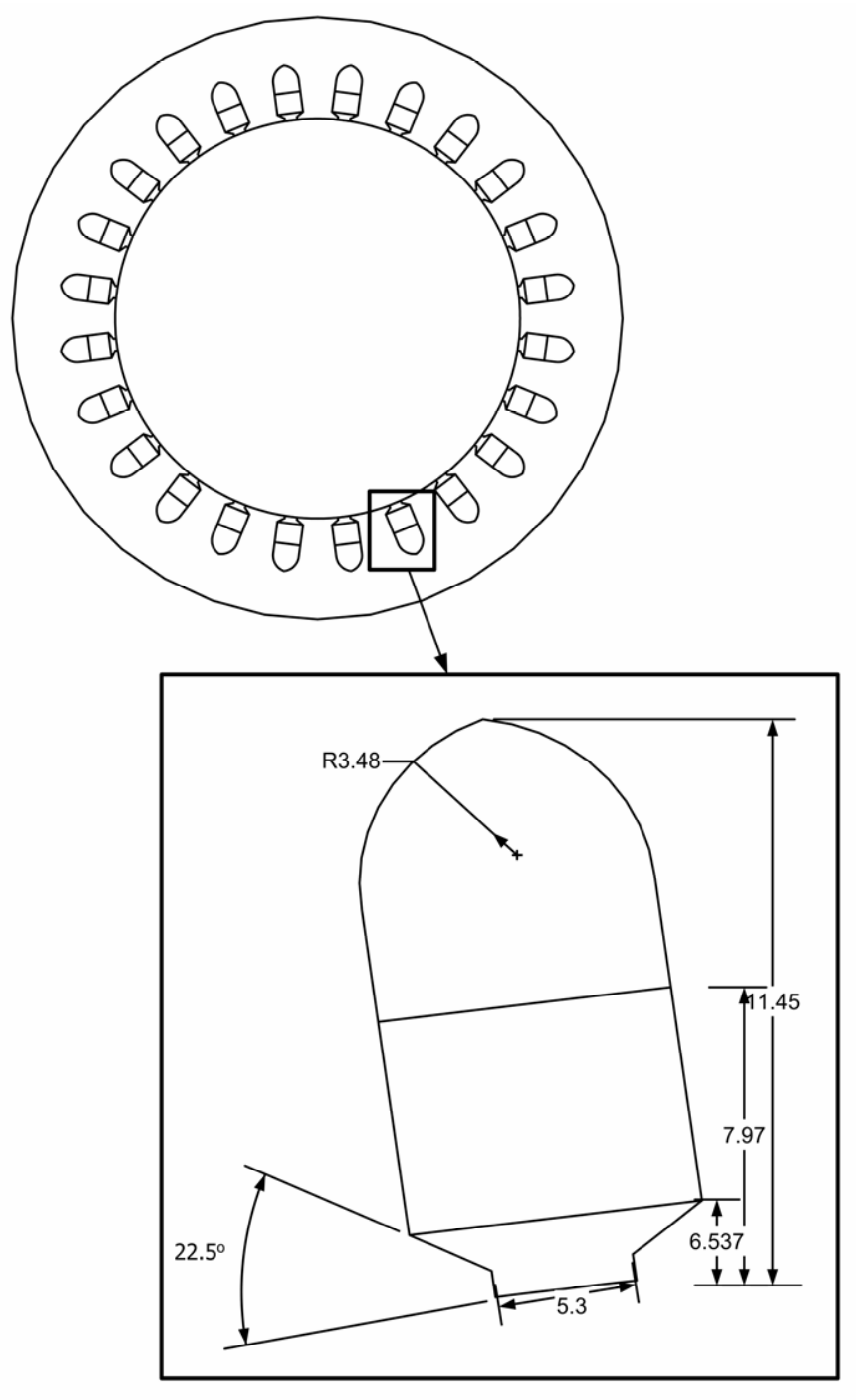

Fig. 4.4 Stator lamination and slot dimensions (in mm)

4.2.3. Description of the rotor

The rotor of the Segmented IPM machine consists of the core and magnet poles. The rotor laminations are made of standard electrical steel grade Lycore140 (0.35mm thick). The magnet poles are segmented and buried in the core as shown in the detailed diagram of the rotor lamination of Fig. 4.5. The main dimensions of the rotor can be found in Table B-2 of appendix B.

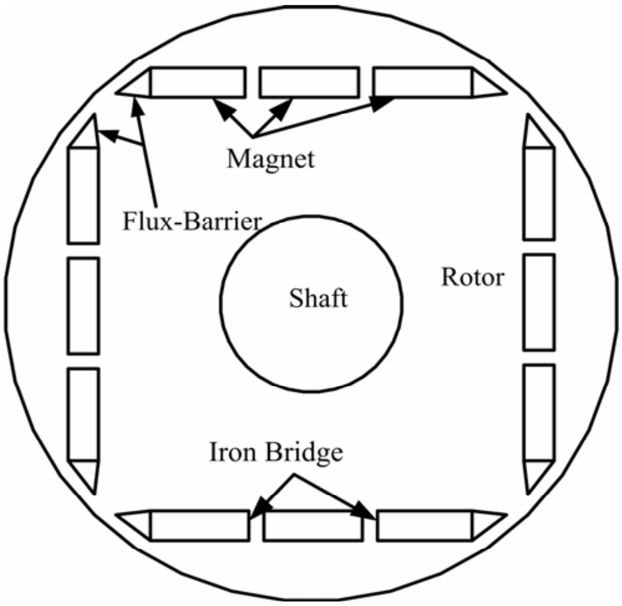

Fig. 4.5 Detailed diagram of rotor lamination

The iron bridges between magnet segments provide additional path for magnet flux canalization during flux-weakening operation. The flux-barriers are provided to prevent the magnetic short circuit between adjacent magnet poles. The selection of core and magnet materials for the rotor, width and thickness of the magnet segments and iron bridges etc. will be described in the following sections.

4.3. Rotor Design Process

The performance characteristic of the Segmented IPM machine greatly depends on its rotor configuration, magnet and core materials. The design optimization process was completed through the flowchart given in the Fig. 4.6. The flow chart shows that the best possible rotor magnet and segment geometry design was achieved through a repetitive trial and error process within the permissible area of machine constants. One of the main targeted performances of the machine is a wide Constant Power Speed Range (CPSR). The power capability of a machine can be calculated from the estimated parameters. It is a good indication of expected CPSR and can be used as a tool of quick performance measurement during the optimization process.

The three main machine parameters such as ψ_{PM}, L_d and L_q depend on the magnetic condition of the machine. Therefore, for any change in the magnetic circuit of the machine can alter them. In the optimization process, the constants were estimated by the finite element method for various magnetic conditions. The power capability of the machine was calculated from these estimated parameters by the procedure described in [11] and was used as a check of targeted performance in the process. The rated voltage and currents are taken as the base quantities and the speed at which the the back EMF becomes equal to rated voltage is taken as the base speed for pu calculations. In the reference [11], the developed pu power of the machine was calculated from the equation (2.25) given in the chapter 2. In all IPM machines, the peak pu power for any speed occurs at an optimum current angle γ^*. When the speed rises above the base value, the terminal voltage at this angle becomes higher than 1pu. In such a case, the current angle needs to be changed to a value at which the terminal voltage will again be 1pu. The output power is then calculated with the new current angle. The process can be repeated of the entire range of speeds. By plotting the pu power against speed, power capability curve can be obtained.

Although, the above mentioned pu power capability curve is for lossless machine, it still can give a good idea about the probable CPSR in a real machine during the optimization process.

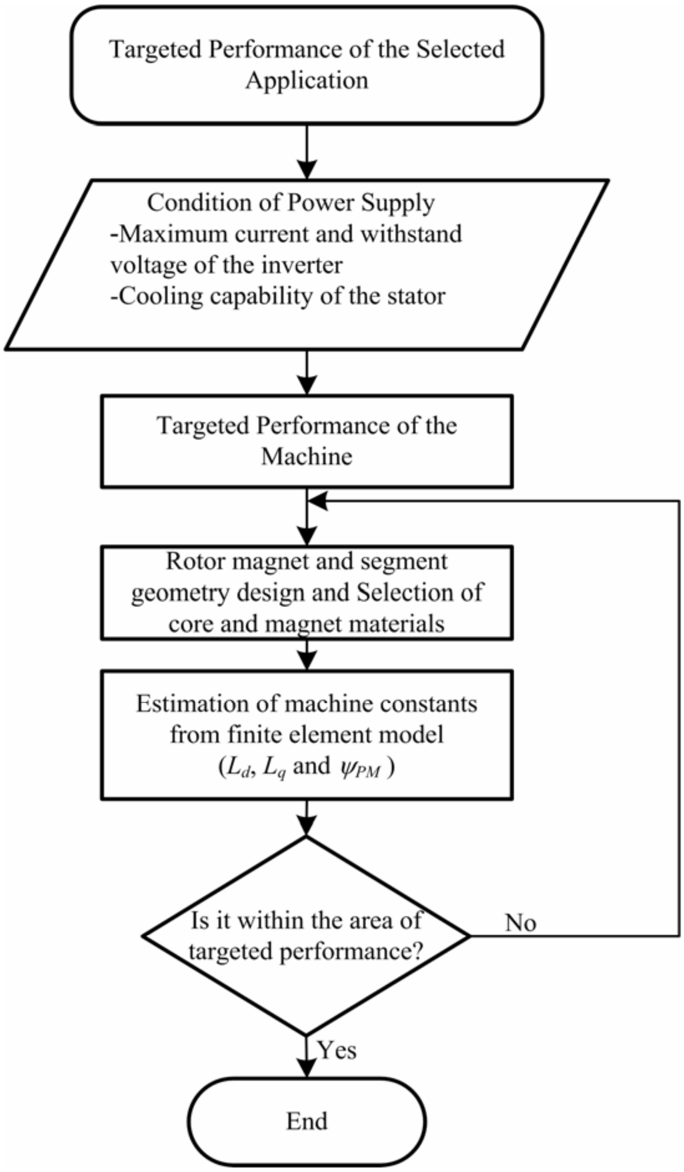

Fig. 4.6 Flow chart of the optimization process

For the prototype Segmented IPM machine, the power capability curves were calculated for different magnet and core materials, size of the segments and iron bridges. The best possible solution was determined depending on the resultant CPSR. After completion of the optimization process, the values of actual developed power for various speeds in the prototype Segmented IPM machine were calculated from the finite element method which is described in detail in the chapter 6. These predicted results are verified with the measured values also in the same chapter. In this section, we will concentrate more on the optimization process. The estimation of machine parameters and their variation will be discussed in section 4.4.

4.3.1. Selection of permanent magnet material

The open circuit air-gap flux density of the IPM machine is directly related to the remanance of the permanent magnet material used in the poles. Hence, the selection of the magnet grade was decided on the criterion of maximum allowable open circuit air-gap flux density.

The open circuit induced EMF of the IPM machine can be expressed as,

$$E_{rms} = \frac{\pi f}{\sqrt{2}}(k_{w1}N_{ph})B_{g1}Dl \qquad (4.11)$$

where, f is the frequency, B_{g1} is the air-gap flux-density. From the equation (4.11), the allowable fundamental air-gap flux-density of the prototype machine can be estimated. Values of the effective axial length of the rotor l, the stator bore diameter D and allowable induced voltage at maximum speed of 6000r/min in the (4.11), came from the design constraints. Therefore, the allowable open circuit fundamental air-gap flux-density of the machine can be calculated as,

$$B_{g1} \approx 0.30\,[\mathrm{T}] \qquad (4.12)$$

The required magnet remanance can be roughly estimated from the relation given in (4.13).

$$B_g \approx \frac{B_r}{1 + \frac{\mu_{rrec} g}{l_m}} \tag{4.13}$$

where, B_r is the remanance of the magnet material, g is the air gap length, l_m is the length of the magnet and μ_{rrec} is the relative recoil permeability.

For the air-gap flux density of 0.3T, the remanance B_r calculated from (4.13) is approximately 0.4 T. However, in the above analysis the core material is considered to be infinitely permeable and all leakage fluxes are ignored, which is not true in a real IPM machine. Additionally, a safe demagnetizing margin must be considered against over- load and fault currents.

Considering maximum energy product and cost, the NdFeB is ideal for high performance applications. The two main categories of NdFeB are the sintered and bonded type NdFeB. One grade from each group was selected for the Segmented IPM machine design. The sintered NdFeB has a remanance of 1.08~1.12 T whereas remanance of the bonded NdFeB is 0.68~0.78T at room temperature. The open circuit air gap flux densities of the segmented IPM machine estimated for these two magnet materials are shown in Fig. 4.7. In case of sintered NdFeB, the fundamental peak flux-density is 0.381T where as that of bonded NdFeB is 0.263 T. The torque and power capabilities of the machine with sintered and bonded magnet were also calculated from the parameters and are shown in the Fig. 4.8. Although, with sintered magnet developed power and torque are higher, the CPSR is relatively small. Therefore, bonded NdFeB was selected as the suitable magnet material for the prototype design.

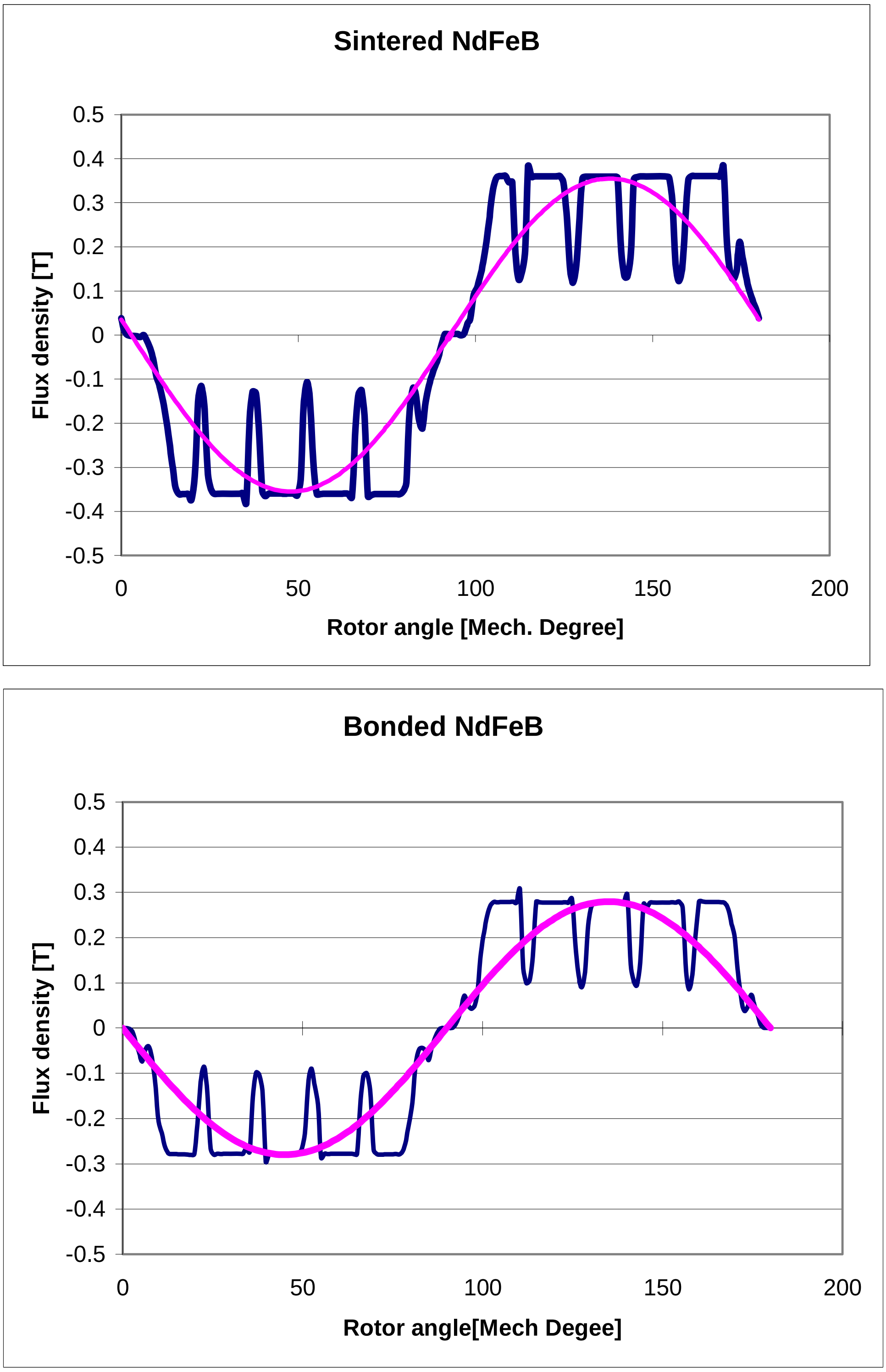

Fig. 4.7 The open circuit air-gap flux density of the Segmented Magnet IPM machine with sintered and bonded NdFeB

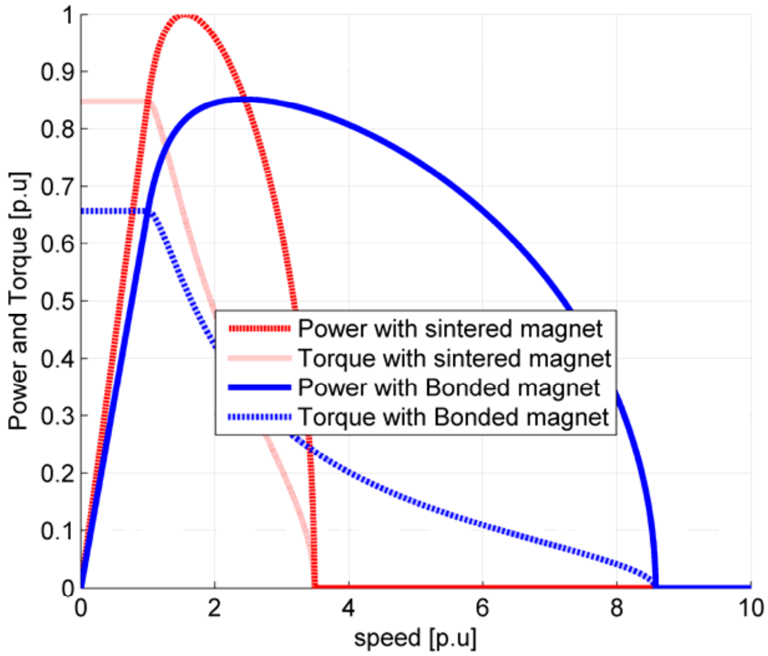

Fig. 4.8 The torque and power capabilities with sintered and bonded NdFeB

4.3.2. Selection of the Rotor Core Material

As discussed in the chapter 2, the Interior Permanent Magnet machine is basically a synchronous machine. Since the rotor rotates at synchronous speed, flux change seen by it is minimal. From this point of view, theoretically, the iron loss in the rotor of the IPM machine is negligible. However, the space harmonics in the flux-density and the rotational variation of the flux also causes localized iron loss in the rotor core which increases with frequency [48, 49]. The constant power operation occurs at higher than rated frequency and the machine operates under voltage and current limit of the system. With such extreme conditions, the harmonics in the current and voltages also increase. Consequently, total core loss can become high to deteriorate the performance of the machine at high operating speed. The loss can be minimized by constructing both the rotor and stator with high grade electrical steel. For the prototype Segmented IPM machine, a standard electrical steel grade (Lycore 140, thickness: 0.35mm and total loss at 50 Hz is 9W/kg) with low loss at the base operating frequency was selected as rotor core material. The hysteresis loop and *BH* characteristic of Lycore 140 are given in the Fig.3.13 (a) and (b) respectively.

4.3.3. The length of Magnet Segments and Iron Bridges

The volume of the magnet is directly related to the output power of the machine and is given in [50] as,

$$V_{PM} = 2phwl = c_v \frac{p_o}{fB_r H_c} \tag{4.14}$$

where, *h*, *w* and *l* are height, width and length of the magnet respectively, P_0 is the output power, *f* is the frequency, B_r and H_c remanance and coercivety of magnet material respectively and c_v is an utilization factor which is function of overload capacity factor, form factor and coefficient of utilization of the permanent magnet. The height of the magnet *h* is decided by the effective axial length of the rotor. The width of each segment depends on the widths of the iron bridges and on the length of the pole shoe. The pole pitch of the machine is given as,

$$\tau = \frac{\pi D_{rot}}{2p} = 63.62\,[\text{mm}] \tag{4.15}$$

The pole shoe arc to pole pitch ratio for the machine was taken as $\alpha_i = 0.756$ and therefore, pole shoe arc length is $b_p = \alpha_i \tau = 48.1\,[\text{mm}]$. The distance from the rotor periphery and length of the pole shoe chord determine total width available for the magnet segments and the iron bridges.

The width of the iron bridge is very critical for the Segmented IPM machine. If they are too wide, a large amount of useful magnet flux will be wasted as leakage. On the other hand, a very thin iron bridge will not be effective and rather will become an unnecessary physical limitation to the structure. Since, the iron bridges also retain the magnet segments mechanically, a very narrow iron bridge will not be able to provide adequate structural strength.

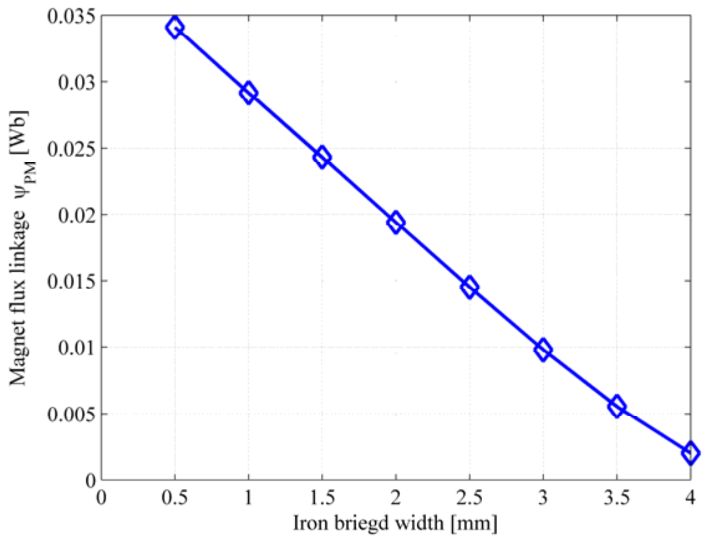

Fig. 4.9 Variation of magnet flux-linkage with the iron bridge width

As seen from the Fig. 4.9 the magnet flux-linkage reduces linearly with the increasing width of the iron bridges. The wider the iron bridges the higher will be leakage in them which will result in reduced magnet flux-linkage. On the other hand, when the width is lower than 1.7 mm, magnet flux-linkage is greater than limiting value of 0.025 Wb found from the (4.3). Considering other two parameters L_d and L_q, and output capability, the optimum iron bridge width was found to be 2 mm.

An empirical formula to calculate the optimum iron bridge width was also derived from saturation flux-density of the bridges. This is given as,

$$w_{brdg} = \left[\frac{k_{brdg}\psi_{\max}}{n_{brdg} l B_{sat\_brdg} N_{ph} k_{w1}} \right] \tag{4.16}$$

where,

k_{brdg} : the ratio of bridge flux linkage to magnet flux linkage

n_{brdg} : the number of iron bridges per pole

B_{sat_brdg} : the saturation flux density at iron bridges

N_{ph} : the number of series turns per phase

k_{w1} : the winding factor .

The increasing numbers of iron-bridge per pole has same effect as widening them. The two bridges and three magnet segment structure was found to be the optimum for the prototype machine. Once the number and width of iron bridges were fixed, the width of the magnet segments can be determined from the pole shoe chord length as,

$$w_{sm} = (l_p - n_b w_b) / n_{sm} \tag{4.17}$$

where, w_{sm}, n_{sm} are the width and number of magnet segments per pole respectively, w_b, n_b are the width and number of iron bridges per pole respectively and l_p is the chord length of pole shoe arc.

The length of magnet segment (l_{PM}) in the direction of magnetization is another important design parameter. The permeance coefficient of a magnet given in (2.1) of chapter 2 is directly proportional to l_{PM} of the magnet. The safe limit of demagnetization reduces when permeance co-efficient is low because the load line will operate close to the demagnetizing limit. In other word, a thinner magnet can become irreversibly demagnetized easily. The magnet length in the direction of magnetization also affects the performance characteristic of the machine. A very thick magnet needs a large negative d-axis current to offset the magnet flux-linkage during flux-weakening. The Fig. 4.10 shows power capability of the segmented for three different magnet lengths. It is clear from the figure that magnet length with 4mm shows a wider capability and hence, it was selected as the optimized magnet length in the direction of the magnetization. When l_{PM} is 8 mm, relatively large negative field is required for flux-weakening. Hence, in this case, the CPSR range is smaller as shown in the Fig. 4.10. On the other hand when l_{PM} is 2 mm, the load line of the proposed machine lies very close to the lower end of the demagnetizing characteristic. Consequently, there is not enough range of flux-weakening. Hence, the CPSR of the prototype segmented IPM for this case is also lower. Moreover, with 2mm the risk of irreversible demagnetization of the pole magnet increases.

The reduced l_{PM} results in decreasing magnet flux-linkage and hence, the maximum speed should increase with decreasing l_{PM} i.e. for 2mm, 4mm and 8mm, the highest maximum speed should result with 2mm. This is true only when the d-axis inductance is unaffected by $l_{PM.}$ The d- and q-axis inductances are inversely proportional to the effective air-gap length of their respective axis. The effective air-gap length of d-axis inductance is influenced by the $l_{PM.}$ Consequently, d-axis inductance is also affected by the $l_{PM..}$ In the studied machine, change of d-axis inductance with $l_{PM,}$ was taken into account, and it was seen that for the studied segmented magnet IPM machine the highest maximum speed is associated with 4mm rather than 2mm. Hence, 4mm is selected as optimum $l_{PM.}$

The detailed drawing of the rotor lamination with the dimensions and magnet segment are provided in the appendix B. The Fig. 4.11 shows various stages of the prototype rotor assembly during construction.

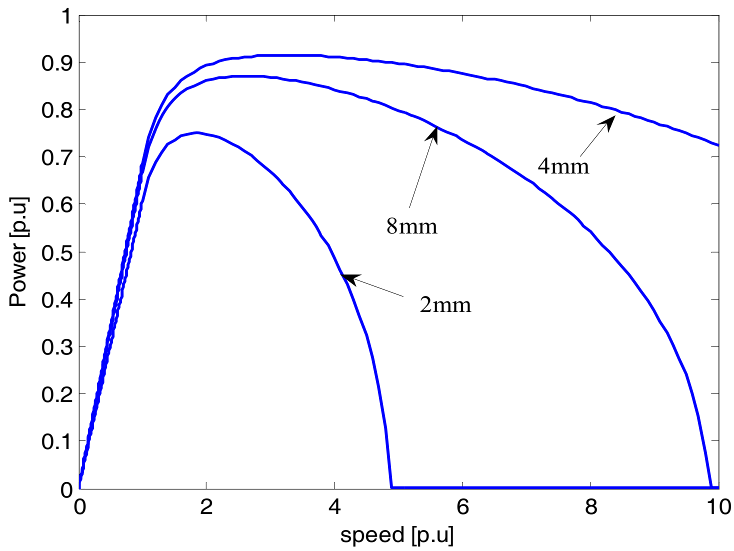

Fig. 4.10 The power capabilities of the Segmented Magnet IPM for three different magnet lengths

a) The stack of rotor laminations

b) Front view

c) Front view after covering with

d) Completed assembly

Fig. 4.11 Various stages of the proposed segmented IPM rotor assembly

4.4. Parameter Study

4.4.1. The Back EMF Constant and Magnet Flux Linkage

The induced EMF by the permanent magnet machine is proportional to the speed of the rotor. The back EMF constant of the machine K_e is defined as the ratio of the induced EMF to the mechanical speed of the rotor. The magnet flux linkage, designated as ψ_{PM} is related to back EMF constant by the relation given as,

$$\psi_{PM} = \frac{K_e}{p} \tag{4.18}$$

The EMF can be calculated by analytical method or by time stepping finite element method. In analytical method, when the EMF is calculated from (4.11), the air-gap flux-density B_g can come from either a magneto-static finite element analysis or from an empirical formula. However, in this work, time-stepping finite element model coupled to an external circuit was used to estimate the induced EMF for different speeds. The EMF induced in a machine is calculated from the Faradays's law as,

$$E = -N_{ph}\frac{d\phi}{dt} \tag{4.19}$$

The flux ϕ is related to flux-density as,

$$\phi = \int_s B ds \tag{4.20}$$

Hence,

$$E = -N\frac{d}{dt}\left(\int_s B ds\right) = -N\int_s \frac{\delta B}{\delta t} ds \tag{4.21}$$

On the other hand, from Stoke's theorem

$$E = \oint_l E_i dl = \int_s (\nabla \times E_i) ds \tag{4.22}$$

where, E_i is the induced electric field intensity.

From the equations (4.21) and(4.22),

$$\nabla \times E_i = -\frac{\delta B}{\delta t} \tag{4.23}$$

The flux-density B in (4.23)can be expressed in terms of magnetic vector potential A.

Therefore,

$$\begin{aligned} \nabla \times E_i &= -\nabla \times \frac{\delta A}{\delta t} \\ \nabla \times (E_i + \frac{\delta A}{\delta t}) &= 0 \end{aligned} \tag{4.24}$$

Since curl of gradient is zero, the induced electric field intensity per unit length for one turn becomes,

$$E_i = -\frac{\delta A}{\delta t} \tag{4.25}$$

Integrating E_i over one stator slot area, multiplying by number of turns and actual depth of the machine, gives the induced EMF per phase as,

$$E = -\frac{lN_{ph}}{S} \int_s \frac{\delta A}{\delta t} ds \tag{4.26}$$

Here, $\frac{\delta A}{\delta t}$ is determined from the time-stepping finite element method. The finite element model of the one pole and its externally coupled circuit to calculate the EMF for the Segmented IPM machine is shown in Fig. 4.12.

In this figure, the coils PA, MA, PB and MC represent phase coils present in one pole pitch. The L_{eA}, L_{eB} and L_{eC} are the end turn inductances. As mentioned earlier, the 2D finite element method can not incorporate end-turn leakage inductances which need to be calculated by empirical formulae. The formulae used in this work is from the reference [51] and given as,

$$L_{end} = \frac{2N_{ph}^2}{p}\left(\frac{l_{avg}}{2} - l_i\right)\psi_{end} \qquad (4.27)$$

where, l_{avg} is the average length of one turn of the winding, l_i is the effective axial length of the machine and ψ_{end} is the end-turn flux linkage. The end-turn flux linkage is function of length of end-turn, coil span and geometrical coefficient.

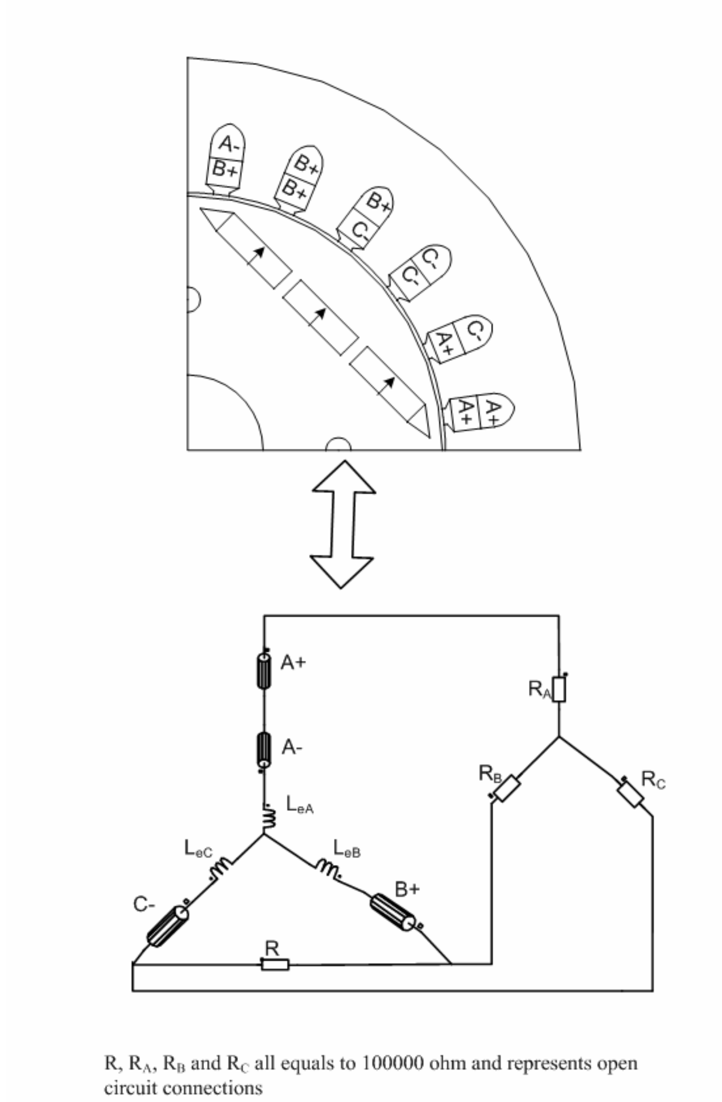

Fig. 4.12 The finite element model of the one pole and its coupled circuit for the EMF calculation of the Segmented IPM machine

The estimated line to line back EMFs across resistor 'R' of the Segmented IPM machine at 1500r/min and 6000r/min are presented in Fig. 4.13. As seen from the figure, the EMF contains higher harmonics. Therefore, the magnet flux linkage per phase is calculated from the fundamental of the induced EMF. For example, the peak of the fundamental line to line EMF at 6000r/min is 45.19V. Therefore, the estimated magnet flux-linkage is,

$$\psi_{PM} = \frac{\hat{E}}{\sqrt{3}p\omega_r} = 0.021 \text{ [Wb]} \tag{4.28}$$

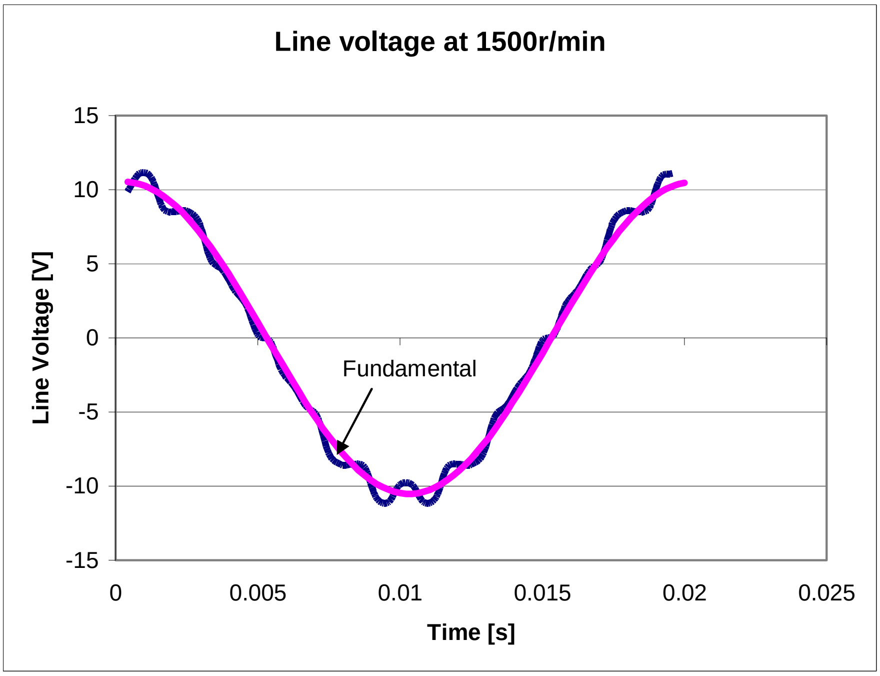

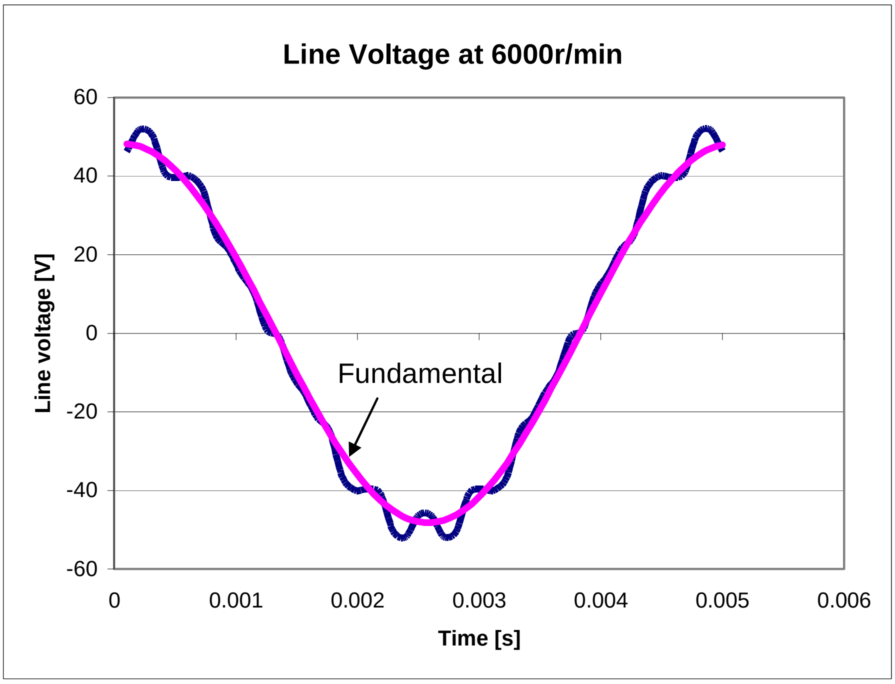

Fig. 4.13 The predicted induced EMFs and their fundamentals at 1500r/min and 6000 r/min of the proposed segmented IPM machine

4.4.2. The d- and q-axis Inductances

The accuracy of predicted steady state performance of the IPM machine during design process depends largely on the precise calculation the synchronous reactances (or inductances) in the d- and q-axis.

The physical definition of synchronous reactance arises from the rotating flux-wave established by the armature reaction. Three sine-distributed phase windings carrying balanced three-phase sinusoidal current produce a sine-distributed MMF wave that sets up rotating flux in the space. This flux is responsible for generating voltage drops in the three phases. The voltage drop is proportional to current and therefore can be regarded as the voltage drop across a fictitious reactance which is know as synchronous reactance of the machine. The three phase synchronous reactance can be transformed into d- and q-axes reactances or inductances by using standard transformation technique.

The finite element method is widely used to estimate d- and q-axis inductances of the IPM machine. In 2D finite element model, the line integral of vector potential along the boundary of a surface area gives the total magnetic flux passing through that area. Hence, flux in filament wire of negligible cross-sectional area is calculated simply by $\phi = l(A_1 - A_2)$ where, l is the length of the wire and A_1, A_2 are magnetic potential of two points at the intersection of domain boundary and FE plane. However, the cross sectional area of the winding coils in an electrical machine is not filament like and for such case, fluxes linkage can be calculated as,

$$\psi = l\left[\frac{\iint_{s_1} A_1 ds}{S_1} - \frac{\iint_{s_2} A_2 ds}{S_2}\right] \tag{4.29}$$

where S_1 and S_2 are the total areas of a winding carrying positive and negative current respectively and l is the core length of the machine [52]. Alternatively, the flux linkage of a current carrying conductor can be expressed as,

$$\psi = \left(\frac{l}{I}\right)\iint_s (J.A)ds \tag{4.30}$$

where, I is the current through the winding and s is the cross-sectional area of the winding.

Once the flux linkage is calculated, the synchronous inductance can be obtained from $L_s = \psi / I$.

In order to calculate d- and q-axis inductances, the finite element model need to be excited with the appropriate stator excitation so that flux-linkages in both axes can be estimated. In the reference [53], Pavlik et al. described a method, where the ampere-turns of individual slot are arranged in such a way that MMF coincides with a specific axis. The individual current of each slot is given as,

$$I_{Si} = F_{pk}[\cos(\theta_i + \beta) - \cos(\theta_{i+1}\beta)] \tag{4.31}$$

where,

I_{Si} : current in the i^{th} stator slot [A]

θ_i : angle from the d-axis to the i^{th} stator tooth [Mech. Deg]

β : angle where peak of MMF wave occurs [Elec. Deg]

F_{pk} : peak of the fundamental MMF [A turn]

The value of β is kept as 0^o or 90^o depending on required axis excitation. The d- and q-axes fluxes calculated by this method are shown in the Fig. 4.14. Here, the magnet field is kept off and only either d- or q-axis current excitation is present at one time.

Consequently, this method will not reflect any effect of cross-saturation and magnet flux on the inductance values.

A second method to calculated inductances in the finite element is to excite the stator winding with three phase currents in presence of magnet field which gives three phase flux linkages [54]. The d- and q-axes flux linkages are calculated from the three-phase flux linkages using Park's transformation. Since in this method, both d- and q-axis currents are present, the inductances are considered to be function of both axes currents and are given in (4.32) and (4.33). In order to remove the cross coupling component while calculating inductance of one axis, flux-linkage of two close by operating points are required where current of that axis is varied keeping the other axis current constant. The inductance is the ratio of difference between flux linkages to difference in axis current. We will call this method as 'three-phase flux linkage method'. This method can be used to calculate both the absolute inductance and incremental inductance. In this work, the method was used to calculate incremental inductance. The 'Pavlik's method' was used to calculate the absolute inductance.

$$L_d = \frac{\partial \psi_d(i_d, i_q)}{\partial i_d} \approx \left. \frac{\Delta \psi_d}{\Delta i_d} \right|_{i_q = \text{constant}} \tag{4.32}$$

$$L_q = \frac{\partial \psi_q(i_d, i_q)}{\partial i_q} \approx \left. \frac{\Delta \psi_q}{\Delta i_q} \right|_{i_d = \text{constant}} \tag{4.33}$$

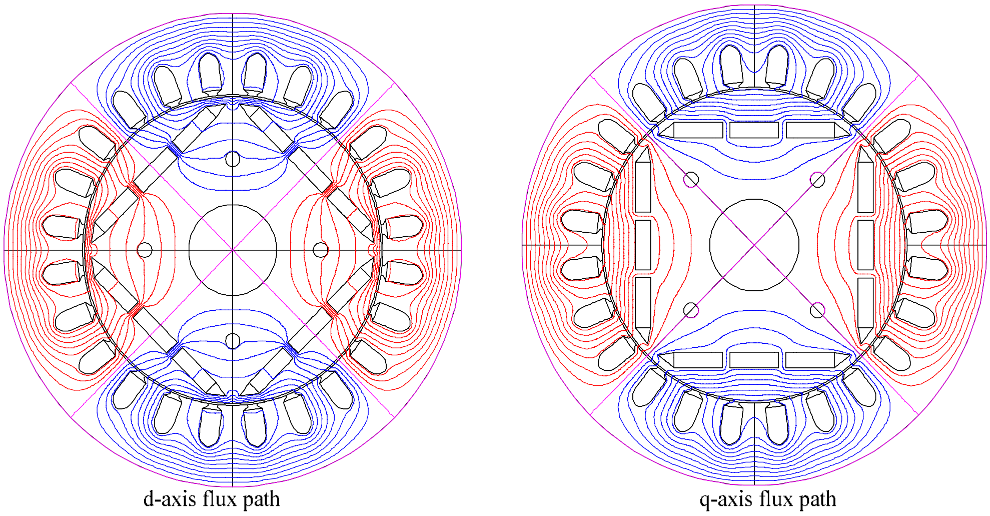

Fig. 4.14 The d- and q-axis flux path when magnet field is kept off

In both cases the end-turn inductance is calculated from the empirical formulae given in (4.27) and added to the estimated inductances. Interestingly, d-axis inductance from Pavlik' method varies with current whereas the three-phase flux-linkage method gives a constant value for all currents. This peculiar phenomenon of the segmented IPM machine can be explained in following way-

In Pavlik's method when magnet field is absent, the path of d-axis flux due to the current alone can be observed. In the Segmented IPM machine, iron bridges lies directly on the path of d-axis flux. In the absence of magnet leakage flux, they offer paths of the least reluctance to the d-axis flux. As current increases, the flux-density in the iron-bridges approaches saturation. A large d-axis inductance can be noticed in the Fig. 4.15 at low current when the magnet field is absent. It reduces subsequently with rising current. This variation of d-axis inductance is contributed by the variation of the flux-density at the iron bridges. In the presence of the magnet field, the reluctances of the bridges are less likely to change sharply. Hence, in such case, a near constant d-axis inductance can be observed in the Fig. 4.15. The presence of saturation due to the magnet also reduces the amplitude of the d-axis flux-linkage which results in a lower L_d for the same current.

In order to verify the above facts, inductances were also measured before and after inserting the magnet in the prototype Segmented IPM machine. The test method of inductance measurement in the IPM machine was described in the appendix C.

The q-axis inductances were also calculated and measured with and without magnet. The Fig. 4.16 shows measured and predicted values of q-axis inductances for various current. The variation of q-axis inductance with current is minimal in this machine. Hence, there should not be any major effect of q-axis saturation on the control and performance of the machine.

The measured and predicted q-axis inductances are also higher when magnet field is absent than those measured or predicted with magnet field. Without magnet field, any cross saturation of the magnet flux on the path of q-axis was absent. As a result, L_q is higher for the same current value when the magnet field is absent.

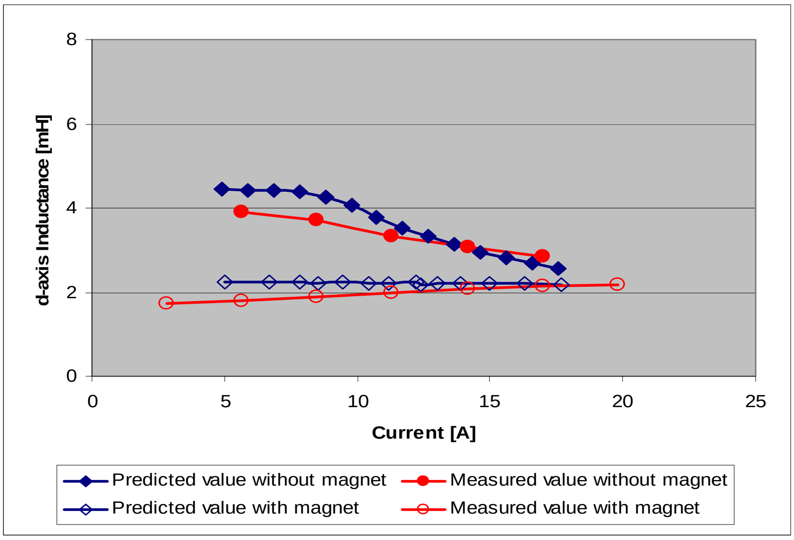

Fig. 4. 15Measured and predicted d-axis inductance with and without magnet field

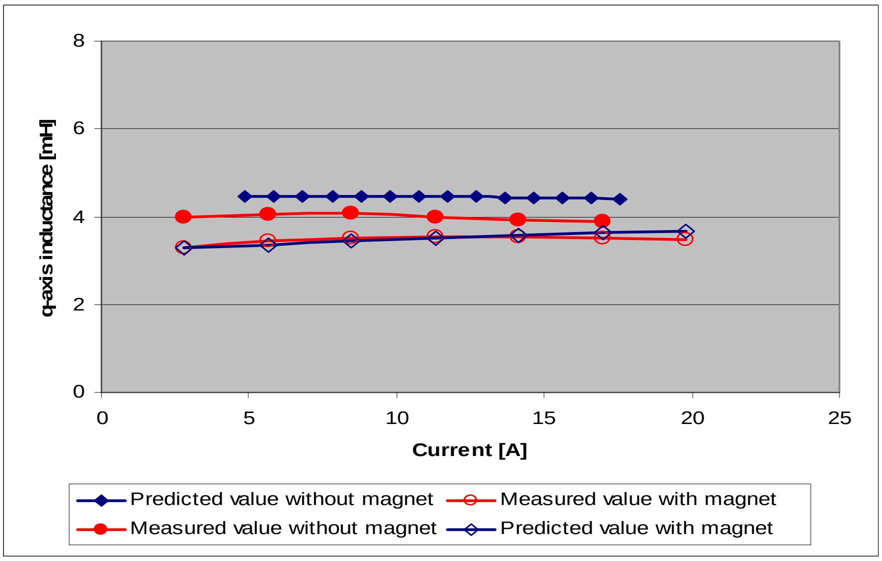

Fig. 4.16 Measured and predicted q-axis inductances with and without magnet

The three-phase flux linkage method is suitable to measure the effect of the cross-coupling over the inductances. In order to investigate the cross-coupling in the segmented IPM machine the d- and q- axis flux-linkages were calculated for various values of i_d and i_q current and plotted in the Fig. 4.17.

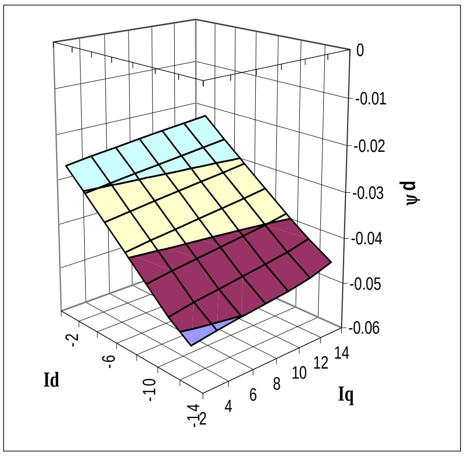

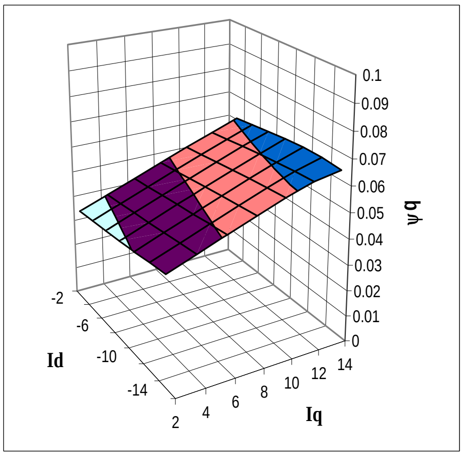

Fig.4.17 Variation of d- and q-axis flux-linkage under influence of two axes currents

Accuracy of the estimated values of inductances are affected sometime by errors such as the inaccuracy in the permeability characteristics of the core material at low flux density, small flaws in the BH curve of magnet, the small geometrical errors in the iron bridges, unaccounted three dimensional fringing fluxes, and slot ripples of the unskewed stator etc. These errors are minimized with careful modeling of the materials and machine geometry.

4.5. Cogging Torque

The cogging torque in the Permanent Magnet machines is a concern for low speed applications. The cogging torque is caused by the magnetic attraction between rotor permanent magnets and stator teeth. The circumferential component of the force attempts to maintain the alignment between the stator teeth and the magnet poles. The Fig. 4.18 displays two positions of the magnet pole with respect to stator teeth. At the position ‘A’, the magnet is aligned with the maximum number of stator teeth and net circumferential force of magnet is zero. After the rotor has rotated in the counterclockwise direction to the position ‘B’, the circumferential component of the force is no longer null. Consequently, at this position, a peak cogging torque develops and attempts to return the magnet to the previous aligned position.

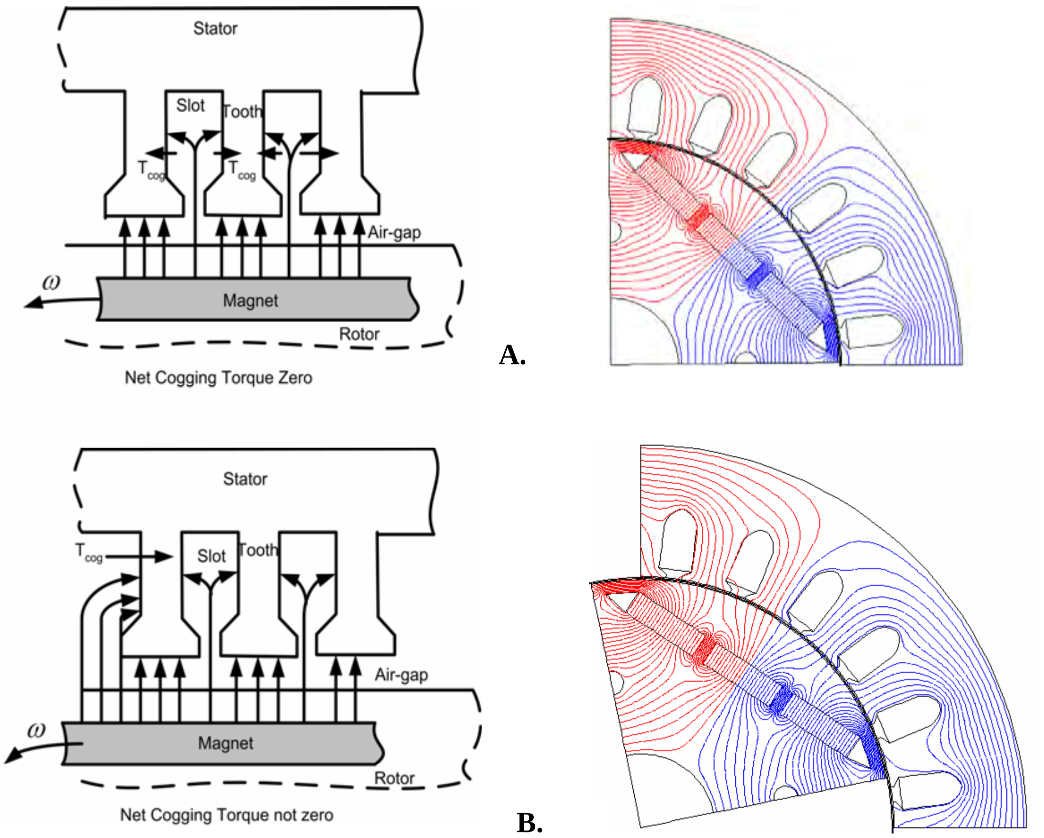

Fig. 4. 18 Cogging torque in the IPM machines

In the finite element model, the cogging of a machine can be estimated from the principle of virtual work based on the energy of the moving air gap [55]. The cogging torque is expressed in terms of rate change of reluctance in the machine by(4.34).

$$T_{cog} = \sum_{1}^{2p} \left(-\frac{1}{2}\phi_g^2 \frac{d\Re}{d\theta}\right) \tag{4.34}$$

Generally, the cogging torque values are small and can be affected by the numerical errors of the mesh when calculated by the finite element methods. In order to avoid such errors, special considerations are needed while forming the mesh distribution in the rotating air gap of the machine.

In the Flux2D, the errors are minimized by using three-layer air-gap method. In this method, the air gap is subdivided into three layers. The first layer is between the rotor diameter and the moving air gap. The second layer is the moving air gap itself and the third layer is between the moving air gap and the stator inner diameter. Thus, the moving air gap boundary is subdivided evenly so that boundaries of one time-step overlap the subdivision of the next time step. In this way, the mesh topology is kept constant in the moving air gap at each position and the influence of finite element residual error on the small torque value is minimized. The three layers in the air gap of the Segmented IPM machine are shown in Fig. 4.19.

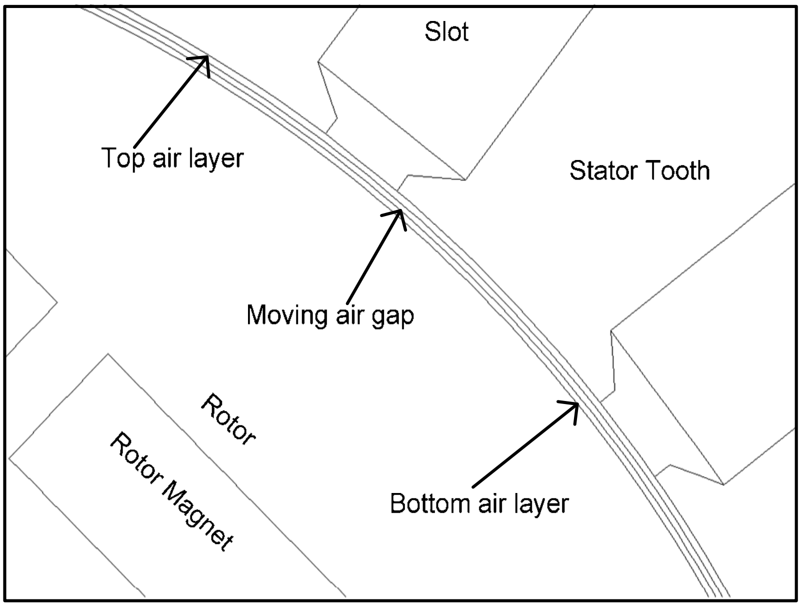

Fig.4.19 Three layer of air gap for cogging torque

The Fig. 4.20 shows the estimated cogging torque of the Segmented IPM machine compared to the IPM machine-I. The peak cogging torque of the Segmented IPM machine is almost 5 times less than that of the IPM machine-I. It should be reminded here that in both machines, the configuration of the stator is same. Some of the obvious factors behind the reduced cogging torque in the Segmented IPM machine are:

(i) Reduced magnet strength in the Segmented IPM machine. B_r of the Segmented IPM machine is 0.68 ~0.78 T whereas that of the IPM machine-I is 1.14 T.

(ii) The magnet span or pole length are different in two machines. In the segmented IPM machine, it is 134^0(Elect. Deg) and that of IPM machine-I is 125^0(Elect. Deg).

(iii) The presence of iron-bridges in the pole piece reduces air gap flux of the Segmented IPM machine further.

From above observations, we can safely conclude that there is no adverse effect of the magnet pole segmentation on the cogging torque for the prototype Segmented IPM machine. On the contrary, for the segmented IPM machine design, the cogging torque is much smaller than the IPM machine-I which uses the same stator and windings.

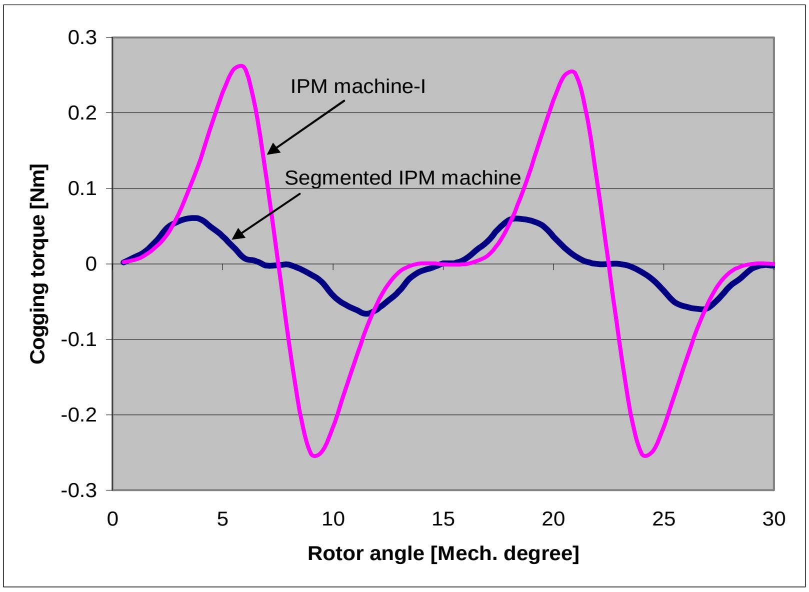

Fig.4.20 Cogging torque of the Segmented magnet pole IPM machine and IPM machine-I

4.6. Core or Iron loss

The loss in the IPM machine comprises of stator copper or winding loss, mechanical loss, and iron loss of the stator and rotor cores. The iron loss becomes significant at high frequency applications, since, its rise is directly related to the operating frequency. It can become the ultimate limiting factor to the output power capability of an IPM machine at high speed.

The precise prediction of iron loss during design process is useful to ensure high efficiency at all speeds. The core loss of magnetic material is mainly caused by hysteresis of B-H curve and induced eddy current in the surface. Conventionally, core or iron loss of a material is measured with sinusoidal flux density of varying frequencies. The loss density [W/m^3] in a core material is expressed as,

$$p_{core} = p_{hys} + p_{eddy} = k_f k_{hys} \hat{B}^{\zeta} f + k_f k_{eddy} \hat{B}^2 f^2 \qquad (4.35)$$

where, f is frequency [Hz], $\hat{B}$ is peak of the sinusoidal flux density [T], ζ is Steinmetz constant, k_{hys} is hysteresis constant and k_{eddy} $\left(= \dfrac{\sigma \pi^2 d^2}{6\rho} \right)$ is eddy current constant, k_f is the lamination stacking factor, d is the lamination thickness, σ is the conductivity of the material and ρ is the density of material. However, the flux density in the core laminations of most of the electric machines including the IPM is not pure sinusoid. In such cases, core loss is not only caused by the fundamental but also by the higher harmonics present in the flux density. Hence, loss density calculated from (4.35) using only the peak value of the fundamental component results in a large discrepancy between measured and estimated values. The harmonic components of the flux density primarily affect the eddy current loss and it can be accounted for by taking the square of rate of change of flux density for the duration of one time period [56].

$$p_{eddy} = \frac{2k_{eddy}}{T}\int_0^T \left(\frac{dB}{dt}\right)^2 dt \tag{4.36}$$

Alternately, the flux density wave-form can be expanded as Fourier series of harmonics and the total core loss can be calculated as the summation of loss contributed by each harmonics [49, 57]. Apart from hysteresis and eddy current losses, in electric machines , there exists an additional loss component known as excess or anomalous loss which is associated with continuous arrangement of magnetic domain configuration in the core [58]. It is expressed as,

$$p_{exe} = k_f \frac{k_{exc}}{T}\int_0^T \left(\frac{dB}{dt}\right)^{1.5} dt \tag{4.37}$$

where, k_{exe} is excess loss constant. Hence, the total core loss of an electric machine is summation of all three loss components- hysteresis, eddy current and excess loss.

In above discussion, variation of flux density is assumed to be alternating only. However, recent studies shows that in rotating electric machine, variation is not only alternating but also rotating in many parts of the core and loss caused by rotating variation of flux is substantial and should be included in loss estimation for better accuracy [59].

There are number of analytical and numerical methods available in the literature to estimate iron loss of the PM machine [60-63] . However, for accurate estimation of the iron loss in IPM machine which involves saturation and complicated geometry, a finite element method seems to be a proper choice. There exist two different approaches to calculate core loss in the PM machine by the finite element method. In the first method, the flux density vector of each element is spread out as a Fourier series of n^{th} elliptical harmonics. The major axis and minor axis flux densities and their ratio δ_e are determined. The total core loss is calculated as the summation of hysteresis, eddy current and excess loss of each harmonic [57]. The loss densities are expressed as,

$$p_{hys} = \sum_{n=0}^{\infty} [\delta_{e_n} p_{r\_hys_n} + (1-\delta_{e_n})^2 p_{a\_hys_n}] \tag{4.38}$$

$$p_{eddy} = k_{eddy} \sum_{n=0}^{\infty} \left[(nf)^2 (B^2_{(maj)_n} + B^2_{(min)n}) \right] \tag{4.39}$$

$$p_{exe} = k_{exe} \frac{1}{T} \int_0^T \left[\left(\frac{dB_x}{dt}\right)^2 + \left(\frac{dB_y}{dt}\right)^2 \right]^{3/4} \tag{4.40}$$

where, p_{r_hys} and p_{a_hys} are rotational and alternating hysteresis losses calculated with flux density of B_{maj} at fundamental frequency of f, B_x and B_y are the x and y components of flux density vector. In this method, the loss due to rotational magnetic field is included; hence, can give a fairly good estimation of the core loss in the IPM machine. However, it is cumbersome and need a large number of iteration for every operating condition.

The second approach to calculate core loss in finite element model is to use time-stepped FE analysis with a rotating air- gap. The core loss over one complete period of a magnetic region is expressed as,

$$p_{core} = pk_f \sum_{i=1}^{l} A_i l \left[k_{hys} B_m^{\beta} f + \frac{2k_{eddy}}{T} \int_0^T \left(\frac{dB}{dt}\right)^2 dt + \frac{k_{exe}}{T} \int_0^T \left(\frac{dB}{dt}\right)^{3/2} dt \right] \tag{4.41}$$

where, p is the number of pole pairs in the machine, A_i is the area of i^{th} element, l is the total depth of the machine, k_f is the stacking factor and B_m is the peak flux density in the i^{th} element. This method is capable to take in to account of losses due to alternating field and its harmonics but unable to do so for the rotating field. Since loss due to rotational flux density is significant in IPM machine, losses calculated from (4.41) tend to be lower than measured ones.

In stator core, rotational variation can be observed at the roots and forefront of the teeth and back side of the slots. The additional loss caused by the rotational variation depends on the ellipticity of the flux density wave form. In the [49] a simplified expression has been derived for rotational loss. The flux density wave-form over one time period is estimated at various points of stator tooth and yoke. The ellipticity of these waveforms are determined and loss density due to rotational filed is calculated as,

$$\begin{aligned} p_{r\_core} &= \kappa\delta_e p_{a\_core} \\ &= \kappa\sum_{n=1}^{N}\sum_{i=1}^{l}\delta_{e(ni)} g_i \{k_{hys} n f B_{m(ni)}^{\beta} + k_{eddy}(n f)^2 B_{m(ni)}^2\} \end{aligned} \tag{4.42}$$

where, p_{a_core} is the core loss due to alternating field variation, $B_{m(ni)}$ is $L_{maj(ni)}/2$, $L_{maj(ni)}$ is the length of major axis of the n^{th} harmonic flux density vector of the i^{th} element, l is total number of elements, N is total number of harmonics, g_i is the mass of i^{th} element, and κ is the rate of core loss increment under rotational field to alternating field. The total loss due to rotational and alternating flux density can be expressed as,

$$p_{core} = (1+\kappa)\sum_{n=1}^{N}\sum_{i=1}^{l}\delta_{e(ni)} g_i \{k_{hys} nf B_{m(ni)}^{\beta} + k_{eddy}(nf)^2 B_{m(ni)}^2\} \tag{4.43}$$

The predicted core loss by this method is fairly close to the measured values. Advantage of this method is that once p_{a_core} , κ and δ_e are known, p_{r_core} can be calculated quite easily for any machine. However, determination of γ is complex as it varies with saturation level.

During design process, the core or iron loss of the Segmented IPM machine was estimated in the finite element model. The core loss due to the alternating flux variation p_{a_core} is calculated using built in tool of Flux 2D which uses equation (4.41). The losses were calculated for no-load condition at various speeds. The loss constant of the stator and rotor laminations are given in the Table 4.1.

For the core loss due to the rotational flux variation δ_e need to be calculated. The κ can be taken as unity for shake of simplicity. As mentioned earlier, δ_e depends on the ellipticity of the harmonics. The harmonic contents of the flux density, at the tooth area and yoke, changes sharply with higher frequencies. Hence, it can be assumed that major portion of the rotational core loss is contributed from these areas. The radial and circumferential component of flux-densities are calculated at the stator tooth and back of the yoke of the studied machine. These two components of the flux-density obtained from the FEM at the centre of the tooth for the fundamental frequency of 166.67 Hz is shown in the Fig. 4. 21(a) and their harmonic spectrums are shown in the Fig. 4. 21(b). The Fig. 4.22 shows the ellipticity of 1st and 2nd harmonics of flux density at the centre of the tooth. From the ellipticity, the δ_e is calculated for each region. The alternating core loss of these are also calculated with the built in tool of the Flux 2D and then rotational core loss component is calculated by (4.42) . The summation of the rotational core loss of the tooth and yoke area gives the total rotational core loss for certain speed. For total core loss, this component is added to the total alternating core loss of the machine obtained from the Flux 2D for the same speed. The process is repeated for various speed.

The predicted total iron losses of the machine are verified from experimental measurement in the constructed segmented IPM machine and are shown in the Fig. 4.23.

Table 4-1 Core or Iron loss constants of electrical steel used for the prototype Segmented Magnet IPM machine [1]

Name	Stator	Rotor
Hysteresis Constant K_{hys}	0.042	0.036
Eddy current Constant K_{eddy}	0.00016	0.3314e-5
Excess loss Constant K_{exe}	0.0013	0.7280e-4
Density ρ	7800 [Kg/m^3]	7800[Kg/m^3]
Lamination thickness	0.5 [mm]	0.35[mm]

The core losses of the prototype machine were obtained from the measured no-load power at various speeds. The no-load power were measured by a power analyzer (Yokogawa PZ 4000) at each speed. The no-load current is also measured so that copper loss can be segregated. The mechanical losses at these speeds were also measured using the rotor before the magnets were inserted. The core loss at each speed step were calculated by subtracting the copper and mechanical losses from the no-load input power. The core loss of the conventional IPM machine-I is also measured using the similar test procedure. The measured core loss of the Segmented IPM was compared with that of the IPM machine-I in the Fig. 4.24. The loss in the Segmented IPM machine remains nearly constant after 3000r/min where as in the IPM machine-I, the loss increases proportionally to the speed. Since, the same stator was used for the both machines, the difference in losses at high speed between the two machines are undeniably contribution of rotor losses. The study in [49, 64, 65] reveals that rotational flux causes localized rotor loss in the IPM machine which was minimized in the prototype Segmented IPM machine by constructing the rotor with high grade electrical steel lamination (Lycore 140, 0.35 mm thickness) whereas the rotor of the IPM machine-I was made of solid iron.

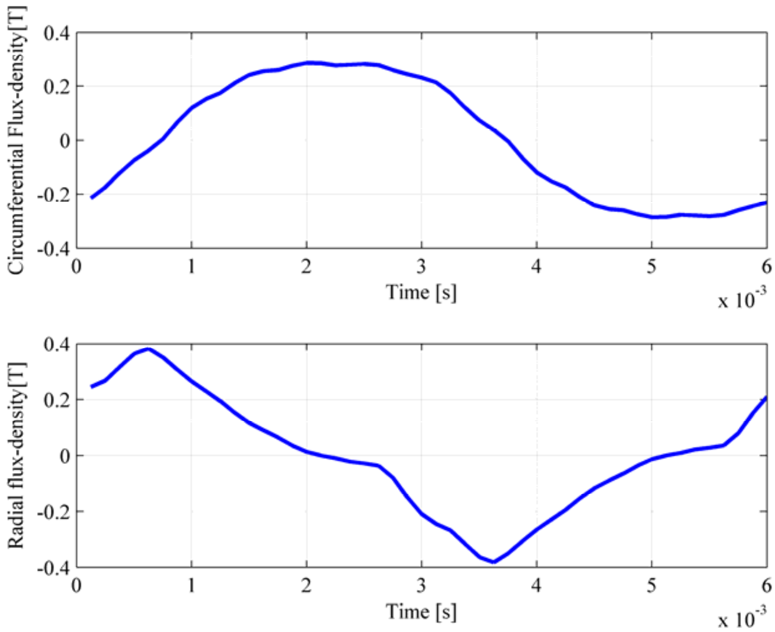

(a)

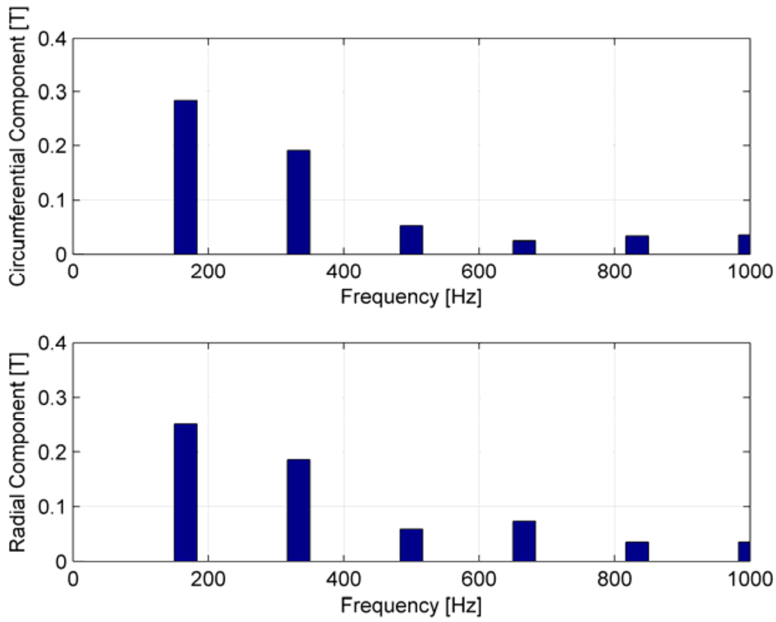

(b)

Fig. 4. 21 (a) The circumferential and radial components of the flux-density at the centre of tooth and (b) Harmonic spectrums of the flux density components from FFT

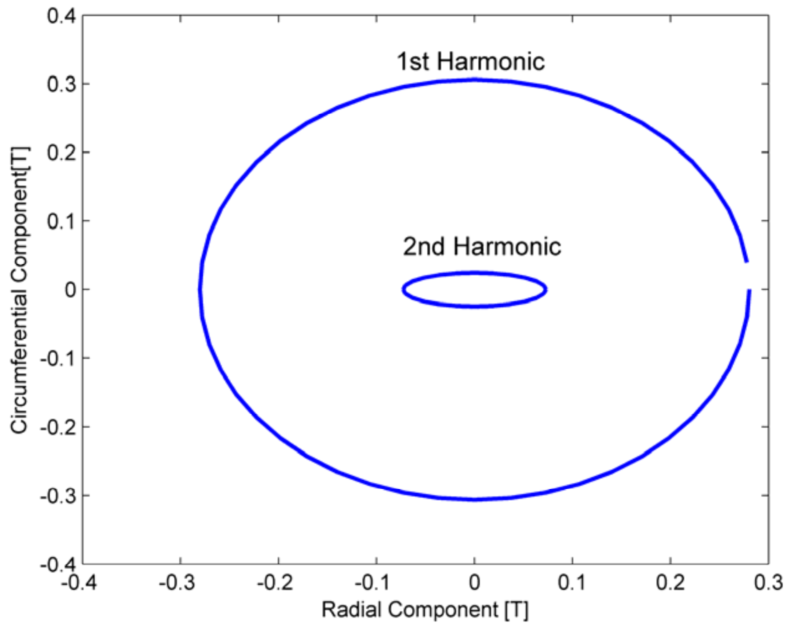

Fig. 4. 22 Ellipticity of the harmonics

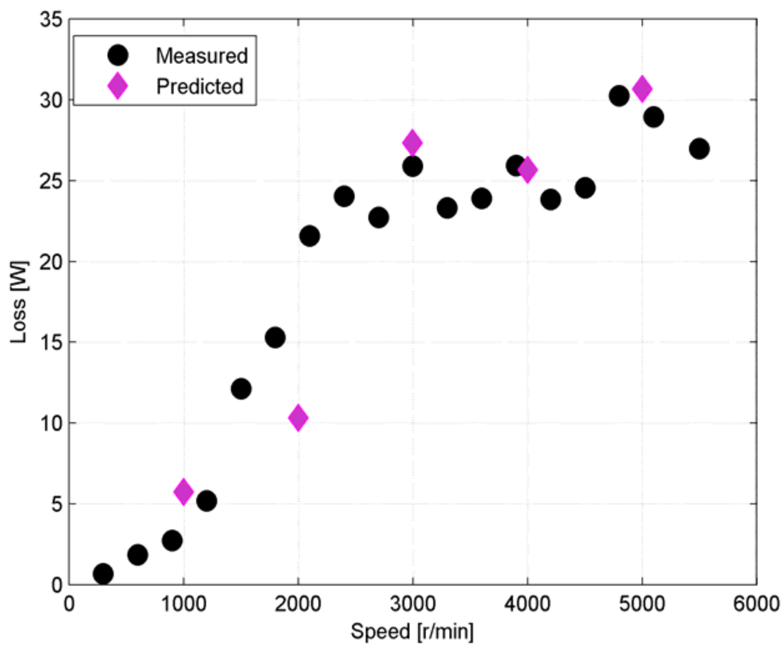

Fig.4. 23 Measured and Predicted Iron loss of segmented magnet IPM machine

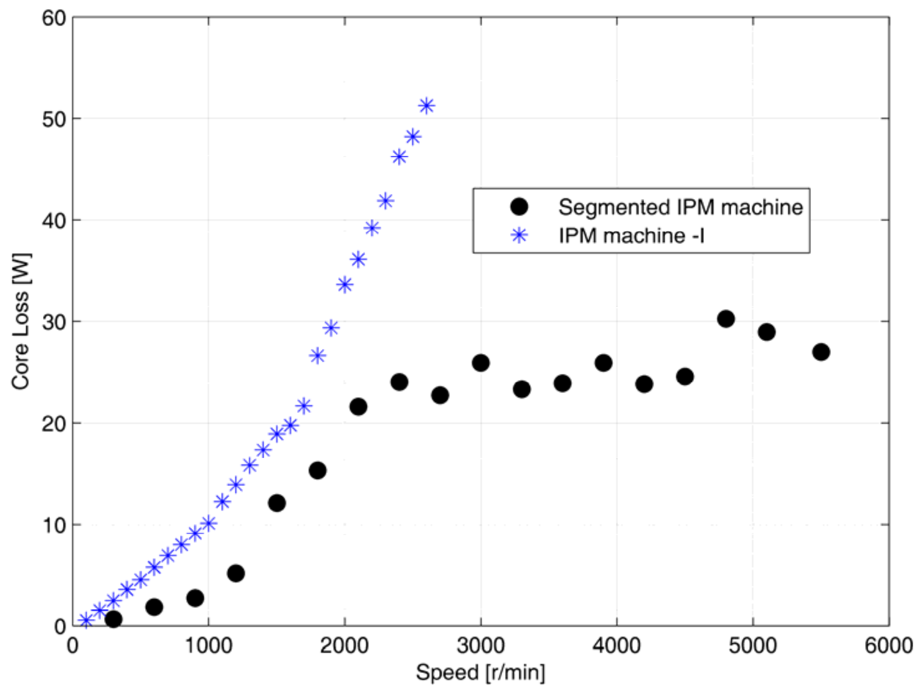

Fig.4. 24 Measured Iron loss of the Segmented IPM machine and IPM machine-I

4.7. Conclusion

In this chapter the design process of the segmented IPM machine was discussed. The machine was optimized for the targeted performance with predetermined design constraints. For performance prediction, machine parameters are estimated first from the finite element model and then verified with experimental measurements. The cogging torque and iron losses were also estimated and compared to the IPM machine-I which has a non-segmented, conventional rotor structure. These verifications have confirmed the predicted performances of the proposed segmented IPM to some extent.

The steady-state performance under maximum torque per ampere control and flux-weakening are discussed in the chapter 5 and 6. The developed torque and power of the Segmented IPM machine at various speeds were also estimated by the FEM before the actual construction. These will be presented in Chapter 6 along with the measured results for experimental verification.

CHAPTER 5

5. Vector Control of the IPM Machine

5.1. Introduction

This chapter discusses the vector current control techniques of the Interior Permanent Magnet (IPM) Machine which were applied to the prototype Segmented IPM machine for measuring its steady state and transient performances.

The term 'vector control' is applied to those control techniques which have ability to control both the amplitude and phase of the AC excitation in the machine. The vector control of currents and voltages results in control of spatial orientation of rotor and stator magnetic fields. Hence, it is sometime also referred as field orientation control [66].

The requirements necessary to control the torque production in an IPM machine are:-

an independently controlled stator current to overcome the effects of stator winding resistances, leakage inductances and induced voltage.

an independently controllable spatial angle γ as defined in the basic phasor diagram of the IPM machine given in the Fig. 2.7 of chapter 2.

The electromagnetic torque production and its control in the IPM machine are reviewed in the following section.

5.2. Torque and Field Control in Reference Frames

The first step to design a vector controlled drive for the IPM machine is to develop its dynamic model in terms of space vectors. The stator winding of the IPM machine is similar to the three-phase windings of the Synchronous or Induction machine. Such windings, when supplied with three phase balance currents, produce a sinusoidal stator MMF which rotates with synchronous speed.

There are mainly two reference frames which are used in the control of the IPM machine. One of them is the stator or stationary reference frame and the second one is the rotor reference frame. The stator reference frame is fixed to the stator and stationary in space. The D-axis of this reference frame aligns with magnetic axis of the phase '*a*' of the stator winding. The rotor reference frame is fixed to the rotor and hence rotates with it. The d-axis of the rotor reference frame aligns with the rotor flux axis. The IPM machine like the synchronous machine is normally analysed using rotor reference frame. The rotor and stator reference frames of an IPM machine with simplified stator winding are shown in Fig.5.1. Any three phase quantities can be transformed to stator and rotor reference frames and vice versa by using the well-known Park's transformation.

The current and voltage equations of the IPM machine are expressed in terms of d- and q-axis components as given in equations (2.7-2.10). The space vectors of the voltage and current in relation with the reference frames are shown in the Fig.5.2. At constant speed, the dq-axes quantities become DC quantities and can be controlled easily with Proportional and Integral (PI) current controllers. It can be seen from the voltage equations (2.7) and (2.8) that there exist cross- coupling terms in the d- and q-axes voltages. Hence, in order to control i_d and i_q independently, they need to be decoupled. Normally, i_d and i_q are decoupled in the IPM machine by using a feed-forward compensation network.

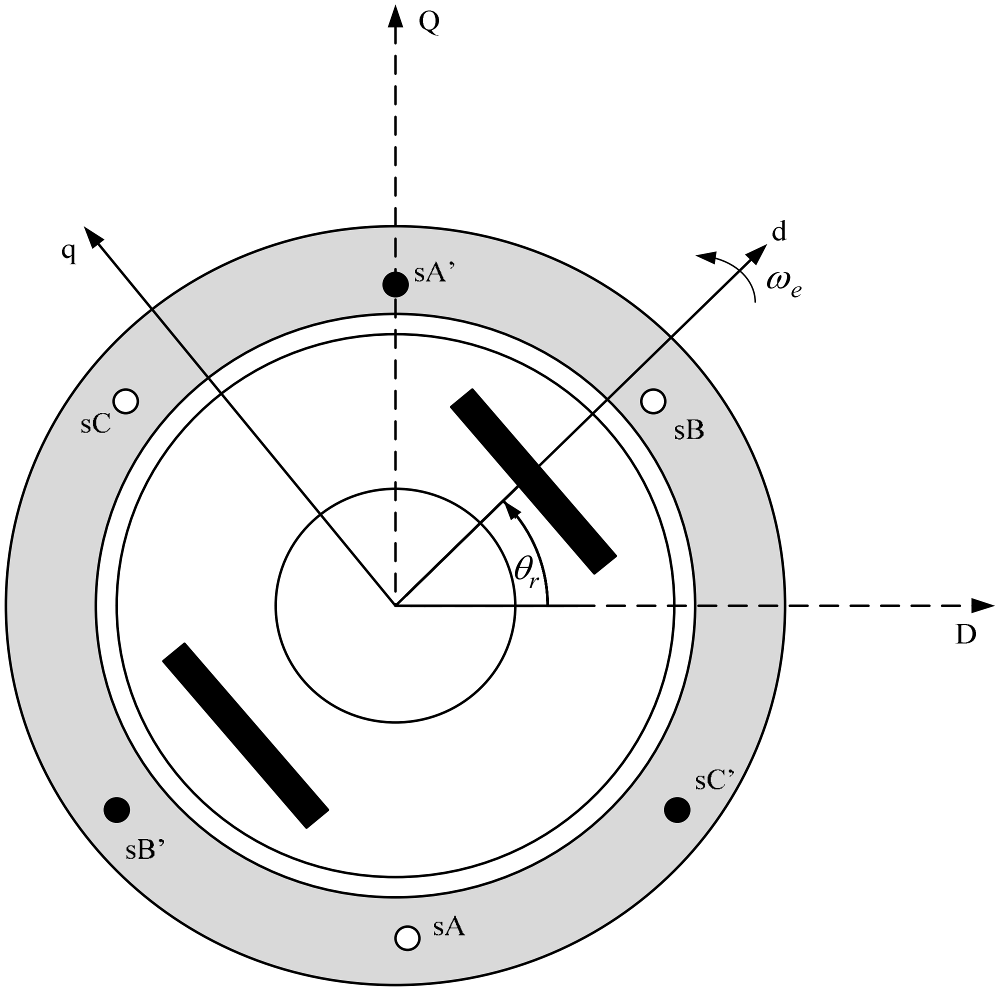

Fig. 5.1 The reference frames of an IPM machine

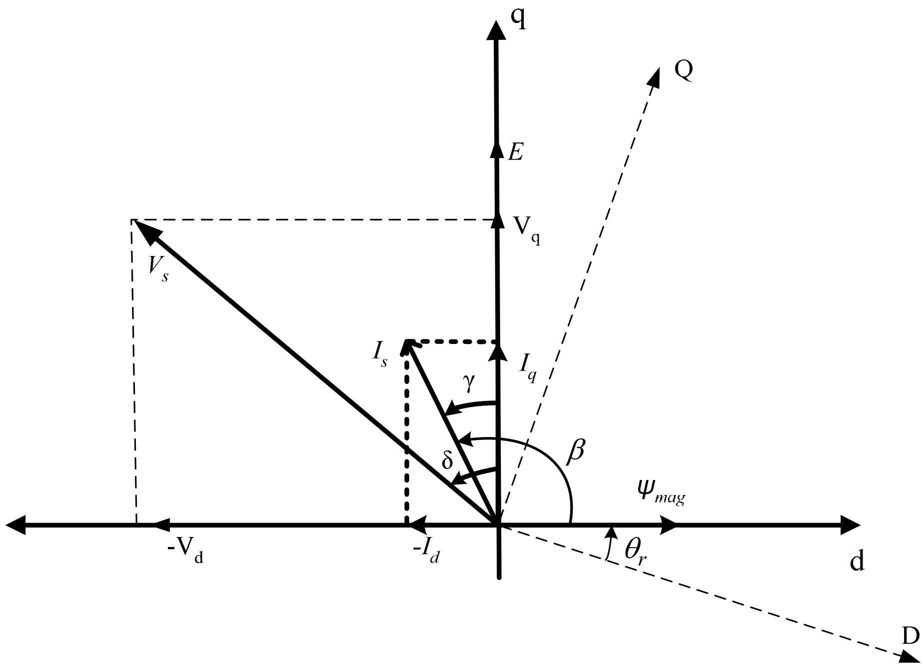

Fig. 5.2 Steady-state Space Vector diagram of IPM machine

Many high-performance drives require instantaneous control of the torque. It is obvious from the torque equation of the IPM machine given in (2.11) that in the absence of any damper windings, an immediate torque response is possible with step change of I_d and I_q currents.

5.3. Stator Current Vector Control

The instantaneous torque equation of (2.11) defines a hyperbola in i_d-i_q plane for every value of torque. As a result, there exist infinite combinations of i_d and i_q which will deliver the same torque [26]. The relationship between calculated torques with d- and q-axis currents in a 3-D plane for the Segmented IPM machine and IPM machine-I are shown in Fig. 5.3 (a) and (b) respectively. The parameters and ratings of these machines are given in appendix A. The table A-1 and A-2 of appendix A show that the back EMF of the conventional IPM machine-I is about 2.5 times that of the segmented IPM machine. This is reflected on the Fig.5.3(a) and (b) where at zero d-axis current, the magnet torque of IPM machine is about 2.5 times of the segmented IPM machine. On the other hand, it can also be seen from the table A-1 and A-2 that the (L_d-L_q) for the segmented IPM machine is about twice that for the IPM machine-I. Consequently, even despite lower magnet torque, the greater reluctance torque of the segmented IPM machine allows it to achieve comparable total output torque.

Since the high efficiency is one of the important requirements of many high performance drives, the maximum torque per stator current is considered as the control criteria. The control criteria are also influenced by the voltage and current limit of the drive which can be explained with the help of the circle diagram of the machine.

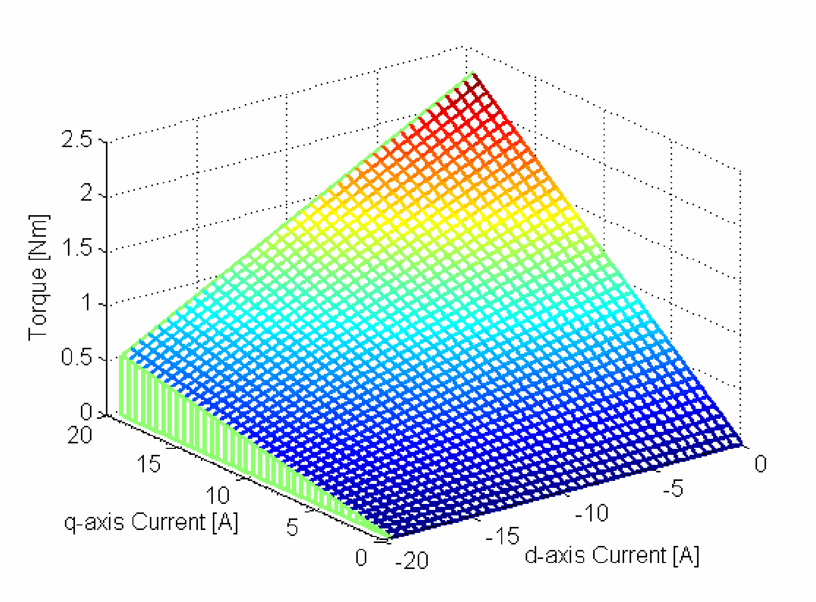

(a)

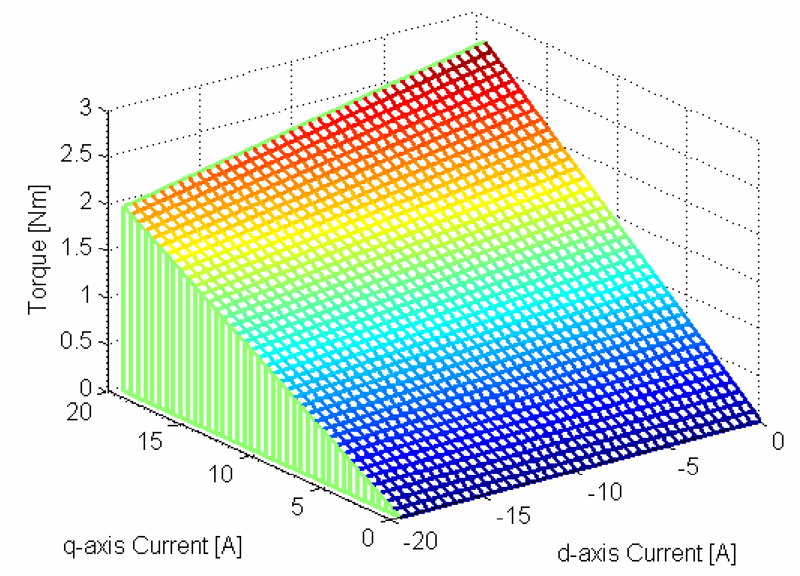

(b)

Fig. 5.3 Torque of the (a) the proto-type Segmented IPM machine and (b) IPM Machine-I in 3-D plane

5.3.1. Circle diagram

In Chapter 2, the current limit circle and voltage limit ellipses of the IPM machine were mentioned briefly. This section discusses the development of the current trajectory control according to these limits. Considering inverter capacity and machine rating, there exist a voltage limit and a current limit for the drive system. For the satisfactory operation of the machine drive, these limits must not be exceeded in any operating condition. The current limit is decided by the continuous armature current rating and/or the rating of the inverter switches. The current limit equation given in the (2.20) when plotted in the d- and q-axis current plane gives a circle as shown in the Fig. 5.4 for the segmented IPM machine. The voltage limit of the system is imposed by the maximum available voltage from the DC bus of the inverter. The maximum voltage output of an inverter is $\frac{2V_{dc}}{\pi}$ for unity modulation index. The equation of voltage limit given in (2.22) can also be expressed as,

$$(\psi_{PM} + L_d i_d)^2 + (L_q i_q)^2 = \left(V_{sm} / \omega_e \right)^2 \tag{5.1}$$

For various speeds this equation produces a set of concentric ellipses in the i_d-i_q plane as plotted in the Fig. 5.4 for the segmented IPM machine. The center of these ellipses lies at the point $(0, -\frac{\psi_{PM}}{L_d})$. The length of the long and short half axes of the ellipses are $\frac{V_{sm}}{\omega_e L_d}$ and $\frac{V_{sm}}{\omega_e L_q}$ respectively. It is should be noted here that while plotting the circle diagram of the voltage and current limits, normally core loss, resistive drop and effect of the magnetic saturation over the machine parameters are neglected. Also if the q-axis saturation effect are considered the voltage limit ellipses are distorted in vertical direction and inclusion of resistive drop in the current and voltage limit equations shows noticeable counter clock-wise tilt in the horizontal direction of the ellipses [67] . In the evaluation of the prototype segmented IPM machine, these changes of the control trajectories are not included. Hence, further discussion of them is omitted.

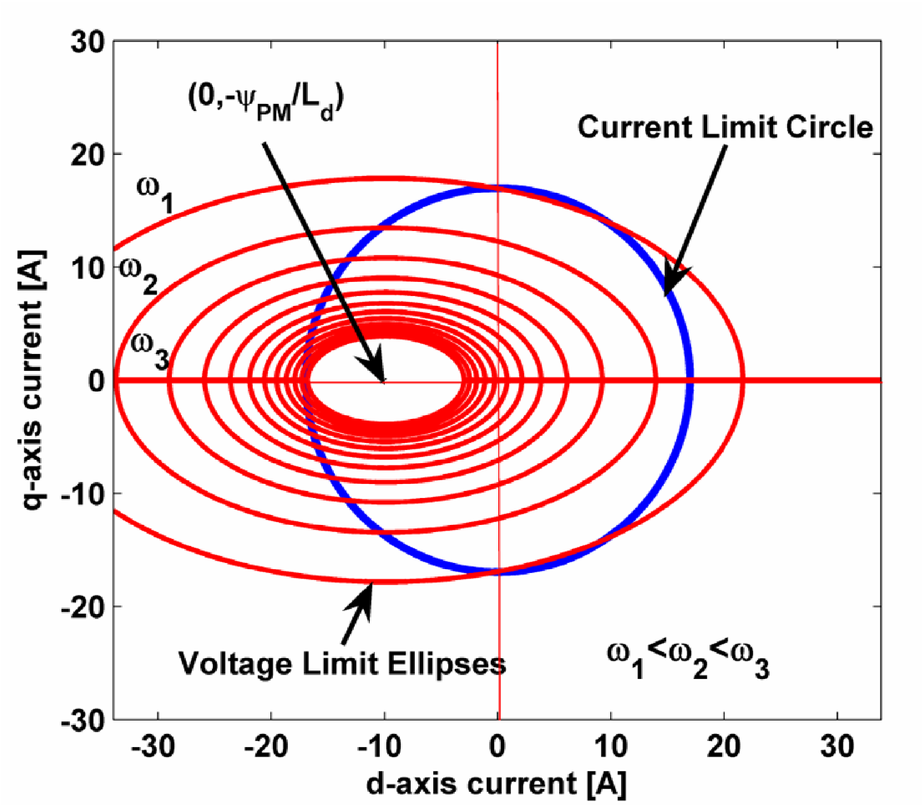

Fig. 5.4 The current and voltage limit of the prototype Segmented IPM machine

5.3.2. Current trajectories

The torque equation in terms of the current angle γ is given as,

$$T = \frac{3}{2} p[\psi_{PM} I_s \cos\gamma + \frac{1}{2}(L_q - L_d) I_s^2 \sin 2\gamma] \tag{5.2}$$

The torque vs. current angle γ of the prototype Segmented IPM machine is shown in the Fig. 5.5. It can be shown from the (5.2) that maximum torque per ampere occurs at an optimum current angle which leads to the combination of optimum i_d and i_q values. By plotting these values in the i_d-i_q plane, the maximum torque per ampere (MTPA) trajectory of the Fig. 5.6 can be obtained where upper half of the current and voltage limits diagram (motoring operation) is shown. Using a normalization technique described in the [26], the torque can be expressed as a function of normalized i_d and i_q current. In the i_d-i_q plane, each value of the constant torque produces a hyperbola as shown in the Fig.5.6. The maximum output trajectory under voltage limited condition is also shown in the same figure.

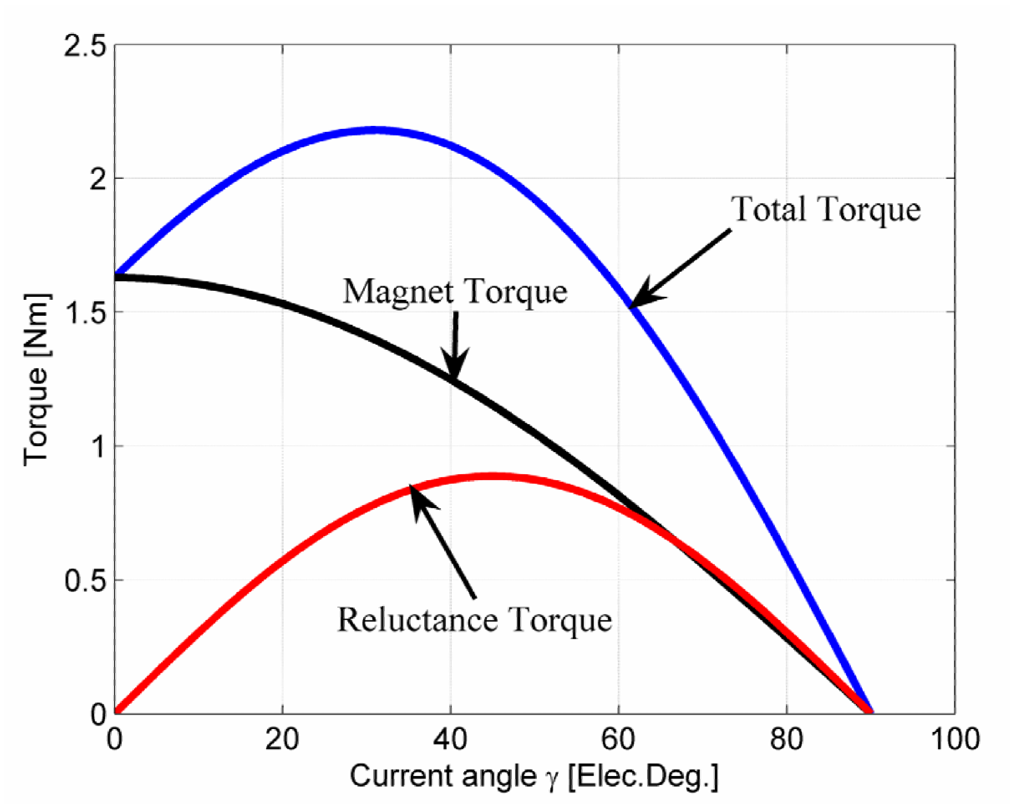

Fig. 5.5 Torque Vs Current Angle γ

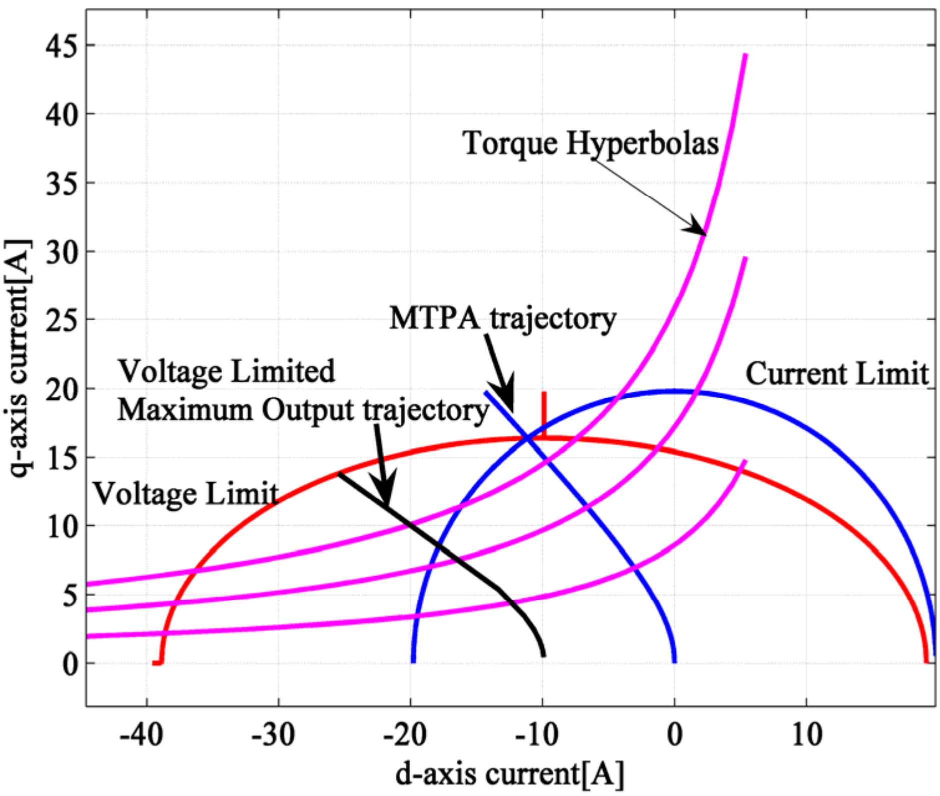

Fig. 5.6 Current Trajectories

5.4. Control Principles

In order to satisfy current and voltage limits, the stator current vector must lie inside the current limit circle and voltage limit ellipse in all operating conditions [68]. Therefore, the control trajectories under the vector control are dictated by these limits. From the Fig. 5.4, it is obvious that for any speed lower than ω_1, the current limit circle lies inside the voltage limit ellipses. In such cases, the maximum torque per ampere control algorithm can be applied to the IPM machine without considering any voltage limit. However, for speeds greater than ω_1, the terminal voltage will reach the limit value. Consequently, control algorithm need to be changed to a flux-weakening control so that current vector can satisfy both current and voltage limits.

There are a number of vector control schemes available for IPM machine. The control can be either stator flux or rotor flux-oriented. A stator flux oriented control scheme for maximum torque per ampere was given in the [69]. However, the rotor flux-oriented control schemes of [25, 32] are more widely used in the IPM machine for their fast dynamics.

The block diagram of the current control of the IPM machine with rotor flux-orientation is shown in the Fig. 5.7. Usually, in motor drive applications, the reference i_q^* is derived from a speed controller, position controller or torque controller and the reference i_d^* current is calculated from MTPA and/or flux-weakening control algorithms depending on operating conditions. In this work, the vector control scheme of [25] was implemented for the testing of the proto-type Segmented IPM machine which will be discussed in detail in the following sections.

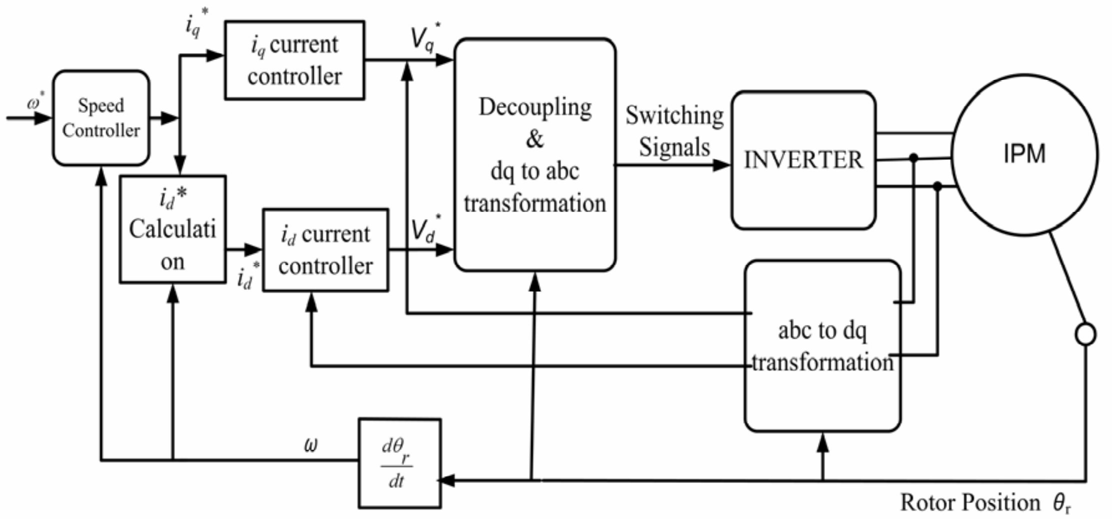

Fig. 5.7 Block diagram of Current vector control during motoring

5.4.1. Maximum Torque per Current Control

From the torque equation of (2.11), a relationship between i_q^* and i_d^* can be derived for maximum torque per ampere (MTPA) condition which is given as,

$$i_d^* = \frac{\psi_{PM} - \sqrt{\psi_{PM}^2 + 4(L_q - L_d)^2 (i_q^*)^2}}{2(L_q - L_d)} \tag{5.3}$$

From this relationship, the MTPA trajectory of the current in the Fig. 5.8 is obtained. The machine operates with the limit current I_{sm} at the full load condition and the maximum torque per ampere occurs at point 'A' of the Fig.5.8. It is the intersecting point of the MTPA trajectory and the current limit circle. The d- and q-currents of the operating point 'A' can be derived from (5.3) and current limit condition given in (2.20) as,

$$i_{da} = \frac{\psi_{PM}}{4(L_d - L_q)} - \sqrt{\frac{\psi_{PM}^2}{16(L_q - L_d)^2} + \frac{I_{sm}^2}{2}} \tag{5.4}$$

$$i_{qa} = \sqrt{I_{sm}^2 - i_{da}^2} \tag{5.5}$$

Under the MTPA control, the IPM machine is able to accelerate with maximum constant torque till the speed reaches a value at which the terminal voltage V_s reaches the limit value V_{sm}. Thus, the maximum speed under constant torque is given by,

$$\omega_b = \frac{V_{sm}}{\sqrt{(\psi_{PM} + L_d i_d)^2 + (L_q i_q)^2}} \tag{5.6}$$

This speed can also be called as the base speed of the IPM machine since, above this speed the machine needs to be operated with flux-weakening control.

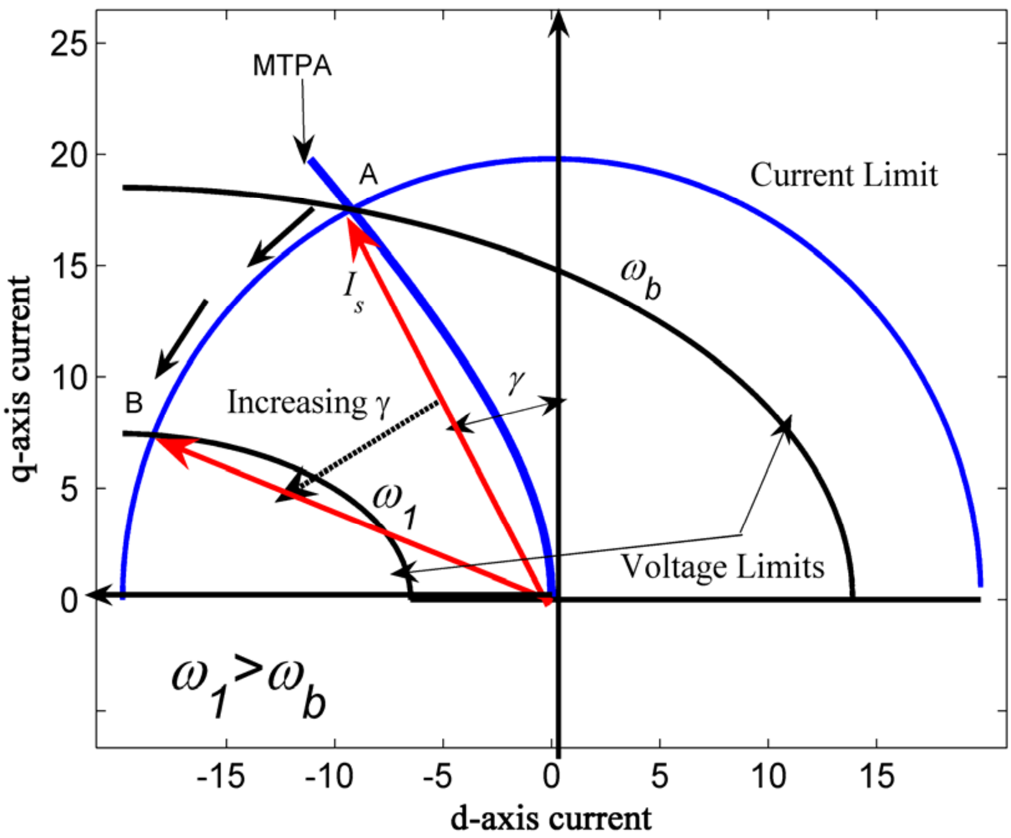

Fig. 5.8 Vector control during flux-weakening

5.4.2. Flux-weakening Control

As the voltage of the machine reaches the limiting value, current vector need to be controlled in such a way that it lies inside the limiting ellipse. For simplification, the resistive drop of the system can be taken into account in the limiting value itself by the modifying the limiting value as (5.7) [25].

$$V_{om} = V_{sm} - I_{sm} R \tag{5.7}$$

The function of the flux-weakening algorithm is to control the d- and q-axis current in such a way that the voltage of the machine can be maintained at V_{om}. The relationship between i_d and i_q for the flux-weakening control algorithm can be derived from (5.1) by replacing V_{sm} with V_{om} as,

$$i_d = -\frac{\psi_{PM}}{L_d} + \frac{1}{L_d}\sqrt{K}\text{ , where } K = \frac{V_{om}^2}{\omega^2} - (L_q i_q)^2 \tag{5.8}$$

The above equation results in a real number only if $\left|i_q\right| \le \frac{V_{om}}{\omega L_q}$.

Thus, from (5.8) and (2.20) the maximum torque per ampere under voltage limit condition can be obtained which is the intersecting point of the current limit circle and voltage limit ellipse of the operating speed. The limiting values of d- and q-axis currents are determined from the (5.9) and (5.12).

$$i_{dv} = -\frac{\psi_{PM} L_d}{a} + \frac{1}{a}\sqrt{\psi_{PM}^2 L_d^2 - ab} \tag{5.9}$$

where,

$$a = L_d^2 - L_q^2 \tag{5.10}$$

$$b = I_{sm}^2 L_q^2 + \psi_{PM}^2 - \frac{V_{am}^2}{\omega^2} \tag{5.11}$$

$$i_{qv} = \sqrt{I_{sm}^2 - i_{dv}^2} \tag{5.12}$$

Under flux-weakening control, for any speed $\omega_1 \ge \omega_b$, the operating point 'A' moves to 'B'. In other words, the current angle γ has increased to provide a larger negative d-axis current to weaken the magnet flux.

The maximum flux-weakening speed is infinite when $\left|I_{sm}\right| = \left|\frac{\psi_{PM}}{L_d}\right|$, which is also the condition of optimum flux-weakening. However, in most of the practical IPM machine I_{sm} is either larger or smaller than $\frac{\psi_{PM}}{L_d}$ depending on other parameters and operating conditions. The center of the voltage limit ellipses lies outside of the current limit circle when $\left|I_{sm}\right| < \left|\frac{\psi_{PM}}{L_d}\right|$ and inside the current limit circle when the reverse is true. The Fig.5.9 (a) and (b) show voltage and current limits of the two different IPM machines with above conditions. The IPM machine whose center of the voltage limit ellipses lies outside will be called here as 'Type-I IPM machine' and the IPM machine for which the opposite is true will be called 'Type-II IPM Machine'.

Type-I IPM machine: $\left|I_{sm}\right| < \left|\frac{\psi_{PM}}{L_d}\right|$

Type-II IPM machine: $\left|I_{sm}\right| > \left|\frac{\psi_{PM}}{L_d}\right|$

In Type-I IPM machines the flux-weakening speed is limited by the fact that after certain speed voltage limit ellipses lie outside of the current limit. Since, above this speed, voltage and current limit both can not be satisfied together, further flux-weakening is impossible. Thus, it has a limited flux-weakening speed range and a very wide Constant Power Speed Range (CPSR) is not possible.

Conversely, in the Type-II IPM machines, the voltage limit ellipse shrinks inside the current limit circle and becomes the centre itself at the maximum speed. In this type of IPM machine, the constant power operation is limited to a finite speed range but theoretical maximum speed limit is infinite [70]. The flux-weakening range can be extended by using a voltage limited maximum output trajectory shown in the Fig. 5.9 (b).

The relationships between i_d and i_q for the voltage limited maximum output trajectory are given as,

$$i_d = -\frac{\psi_{PM}}{L_d} - \Delta i_d \tag{5.13}$$

$$i_q = \frac{\sqrt{(\frac{V_{sm}}{\omega})^2 - (L_d \Delta i_d)^2}}{\xi L_d} \tag{5.14}$$

where,

$$\Delta i_d = \frac{-\xi \psi_{PM} + \sqrt{(\xi \psi_{PM})^2 + 8(\xi - 1)^2 (\frac{V_{sm}}{\omega})^2}}{4(\xi - 1) L_d} \tag{5.15}$$

The minimum speed for the voltage-limited, maximum output operation can be defined as critical speed ω_c. For speed lower than ω_c, the voltage-limited, maximum output trajectory intersects voltage-limit ellipses outside the current limit circle; hence, it can not be applied below this speed [68]. With voltage-limited, maximum output trajectory, the current vector will follow the path of 'BC' which asymptotically approaches to the centre point $(-\frac{\psi_{PM}}{L_d}, 0)$.

In some IPM machines where V_{sm} is relatively small, the $\left(\frac{V_{sm}}{\omega}\right)^2$ can become lower than $\left(L_d \Delta i_d\right)^2$ in equation (5.14) after certain speed. In this type of the machine, the d-axis current i_d is calculated as $-\frac{\psi_{PM}}{L_d}$. The current trajectory for such case is the straight line 'AC' as shown in the Fig. 5.9(b). The current trajectory during flux-weakening for such machine is BXC rather then BC .

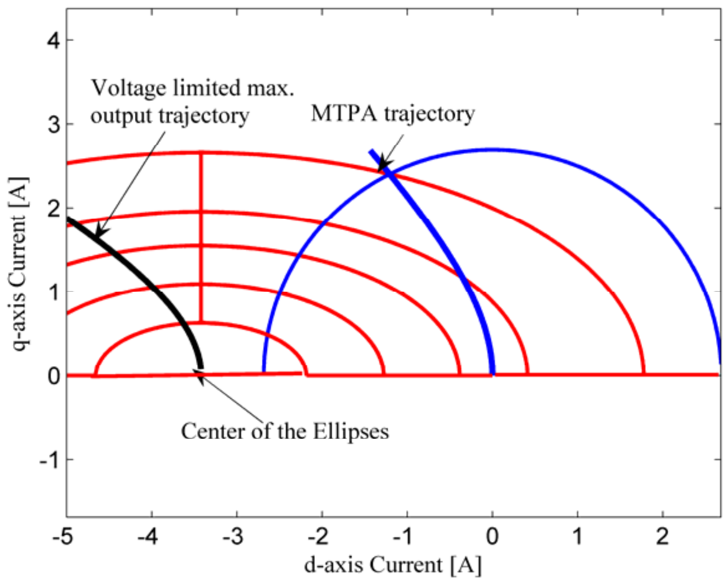

(a)

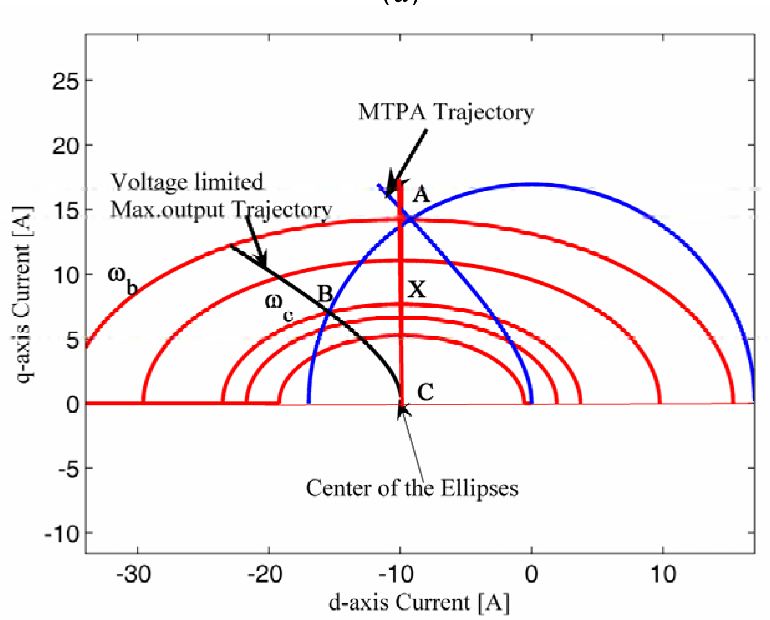

(b)

Fig. 5.9 The current and voltage limits diagram of the (a)Type –I and (b) Type-II IPM machine

5.4.3. Transition of the Control Modes

The IPM machine operates with maximum torque per ampere (MTPA) algorithm until the voltage reaches its limits. In the IPM machine, there exists a cross-over speed at which the back EMF reaches the limiting value. Above this speed, the flux-weakening control must be selected other-wise MTPA trajectory will lie outside of voltage limit ellipse. The base speed ω_b of the (5.6) depends on current. As a result, in the speed range between ω_b and cross-over speed ω_{cross}, the control mode is determined mainly by the load condition. However, at no-load condition, when armature current is nearly zero, the flux-weakening starts near the cross-over speed. The transition between the MTPA and flux-weakening control is determined by the flow chart given in the Fig. 5.10.

In case of type-II IPM machines, after critical speed ω_c, the voltage limited maximum output trajectory should be followed. This critical speed ω_c can be derived from equating (5.9) to (5.13) and then solving for speed ω .

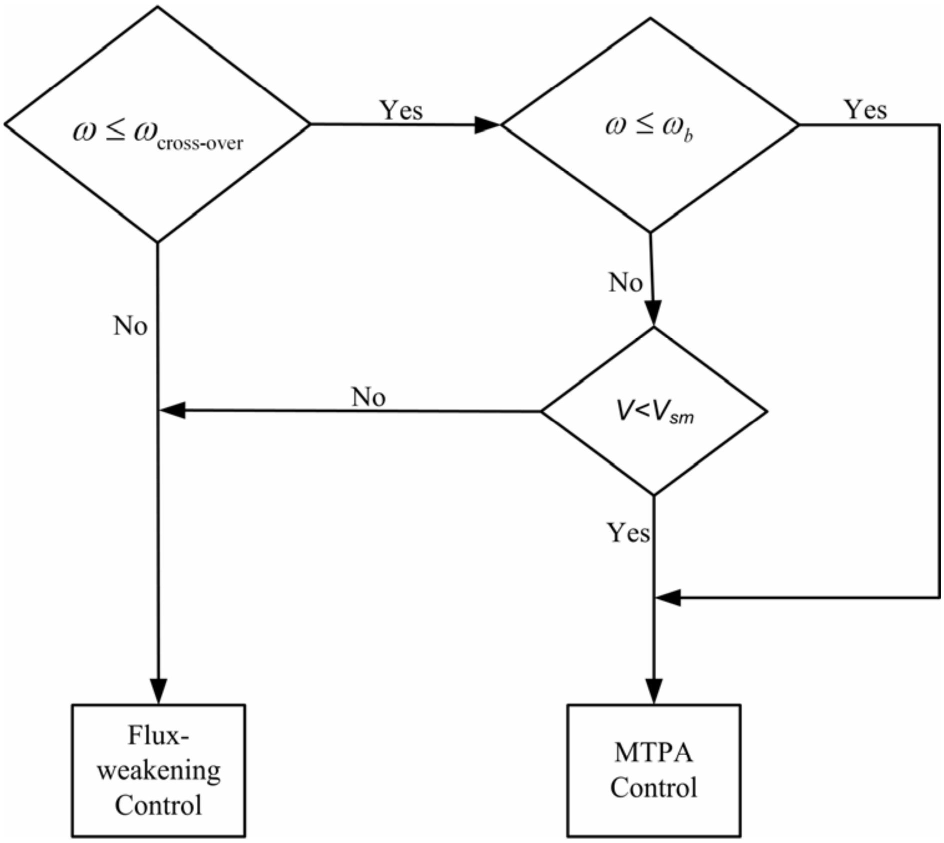

Fig. 5.10 Flow chart of control mode transition

5.4.4. Control as generator

Above mentioned control algorithm can also be applied for generating operation. In this case, the controlled torque is negative and current vector operates in the third quadrant of the i_d-i_q plane. In application such as Integrated Starter Alternator (ISA) of automobile, the DC bus voltage of the converter is regulated and the reference i_q^* current comes from the DC bus regulator. The block diagram of a DC bus control scheme is shown in the Fig. 5.11.

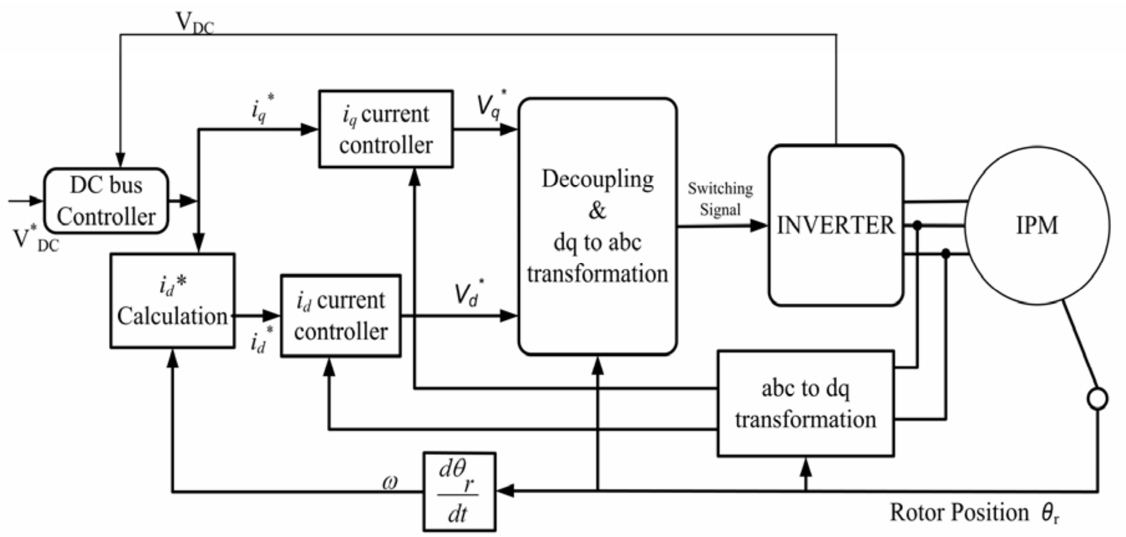

Fig. 5.11 Block diagram of the current vector control during generation

5.5. Vector Control of the Segmented IPM Machine

The vector current control scheme described above was applied to the prototype Segmented IPM machine. The reference i_q^* current was determined by the outer speed control loop during motoring and from the DC bus regulator during generation. The reference i_d^* is calculated using (5.3), (5.8) or (5.13) depending on speed and load conditions. The segmented IPM machine drive was first modeled in Matlab-Simulink.

The modeling results were later confirmed by real-time implementation with DS1104 board.

5.5.1. Modeling in Matlab-Simulink

The control strategies shown in the Fig. 5.7 and Fig. 5.11 during motoring and generation respectively are modeled using Matlab-Simulink for the Segmented IPM machine. It has been seen that the segmented IPM machine is capable of operating with good dynamics at both constant torque and flux-weakening region. The current trajectories of the Segmented IPM machine in d- and q-axis current plane are shown in Fig. 5.12.

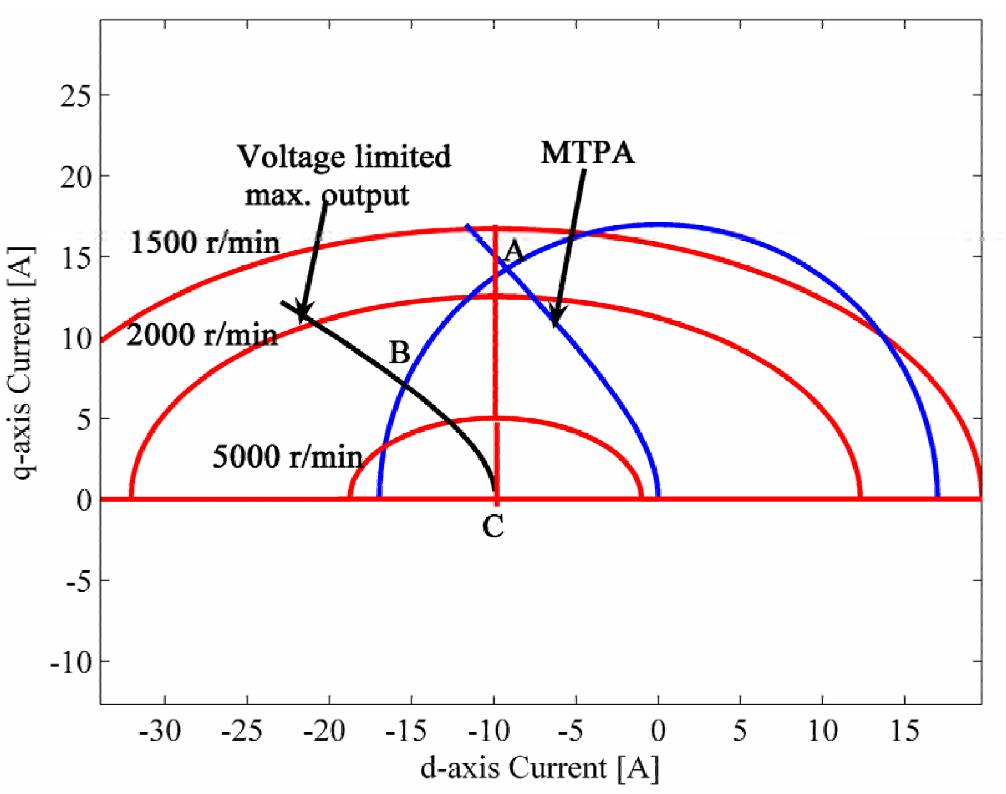

Fig. 5.12 Current Trajectories of the prototype Segmented IPM Machine

Maximum Torque per Ampere (MTPA) Control: The Segmented IPM motor runs with the MTPA control until the terminal voltage approaches to the limit value. The dynamic response of i_d, i_q and speed with respect to a step change in speed from 0 to 1500 r/min is shown in Fig. 5.13. At 1500 r/min, voltage is still under the limit value. Hence, the machine is operating with maximum torque per ampere control. The trajectory shown in Fig. 5.14 indicates that current vector was at the intersection of MTPA trajectory and current limit circle during acceleration and moves along the MTPA trajectory when speed approaches to the reference value. It settles near the origin when a no load condition is considered; otherwise will settle at a point that is appropriate for the load torque.

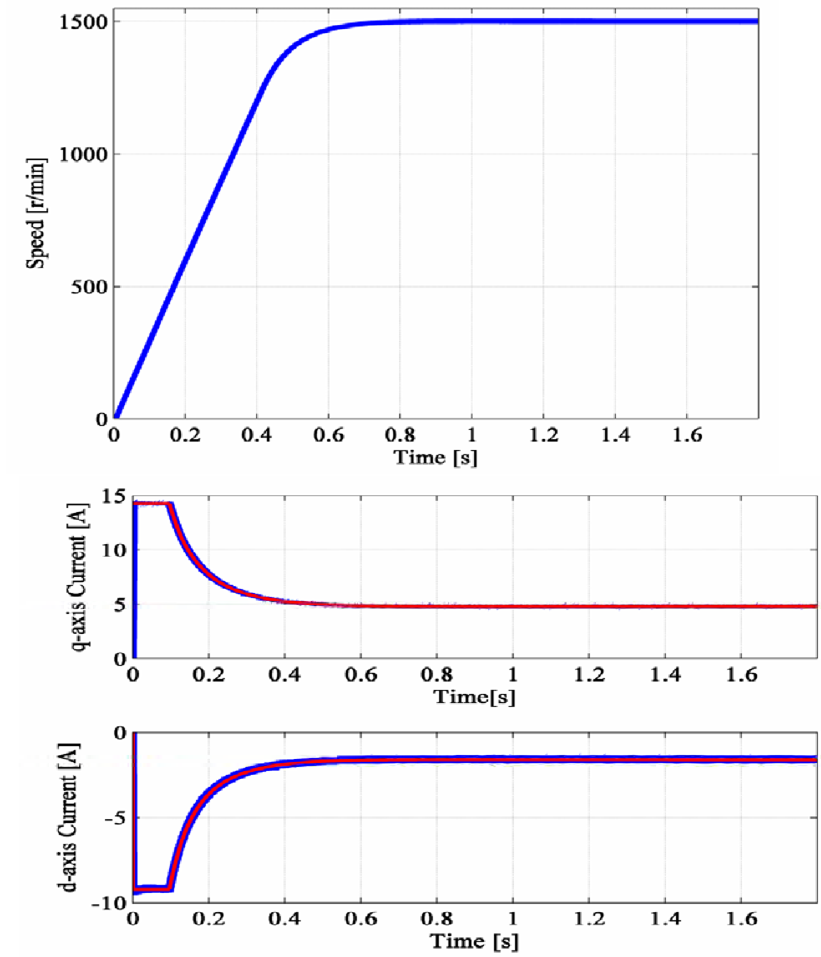

Fig. 5.13 Speed and dq-axis current response for speed step of 0 to 1500r/min

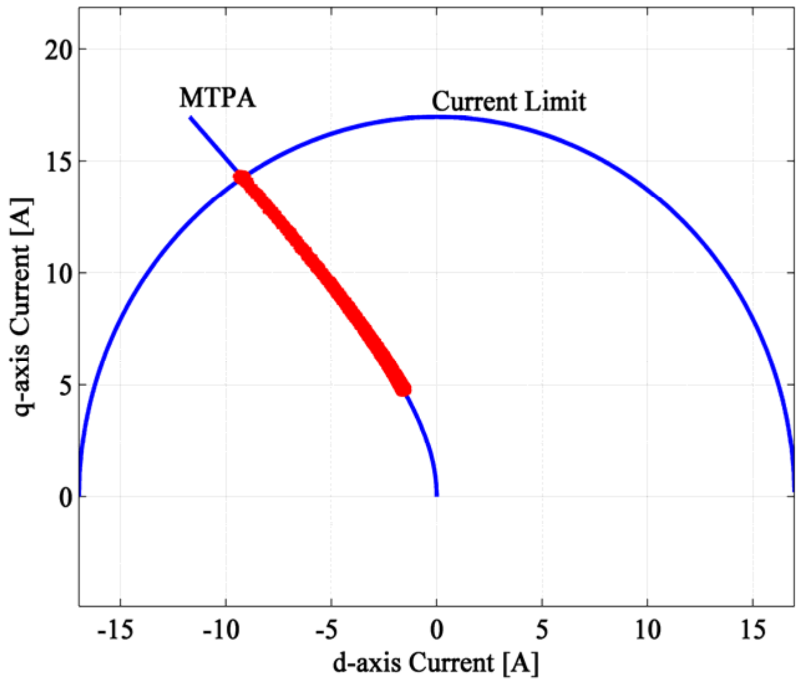

Fig. 5.14 Current trajectory with MTPA control from Matlab-Simulink model

Flux-weakening Control: The flux-weakening control starts as soon as the terminal voltage reaches the limiting value. The transition from MTPA control to flux-weakening occurs according to the flow chart of Fig. 5.10. It can be seen from the current trajectories of the Segmented IPM machine given in the Fig. 5.6 that the centre "C" of the voltage limit ellipses lie inside the current limit circle. Therefore, it falls under the category of type-II IPM machine. Since, the machine is run in the 42V PowerNet condition; the voltage limit V_{sm} is relatively small. It is seen that K of (5.8) becomes negative very quickly which will result in a imaginary number. In such cases, i_d^* current is kept as $-\frac{\psi_{PM}}{L_d}$ which reduces the current limit prematurely. It can be avoided by calculating $i_d^* = \sqrt{I_{am}^2 - i_q^{*2}}$ where, limiting value of i_q^* to $\frac{V_{om}}{\omega L_q}$.

Above critical speed, the machine runs with voltage limited maximum output trajectory. The speed and dq-axis current responses obtained from the Matlab Simulink model for a step speed-change of 0 to 4500 r/min is shown in Fig. 5.15 and the current trajectories obtained from this operating condition are shown in Fig. 5.16.

The critical speed ω_c of the segmented IPM machine is approximately 3600r/min; above this speed, the machine operates with the voltage limited maximum output trajectory. Therefore, in the Fig. 5.16 the operating point moves from 'A' to 'B' and then follow the path of 'BC' which is the voltage limited maximum output trajectory.

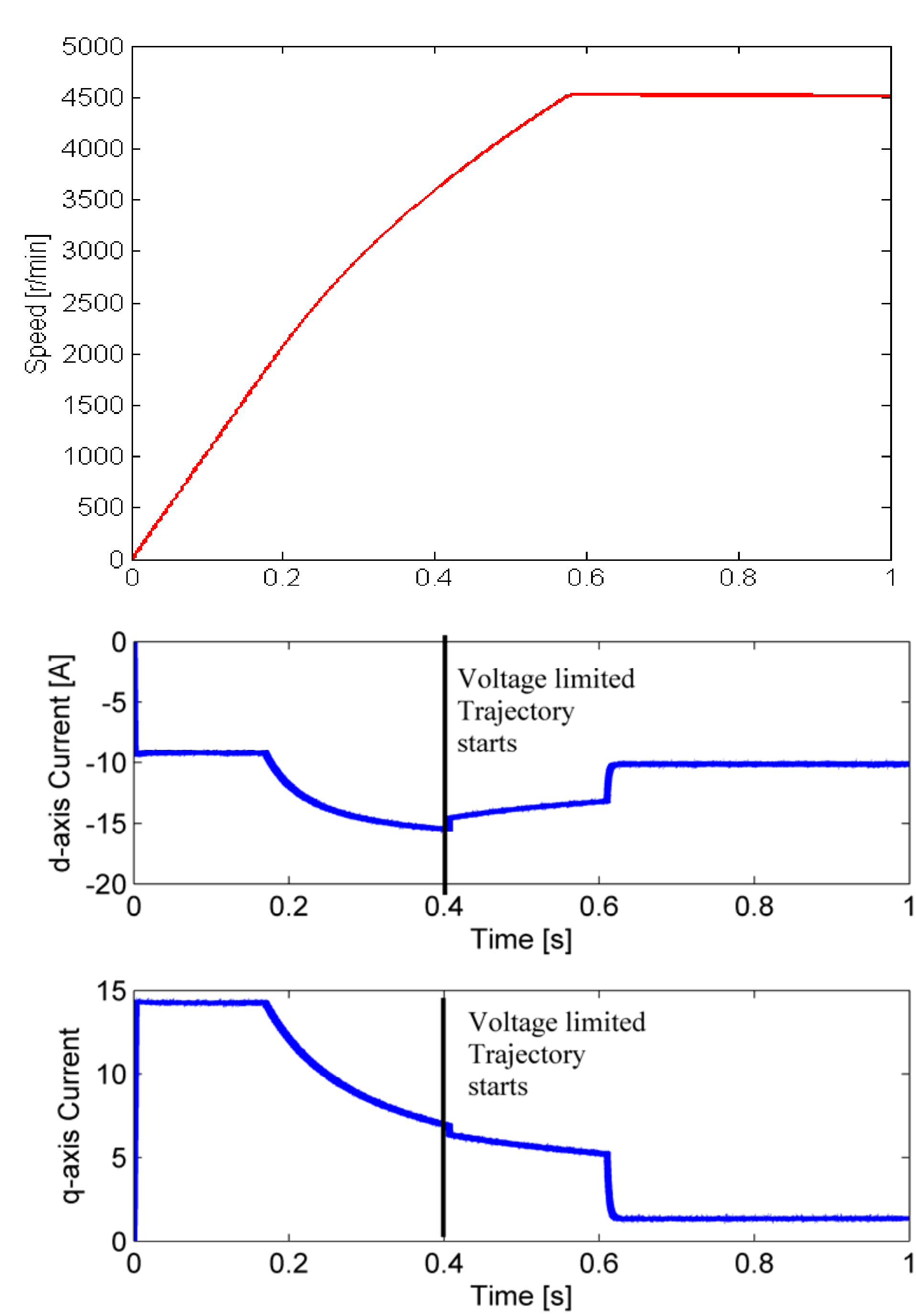

Fig. 5.15 Speed and dq-axis current responses for a step speed change from 0 to 4500r/min (from modeling)

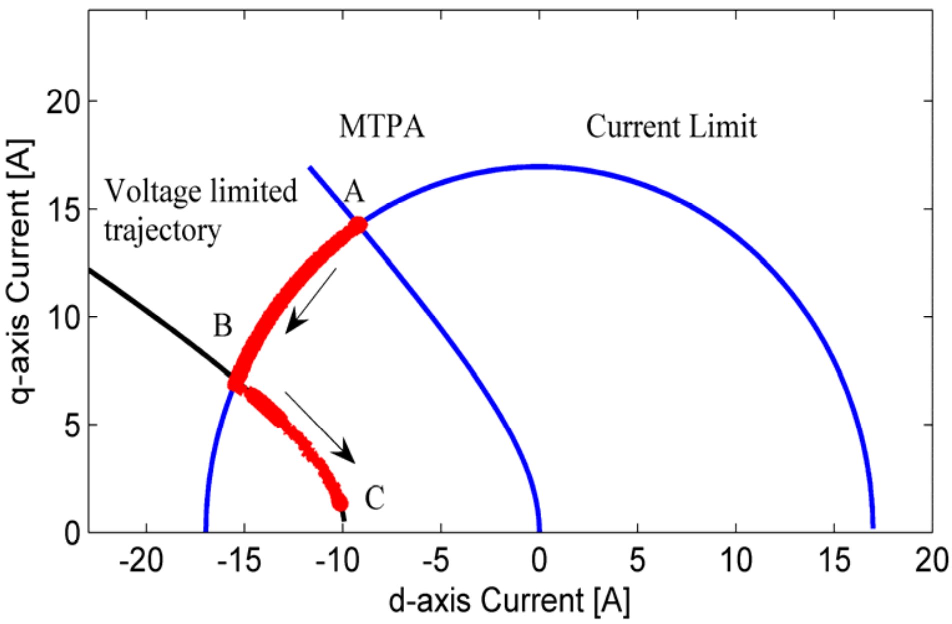

Fig. 5.16 Current Trajectories during flux-weakening from the Matlab-Simulink Model

DC bus regulation during generation: During generation, the DC bus of the system is regulated to 42V. The reference q-axis current i_q^* is derived from the PI controller of the DC bus voltage regulator. Thus, in the case of generation, the outer speed loop of motoring was replaced by the DC bus regulator loop. The block diagram of the control scheme is shown in Fig. 5.11.

The system was modeled in Matlab-Simulink to investigate the dynamics of the DC bus regulator. The Fig. 5.17 shows variation of the DC bus voltage and d- and q-axis current controller response for a step load change. The DC bus voltage drops when the load is switch on and by the action of the regulator it recovers back within a few hundred milliseconds. The d- and q-axis currents are increased and settle at the new operating point according to the load value.

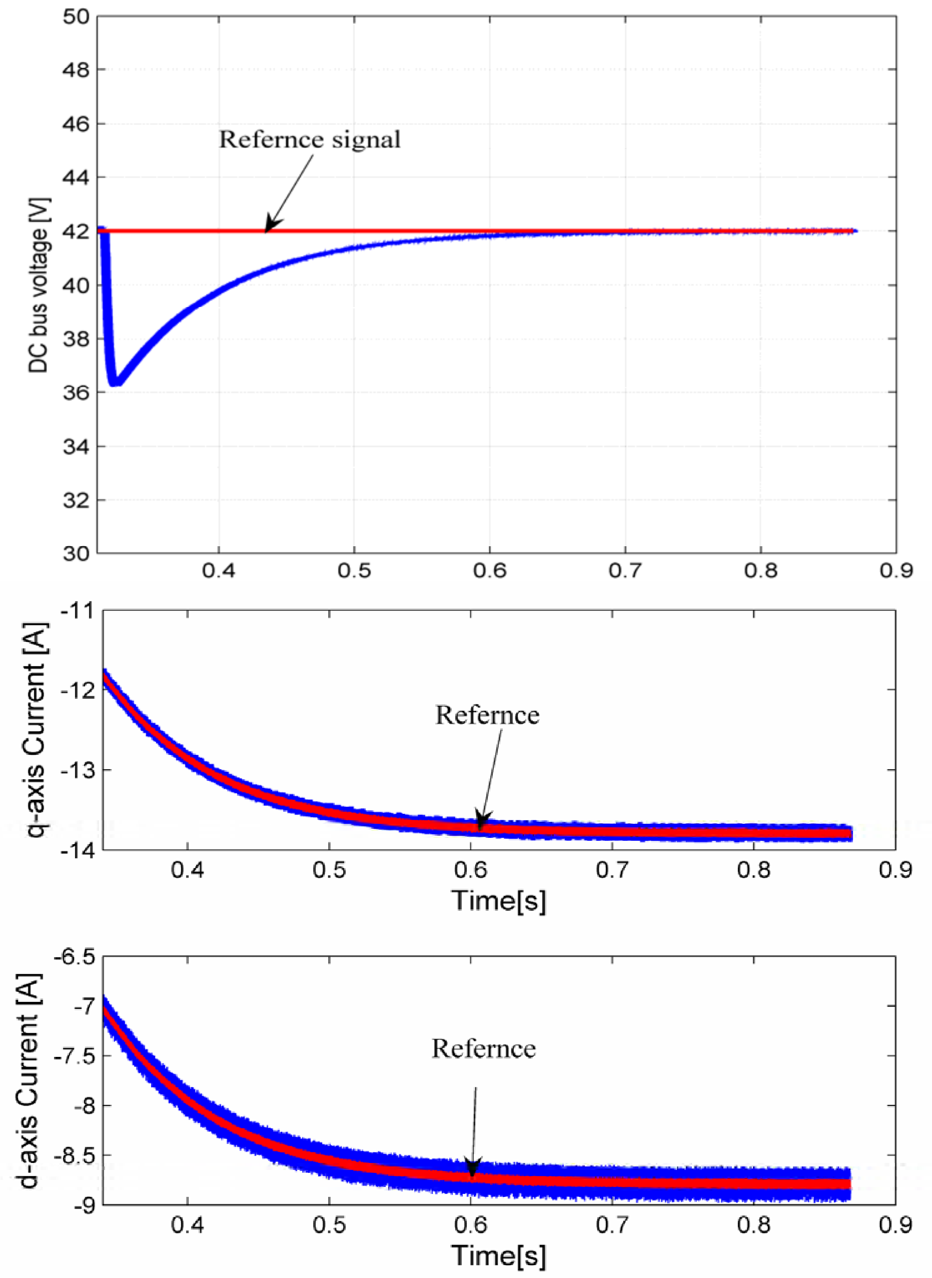

Fig. 5.17 Response of DC bus regulator, d- and q-axis current controller for a step change of load at 2200 r/min and the load step is 200W to 400W.

5.5.2. Experimental Setup

The modeling results discussed above were confirmed by experimental results in this section. The vector control schemes discussed in the previous sections were implemented in real-time using dSPACE 1104 board. The sampling time of the inner current loops was kept at 100μs and that of the outer speed control loop was set as 500μs. The rotor position and speed are obtained from an incremental encoder with 5000 pulses per revolution. The two phase currents and DC bus voltage signals were measured using current and voltage transducers. These signals were fed through ADCs (Analogue to Digital Converters) of the DS1104 to the controllers. The PWM signals generated by the slave DSP of the dSPACE1104 board were used for switching the IGBTs of a Voltage-Source Inverter (VSI). The Fig. 5.18 shows the experimental set up for motoring operation. The detailed descriptions of the experimental implementation are provided in chapter 6 and specification of various components can be found in appendix E.

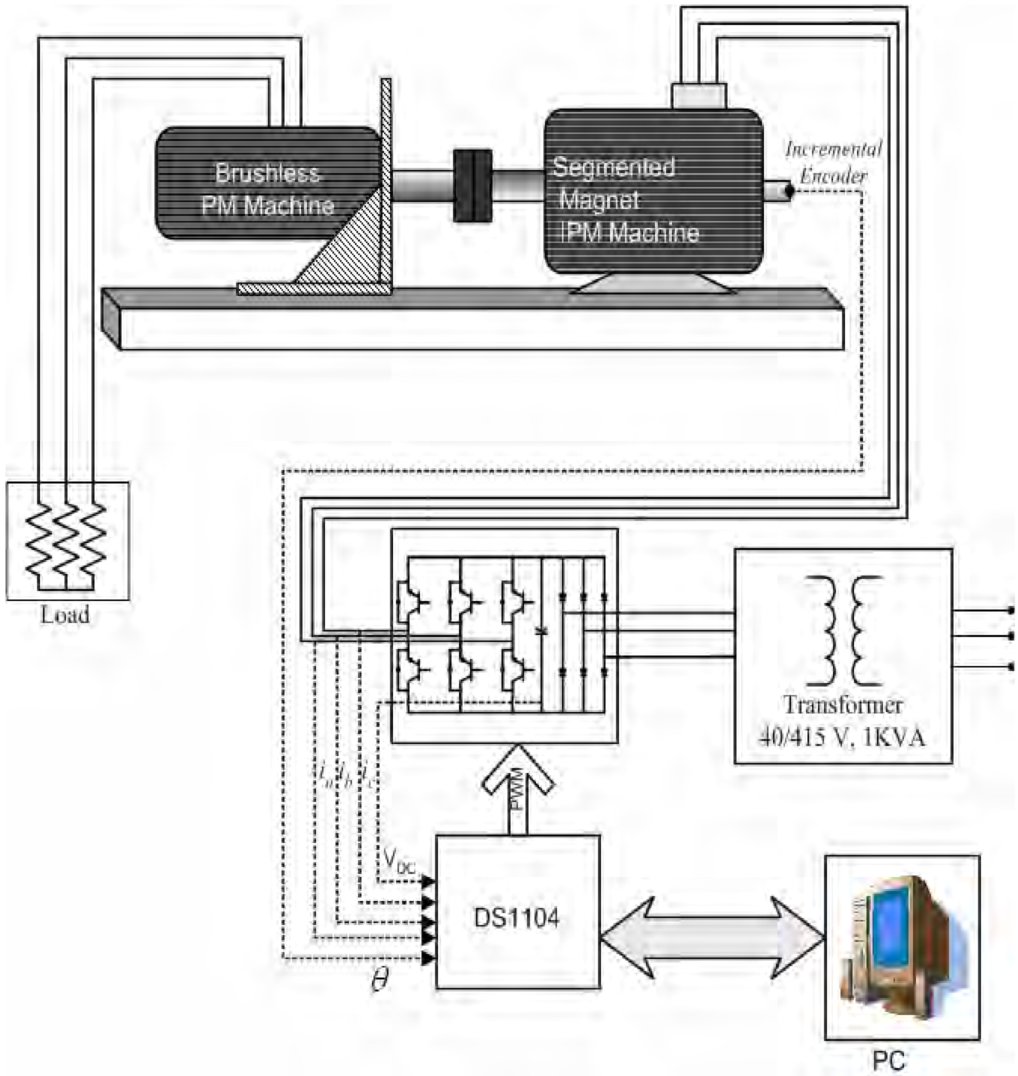

Fig. 5.18 Experimental Setup during motoring

Maximum Torque per Ampere operation: The constant torque operation of the drive is investigated with a step change of speed from 0 to 1500 r/min. The dynamic responses of the system are presented in Fig. 5.19.

The current trajectory obtained from the measured i_d and i_q are given in Fig. 5.20. During acceleration the i_d and i_q jumps to the limiting value of the current to produce the required maximum torque. As the speed approaches to the reference value, the i_d, i_q currents move along the MTPA trajectory and settles at a point defined by the no load torque. The dynamic response and trajectory obtained from the experiments closely match the results obtained from modeling.

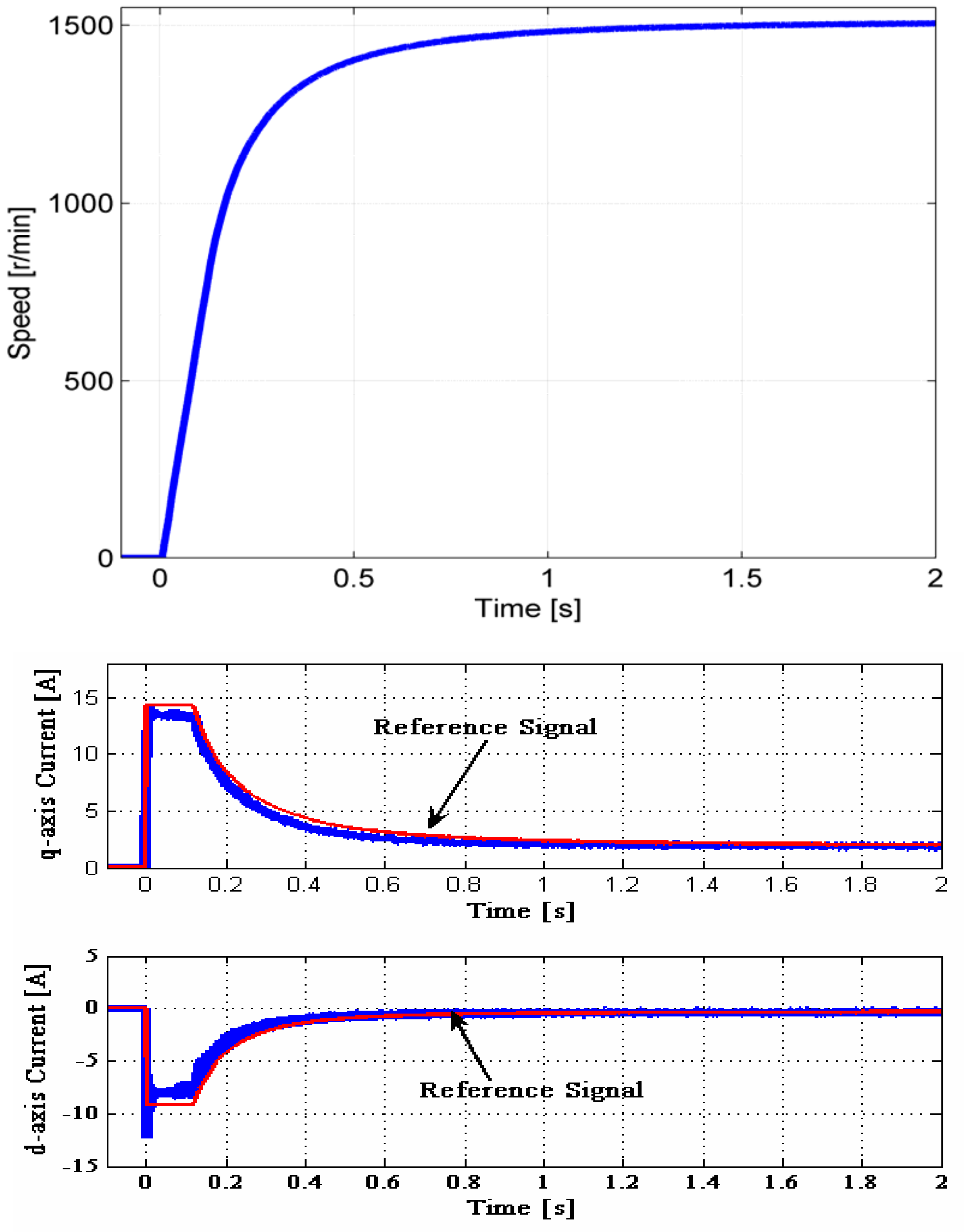

Fig. 5.19 Speed and dq-axis current response for speed step change of 0 to 1500r/min (from experiment)

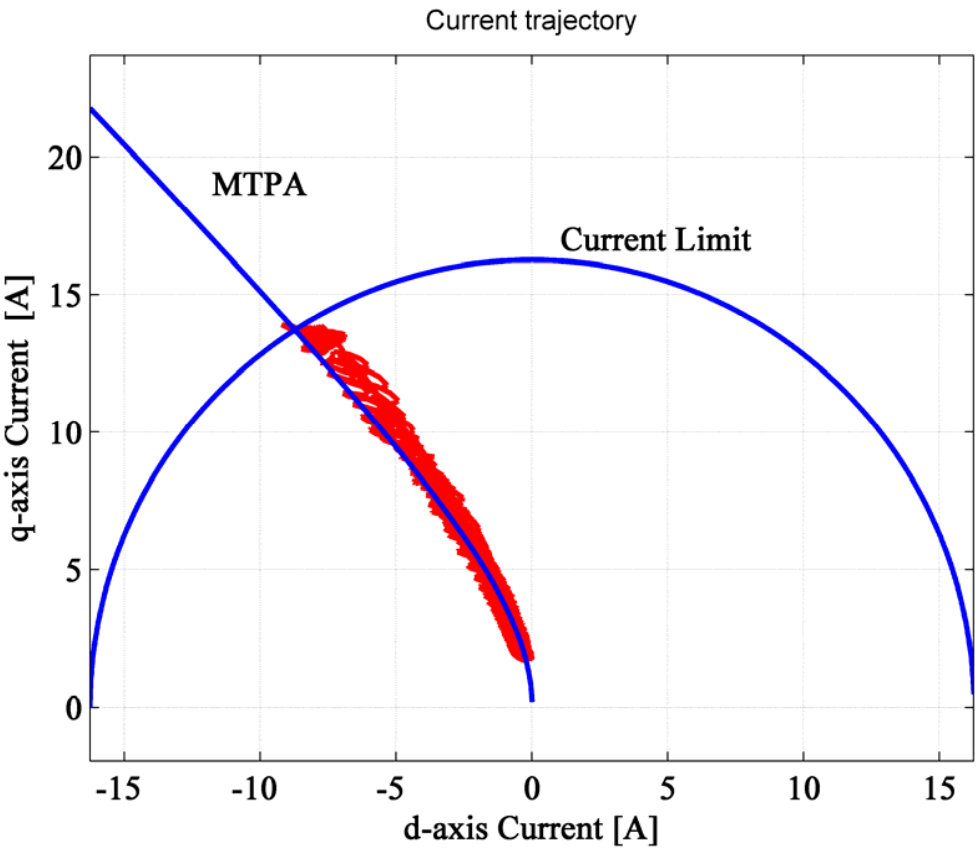

Fig. 5.20 MTPA Current Trajectory from experiment

Flux-weakening Operation: The flux-weakening operation of the machine starts approximately at the base speed of 1750r/min when run with full load. In no-load, flux-weakening starts at near the cross over speed of 4480r/min. At load condition, it follows voltage limited maximum output trajectory when the speed is greater than the critical speed of 3600r/min. The speed and dq-axis current responses for a speed step change from 0 to 4500 r/min are shown in the Fig. 5.21. The current trajectory is shown in the Fig. 5.22 where operating point follows a path of 'A' to 'B' for flux-weakening control and then itt approaches 'C' asymptotically forming the voltage limited maximum output trajectory. Again modeling and experimental results found to be of close proximity. Although, in the experimental results the transition to voltage limited trajectory was not as smooth as it is seen in the modeling results. The probable reason behind this is a higher mechanical constant then that is modeled in Simulink.

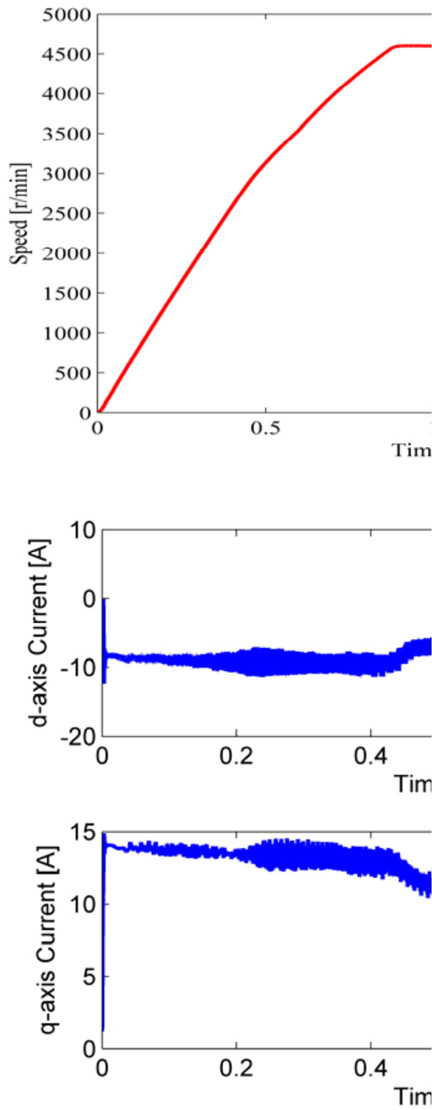

Fig. 5.21 Speed and dq-axis current
r/min

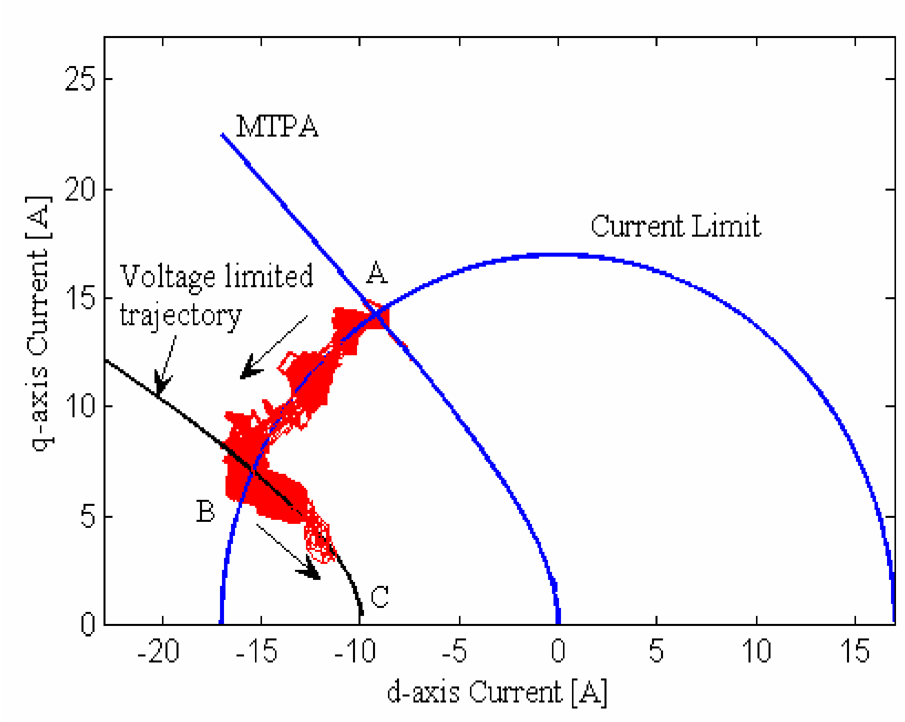

Fig. 5.22 Flux-weakening current trajectory from experiment

5.5.3. Generation

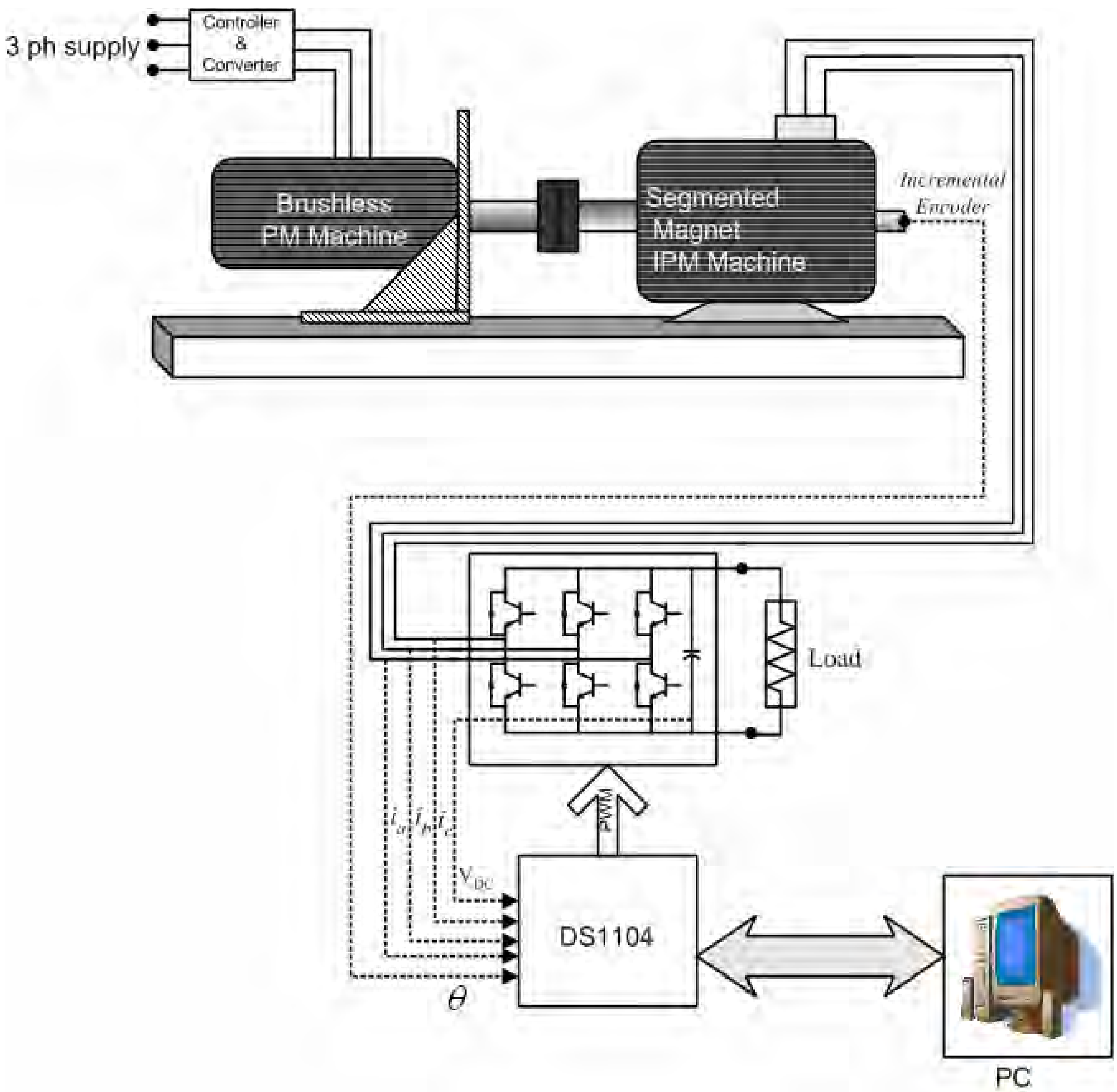

Fig. 5.23 Experimental Setup during generation

The experimental set up for generation operation is shown in Fig. 5.23. For generating operation, the segmented IPM machine was driven by a drive motor capable of running up to 8000r/min. The control was again implemented in real time through the DS1104. The dc bus is regulated at 42V. The dq-axis current response and DC bus regulation at 1500r/min and 4500r/min for step load change are shown in the Fig. 5.24 (a) and (b) respectively.

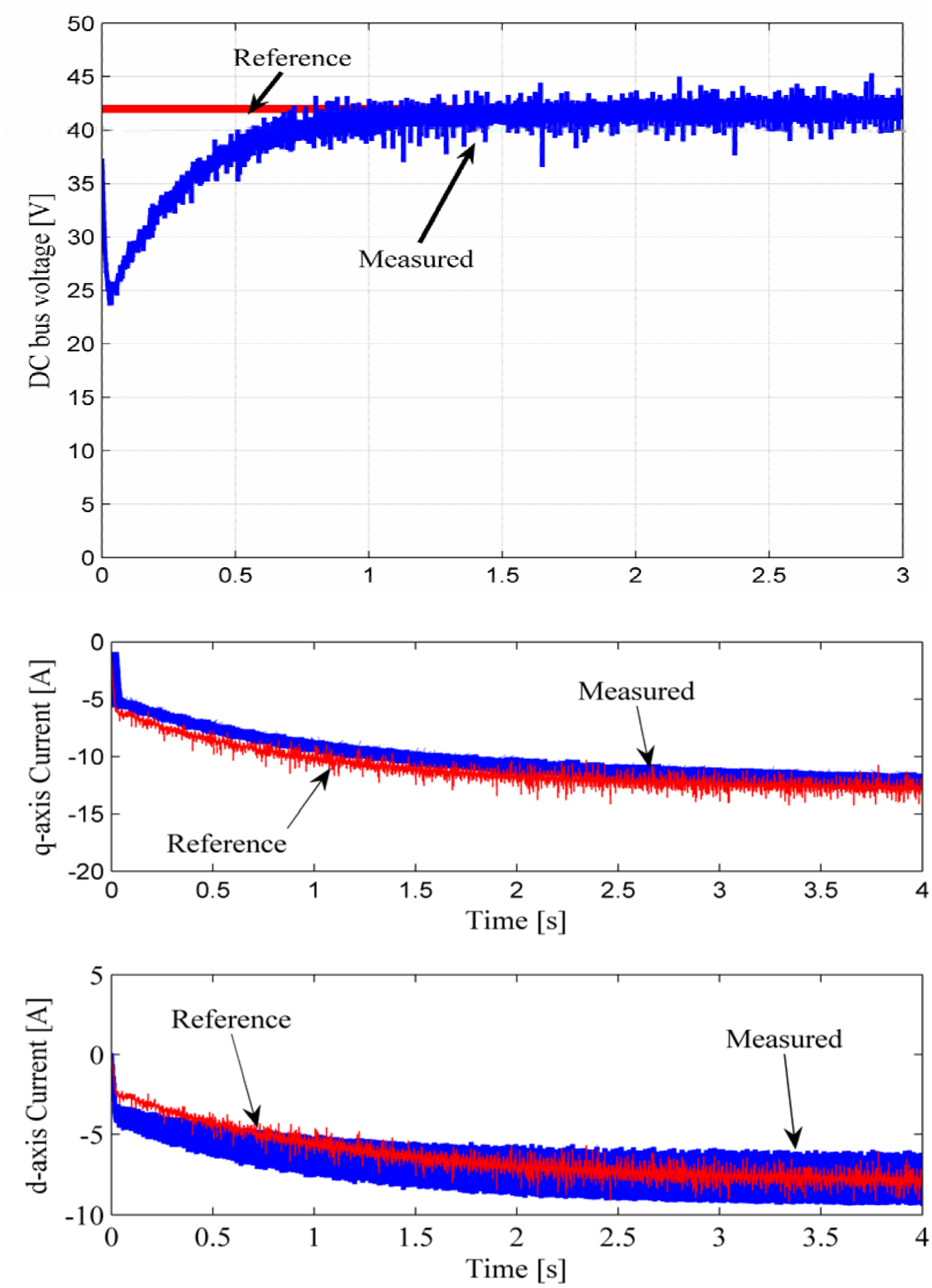

(a)

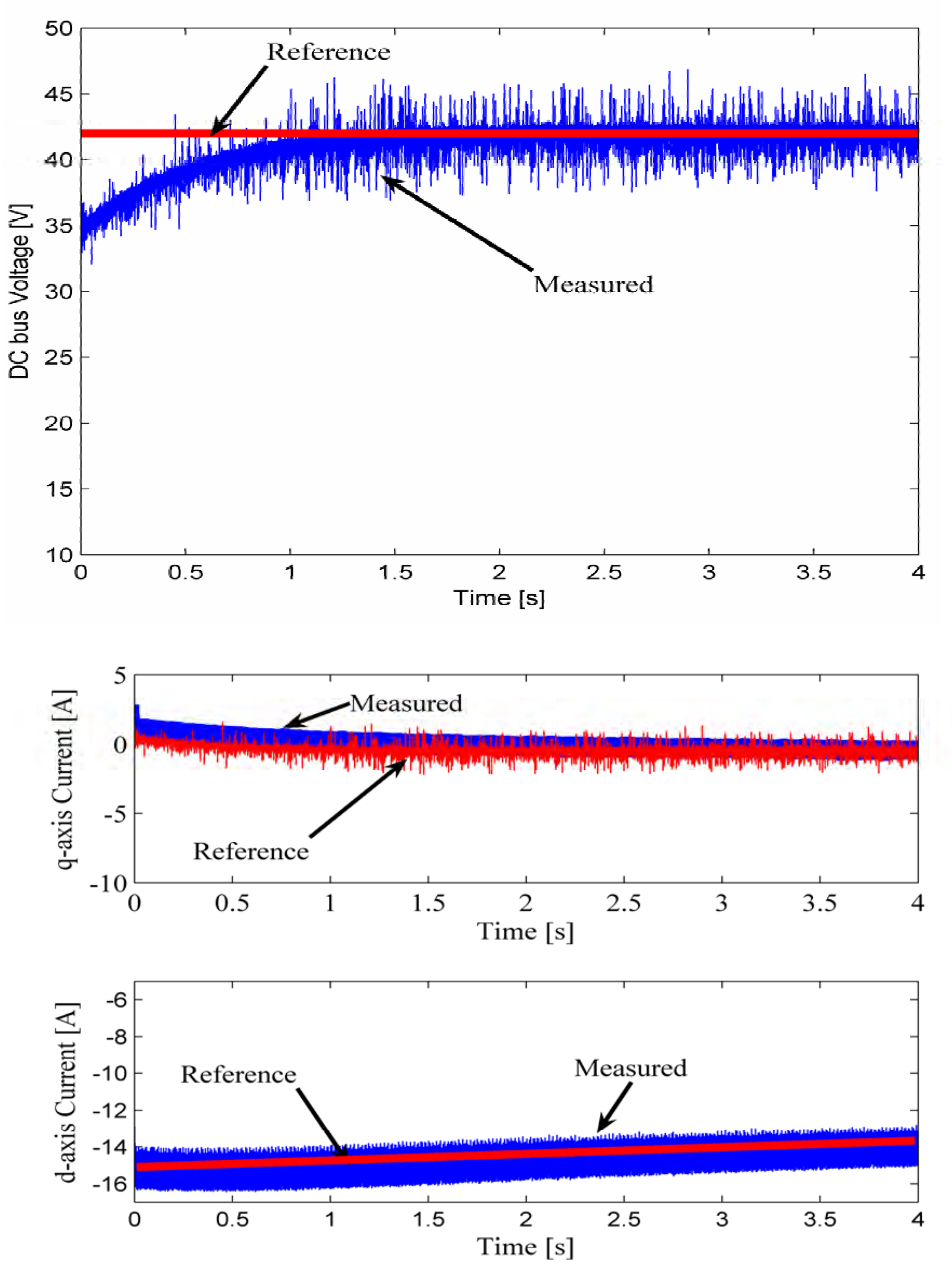

Fig. 5.24 Measured response of the DC bus and currents for a load step change (from no-load to 200W) at (a)1500r/min and (b) at 4500r/min

5.6. Issues Relating to Vector control

The control of the IPM machine by current vector is one of the most common methods. The advantage of vector current control is that it robust and relatively simpler. However, there are number of issues relating to the vector control which yet to be resolved, especially the flux-weakening control.

The control technique of the IPM machine described above is also known as feed-forward control. In such control, parameter mismatch can affect the performance of various controllers. It is well-known that flux density or rare earth magnet falls with rise in temperature, which in turn affects all three main parameters $(\psi_{PM,} L_d, L_q)$ of the IPM machine. The variation of parameter with operating condition is especially true for the Segmented IPM machine, where the magnet flux-linkage reduces in the flux-weakening mode of operation because of the unique rotor construction. It also has been observed that the effectiveness of the control falls when the current controllers saturate due to insufficient DC bus voltage at high speed [32]. As the current controllers saturate, the stator voltage excitation changes to six-step waveform prematurely. By improved flux-weakening control, premature current controller saturation due to machine parameters uncertainty and variation can be prevented.

Although in vector current control a fairly fast dynamics is achievable, its capability is constraint to some degree by the mandatory requirement of rotor position sensor. Moreover, due to PWM modulation, there exist a signal delay between the reference and actual output voltage. It can hinder in vary fast flux and torque control.

5.7. Conclusion

In this chapter, vector control of the interior permanent magnet machine was reviewed. The vector control via d- and q-axis current control was applied to the prototype segmented magnet IPM machine. The current and speed responses of the controllers for maximum torque per ampere (MTPA) control and flux-weakening control obtained from Matlab-Simulink models and experimental measurements were presented. The DC bus regulation control for the generating operation of the same machine was also presented.

Thus the control trajectories for the proposed segmented IPM machine for both motoring and generation operations have been fully designed and implemented. This lays the foundation for study of the power capability of the proposed segmented IPM machine which is presented in the chapter 6.

CHAPTER 6

6. Performance Analysis of the Segmented IPM Machine

6.1. Introduction

This Chapter presents the performance analysis of the prototype Segmented IPM machine. The steady state and transient performances of the machine as a motor and generator were investigated from no load to full load conditions. In order to measure the various performance characteristics a simple but reliable experimental set up has been developed. The detail description of the set up is included in appendix E.

This chapter includes the comparison of the measured performance data with those predicted from the finite element analysis and thereby validating the predicted performances and CPSR of the Segmented IPM machine. The measured torque, power capabilities of the prototype machine were also compared with those of the conventional non-segmented IPM machine-I.

6.2. Steady State Analysis of the Segmented IPM Motor

This section describes the process of determination of important steady state performance indicators such as induced EMF, torque- and power-speed capabilities and CPSR, no load characteristics and efficiency of the prototype segmented IPM machine.

6.2.1. Induced EMF

The induced EMF is a significant indicator of the machine's electromagnetic capabilities. It provides the information about contribution of permanent magnet field in the overall capability. The information about the magnet flux-linkage obtained from the back EMF is essential for correct control strategy and design of controllers.

As described in the 4.4.1, the time-stepping finite element solver was used to estimate the induced EMF for various speeds.

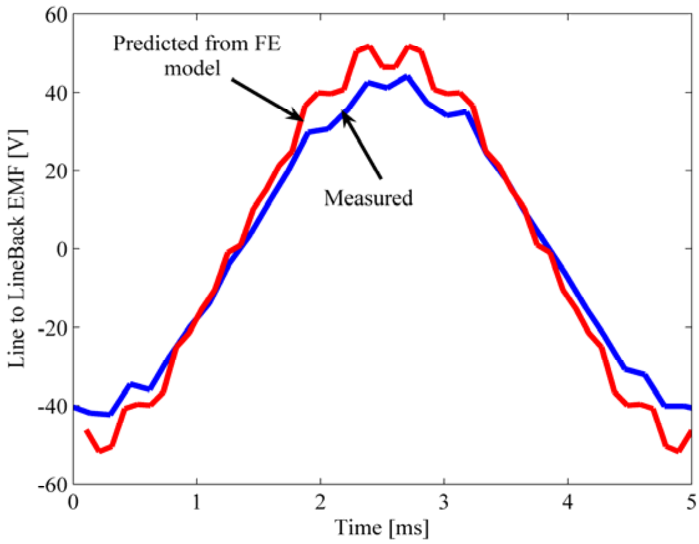

Fig. 6.1 Comparison of predicted and measured back EMF at 6000r/min

The back EMF was measured at the machine terminals by driving it with a mechanically coupled driver PMSM machine as shown in the Fig. E.2 of appendix E. The Fig. 6.1 compares the predicted back EMF of the FE model with the measured value for speed 6000 r/min.

The computed back EMF of the Fig. 6.1 was 14.46% higher than the measured value. This difference was attributed by a number of modeling and practical issues. One of them is the unaccountable stray fluxes which can not be included in the FE model.

On the other hand, the bonded NdFeB (BN12) was modeled by its remanance flux density of 0.72 T in the FE analysis. However, sometime it has been seen that the actual remanance of the magnet material is lower than the publicized value given by the manufacturers. Since, the back EMF is directly related with the remanance of the magnet material, a lower remanance of the magnet will result in a smaller back EMF. Moreover, small errors in the bridge dimension can also lead to reduced back EMF in the prototype machine.

As it can be seen from the above waveforms, the back EMF of the segmented IPM machine contains some higher order harmonics. In order to measure the back EMF constant and magnet flux-linkage, the fundamental rms amplitude was extracted from the measured phase voltage by least square optimum curve fitting technique. The fundamental voltage superimposed on the measured voltage for 1500r/min was shown in the Fig. 6.2. The induced line to line voltage of the figure can be approximated as,

$$E = 10.56\sin(\omega t) + 0.0021\sin(3\omega t) \tag{6.1}$$

The EMFs were measured for the whole speed range. The fundamental amplitudes of the phase EMF over the whole speed range is shown in Fig. 6.3. The back EMF constant K_e was determined from the fundamental of the measured EMF which was used to calculate the magnet flux-linkage using (4.18).

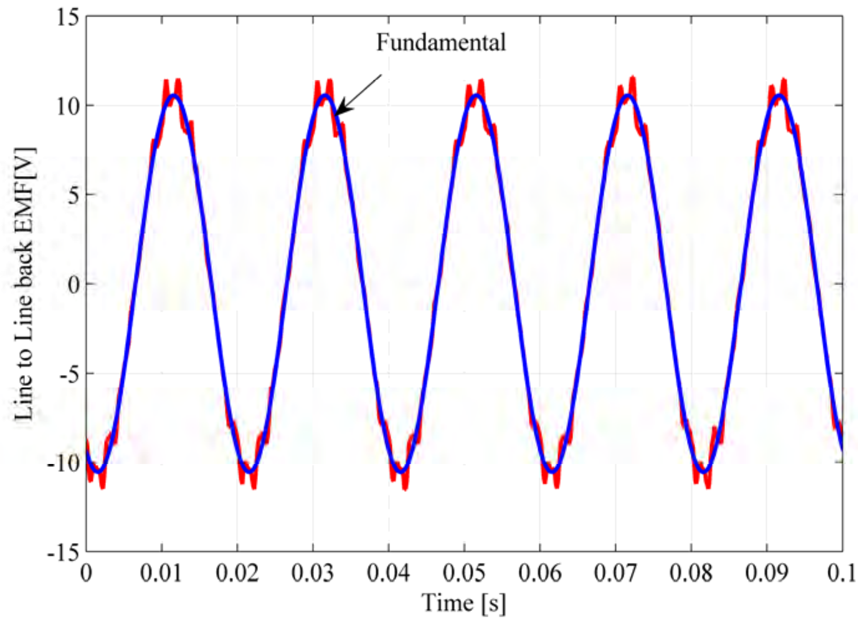

Fig. 6.2 Line to line EMF at 1500 r/min with superimposed fundamental wave

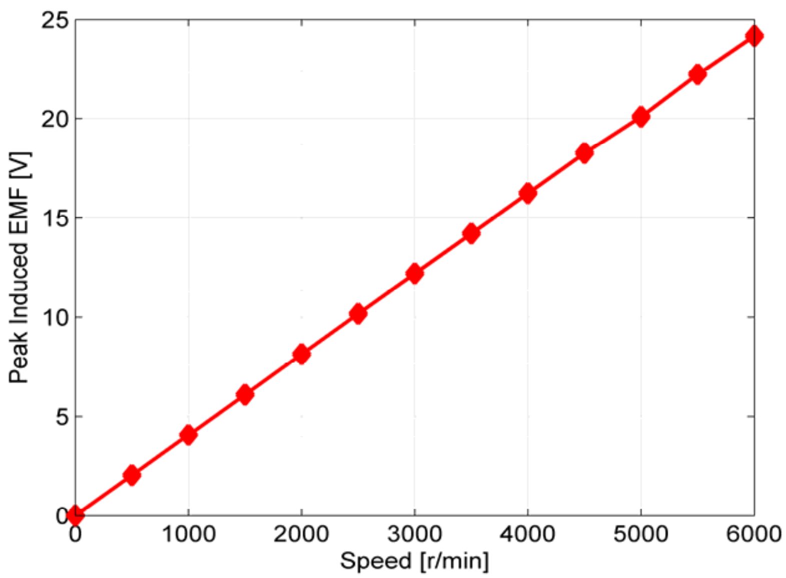

Fig. 6.3 Measured fundamental Phase EMF over the full speed range

6.2.2. No load characteristic

In the IPM motor, any change to the input voltage results in a change of the armature current and power factor for no-load and constant load torque. Consequently, a change in the input power can be noticed when plotted against input voltage. The input power P_{in} as function of voltage is limited by the threshold voltage and the maximum allowable current of the stator winding. The Fig. 6.4 shows the variation of measured input power with terminal voltage of the Segmented IPM motor at no load condition. The motor was run with the inverter at a constant speed and the line-voltage is varied by changing the DC bus voltage which is obtained from a rectifier. The input of the rectifier is varied from the auto-transformer. At no-load condition, when the negative d-axis current and the current angle γ are zero, the power factor angle ϕ is equal to the load angle δ (angle between EMF and terminal voltage V). The minimum power point occurs at unity power factor. The motor is under-excited or have a lagging power factor at the left hand side of this point and leading power factor corresponding to an over-excited motor is on the right hand side of the same point. The power-factor can be kept constant by increasing the voltage proportional to the current increase. On basis of this theory, the power factor control of the IPM machine can be achieved. The power-factor control is out of scope of this work and will not be discussed further.

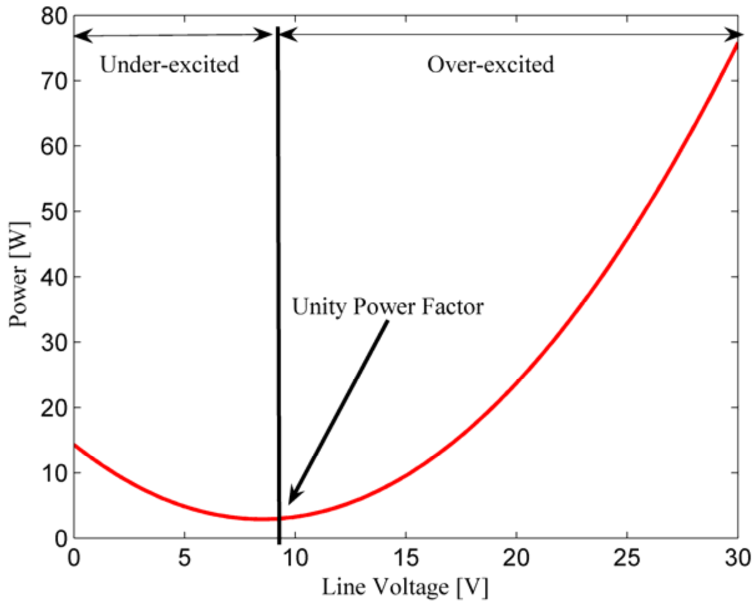

Fig. 6.4 No load characteristic of power as function of line voltage

6.2.3. Determination of Torque and Power Speed Characteristic

The relationships of torque and power with speed dictate the operating characteristic of an IPM motor. The torque speed characteristic represents the steady-state capability of the motor to drive various loads. On the other hand, in many applications constant output power for a wide speed range is desirable and the power-speed characteristic of a motor is a good measure of its constant power capability. The torque- and power-speed of the segmented IPM motor was first calculated from the finite element analysis and then verified by the experimental measurements.

The developed torque is calculated using virtual work method in the finite element analysis where torque exerted in a given direction is obtained by differentiating the magnetic energy W of the system with respect to a virtual displacement of the object in the direction. The precondition of virtual work method is that displacements must not alter the mechanical state of the system. The magnetic torque exerted on ferromagnetic region with high permeability can also be calculated using Maxwell's stress tensor method [71].

In the finite element model of the Segmented IPM motor, stator excitation and rotor magnet field contribute to the magnetic energy *W*. In the torque calculation, the stator excitation is assumed to be sinusoidal. Since, in current controlled IPM machine, the stator current is nearly sinusoidal, stator excitation with sinusoidal current source in the finite element model is justifiable, as long as harmonics generated by the PWM can be neglected. The phase currents of the stator excitation are expressed as,

$$i_a = I_{\mathrm{m}} \sin(\omega t + \gamma) \tag{6.2}$$

$$i_b = I_m \sin(\omega t + \gamma - 120^0) \tag{6.3}$$

$$i_c = I_m \sin(\omega t + \gamma + 120^0) \tag{6.4}$$

where, $\hat{I}$ is the peak value of the stator current and γ is the phase angle. The rotor starting position at $t = 0$ is chosen in such a way that magnet axis of phase '*a*' is aligned with the direct axis of the rotor. In such case, the initial phase angle γ of the stator current is also the electrical angle between stator MMF and rotor *q*-axis [45]. In the steady-state condition, for a constant load and frequency, the electrical angle γ remains constant. The instantaneous terminal voltage of the phase-*a* winding is given as,

$$v_a(t) = Ri_a(t) + \frac{p}{a}\frac{d\psi_a(t)}{dt} + L_e \frac{di_a(t)}{dt} \tag{6.5}$$

where, *R* is the stator winding resistance, ψ_a is the instantaneous flux-linkage of phase-*a* per pole, L_e is the end turn inductances, *p* is the number of pole pairs and *a* is the number of parallel path in one pole pitch. The terminal voltage v_a(t) increases with speed and reaches the rated value at a particular speed. Up to this speed, the current angle γ is kept at its optimum value so that maximum torque per ampere can be obtained. Above this speed, the current angle γ is increased until the terminal voltage reduces to the rated value. At the maximum torque per ampere (MTPA) region, the current angle γ is calculated from the maximization of torque equation (5.2) given in section 5.3.2 of the chapter 5. This angle remains constant for all speeds at the MTPA region. The torque and line-line voltage are calculated for each speed in the finite element model. Once the line-line voltage exceeds the maximum allowable voltage limit, the flux-weakening control should start. In other word, the current angle γ should increase for the speeds of which the line-line voltage is higher than the limit value. For these speed, the line-line voltages are calculated in the finite element model for series of current angle γ using the parametric feature of the Flux 2D. With the increasing γ angle, the line-line voltage reduces. The torque and power are calculated for the angle γ at which the line-line voltage is equal to the limit value. The process is repeated for each speed in the flux-weakening range.

In the experimental setup of the Fig. E.1, the Segmented IPM motor was run with vector current controlled algorithm. The speed of the motor was controlled with the PI controller of the outer loop. The mechanical load variation of the machine was achieved through a coupled generator with resistive load. The input powers of the motor were measured at the terminals for different speeds. The output power and shaft torques were calculated from the measured input power by subtracting the copper and core losses. The predicted and measured torque- and power-speed characteristics are shown in the Fig. 6. 5(a) and (b) respectively.

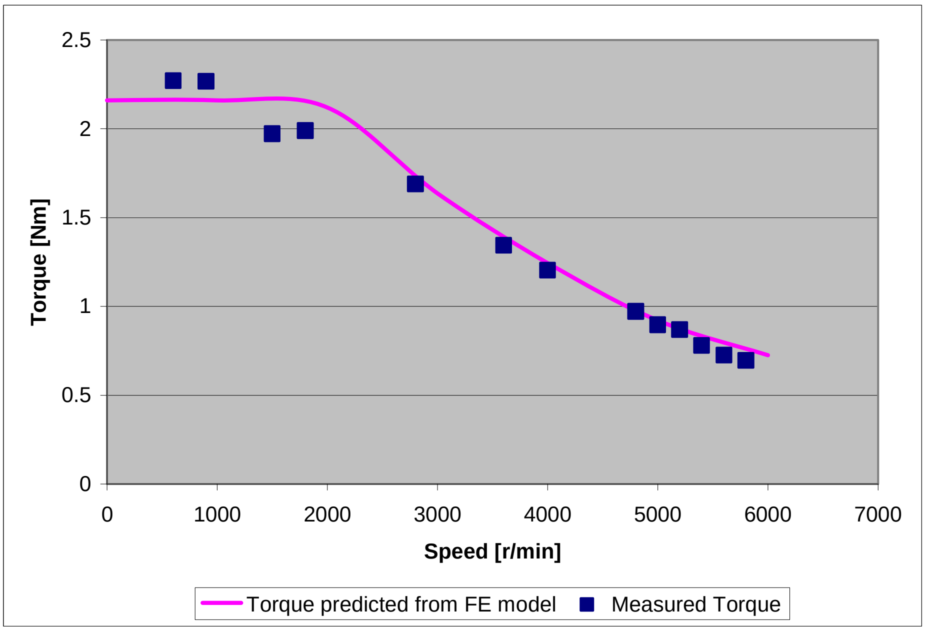

(a)

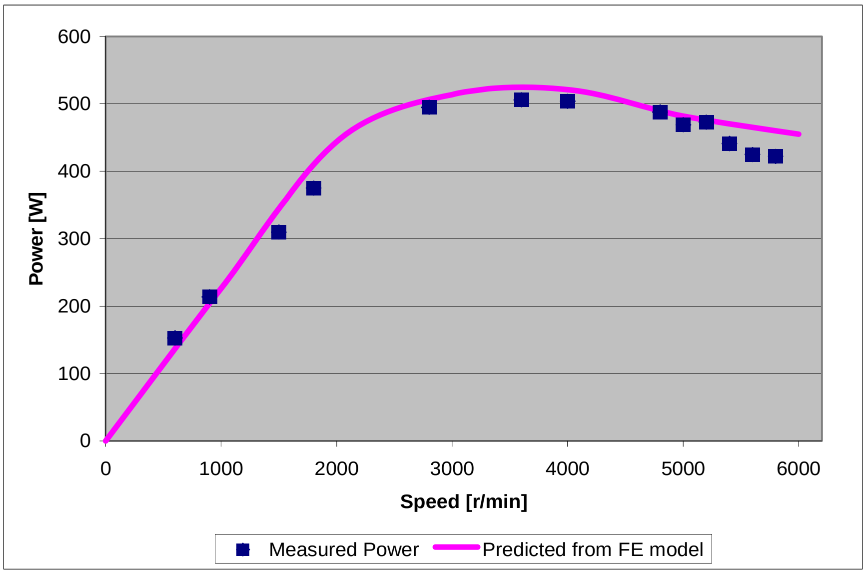

(b)

Fig. 6.5 (a)Torque-speed characteristic and (b) Power-speed characteristic

It can be seen from the above performance characteristics that the predicted results are fairly close to the measured values. The constant torque operation was found to be up to about 1750r/min when run with full load. The flux-weakening operation was measured up to about 6000r/min. The machine runs nearly with constant power from 2400 r/min to the 6000r/min. However, looking at the trend of the measured characteristic, possibility of a higher CPSR can not be ruled out. Due to the requirement of over-modulation in the inverter; the operating speed was limited to 6000r/min in motoring. The slave DSP of the dSPACE1104 was used in the experimental setup to generate the PWM switching signals of the inverter. There is no provision of over-modulation in this arrangement. Therefore, the requirement of over-modulation could not be applied in the experimental setup of this work and system voltage was therefore restricted to $\frac{V_{dc}}{\sqrt{3}}$ which is the limit for Space Vector Modulation (SVM) of the PWM generation.

The DC bus voltage of the Voltage Source Inverter (VSI) was maintained all the time at 42 V. The measured rms values of the line to line voltage against speeds are shown in the Fig. 6.6. It is obvious from this figure that the line voltage was maintained at the limit value throughout the flux-weakening region. The time trace of line to line PWM voltage and current at 750 r/min, 1500r/min, 3000r/min and 45000r/min are presented in the Fig. 6.7(a), (b), (c) and (d) respectively.

As mentioned in chapter 5, a commonly used feed-forward vector current control was used to generate the PWM signals. The performance of such controls deteriorates when parameter uncertainty increases at high speed and load condition. The distortions in the line voltages noticed at 6000 r/min of Fig. 6. 8(a) and (b) under full load condition were caused by this deterioration as well as by the requirement of over-modulation in the inverter. An improved control algorithm and provision for over-modulation in the inverter should enhance the performance further more. Over-modulation can be avoided by reducing the voltage limit to calculate the flux-weakening operating trajectory. However, in such case, the machine capability will no be fully realized.

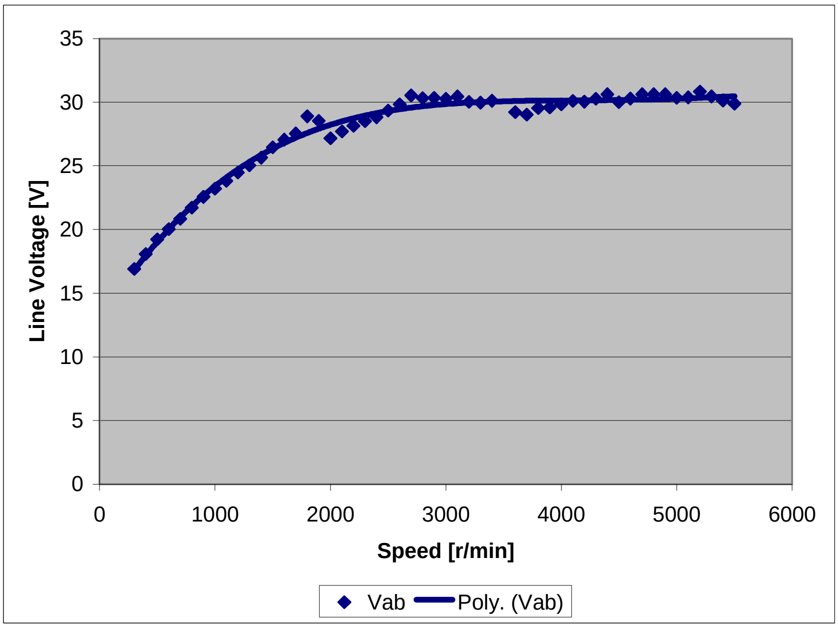

Fig. 6.6 Line to Line RMS voltage values against Speed

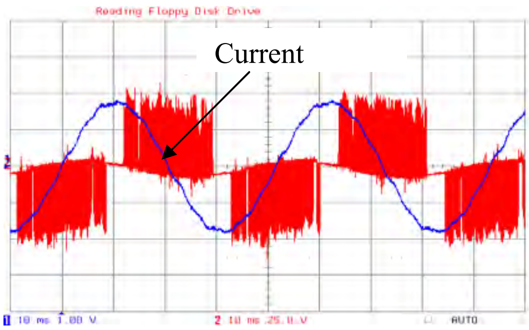

(a) 750r/min

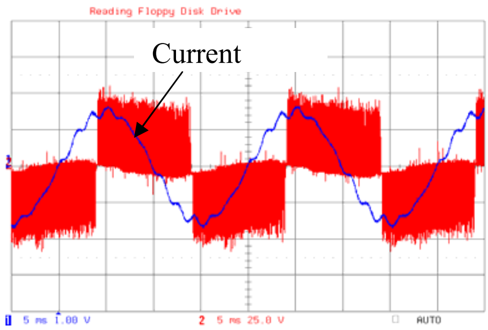

(b) 1500 r/min

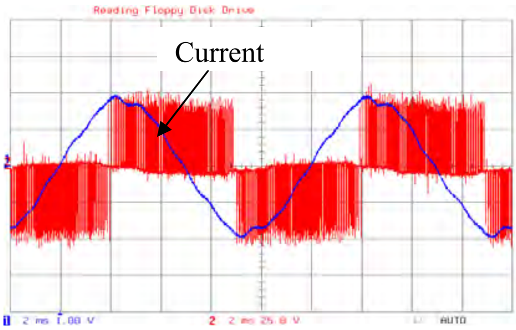

(c) 3000 r/min

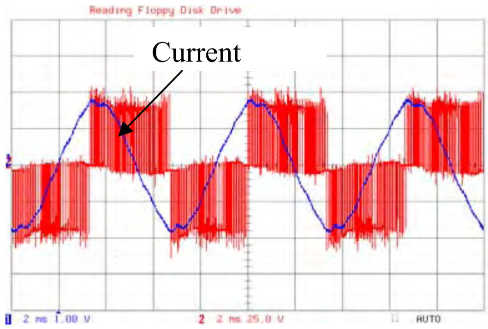

(d) 4500 r/min

Fig. 6.7 Time trace of terminal voltage and current at (a) 750r/min, (b) 1500r/min, (c) 3000r/min and (d) 4500r/min (100mV/A)

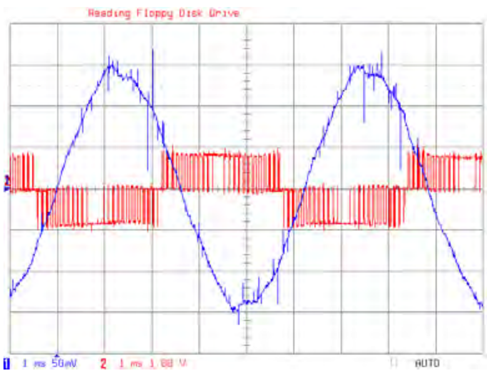

10mV/A and 50/V

(a)

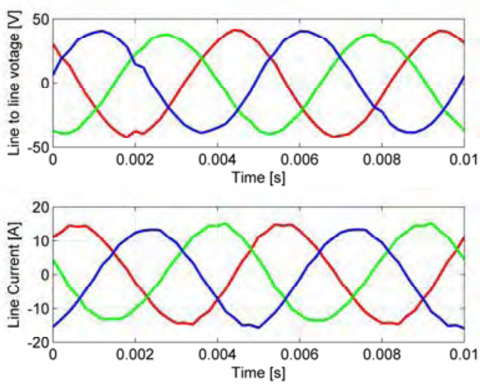

(b)

Fig. 6.8 The line voltages and currents at 6000r/min(a) one line current and line to line voltage (b) three line currents and voltages (after low pass filter of cut off frequency 80 Hz)

6.2.4. Efficiency

The true efficiency of a machine is defined as the ratio of output power to input power under specified operating condition. The input power is measured at the motor terminal by a power analyzer and output power can be measured at the shaft by help of torque sensor. In absence of torque sensor, the mechanical output power can not be measured accurately. In such case, a conventional efficiency is used on basis of the segregated losses [72]. The conventional efficiency is related to the sum of the segregated losses as,

For a motor, $$Efficiency(\%) = 100 - \frac{Losses \times 100}{input\ power} \tag{6.6}$$

For a generator, $$Efficiency(\%) = 100 - \frac{Losses \times 100}{(Output + Losses)} \tag{6.7}$$

The input, output power and losses in (6.6) and (6.7) are all in the same unit of measurements.

The segregated losses in the IPM machine, include- friction and windage loss, core loss, stray-load loss and stator winding copper loss. The copper loss is determined using the stator current at the specified load and DC winding resistance corrected to a specified temperature. The mechanical loss of friction and windage can not be separated from the open circuit core loss in the PM machine unless magnet field are removed or pseudo rotor is used. The measurement of core loss of the Segmented IPM machine was discussed in section 4.6.

The input power and segregated losses of the Segmented IPM were measured for the various speeds under full-load condition. The efficiency was calculated from (6.6) for entire speed range and is presented in the Fig. 6.9. The full load power was measured with a speed step of 100r/min for the whole speed range. In the Fig.6.9 efficiency of all these points were shown whereas in the torque- and power-speed characteristics of Fig. 6.5(a) and (b), only some of the measured points were shown just for shake of clarity. An aggregate efficiency of 0.85 was maintained in the constant power speed range. Thus, it can be ensured that segmentation of the magnet pole has minimum adverse effect on the efficiency. It is worth noting here that the stator of the machine was originally built for a 550, 4-pole Induction motor whose rated efficiency was only 0.74. The aggregate efficiency of the conventional IPM machine for full load was also measured and found to be close to 0.78 only.

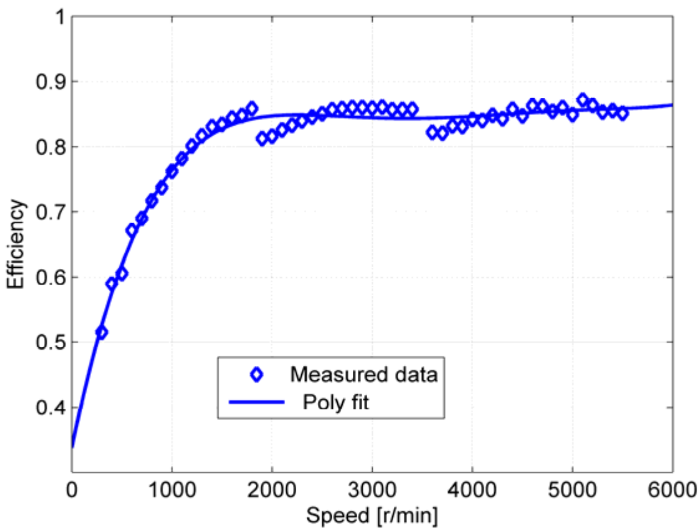

Fig. 6.9 Efficiency Vs Speed of Segmented IPM motor

6.3. Transient Analysis of the Segmented IPM motor

The transient behaviour of the Segmented IPM motors were analysed by experimental measurements of voltage, current and torque response for acceleration in a step speed change. The dynamics of the motor was also studied for a step load change at various speeds.

6.3.1. Step change variation of speed

The step change of speed occurs when motor speed is controlled through an outer speed or torque control loop. The Fig. 6.10 (a) and (b) shows the responses of speed, torque, line current and voltage for the step changes of speed from 0 to 1500r/min and 0 to 5000r/min of the Segmented IPM motor. During acceleration current reached its peak value and then settles at a value required by the load torque. In the first case of 0 to 1500r/min, the motor was operating with maximum torque per ampere control. Hence, a constant torque was seen in the Fig. 6.10 (a) during acceleration. On the other hand, for the step speed of 0 to 5000r/min, a transition of control from MTPA to flux-weakening occurs which is noticeable in the acceleration torque of the Fig. 6. 10(b). The increase in the line voltage can be noticed till 0.25s after which it remains constant at limit value by the flux-weakening. It should be noted here that torque shown are estimated from the machine parameters and measured d- and q-axis currents. The measured line voltage is pass through a low pass filter and then captured through data acquisition in dSPACE.

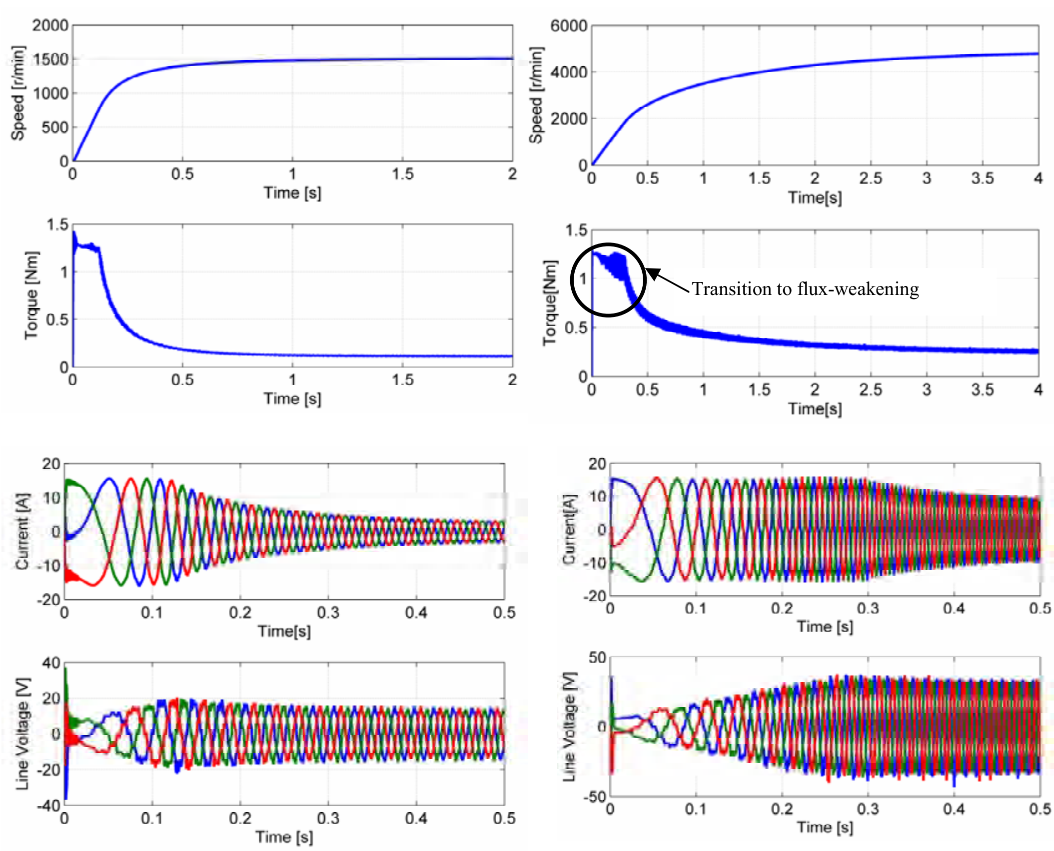

(a) (b)

Fig. 6.10 Measured torque response, line current and voltage (after a low pass filter with cut off frequency of 80 Hz) for a speed step of (a) 0 to 1500r/min and (b) 0 to 5000r/min

6.3.2. Step change variation of mechanical load torque

The transient response of the Segmented IPM motor was analysed for a step increase of the mechanical load torque from no load to 0.5 Nm and then to 1.2 Nm at a speed of 3000r/min. The response of the torque and line current are shown in the Fig. 6.11 The response of speed during the load change given in the Fig. 6.12 shows that it decreases from 3000r/min to 2880r/min within 0.5 s whereas stator current increases proportionally to load torque so that electromagnetic torque developed in the machine can counter balance the rising load torque. In this way, the motor dynamically adjusts its operating condition to accommodate the change in load condition.

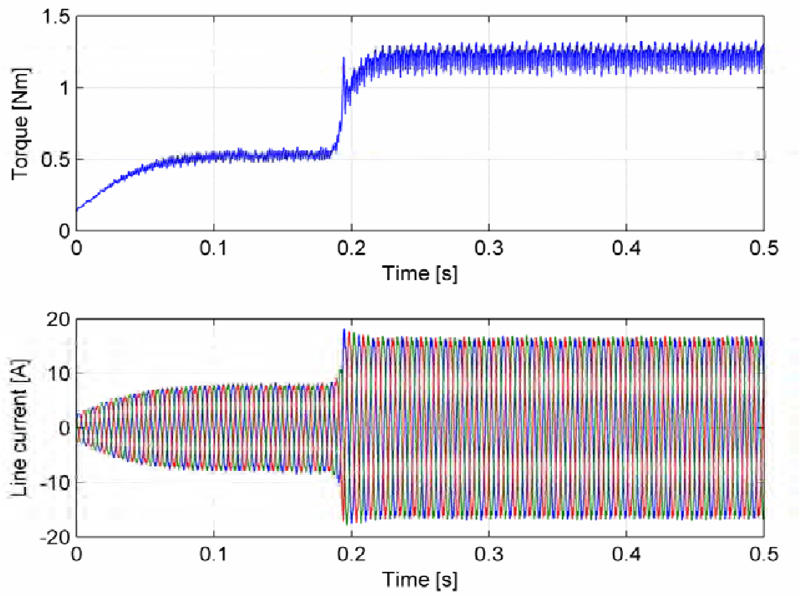

Fig. 6.11 Measured torque response and line current for a step change in load torque

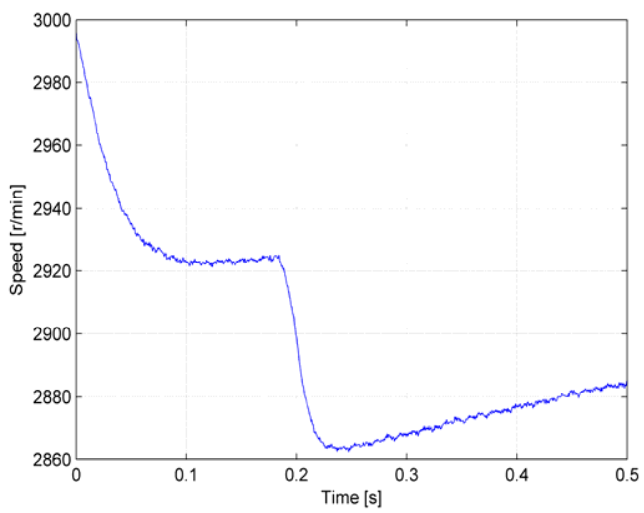

Fig. 6.12 Speed response for step load torque change

6.4. Analysis of the Segmented IPM Generator

This section presents the steady state performance of the segmented IPM machine operating as a generator. The power-speed characteristic curve of the machine as a generator was measured and compared with the predicted values of FE model.

6.4.1. Performance Analysis

The experimental set up of the segmented IPM machine as a generator was presented in the Fig.E.4 of the appendix E. The IPM machine was mechanically coupled to a brushless motor (Kollmorgen AKM brushless servomotor PMSM) that act as a prime mover. The speed of the servomotor was regulated continuously through a controller/converter (Kollmorgen, SERVOSTAR 300). The generated three phase voltages of the Segmented IPM machine were fed to a voltage source inverter (VSI). The DC bus of the VSI was regulated to 42V by the current vector control of the section 5.5.3. The segmented IPM generator was loaded through this regulated DC bus of the VSI.

The DC bus voltage, terminal voltage and current of the generator at steady state were measured for various speed and load conditions. The, Fig. 6.13, Fig. 6.14 Fig. 6.15 and Fig. 6.16 show (a) the DC bus voltage and (b) the generator line current and voltage for the full load condition at a speed of 1500r/min, 3000r/min, 4500r/min and 6000r/min respectively. It can be concluded from these figures that a good regulation of the DC bus at 42V can be maintained for various speeds and loads.

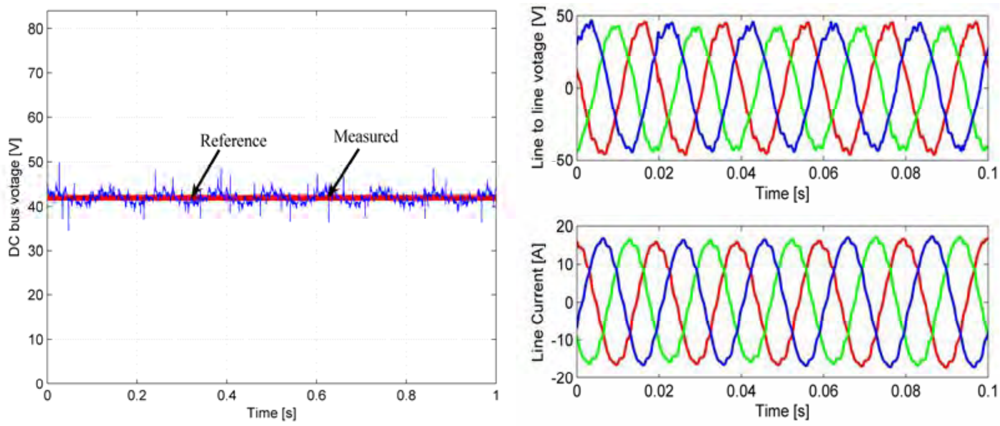

(a) (b)

Fig. 6.13 (a) DC bus voltage and (b) line to line terminal voltage and current of the segmented magnet IPM generator at 1500r/min

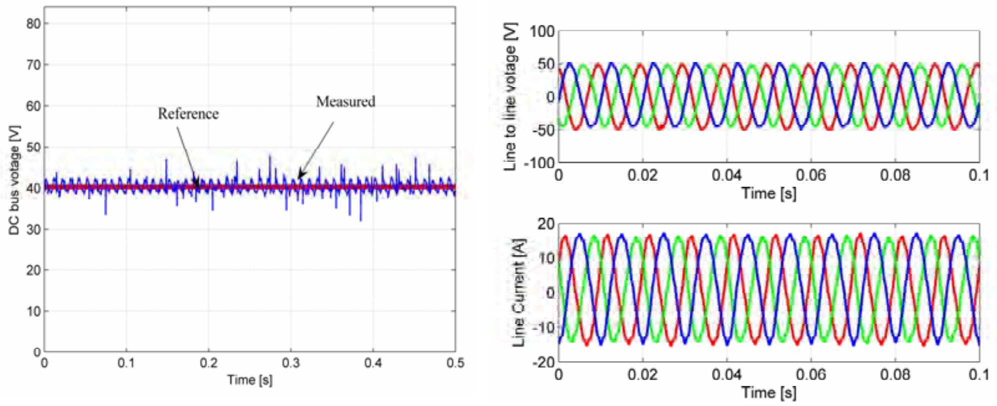

(a) (b)

Fig. 6.14 (a) DC bus voltage and (b) line to line terminal voltage and current of the segmented IPM generator at 3000r/min

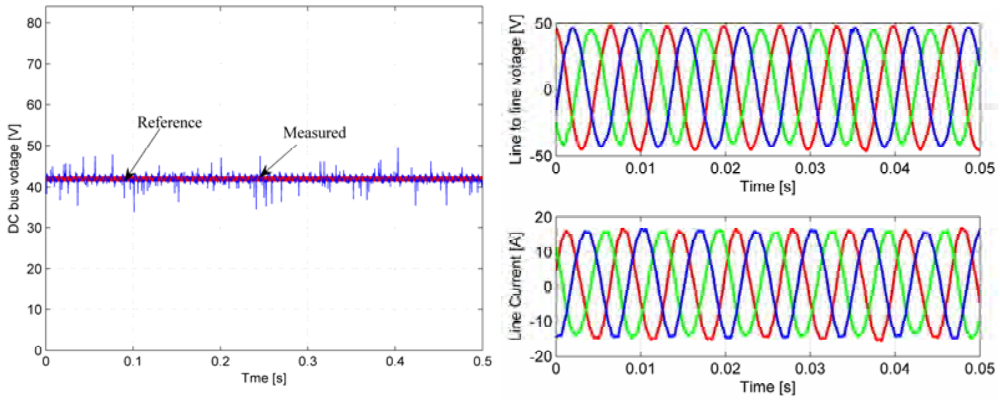

(a) (b)

Fig. 6.15 (a) DC bus voltage and (b) line to line terminal voltage and current of the segmented IPM generator at 4500r/min

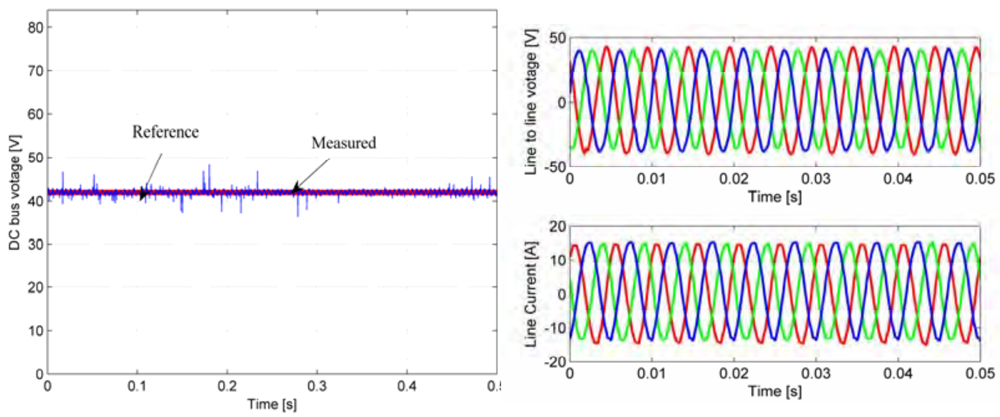

(a) (b)

Fig. 6.16 (a) DC bus voltage and (b) line to line terminal voltage and current of the segmented IPM generator at 6000r/min

6.4.2. Load Stepping

The transient performance of the segmented IPM generator was tested with load stepping. Initially, the machine was running at 1500r/min with no load and DC bus voltage was maintained at 42V. Suddenly, a step load was applied to the system by switching on a resistive load connected to the DC bus. As shown in the Fig. 6.17, the DC bus voltage drops by nearly 10V and then recovers to the reference value quickly.

The effect of load stepping on the line voltage and current were also shown in the same figure.

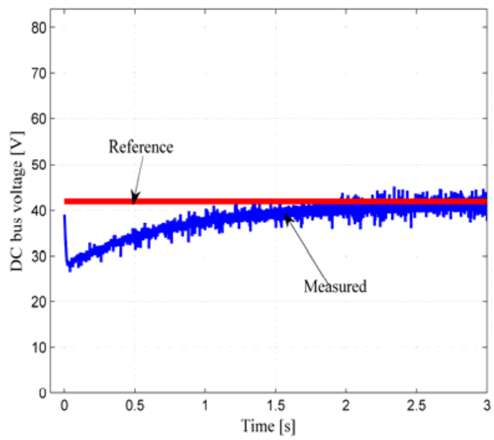

(a)

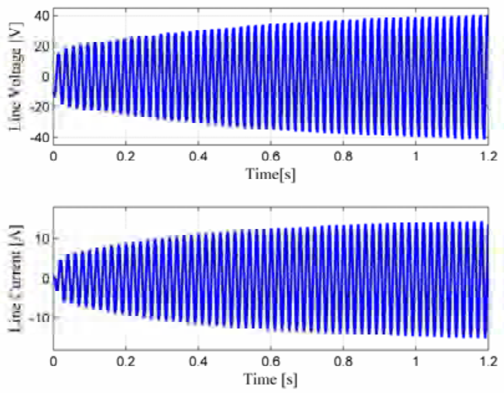

(b)

Fig. 6.17 Load stepping at 1500r/min (a) Transient in the DC bus and (b) Transient in line voltage and current

6.4.3. *The Power Speed Characteristic of the Segmented IPM generator*

The power-speed capability of the generator at various speeds were measured with a power analyzer (YOKGAWA PZ400) and compared to the predicted values obtained from the finite element model. The machine operates in the third quadrant of the dq-plane during generation. Hence, in the finite element analysis, the current angle γ was varied between 90 to 180 electrical degrees. The Fig. 6.18 shows the predicted and measured power capability of the generator up to the speed 7800 r/min. Again, measured values were found to closely match the predicted ones. The power remains nearly constant from 2400 r/min to the 7800 r/min. The measured rms values of line to line voltage at the machine terminal (after low pass filter) against speeds are presented in the Fig. 6.19.

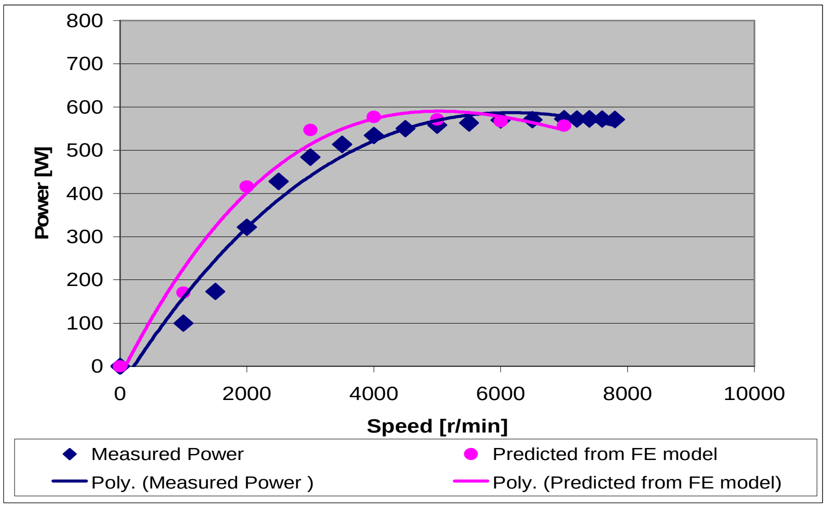

Fig. 6.18 Power Capability curve of the segmented IPM machine during generation

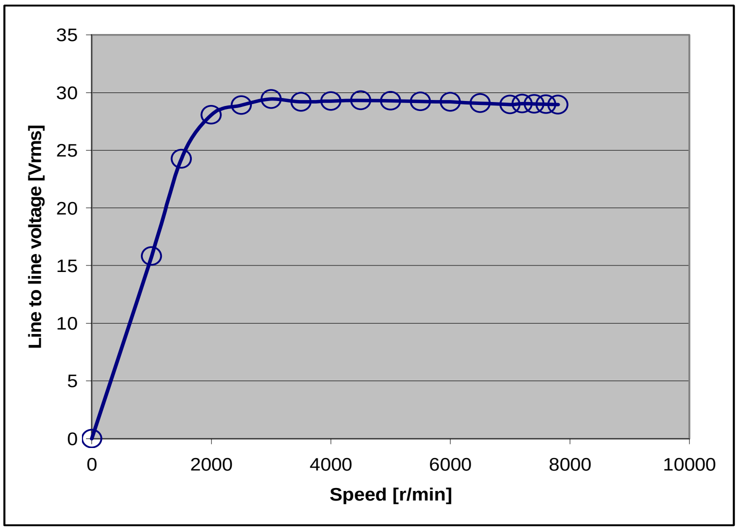

Fig. 6.19 Line to line voltage (rms) Vs speed

6.5. Comparison of the Performance Characteristics with IPM machine-I

In this section, the performances of the segmented IPM machine were compared with that of IPM machine-I. It is worth mentioning here that both the machines are similar in respects of rating and dimensions. The only difference between two machines lies in the magnet configuration of the rotor.

(a) (b)

Fig. 6.20 Rotor of (a) the segmented IPM machine and (b) the prototype IPM machine-I

The pole magnets of the segmented IPM machine are segmented whereas that of the IPM machine-I contains conventional, non-segmented magnet poles. The rotors of the two machines are shown in the Fig. 6.20. The parameters and ratings of both machines can be found in Table A-1 and A-2 of appendix A. The measured line to line back EMFs of both machines at 1500r/min are presented in the Fig. 6.21(a) and (b). The induced EMF of the Segmented IPM machine is closer to sinusoid than that of the IPM machine-I, but the amplitude is less because of the lower remanance permanent magnet in the pole. The bonded NdFeB (Br= 0.69~0.78T) was selected for the Segmented IPM machine to restrict the EMF at maximum speed under the 42 V PowerNet of the automobile.

The measured torque- and power speed characteristic of both the machines are compared in the Fig. 6.22. and Fig. 6.23 respectively. The peak torque of the segmented IPM machine in constant torque region is slightly less where as constant power speed range of this machine much wider than that of the IPM machine-I.

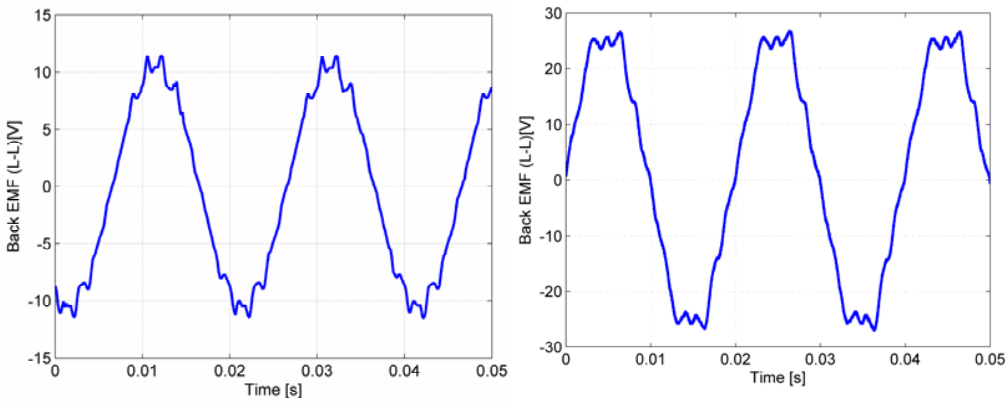

(a) (b)

Fig. 6.21 Measured Back EMFs of (a) the segmented IPM machine and (b) IPM machine-I at 1500r/min

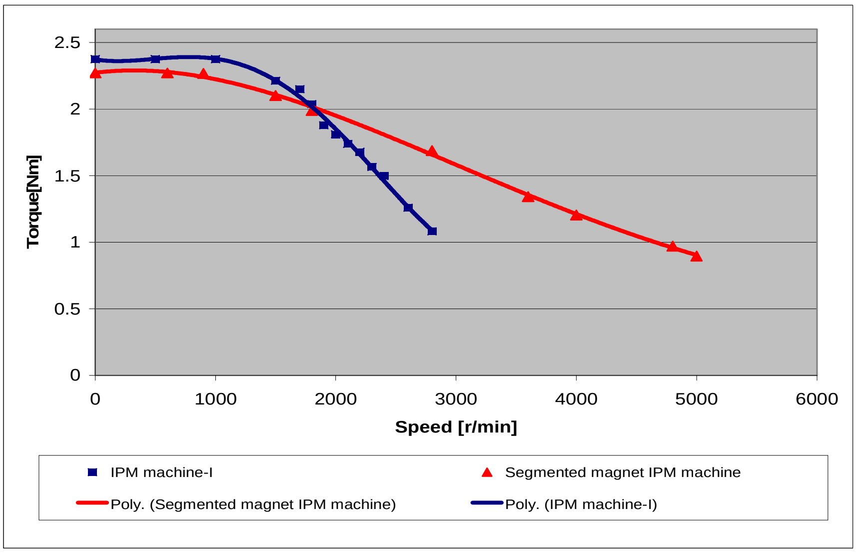

Fig. 6.22 Comparison of the torque-speed characteristics of the IPM machine-I and the segmented IPM machine

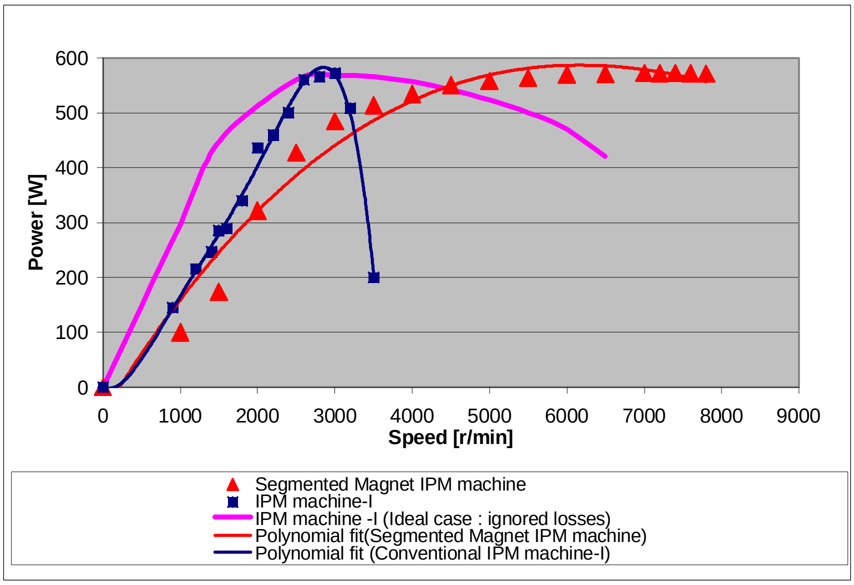

Fig. 6.23 Comparison of the torque-speed characteristics of the IPM machine-I and the segmented IPM machine

The comparison of the core loss and cogging torque of the two machines are presented in the chapter 4.

The figure 6.23 also shows the power speed characteristic of the IPM machine-I calculated for the ideal case i.e. all the rotational losses in the machine ignored. It suggests that a wider CPSR is possible in the machine than that was achieved with the experimental measurements. This discrepancy can be explained by the high iron loss seen in the IPM machine-I (referred to Fig.4.24). It should be noted here that the rotor of the IPM machine-I was constructed as solid iron rotor assuming rotor iron loss of the synchronous machine to be negligible. However, recent studies show that rotor iron loss in the IPM machine is not negligible especially at high frequency range. Since both the segmented IPM machine and the IPM machine-I use the same stator, it can be concluded that the higher iron loss seen in the IPM machine-I was mainly contributed from the solid rotor. The experimental measurement shows that output power at 3500r/min is around 200W and it is very close to no load power of the machine at this speed. Hence, the IPM machine-1 is not capable to take any load above this speed.

Thus, it could be concluded from these comparison that the performance of segmented IPM machine as a wide constant power speed range (CPSR) machine is far better than the IPM machine-I.

6.6. Conclusion

In this chapter the performances of the segmented magnet IPM machine as a motor and generator were presented. The predicted power and torque capability of the machine from the finite element model were validated by the experimental results. The performance of the segmented magnet IPM machine was also compared with the prototype IPM machine-I. The steady state and transient performances were found to be satisfactory. The segmented magnet IPM machine gives a wide constant power range both as a motor and generator. For the same stator, the CPSR obtained in the Segmented Magnet IPM machine is much wider than that of the IPM machine-I. It is also capable of maintaining an efficiency of 85% in the constant power operation region at full load condition.

CHAPTER 7

7. Application of Segmented IPMM as Integrated Starter Alternator (ISA) of automobile

7.1. Introduction

The onboard power demand on the automotive electric system is increasing as more and more subsystems are converted to electrical ones to improve the fuel economy by making the whole system more efficient. The capability of the existing Lundell system will soon exceed [73]. It has been predicted that power demand could be as high as 6~8 kW compared to present demand of 2~3 kW. In hybrid or electrical vehicles where propulsion is achieved with high power electric motors, power demand will be farther more. In order to cope with the increasing load, the DC bus voltage was proposed to increase from 15 to 42V. A key to make this new system economically viable is to develop an integrated starter alternator (ISA) system. A number of electrical machines have been considered for this application. The Interior Permanent Magnet machine with wide Constant Power Speed Range (CPSR) is an ideal choice [9]. Since, the segmented IPM machine can provide a very wide CPSR, it can be used for applications such as ISA. This chapter will investigate the feasibility of a segmented IPM machine as ISA of mild hybrid car. First, we will look into the requirements of an Integrated Starter Alternator system. Then, a segmented IPM machine will be optimized for this particular application. The steady-state performance of the optimized machine will also be investigated.

7.2. Integrated Starter Alternator System for automobiles

As mentioned earlier, a higher output power alternator system for the future generation car is imminent. With increase in onboard power demand, the motoring and generating requirements are gradually converging toward a common point. Therefore, it has been proposed by the various experts that the both functions should be integrated to one machine. It is not only economical but also a space saver, specially, when the machine is directly coupled to the engine. Some of the modern day mild hybrid cars such as Honda insight and Toyota Prius have already adopted ISA type system. The Fig. 7.1 shows a schematic diagram of a directly coupled ISA system.

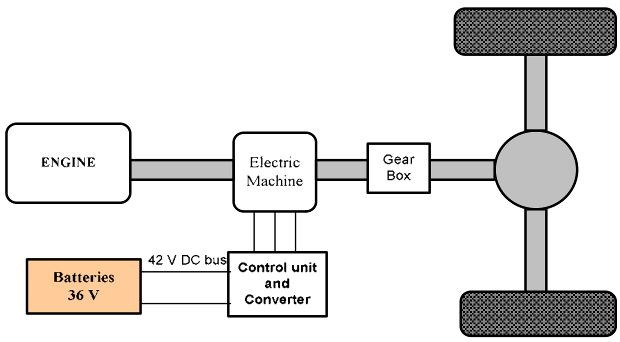

Fig. 7.1 Directly Coupled ISA system

7.2.1. Electrical Requirements of an ISA system

The specification of engine starting torque was set by the MIT/Industry consortium on advance automotive as 150 Nm or more from standstill up to 100~150 r/min engine speed. The approximate generating requirement is 4kW output power at 600 r/min of engine idle speed which will rise to 6kW and remain constant till maximum speed of

6000r/min. The minimum efficiency of the alternator system which includes electric machine and converter was set as 75% of the rated load at 1500r/min and. The transient current winding density for starting is set at 50A/mm^2 and steady state current density for generation is 20A/mm^2 provided liquid cooling will be available for the machine if required. In a dual voltage system proposed in [74] where high power loads such as ISA will be connected to a 42V DC bus and low-voltage electronics and incandescent lighting will be connected to a 14V bus so that output current requirement can be minimized. The approximated starter/alternator torque capability is shown in Fig. 7.2 which indicates that starting torque (150Nm) is significantly higher than the peak generating torque requirement (85Nm). Hence, size of the ISA machine will be predominately determined by the starting torque requirement. On the other hand, the alternator should be able to provide high power ($\geq$4kW) from the speed of 600 to 6000r/min. Thus, it requires generating power speed ratio of 10:1. In addition to these requirements, a constraint of torque ripple variation of 15% on the starting torque was also imposed to limit unwanted acoustic noise.

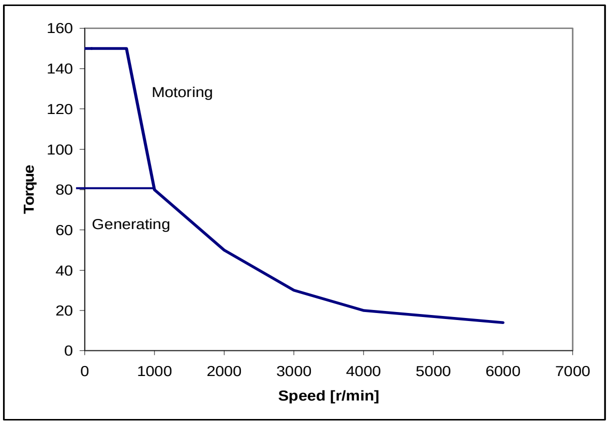

Fig. 7.2 Torque requirement of an ISA system

7.2.2. Suitable Electric Machines for ISA

The Induction machine, Switch Reluctance machine and Permanent Magnet Synchronous (both with surface permanent magnet and Interior Permanent magnet rotor) Machine are considered for the ISA applications. All these machines have their own merits and drawbacks which are tabularized as follows:

Table 7-1 Merits and demerits of three different types of electrical machines for ISA application

Types of Electric machine	Merits	Demerits
Induction Machine	Mature technology Low cost production Robust construction	Limited constant power speed range Special arrangement to extend CPSR may lead to complex and unreliable system
Switch Reluctance Machine	Robust construction Wide CPSR is possible	Because of non-sinusoidal excitation torque ripple and noise are inherent.
Permanent Magnet Synchronous Machine	Possible to achieve wide constant power speed range with Interior Permanent magnet rotor. With fractional slot concentric winding wide CPSR is also possible with SPM Zero copper loss in the rotor A compact design is achievable without compromising performance	New emerging technique. Because of rare earth magnet, the machine can be dearer than the other. Thermal degradation of magnet is a risk factor.

Although all these machines have potential for use as ISA, a detailed trade off study conducted by the MIT/Industry Consortium favoured the permanent magnet synchronous machine with interior permanent magnet rotor configuration. However, as mentioned earlier the IPM machine with conventional rotor structure shown in the Fig. 1.3(b) does not have wide CPSR.

The multilayer IPM machine and axially laminated IPM machines are capable of wide flux-weakening range. However, the significant q-axis saturation seen in these machines can cause problem during high load and speed condition [14].

In the following sections we will investigate the feasibility of the segmented IPM machine for ISA application. In favour of segmented IPM machine, it can be said that it can offer a wide CPSR with a simpler rotor configuration.

7.3. Segmented IPM machine as ISA

The predicated performance characteristic of the 6kW, 12 pole segmented IPM machine suitable for ISA application are presented in this section. The design tool used for this investigation is same as what have been used for designing the 4-pole, 550W segmented IPM machine. The circuit-coupled, time-step finite element method was used to estimate the back EMF and generated power of the machine.

The stator dimension given in the reference [75] was used in this work in order to compare the performance of the segmented IPM machine with the multilayer IPM machine designed for ISA application in [75]. The rotor geometry of the segmented IPM machine is optimized by the flow chart given in Fig. 4.6 of chapter 4. The width of the iron-bridges are optimized and found to be 1.5mm. The optimum length of the magnet in the direction of magnetization is found to be 8 mm and a bonded NdFeB with remanance 0.71 [T] is selected as the suitable magnet material. The standard electrical steel grade (Lycore 140) is selected for the stator and rotor core.

The top view of 12 pole segmented IPM machine is shown in Fig. 7.3. The major stator parameters and dimensions of the segmented IPM machine and a double magnet layer IPM machine of [75] are presented in the Table 7-2 and Table 7-3.

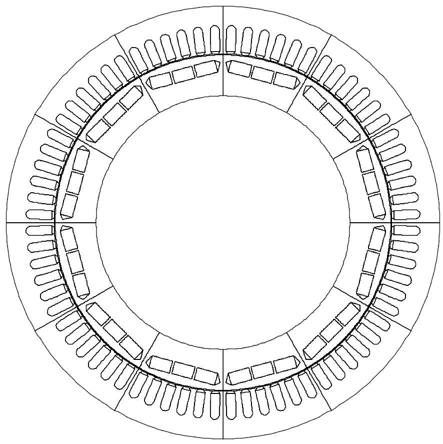

Fig. 7.3 12-pole, 6 kW Segmented Magnet IPM machine

Table 7-2 Parameter of the 12 pole, 6kW Segmented Magnet IPM machine and double magnet layer IPM machine of same rating

Item	**6 kW, 12 pole , Segmented IPM machine**	**6kW, 12 pole, double magnet layer IPM machine of [71]**
Magnet Flux-linkage(peak)	8.3 [mWb]	6.3 [mWb]
Continuous RMS rated Current	141.42 [A]	-
d-axis inductance	92.32[μH]	64.97 [μH]
q-axis inductance	242.58[μH]	305.05 [μH]
Peak Torque at 150r/min	139.8 [Nm]	150 [Nm]

Table 7-3 Dimensions of the 12 pole, 6kW Segmented IPM machine and double magnet layer IPM machine of same rating

Item	**6 kW, 12 pole , Segmented IPM machine**	**6kW, 12 pole, double magnet layer IPM machine of [71]**
Number of Poles	12	12
Number of phase	3	3
Number of slots	72	72
Series turn	24	24
Magnet Remanance Flux-density	0.71 [T]	0.38[T]
Iron bridge thick ness	1.5 [mm]	-
Stator outer diameter	217.7[mm]	217.7[mm]
Active length	60 [mm]	60[mm]
Rotor outer Radius	108.4[mm]	108.4[mm]
Rotor Inner Radius	83.1[mm]	83.1[mm]
Air gap length	0.60[mm]	0.635[mm]
Air gap radius	109[mm]	109[mm]
Winding factor	0.933[mm]	0.9224[mm]
Thickness of the magnet	8[mm]	Inner magnet 2.9[mm], Outer magnet 5.7[mm]
Magnet Span	120 [Elec. deg]	Inner magnet 86.28[Elec. deg], Outer magnet 140.8 [Elec. deg]

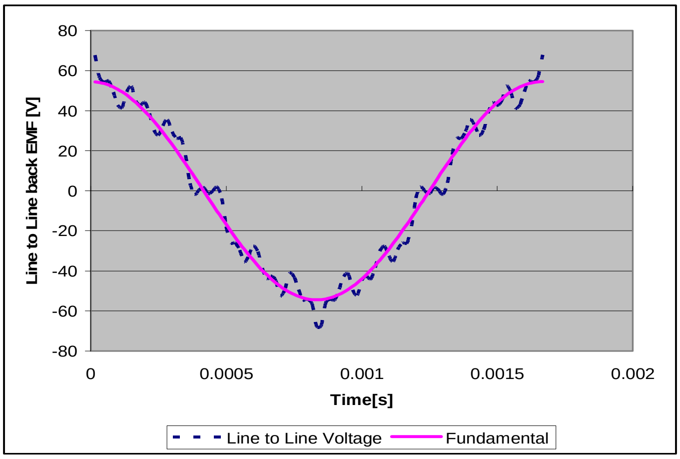

Fig. 7.4 Line to line back EMF at 6000 r/min

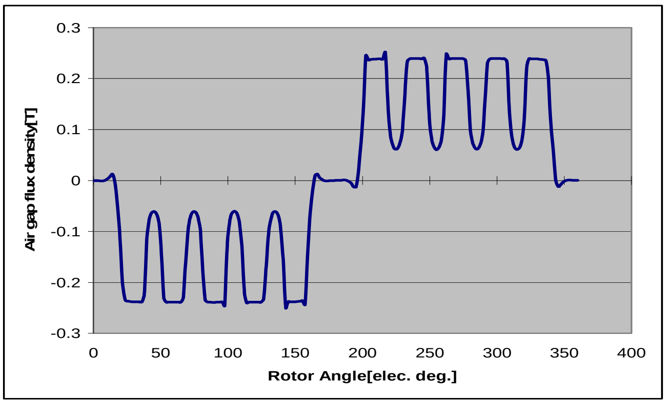

Fig. 7.5 Air-gap flux density at open circuit

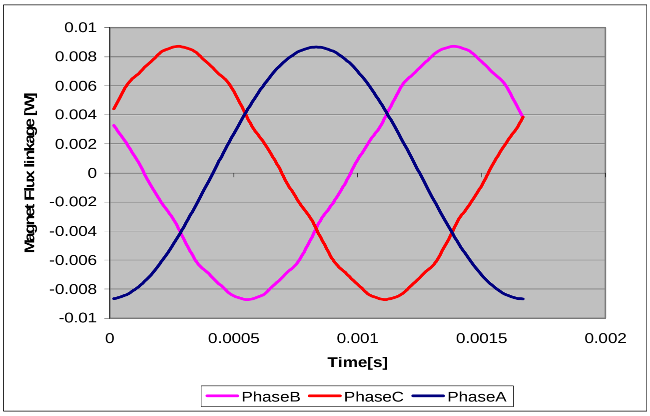

Fig. 7.6 Three-phase flux-linkages of the magnet at open circuit

Considering the constraints on the maximum allowable back EMF as discussed in section 4.2.1, allowable maximum flux linkage for 12-pole machine from the (4.3) is found to be 8.3 [mWb]. The predicated back EMF and its fundamental at 6000r/min are shown in the Fig. 7.4. The predicted air gap flux density produced by the magnet over one pole pair is shown in Fig. 7.5. The slotting effects are also indicated in the flux-density wave form. The magnet flux linkages for three phases are presented in the Fig. 7.6.

The other two crucial machine parameter d- and q-axis inductances are also estimated in the finite element model. The variation of these two parameters with current is presented in the Fig. 7.7. In this calculation effect of cross-coupling is assumed negligible. As current increases both the inductances reduces. The rates of reduction in both the inductances are nearly equal which means a constant ratio of q-axis to d-axis inductances is maintained.

The cogging torque of the machine was calculated in the finite element by the method discussed in the section 4.5. The predicted cogging torque over two slot pitches is shown in the Fig. 7.8. The peak cogging torque is approximately 0.8 Nm which is less than 2% of the rated continuous torque.

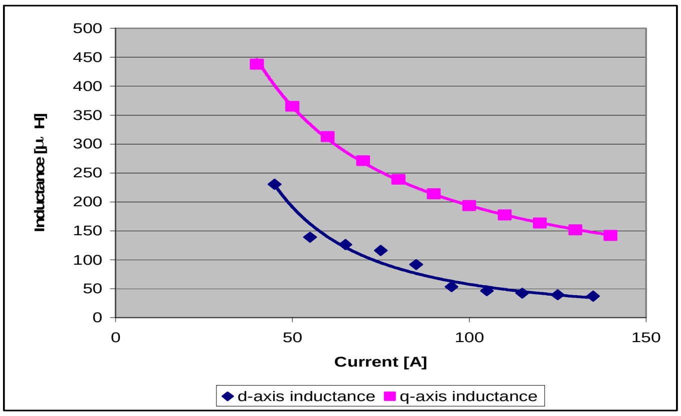

Fig. 7.7 d- and q-axis inductances variation

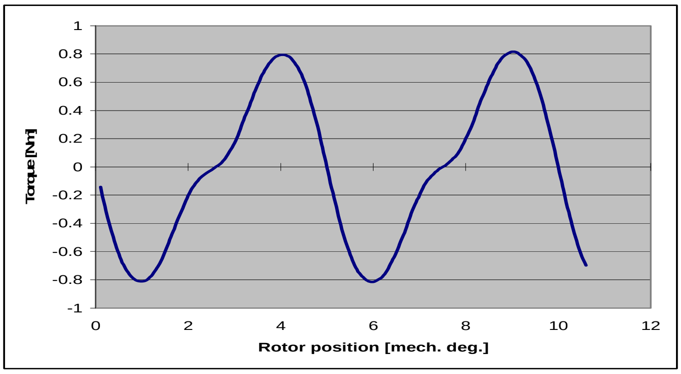

Fig. 7.8 Cogging torque

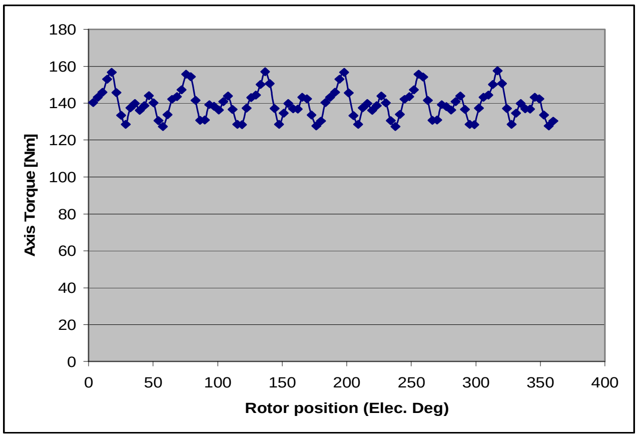

Fig. 7.9 Developed Torque at 150r/min during motoring (Current limit: 424.3Arms and voltage limit: 18.9 V)

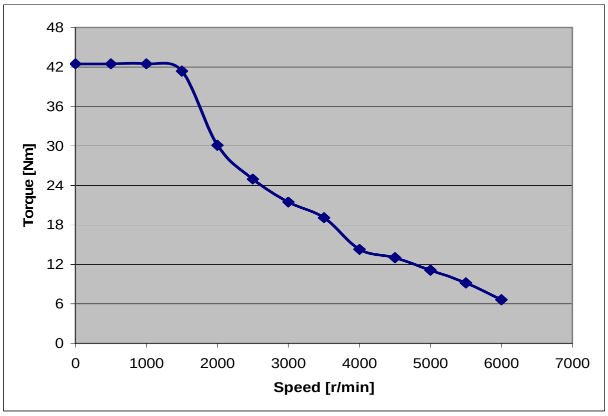

Fig. 7.10 Torque-Speed Envelope during generation

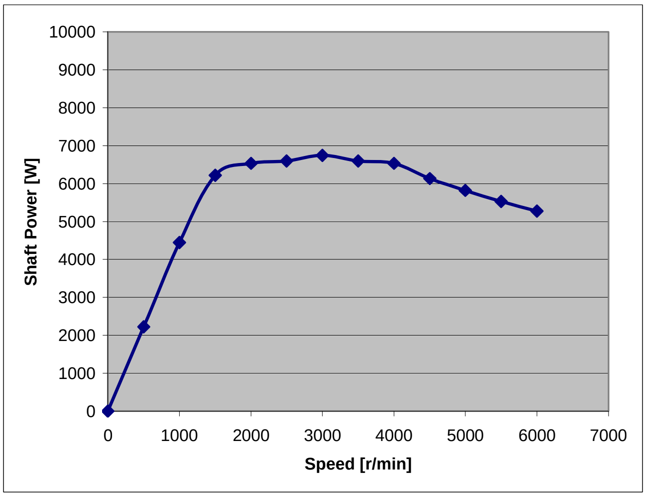

Fig. 7.11Predicted Power Capability curve

During starting, the ISA machine work as a motor which is fed from the 42 V DC bus of the system. The torque developed in the segmented IPM motor with stator excitation limited by the 42V DC bus and with the current limited to 424.3A rms at 150r/min is shown in Fig. 7.9. The rated continuous torque-speed envelope and power capability of the segmented IPM machine for generation is also estimated. Both these curves are shown in Fig. 7.10 and Fig. 7.11 respectively. The constant torque is available up to around 1200 r/min and above this speed constant power operation starts that needs the flux-weakening control.

The table 7-4 shows a comparison of performances between the proposed segmented IPM machine and the double magnet layer IPM machine of [75]. It can be noted here that the performance of the segmented IPM machine is comparable, although not better than the double layer IPM machine. It can be concluded from this study that the performance comparable to a multi-layer IPM machine is achievable with the single magnet layer IPM machine when segmentation technique is applied to it.

Table 7-4: Comparison of performance between the 6 kW, 12 pole segmented IPM machine and the double magnet layer IPM machine of [71]

Item	**6 kW, 12 pole , Segmented IPM machine**	**6kW, 12 pole, double magnet layer IPM machine of [71]**
Required stator current to achieve 150 Nm during starting	424[A rms]	327[A rms]
Speed at which 4 kW can be reached during generation	1000 [r/min]	600 [r/min]
Torque ripple when producing 150 Nm	13.33%	<10%
Cogging torque (peak)	0.8 [Nm]	-
Maximum back EMF at 6000 r/min	38.52 [$V_{L\text{-}L\ RMS}$]	23.9[$V_{L\text{-}L\ RMS}$]

7.4. Conclusion

This chapter presents a design of a 12 pole, 6kW segmented IPM machine that can be considered for applications such as Integrated Starter Alternator of automobiles. The various machine parameters estimated and predicted performance capabilities are presented. The construction of the machine and experimental verification of these results will be taken as future work of this project.

CHAPTER 8

8. Conclusion of the Thesis and Suggestion for future work

8.1. Conclusion

The extension of the constant power operation region of a permanent magnet machine by various design approaches has been a topic of fervent research for last couple of decades. The main objective of this work was to develop an IPM machine with wide constant power speed range. A detailed investigation on the mechanism of flux-weakening in the IPM machine has led to the concept of segmenting the rotor magnet poles which gives an inherent flux-weakening capability to the IPM rotor so that a wide constant power speed range can be achieved. The machine designed with 'segmented magnet concept' is referred in this work as the Segmented IPM machine. This work reports the design optimization and performance analysis of a prototype Segmented IPM machine which employs distributed windings in contrast to fractional slot concentrated windings which have hitherto been used for achieving wide CPSR in the surface permanent magnet machines.

The thesis start with a review of the IPM machine technology and the problems associated with achieving wide constant power speed in such machine. The concept of segmentation of magnet pole to provide inherent capability of flux-weakening to the rotor of IPM machine was introduced.

Advancement in numerical techniques make it possible to optimize the design of an electric machine according to preset criteria and predict the performance beforehand so that any design misjudgments can be rectified. The proposed machine was first evaluated conceptually using numerical techniques as reported in the chapter 4. In order to give a full meaning to this evaluation, the numerical techniques used in this work such as finite element analysis, time-step and circuit coupled finite element analysis were reviewed in chapter 3. Chapter 4 presents the design optimization of the proto-type Segmented IPM machine for application in 42 V PowerNet environment of automobile. The crucial machine parameters such as magnet flux-linkage, d- and q-axis inductances, the developed cogging torque and variation of core loss with frequencies were estimated. The estimated parameters were used for prediction of performance analysis which was later verified by the experimental results.

Due to its simplicity and constant switching frequency, PWM current control is widely used in the IPM machine drive systems. The vector current control is generally implemented in the synchronously rotating frame for high accuracy and for ease of implementation of the control algorithm. The control trajectories in terms of d- and q-axis components of the stator current, the maximum torque per ampere (MTPA) control technique of constant torque operation region and flux-weakening control technique of constant power region used in the IPM machine drive are reviewed in the chapter 5. In order to conduct a thorough investigation of the steady-state and transient performance of the Segmented IPM machine drive system under current controlled PWM system, a mathematical model of the drive system with a PWM inverter was developed in MATLAB-SINULINK. All the simulated results were later verified by experiments.

A proto-type segmented IPM machine was built on the basis of design optimization presented in the chapter 4. An experimental test bench of the Segmented IPM machine drive system was set up. The detailed description of hardware and DSP based real time implementation of current vector control of the Segmented IPM machine were presented in the appendix E.

For experimental verification, the steady-state and transient performance of the machine were measured and compared with the predicted ones and found to be in good agreement. The experimental and predicted performance analysis of the Segmented IPM machine clearly shows that a wide constant power speed range (CPSR) is possible in this type of machine. Due to the inherent flux-weakening capability of the rotor, unlike other IPM machines, a very high ratio of L_q/L_d is not crucial to achieve wide CPSR. The rotor structure of the Segmented IPM machine is very similar to that of commercially available IPM machines. Hence, it is easy to construct and cost-effective.

The performance of the segmented IPM rotor was also compared to a conventional non-segmented IPM rotor. For direct comparison same stator was used in the both machines. It was clear form the comparative analysis that the Segmented IPM rotor can offer a far wider CPSR. The developed cogging torque is almost 5 times in the segmented design. The increase of the core loss with high frequency was also found to be less in the Segmented IPM machine. However, the developed torque of the Segmented IPM machine was lower than that of the IPM machine-I due to magnet flux canalization and lower remanance of the magnets.

A 6 kW and 12 poles Segmented IPM machine was also investigated for application as Integrated Starter Alternator (ISA) in automobiles. It has been proposed in this work to use this preliminary design to construct the ISA machine for a future project.

It is felt that the segmented IPM design should be a good contender for other applications such as in traction where a wide CPSR is inherently required.

8.2. Suggestion for future work

In this work, during motoring operation of the Segmented IPM machine it has been seen that for the speed above 5000r/min, the PWM inverter requires over-modulation. Since PWM generated by the slave DSP of the DS1104 was used, the over-modulation requirement could not be facilitated. Using additional hardware, FPGA generated PWM can be used so that a SVM with over-modulation technique can be applied.

A feed-forward vector control was implemented in this work where variations of machine parameters were ignored. In the Segmented IPM machine, the magnet flux-linkage is no longer constant, especially during flux-weakening. An improved control technique can be developed to incorporate the variation of the magnet flux-linkage and other machine parameters. The performance of the machine with sensor-less and direct torque control (DTC) can also be investigated.

The effect of magnetic saturation on the performance of control algorithms has not been investigated during this study. More study should be undertaken to investigate the effect of saturation on the controllers.

Due to the mechanical speed limitation, the Segmented Magnet IPM machine was operated up to 7800r/min. The performance analysis of the machine at speed higher than this may be taken in the future. Since, the Segmented Magnet IPM machine shows a considerable reduction in the cogging torque without any skewing, its performance in low speed operation may also be investigated.

A preliminary investigation of a 6 kW, 12pole Segmented Magnet IPM machine for ISA application was initiated in the work. The construction of this prototype machine and development of a 6kW ISA system was suggested for a future project.

Some of the recent preliminary studies indicate that stator with concentrated windings could be a better option for the PM machine when a very wide CPSR is required. However, the concentrated winding will reduce back emf because of lower winding factor and will also decrease saliency ratio by increasing d-axis inductance in the IPM machine. On the other hand, the optimum flux-weakening condition may be achieved by using properly designed concentrated windings. In other word, the concentrated winding may give some design flexibility to achieve wide CPSR in the IPM machine. Therefore, the IPM machine with concentrated windings needs a detailed investigation. It will be interesting to investigate the performance of the segmented IPM rotor (which has an inherent flux-weakening capability) with a concentrated winding stator.

REFERENCES

[1] S. Y. R. Hui, J. G. Zhu, and V. S. Ramsden, "A Generalized Dynamic Circuit Model of Magnetic Cores for Low- and High-Frequency Applications-Part II: Circuit Model Formulation and Implementation," *IEEE Transaction on Power Electronics*, Vol. 11, No. 2, pp. 251, 1996.

[2] P. B. Zhou, *Numerical Analysis of Electromagnetic fields*. New York: Springer-Verlag, 1993.

[3] M. V. K. Chari and S. J. Salon, *Numerical Methods in Electromagnetism*: Academic Press, A Harcourt Science and Technology Company, 2000.

[4] K. Hameyer, J. Driesen, H. De Gersem, and R. Belmans, "The classification of coupled field problems," *Magnetics, IEEE Transactions on*, Vol. 35, No. 3, pp. 1618-1621, 1999.

[5] S. J. Salon, R. Palma, and C. C. Hwang, "Dynamic modeling of an induction motor connected to an adjustable speed drive," *Magnetics, IEEE Transactions on*, Vol. 25, No. 4, pp. 3061, 1989.

[6] H. n. Phyu, "Numerical Analysis of Brushless Permanent Magnet DC Motor Using Couple Systems," PhD Thesis, Department of Electrical and Computer Engineering, National University of Singapore,2004

[7] S. W. Moore, K. M. Rahman, and M. Ehsani, "Effect on Vehicle Performance of Extending the Constant Power Region of Electric Drive Motors," in *International Congress and Exposition*. Detroit, Michigan, 1999.

[8] Z. Rahman, K. L. Butler, and M. Ehsani, "Effect of Extended-Speed, Constant-Power Operation of Electric Drives on the Design and Performance of EV-HEV Propulsion System," in *Future Car Congress*. Arlington, Virginia, USA, 2000.

[9] E. C. Lovelace, T. M. Jahns, J. L. Kritley Jr., and J. H. Lang, "An Interior PM Starter/Alternator for Automotive Aplications," presented at *International Conference on Electric machines(ICEM'98)*, Istanbul, Turkey,Sept 2-4, 1998 Vol. 1, pp.

[10] T. M. Jahns, "Flux-Weakening Regime Operation of an Interior Permanent Magnet Synchronous Motor Drive," *IEEE Transaction on Industry Applications*, Vol. IA-23, No., pp. 681-689, 1987.

[11] R. Schiferl and T. A. Lipo, "Power Capability of Salient Pole Permanent Magnet Synchronous Motor In Variable Speed Drive Applications," *IEEE Transaction on Industry Applications*, Vol. IA-26, No. 1, pp. 115-123, 1990.

[12] W. L. Soong and N. Ertugrul, "Field-weakening performance of interior permanent-magnet motors," *Industry Applications, IEEE Transactions on*, Vol. 38, No. 5, pp. 1251 - 1258, 2002.

[13] W. L. Soong, D. A. Staton, and T. J.E.Miller, "Design of a New Axially-Laminated Interior Permanent Magnet Motor," *IEEE Transaction on Industry Applications*, Vol. 31, No. 2, pp. 358-367,March/April, 1995.

[14] E. C. Lovelace, T. M. Jahns, J. Wai, T. Keim, J. H. Lang, D. D. Wentzloff, F. Leonardi, and J. M. Miller, "Design and Experimental Verification of a Direct-Drive Interior PM Synchronous Machine Using a Saturable Lumped-Parameter Model.," presented at *Industry Applications*

Conference, 2002. 37th IAS Annual Meeting, 13-18 Oct., 2002 Vol. 4, pp. 2486-2492.

[15] A. M. El-Refaie, T. M. Jahns, P. J. McCleer, and J. W. McKeever, "Experimental verification of optimal flux weakening in surface PM Machines using concentrated windings," *Industry Applications, IEEE Transactions on*, Vol. 42, No. 2, pp. 443 - 453, 2006.

[16] H. Satoh, S. Akutsu, T. Miyamura, and H. Shinoki, "Development of Traction Motor for Fuel Cell Vehicle," presented at *2004 SAE world congress*, Detroit, Michigan, 2004 Vol., pp.

[17] Y. Honda, T. Nakamura, T. Higaki, and Y. Takeda, "Motor Design Consideration and Test Results of an Interior Permanent Magnet Synchronous Motor for Electrical Vehicles," presented at *Annual Meeting IEEE Industry Applications Society*, New Orleans,October 5-9, 1997 Vol., pp. 75-82.

[18] N. Bianchi and S.Bolognani, "Performance Analysis of An IPM Motor with Segmented Rotor for Flux-Weakening Application," presented at *International Conference on Electrical Machine and Drives, Nineth*, 1999 Vol., pp. 49-53.

[19] B. ˇStumberger, M. Anton Hamler, M. Trlep, and M. Jesenik, "Analysis of Interior Permanent Magnet Synchronous Motor Designed for Flux Weakening Operation," *IEEE Transaction on Magnetics*, Vol. 37, No. 5, pp. 3644-3647,September, 2001.

[20] T. J. E. Miller, *Brushless Permanent-Magnet and Reluctance Motor Drives*. Oxford: Clarendon Press, 1989.

[21] J. F. Gieras and M. Wing, *Permanent Magnet Motor Technology, Design and Applications*, 2nd ed. New York, Basel: Marcel Dekker Inc., 2002.

[22] P. Beckley, *Electrical Steel for rotation machines*. London: Institute of Electrical Engineers, 2002.

[23] B. K. Bose, "A High-Performance Inverter-Fed Drive System of an Interior Permanent Magnet Synchronous Machine," *IEEE Transaction on Industry Applications*, Vol. 24, No. 6, pp. 987-997,Nov/Dec, 1988.

[24] B. K. Bose, Power Electronics and Variable Frequency Drives *Technology and Applications*. Piscataway, NJ: IEEE Press, 1997.

[25] S. Morimoto, M. Sanada, and Y. Takeda, "Wide-Speed Operation of Interior Permanent Magnet Synchronous Motors wiht High-Performance Current Regulator," *IEEE Transaction on Industry Applications*, Vol. 30, No. 4, pp. 920-926,July/August, 1994.

[26] T. M. Jahns, G. B. Kliman, and T. W. Neumann, "Interior Permanent-Magnet Synchronous Motors for Adjustable-Speed Drives," *IEEE Transaction on Industry Applications*, Vol. IA-22, No. 4, pp. 738-747,July/August, 1986.

[27] L. Zhong, "High Performance Torque and Field Weakening Controllers for Interior Permanent Magnet Synchronous Motors," PhD Thesis, School of Electrical Engineering and Telecom, University of New South Wales,1999

[28] M. E. Haque, L. Zhong, and M. F. Rahman, "A sensorless speed estimator for application in a direct torque controller of an interior permanent magnet synchronous motor drive, incorporating compensation of offset error," 2002 Vol. 1, pp. 276 - 281.

[29] H. Jung-Ik, K. Ide, T. Sawa, and S. Seung-Ki, "Sensorless rotor position estimation of an interior permanent-magnet motor from initial states," *Industry Applications, IEEE Transactions on*, Vol. 39, No. 3, pp. 761, 2003.

[30] J. Ji-Hoon, H. Jung-Ik, M. Ohto, K. Ide, and S. Seung-Ki, "Analysis of permanent-magnet machine for sensorless control based on high-frequency signal injection," *Industry Applications, IEEE Transactions on*, Vol. 40, No. 6, pp. 1595 - 1604, 2004.

[31] P. Guglielmi, M. Pastorelli, G. Pellegrino, and A. Vagati, "Position-sensorless control of permanent-magnet-assisted synchronous reluctance motor," *Industry Applications, IEEE Transactions on*, Vol. 40, No. 2, pp. 615 - 622, 2004.

[32] R. S. MacMinn and T. M. Jahns, "Control Technique for Improved High Speed Performance of Interior PM Synchronous Motor Drives," *IEEE Transaction on Industry Applications*, Vol. 27, No. 5, pp. 997-1004,September/October, 1991.

[33] G. R. Slemon, "Achieving a Constant Power Speed Range for PM Drives," *IEEE Transaction on Industry Applications*, Vol. 31, No. 2, pp. 368-372,March/April, 1995.

[34] E. C. Lovelace, T. M. Jahns, J. L. K. Jr., and J. H. Lang, "An Interior PM Starter/Alternator for Automotive Application," in *International Conference on Electric Machines*. Istanbul, Turkey, 1998.

[35] W. L. Soong and T. J. E. Miller, "Field-weakening performance of brushless synchronous AC motor drives," *Electric Power Applications, IEE Proceedings-*, Vol. 141, No. 6, pp. 331 - 340, 1994.

[36] Y. Honda, T. Higaki, S. Morimoto, and Y. Takeda, "Rotor Design Optimisation of Multi-Layer Interior Permanent-Magnet Synchronous Motor," *IEEE Proceedings on Electrical Power Application*, Vol. 145, No. 2, pp. 119-124,March, 1998.

[37] E. C. Lovelace, T. M. Jahns, and J. H. Lang, "A Saturating Lumped-Parameter Model for an Interior PM Synchronous Machine," *IEEE Transaction on Industry Applications*, Vol. 38, No. 3, pp. 645-650,May/June, 2002.

[38] R. Dutta and M. F. Rahman, "A New Rotor Design of IPM machine suitable for wide speed range," in *The 29th Annual Conference of the IEEE Industrial Electronics Society (IECON 2003)*. Roanoke, Virginia, USA, 2003.

[39] S. L. Ho, H. L. Li, W. N. Fu, and H. C. Wong, "A novel approach to circuit-field-torque coupled time stepping finite element modeling of electric machines," *Magnetics, IEEE Transactions on*, Vol. 36, No. 4, pp. 1886 - 1889, 2000.

[40] J. R. Brauer, *What every engineer should know about finite element analysis*. New York: New York: Marcel Dekker, c., 1993.

[41] P. P. Silvester and R. L. Ferrari, *Finite Elements for electrical engineers*, 3rd ed: Cambridge University Press, 1996.

[42] CEDRAT, "Flux 9.1 User's Guide Vol. 3," 2005.

[43] J. R. Brauer, ed, What every Engineer Should Know about Finite Element Analysis. New York: Marcel Dekker, 1998.

[44] CEDRAT, "Flux 9.1 User's Guide Vol. 2," 2005.

[45] C.-M. Ong, Dynamic Simulation of Electric Machinery using MATLAB/SIMULINK: Prentice-Hall, Inc, 1998.

[46] P. Zhou, M. A. Rahman, and M. A. Jabbar, "Field circuit analysis of permanent magnet synchronous motors," *Magnetics, IEEE Transactions on*, Vol. 30, No. 4, pp. 1350 - 1359, 1994.

[47] B.-H. Bae and S.-K. Sul, "Practical design criteria of interior permanent magnet synchronous motor for 42V integrated starter-generator," presented at *Electric Machines and Drives Conference, 2003. IEMDC'03. IEEE International*,1-4 June 2003, 2003 Vol. 2, pp. 656 - 662.

[48] K. Yamazaki and Y. Seto, "Iron Loss Analysis of Interior Permanent Magent Synchronous Motors- Variation of Main Loss Factors Due to Driving Condition," presented at *International Electrical Machine and Drive Conference(IEMDC 05)*, San Antonio, USA, 2005 Vol., pp. 1633-1638.

[49] L. Ma, M. Sanada, S. Morimoto, and Y. Takeda, "Prediction of Iron Loss in Rotating Machine with Rotational Loss Included," *IEEE Transaction on Magnetics*, Vol. 39, No. 4, pp. 2036-2041,July, 2003.

[50] J. F. Gieras, E. Santini, and M. Wing, "Calculation of synchronous reactances of small permanent-magnet alternating-current motors: comparison of analytical approach and finite element method with measurements," *Magnetics, IEEE Transactions on*, Vol. 34, No. 5, pp. 3712 - 3720, 1998.

[51] R. H. Engelmann and W. H. Middendorf, *Handbook of electric motors*: New York: M. Dekker, 1995.

[52] L. Chang, "An Improved FE Inductance Calculation for Electrical machines," *IEEE Transaction on Magnetics*, Vol. 32, No. 4, pp. 3237-3245,July, 1996.

[53] D. Pavlik, V. K. Garg, J. R. Repp, and J. Weiss, " A Finite Element Technique for calculating the magnet sizes and inductances of Permanent magnet machines," *IEEE Transaction on Energy Conversion*, Vol. 3, No. 1, pp. 116-122.,March, 1988.

[54] B. ˇStumberger, G. ˇStumberger, D. Dolinar, A. Hamler, and M. Trlep, "Evaluation of Saturation and Cross-Magnetization Effects in Interior Permanent-Magnet Synchronous Motor," *IEEE Transaction on Industry Applications*, Vol. 39, No. 5, pp. 1264-1271,September/October, 2003.

[55] C. Studer, A. Keyhani, T. Sebastian, and S. K. Murthy, "Study of cogging torque in permanent magnet machines," presented at *Thirty-Second IAS Annual Meeting, IAS '97.*, New Orleans, LA,5-9 Oct., 1997 Vol. 1, pp. 42 - 49.

[56] G. R. Slemon and X. Liu, "Core Losses in Permanent Magnet Motors," *IEEE Transaction on Magnetics*, Vol. 26, No. 5, pp. 1653-1 655,September, 1990.

[57] J. G. Zhu and V. S. Ramsden, "Improved Formulations for Rotational Core Losses in Rotating Electrical Machines," *IEEE Transaction on Magnetics*, Vol. 34, No. 4, pp. 2234-2242,July, 1998.

[58] F. Deng, "An Improved iron loss estimation for permanent magnet brushless machines," *IEEE Transaction on Energy Conversion*, Vol. 14, no.4, No., pp. 1391-1395,December, 1999.

[59] N. Stranges and R. D. Findlay, " Importance of Rotational Iron Loss Data for Accurate Prediction of Rotating Machine Core Losses," presented at *Annual Meeting of Industry Applications Society*, 2-6 October, 1994 Vol. 1, pp. 123 - 127.

[60] K. Atallah, Q. Z. Zhu, and D. Howe, "An Improved Method for Predicting Iron Losses in Brushless Permanent Magnet DC Drives," *IEEE Transaction on Magnetics*, Vol. 28, No. 5, pp. 2997-2999,September, 1992.

[61] C. Mi, M. Filippa, W. Liu, and R. Ma, "Analytical Method for Predicting the Air-Gap Flux of Interior-Type Permanent-Magnet Machines," *IEEE Transaction on Magnetics*, Vol. 4, No. 1, pp. 50-58, 2004.

[62] Z. Q. Zhu, Y. S. Chen, and D. Howe, "Iron Loss in Permanent-Magnet Brushless AC Machines Under Maximum Torque Per Ampere and Flux Weakening Control," *IEEE Transaction on Magnetics*, Vol. 38, No. 5, pp. 3285-3287,Sept, 2002.

[63] F. Fernandez-Bernal, A. Garcia-Cerrada, and R. Faure, "Determination of Parameters in Interior Permanent-Magnet Synchronous Motors With Iron Losses Without Torque Measurement," *IEEE Transaction on Industry Applications*, Vol. 37, No. 5, pp. 1265-1272,September/October, 2001.

[64] B. ˇStumberger, A. Hamler, and B. Hribernik, "Analysis of Iron Loss in Interior Permanent Magnet Synchronous Motor Over a Wide-Speed Range of Constant Output Power Operation," *IEEE Transaction on Magnetics*, Vol. 36, No. 4, pp. 1846-1849,July, 2000.

[65] G. Bertotti, A. Boglietti, M. Chiampi, D. Chiarabaglio, F. Fiorillo, and M. Lazzari, "An Improved Estimation of Iron Losses in Rotationg Electrical

Machines," *IEEE Transaction on Magnetics*, Vol. 27, No. 6, pp. 5007-5009,November, 1991.

[66] D. W. Novotny and T. A. Lipo, *Vector Control and Dynamics of AC Drive*. New York: Oxford University Press, 1996.

[67] J. Wai and T. M. Jahns, "A New Control Technique for Achieving Wide Constant Power Speed Operation with an Interior PM Alternator Machine," presented at *Industry Applications Conference, Thirty-Sixth IAS Annual Meeting*,30 Sept.-4 Oct, 2001 Vol. 2, pp. 807-814.

[68] S. Morimoto, Y. Takeda, T. Hirasa, and T. Katsunori, "Expansion of Operating Limits for Permanent Magnet by Current Vector Control Considering Inverter Capacity," *IEEE Transaction on Industry Applications*, Vol. 26, No. 5, pp. 866-871,September/October, 1990.

[69] P. Vas, *Vector Control of AC Machines*: Clarendon Press, Oxford, 1990.

[70] Z. X. Fu, J. Xiang, W.C. Reynolds, and B. Nefcy, "Vector Control of An IPM Synchronous Machine Capable of Full Range Operations For Hybrid Electric Vehicle Application," 2003 Vol., pp. 1443-1450.

[71] CEDRAT, "Flux9.1 2D Application: Use's guide Vol.4," 2005.

[72] Standards, " IEEE Guide: Test Procedure for Synchronous Machines," 1983.

[73] K. Bolenz, "Design modifications of the electrical system to use intermittent engine operation," presented at *Machines for Automotive Applications (Digest No. 1996/166), IEE Colloquium on*,4 Nov, 1996 Vol. 2, pp. 1 - 7.

[74] J. G. Kassakian, H. C. Wolf, J. M. Miller, and C. J. Hurton, "Automotive electrical systems circa 2005," *Spectrum, IEEE*, Vol. 33, No. 8, pp. 22-27,August, 1996.

[75] A. M. El-Refaie and T. M. Jahns, "Application of bi-State magnetic material to an automotive IPM starter/alternator machine," *Energy Conversion, IEEE Transactions on*, Vol. 20, No. 1, pp. 71, 2005.

APPENDIX A

A. Ratings and Parameters of the IPM machines Used in this Study

Table A-1 Parameters of the prototype Segmented IPM machine

Phase Voltage (rms)	20.2 [V]
Phase Current(rms)	12 [A]
Rated Power	550 [W]
d-axis inductance L_d	1.96 [mH]
q-axis inductance L_q	3.47 [mH]
Magnet flux linkage ψ_{mag}	0.0194 [Wb]
Stator Resistance R	0.1641[O]
Base Speed ω_b	1750 [r/min]
Number of poles P	4

Table A-2. Parameter of the IPM machine-I in the low voltage system

Phase Voltage (rms)	20.2 [V]
Phase Current (rms)	14[A]
Rated Power	550[W]
d-axis Inductance L_d	2.894 [mH]
q-axis inductance L_q	3.626 [mH]
Magnet Flux-linkage ψ_{mag}	0.04623 [Wb]
Stator Resistance R	0.1641[ohm]
Base Speed ω_b	1450 [r/min]
Number of poles P	4

APPENDIX B

B. Main Dimensions of the prototype IPM Machines

Table B-1 Main dimensions of the Segmented Magnet IPM Machine

Stator bore diameter	82 [mm]
Stator outer diameter	130[mm]
Rotor diameter	81[mm]
Shaft diameter	24 [mm]
Air gap length	0.5 [mm]
No. of slots	24
Slot height	11.45[mm]
Slot width	5.3[mm]
Slot opening	2.5[mm]
Magnet length	4 [mm]
Magnet Segment width	13 [mm]
Magnet Span	134^0 [Elec. deg]
Width of iron bridge	2 [mm]
Dimension of flux guide	4.2 $\times$4[mm^2]
Effective axial length	55[mm]
Winding type	Double layers distributed
No. of series turns per phase	46
Winding factor	0.933
Rotor core material	Lycore 140 (Lamination thickness 35 mm, maximum loss 9W/kg at 50Hz)
Stator core material	Standard Electrical Steel
Permanent magnet material	Bonded NdFeB(BN 12, B_r: 0.69~0.78 T)

Table B-2 Main dimensions of the IPM Machine-I

Stator bore diameter	82[mm]
Stator outer diameter	130[mm]
Rotor diameter	81[mm]
Shaft diameter	24[mm]
Air gap length	0.5 [mm]
No. of slots	24
Slot height	11.45[mm]
Slot width	5.3[mm]
Slot opening	2.5[mm]
Magnet width	34[mm]
Magnet length	8 [mm]
Magnet Span	125^{0} [Elec. deg.]
Dimension of flux guide	diameter 1.2 [mm]
Effective axial length	55 [mm]
Number of poles	4
Winding type	Double layers distributed
No. of series turns per phase	46
Winding factor	0.933
Rotor core material	Non-linear steel (solid core)
Stator core material	Standard Electrical Steel
Permanent magnet material	Sintered NdFeB [N30, Br:1.02~1.06T]

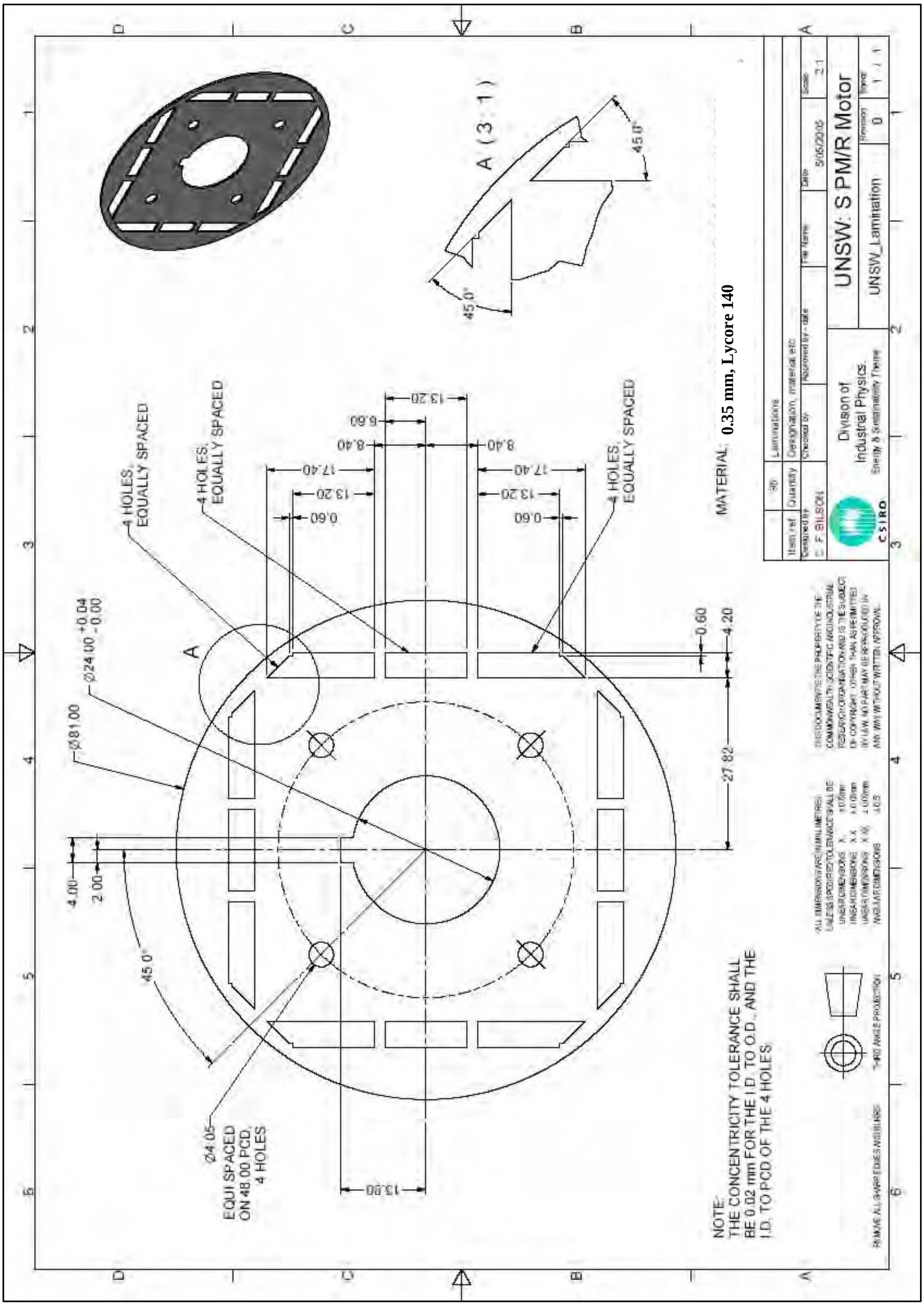

Fig. B.1 Detailed dimensions of the rotor lamination

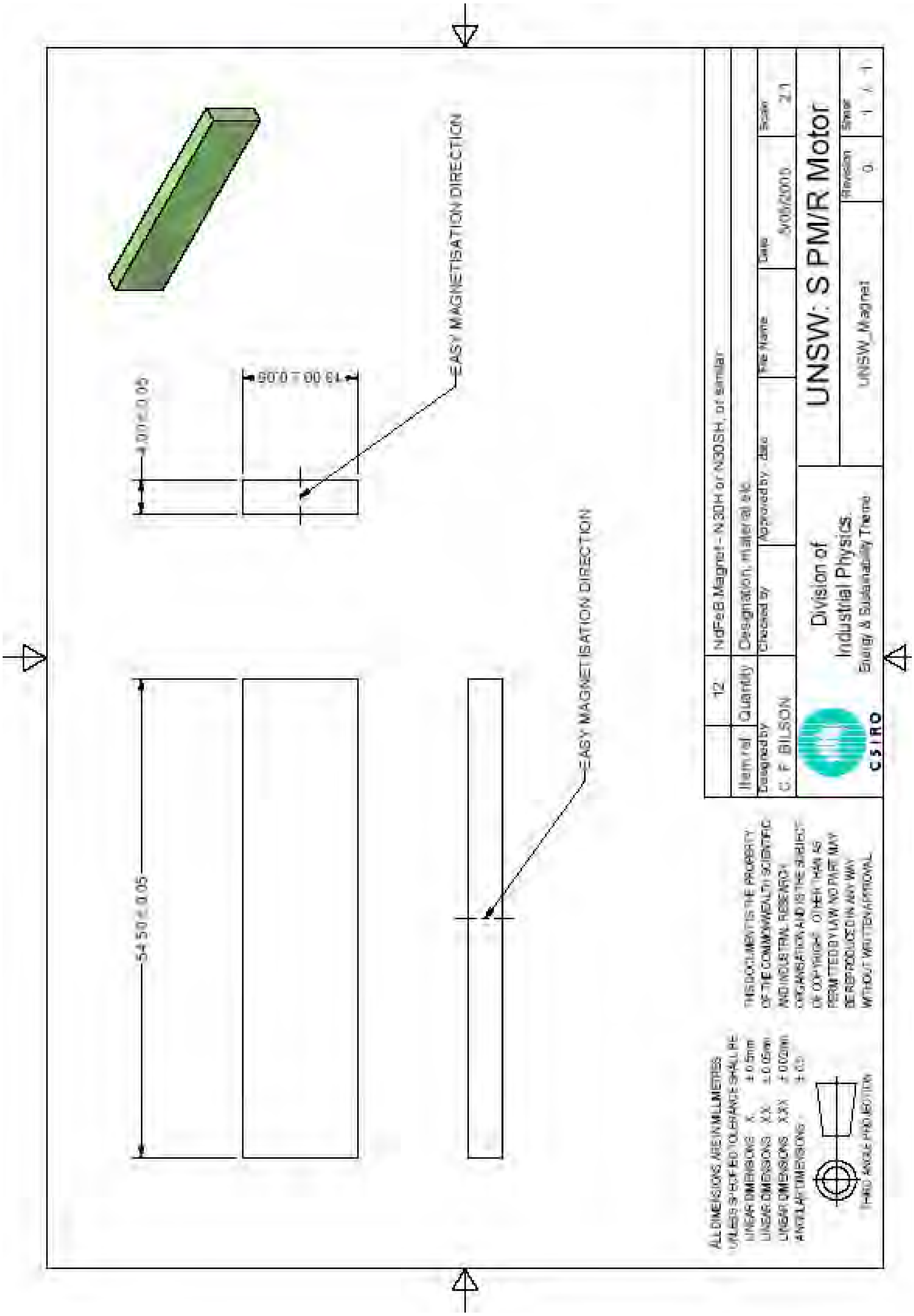

Fig. B.2 Dimensions of the magnet segments

APPENDIX C

C. Measurement of d- and q-axis inductances

The precise knowledge of the d- and q-axis inductances of the IPM machine is needed to design controller and also to develop mathematical model for performance analysis. The d- and q-axis inductances are given as,

$$L_d = L_{dm} + L_{lk} \tag{C.1}$$

$$L_q = L_{qm} + L_{lk} \tag{C.2}$$

where, L_{dm}, L_{qm} are the magnetizing inductances and L_{lk} is the leakage inductance.

A number of different methods are available in the literature to measure d- and q-axis inductances of a salient pole synchronous machine. These methods can be classified into two board categories depending on the operating condition of the machine – (a) Standstill test and (b) Running test. Although conventional running tests are considered to be more accurate, it requires zero rotor fields, which means removal of the permanent magnets from the rotor during the test. The physical removal of the magnets is not possible in the IPM machine. The Standstill tests do not require the removal of magnets and are much easier to perform in a test bench.

There are many different standstill tests available for salient pole machines, such as DC bridge test, the instantaneous flux linkage test, standstill torque test and

AC standstill test. Among them the AC standstill test is the easiest to perform in laboratory environment and yields fairly accurate values of inductance. Hence, it is widely used to measure L_d and L_q of the IPM machine.

In this method, d- and q-axes inductances are obtained from the measured self and mutual inductances of the stator winding. In a sinusoidally distributed winding, the self and mutual inductances of each phase can be expressed as a function of rotor position.

$$L = (L_0 \pm L_1 \cos 2\theta_r) + L_{lk} \tag{C.3}$$

$$M = M_0 \pm M_1 \cos(2\theta_r \pm \frac{2\pi}{3}) \tag{C.4}$$

where, θ_r is the rotor position in mechanical degree, L is the self inductance and M is the mutual inductance . Each inductance has one DC and one second harmonic component. In a sine distributed winding with minimum space harmonics, L_d and L_q can be calculated as,

$$L_d = \frac{3}{2}(L_0 - L_1) + L_{lk}$$

(C.5)

$$L_q = \frac{3}{2}(L_0 + L_1) + L_{lk}$$

(C.6) However, in a real machine, space harmonics are not negligible. For such case, L_d and L_q can be calculated using a more general definition,

$$L_d = (L_0 - M_0) - (L_1 / 2 + M_1) + L_{lk} \tag{C.7}$$

$$L_q = (L_0 - M_0) + (L_1 / 2 + M_1) + L_{lk} \tag{C.8}$$

The circuit connection of the test method for star connected machine with accessible neutral such as the Segmented IPM machine and IPM machine-I are shown in the Fig.C.1. The self and mutual inductances of the winding for a particular rotor position is obtained by exciting one of the phase windings while keeping other two open. They are calculated as,

$$L_a(\theta_r) = \frac{\sqrt{(\frac{V_a}{I_a})^2 - R^2}}{(2\pi f)} \tag{C.9}$$

$$M_{ac}(\theta_r) = \frac{V_c}{(2\pi f)I_a} \tag{C.10}$$

where, R : stator resistance [Ohm], f : supply frequency [Hz], V_a : supplied phase voltage [V], V_c : measured induced voltage in one of the open circuit winding [V] and I_a : measured phase current [A]. The variation of these two inductances with respect to rotor position is found by measuring self and mutual inductances for various rotor positions. By plotting L and M against rotor position, they can be expressed as functions of rotor positions by optimized curve fitting technique. The parameter L_0, M_0, L_1 and M_1 are determined from these functions to calculate d- and q-axes inductances. A series of L_d and L_q values can be obtained for varying current magnitudes. The measured self and mutual inductance waveform of the Segmented IPM machine and IPM machine-I are shown in Fig.C.2 and Fig.C.3 respectively. The variations of the measured d- and q- axis inductances with current for both the machines are shown in the Fig.C.4 and Fig.C.5.

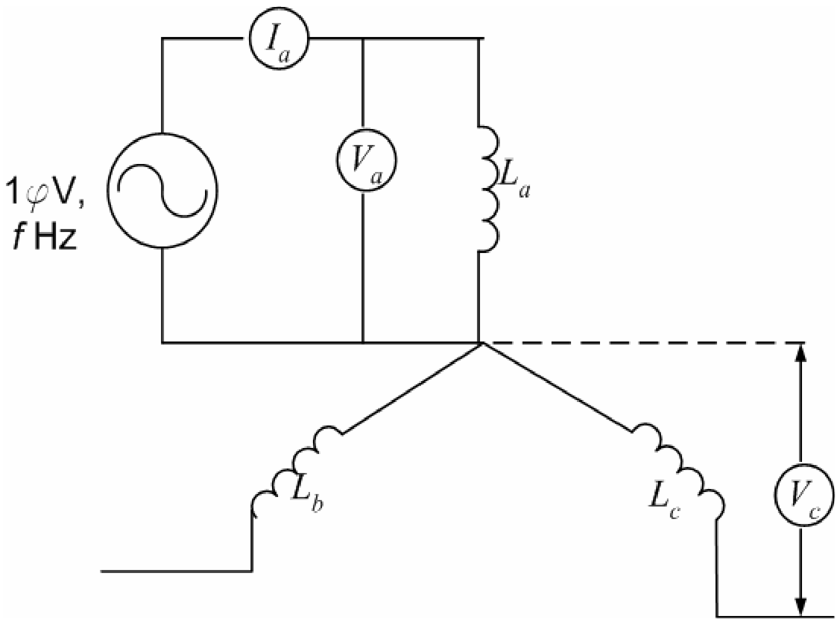

Fig. C.1 AC test method circuit connection

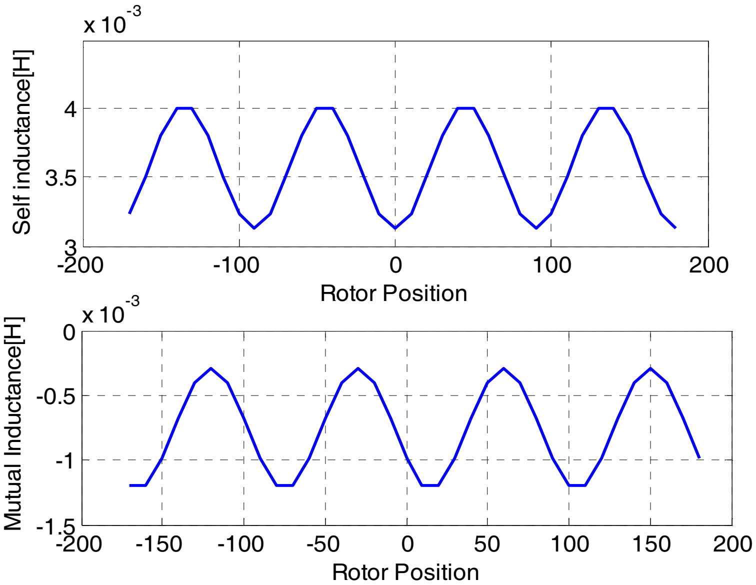

Fig. C.2 Variation of measured self and mutual inductances of the Segmented Magnet IPM machine with a stator current 8A

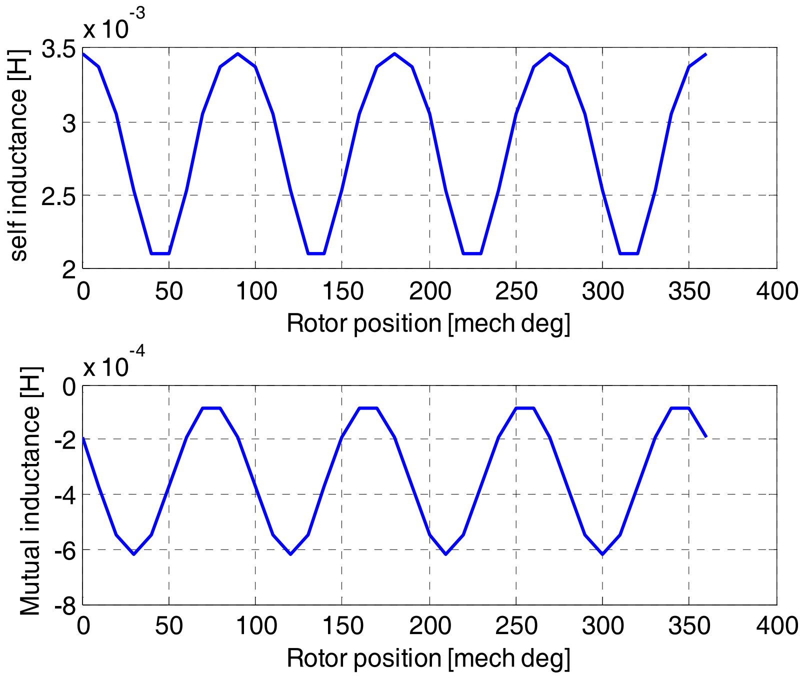

Fig. C.3 Variation of measured self and mutual inductances of the IPM machine-I with a stator current 8A

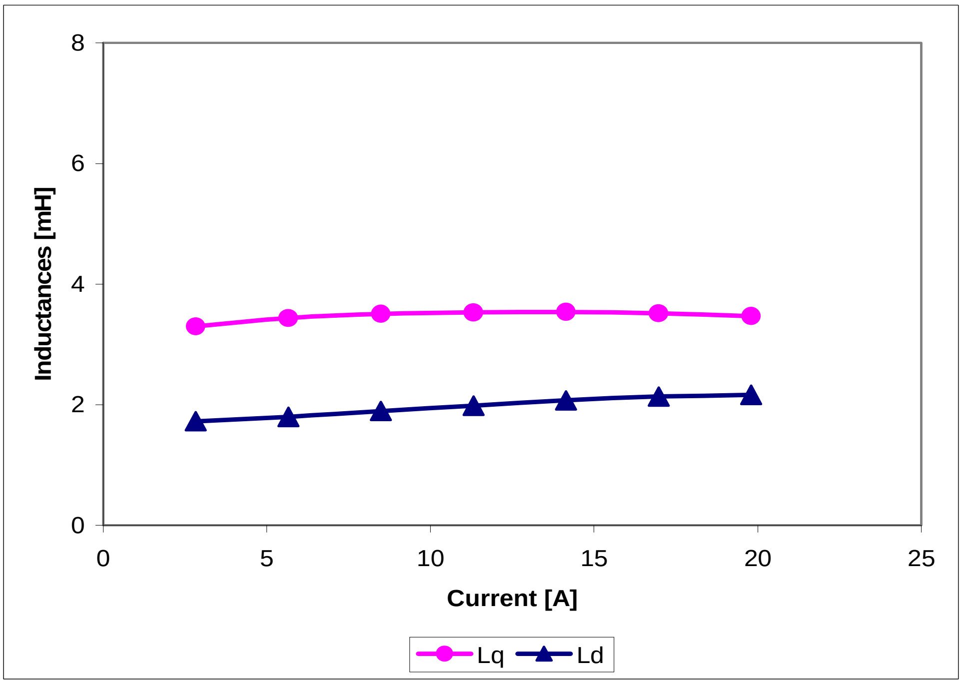

Fig. C.4 Variation of d- and q-axis inductances with current of the Segmented Magnet IPM machine

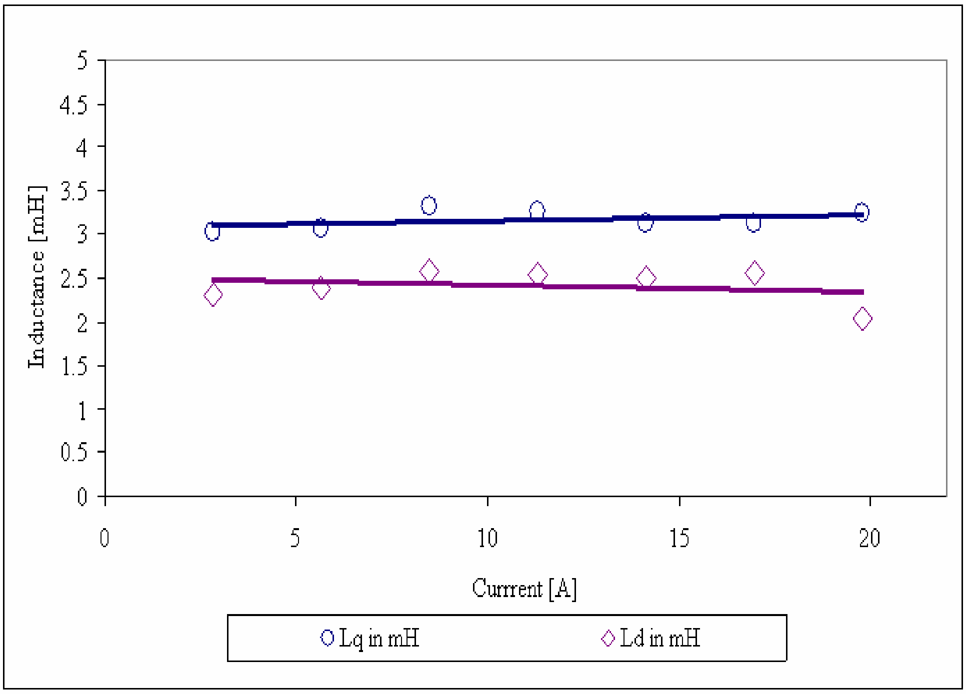

Fig. C.5 Variation of d- and q-axes inductances with current of the IPM machine- I

APPENDIX D

D. Modeling and Real-time Control Programs

The programs used in this work are divided in to three categories: -1) Flux2D finite element program files, 2) Matlab Modeling files and 3) Real-Time Control files. The FLUX 2D files are divided into two groups. One of them contains the geometry and post processing files of the Segmented IPM machine. The second group contains the geometry and post-processing files of the IPM machine-I.

Matlab/Simulink modeling files are developed using the Matlab version 7.0.0.

All programs under Real-time control were prepared for the experiments carried out in this work which were written in a combination of Matlab-Simulink and C program. All of them should run on DS1104 board. The structure of the directories in the attached CD is shown in Fig.D.1.

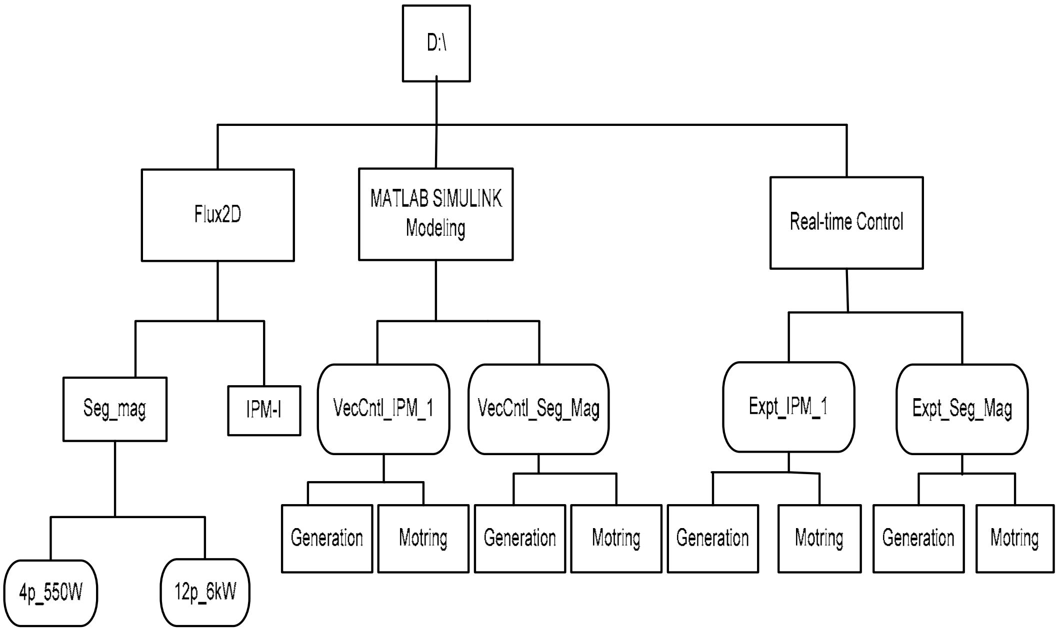

Fig. D.1 Directories in the attached CD

D.1. FLUX2D Finite Element Analysis Files

D.1.1. Program for the Segmented IPM machine

These files are used for design optimization and analysing magnetic characteristics of the Segmented IPM machine.

Directory : 4p_550W

Geometry files:

segmag_IPM.flu

3Layer.flu

bondedironloss.flu

Circuit files:

Segmag.cid

cur_source.cid

Post-processing files:

Segmag_IPM.tra

coggingtorque.tra

feloss_1000.tra

feloss_2000.tra

feloss_3000.tra

feloss_4000.tra

feloss_5000.tra

befm_6000.tra

3phldq_2.tra

3phldq_4.tra

3phldq_6.tra

3phldq_8.tra

3phldq_10.tra

3phldq_12.tra

spd_1000.tra

spd_2000.tra

spd_3000.tra

spd_4000.tra

spd_5000.tra

spd_6000.tra

Directory: 12pole_6kW

Geometry files:

3layers.flu

pole12_8mm.flu

Circuit files:

Segmag.cid

cur_source.cid

Post-processing files :

8mm_bemf.tra

Coggingtorque.tra

Ld.tra

Lq.tra

8mm_150.tra

8mm_500.tra

8mm_1000.tra

8mm_1500.tra

8mm_2000.tra

8mm_2500.tra

8mm_3000.tra

8mm_3500.tra

8mm_4000.tra

8mm_4500.tra

8mm_5000.tra

8mm_5500.tra

8mm_6000.tra

D.1.2. Program for IPM machine-I

These files are used for analysing magnetic characteristics of the IPM machine-I.

Geometry files:

lowkw_0.55kw.flu

3layer_0.55kw.flu

twopoles.flu

Circuit files:

Segamag.cid

cur_soruce.cid

Post-processing files:

befm_0.55kw.tra

Cogtorq_0.55kworg.tra

Magnetalone.tra

Ironloss_500.tra

Ironloss_1000.tra

Ironloss_2000.tra

Ironloss_3000.tra

D.2. Modeling programs using MATLAB-SIMULINK

These files are used to run the vector current control of the Segmented IPM machine and conventional IPM machine-I. Each directory contains an initialization file which must be run first to load the controller and machine parameters. After this, specific SIMULINK model can be run.

D.2.1. MATLAB-SIMULINK Programs for Segmented IPM machine

Directory: VecCont_Seg_Mag

Initialization file: m1_contrl.m

1. Simulink model file: contl_segmag.mdl
   generation.mdl

D.2.2. MATLAB-SIMULINK Programs for IPM machine-I

Directory: VecCont_IPM_1

Initialization file: m1_contrl_IPM1.m

Simulink model file: conlt_IPM1.mdl

generation_IPM1.mdl

D.3. Real-time Control Files

The real-time control programs have been developed under the dSPACE environment for DS1104 board.

D.3.1. Programs for the Segmented IPM machine

Directory: Expt_Seg_mag>Motoring

File name Description

GEN_MOD.C General Functions

controls_pwm.mdl Simulink model file

controls_svm.mdl Simulink model file

m1_control.m m file

controls_pwm.map Map file

controls_pwm.ppc PPC file

controls_pwm.sdf SDF file

controls_pwm_user.cuser defined C program for initialization of rotor position

controls_svm.map Map file

controls_svm.ppc PPC file

controls_svm.sdf SDF file

controls_svm_user.c user defined C program for initialization of the rotor position

svmconv.dll space vector modulation

Directory: Expt_Seg_mag>Generation

File name Description

GEN_MOD.C general functions

Gen_m1.m m file

Gen_cont.mdl	Simulink model file
Gen_cont.map	map file
Gen_cont.ppc	ppc file
Gen_cont.sdf	sdf file
Gen_cont_user.c	user C code for rotor position initialization
Svmconv.dll	SVM modulation

D.3.2. Programs for the IPM machine-I

Directory: Expt_IPM_1>Motoring

File name	Description
GEN_MOD.C	General Functions
controls_pwm.mdl	Simulink model file
controls_svm.mdl	Simulink model file
m1_control.m	m file
controls_pwm.map	Map file
controls_pwm.ppc	PPC file
controls_pwm.sdf	SDF file
controls_pwm_user.c	user defined C program for initialization of rotor position
controls_svm.map	Map file
controls_svm.ppc	PPC file
controls_svm.sdf	SDF file
controls_svm_user.c	user defined C program for initialization of the rotor position
svmconv.dll	space vector modulation

Directory: Expt_Seg_mag>Generation

File name	Description
GEN_MOD.C	general functions
Gen_m1.m	m file
Gen_cont.mdl	Simulink model file
Gen_cont.map	map file
Gen_cont.ppc	ppc file
Gen_cont.sdf	sdf file
Gen_cont_user.c	user C code for rotor position initialization
Svmconv.dll	SVM modulation

APPENDIX E

E. Experimental Implementation

E.1. The Experimental Set up

During the course of this study, a simple and reliable test set up for the two studied IPM machines- the Segmented IPM machine and prototype IPM machine-I were developed. The system consists of the studied IPM machines, shaft-mounted incremental encoder for position sensing, the Voltage Source Inverter (VSI), DS1104 controller board and current sensors. A Permanent Magnet Synchronous (PMSM) machine with its electronic controller was coupled to the studied IPM machine to form a motor-generator set for loading purpose. A Personal Computer (PC) was used to host the dSPACE controller board and control software development.

The software implementation includes development of the control program algorithm based on the real time interface of Matlab-Simulink blocks and dSPACE.

The over all experimental set up is shown in the Fig.E.1. The Fig.E.2 illustrates the IPM machine-I coupled with the DC machine. Since, the maximum allowable speed of the DC machine was limited to 3000 r/min, a PMSM with a maximum allowable speed up to 8000 r/min was used for the Segmented IPM machine. The Fig.E.3 shows the Segmented IPM machine coupled with the PMSM.

Fig. E.1 Over all experimental set up

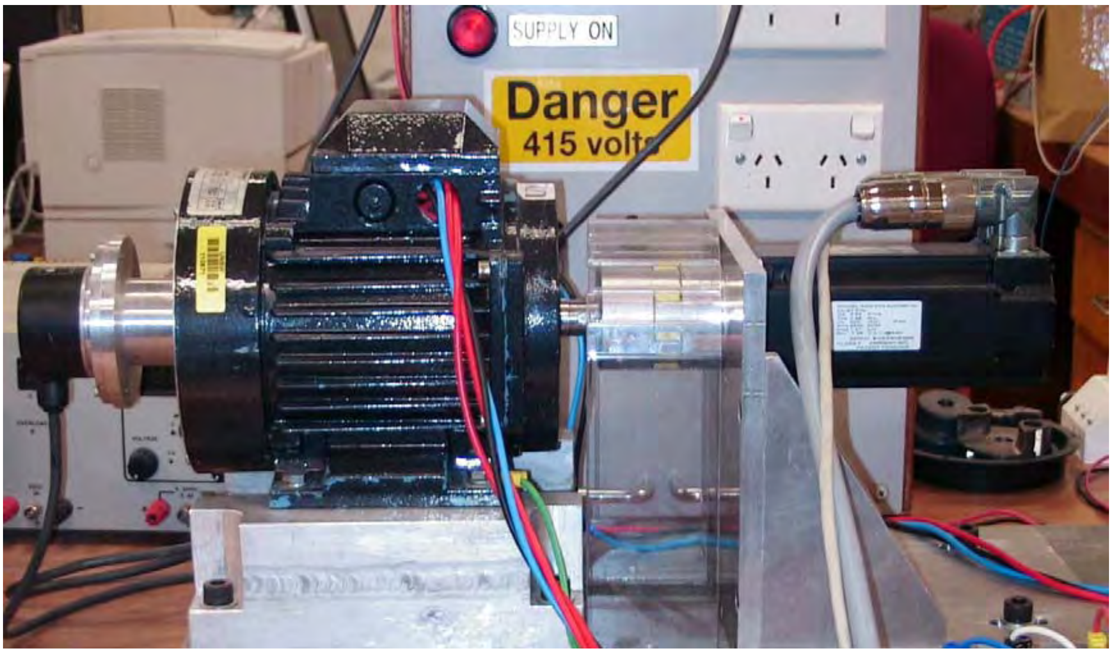

Fig. E.2 Segmented Magnet IPM coupled with PMSM machine

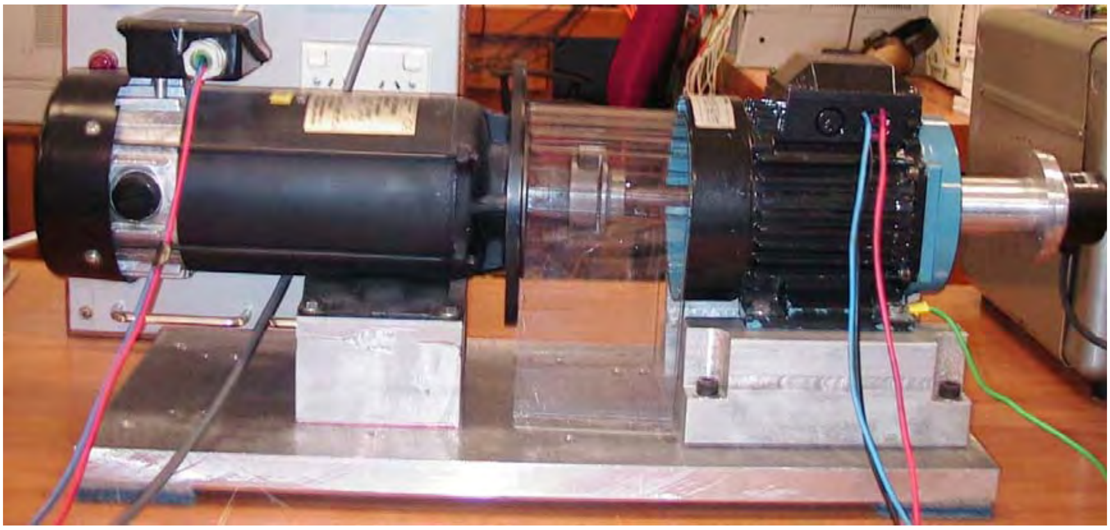

Fig. E.3 IPM machine-I coupled with DC machine

E.2. Hardware Description

The schematic diagram of the IPM motor and its drive system is shown in the Fig.E.4. The system was modified to incorporate DC bus voltage regulation when the IPM machine was run as a generator. As mentioned earlier, the IPM machine was designed for 42V environment of the automobile where a 36V battery with its charger forms the 42V DC bus system. In this work, instead of the battery system, a diode bridge rectifier was utilized to form the 42V DC link for the motoring application. The nominal 415 V of the three phase supply is first step down to 40V via a transformer which is then rectified and filtered by the capacitors to form the 42V DC link voltage for the output stage. An external variac was also connected for fine adjustment of the DC link voltage.

The schematic diagram of the generator system is shown in Fig.E.5 The main components of both system are: 550W, 4pole IPM machine(the IPM machine-I and the segmented IPM machine), the 5kW IGBT Voltage Source Inverter(VSI), shaft-mounted 5,000 pulse/rev incremental encoder, the line current and DC bus voltage sensors, DS1104 controller board and the host PC with Pentium III

800MHz. The individual characteristic and features of the main hardware components are briefly described in the subsequent sections.

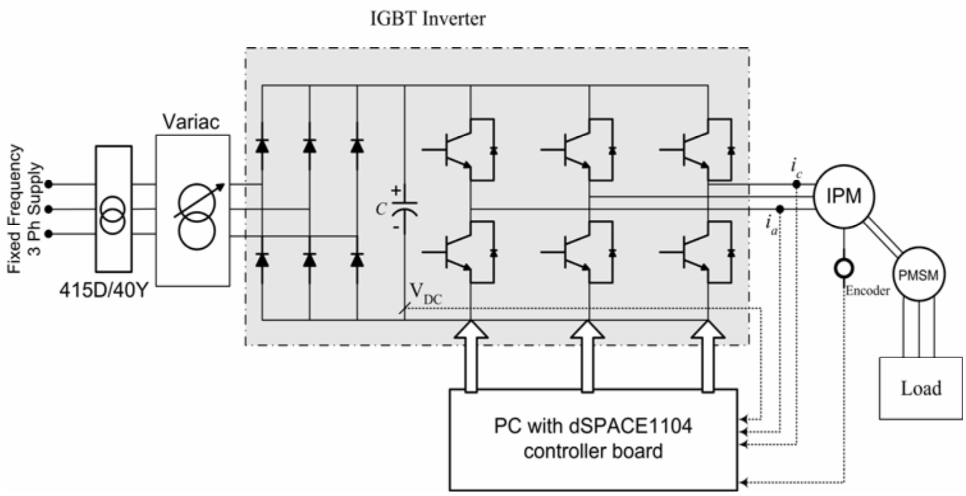

Fig.E.4 Schematic diagram of the IPM drive system

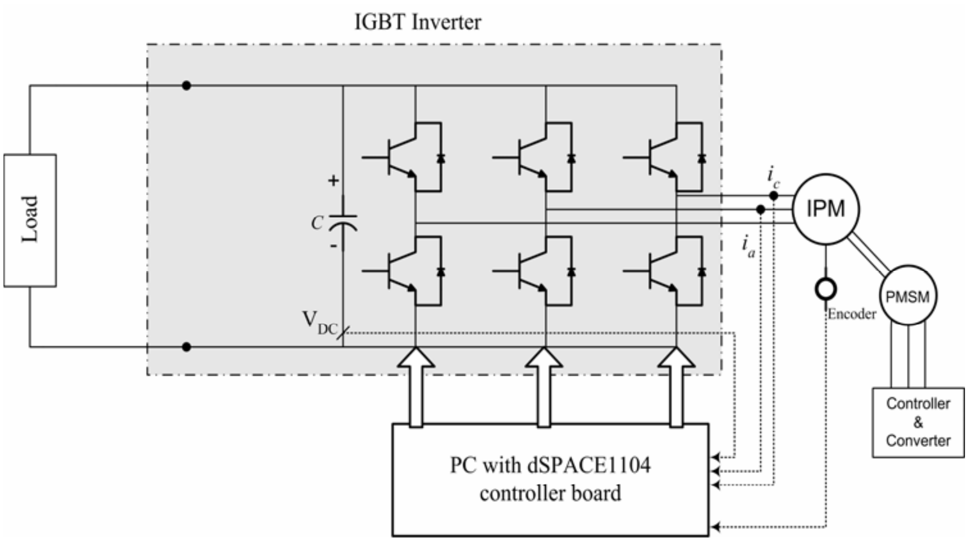

Fig. E.5 Schematic diagram of the IPM generator system

E.2.1. Description and circuit diagram of the Voltage Source Inverter (VSI)

Fig E.6-phase IGBT Inverter

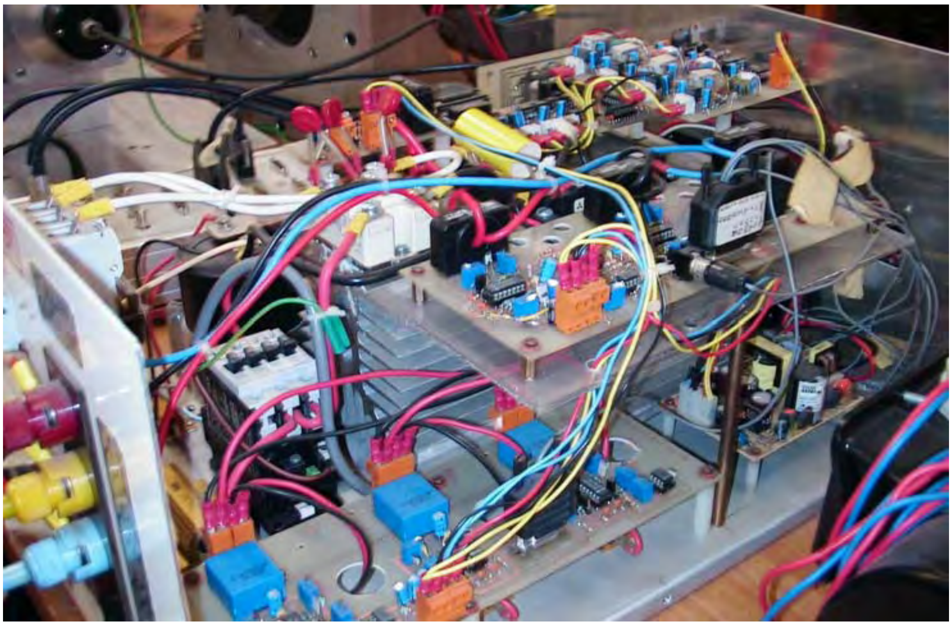

Fig.E.7 Side views of the 3phase IGBT inverter

In the IPM motor drive system the 5kW IGBT voltage source inverter (VSI) was used to generate the variable voltage and frequency whereas in the generator system, the 6 Integrated Gate Bipolar Transistor (IGBT) switches were used for controlled rectification. The 5kW IGBT inverter and its circuits are shown in the Fig.E.6 and Fig.E.7. The detailed VSI circuit diagram is shown in the Fig..E.8.

The output stage of the inverter consists of six individual IGBT switches and freewheeling diodes. The IGBT switch combines the advantages of power MOSFET and bipolar transistor. Similar to the MOSFET in the IGBT switch, gate is isolated and required driving power is low. Its conducting voltage drop is similar to bipolar transistor. In the six switch inverter, two freewheeling diodes in parallel to two IGBT switches forms the individual leg of the three phases. The freewheeling diodes are required to protect the switches against unwanted voltage peak generated from the inductive load current. The three phase legs of the inverter used in this work are built with the intelligent power module (manufactured by Mitsubishi Semiconductors). This type of module is isolated base modules and can be operated with very high switching frequency (up to 20 kHz). The built in control circuits provide optimum gate drive and protection for the IGBT switches and free-wheel diodes.

There exists an additional IGBT switch with free-wheel diode which is connected in series with two resistors R_4 and R_5 for dynamic braking of the drive system, if required. The built in protection of the intelligent power modules includes over current, over voltage and over temperature etc. In case of any fault, a pulse is generated from the module which is captured through a latch circuit in an Optocoupler board. This pulse act as an inhibit signal to prevent switching of the IGBTs. Once the fault is cleared, the signal can be reset through a push button operation. The Optocoupler board uses 4 isolated 15V DC power supplies to drive the IGBTs inside the module. A quad DC-DC converter provides this isolated power supply. The inverter is also provided with isolated LEM Current and Voltage sensors to feed back the line current and voltages. The details of the auxiliary circuit boards are given in the Fig.E.9-E.14.

The pulse width modulation (PWM) technique is commonly used to switch the IGBTS for producing variable voltage and frequency output. There are a number of PWM switching scheme available. Among them, the space vector modulation (SVM) technique is the best suitable with digital microprocessor such as DS1104. The method exploits interaction between all three motor phasor and instead of using separate modulator for each of the phases; the complex reference voltage phasor is processed as whole. As an added advantage, the SVM technique produces less harmonic distortion in both current and voltage applied to the phases of the motor and provides more efficient use of the supply voltage in comparison with other PWM technique. The real time implementation of SVM PWM will be discussed in the section E.3.2.

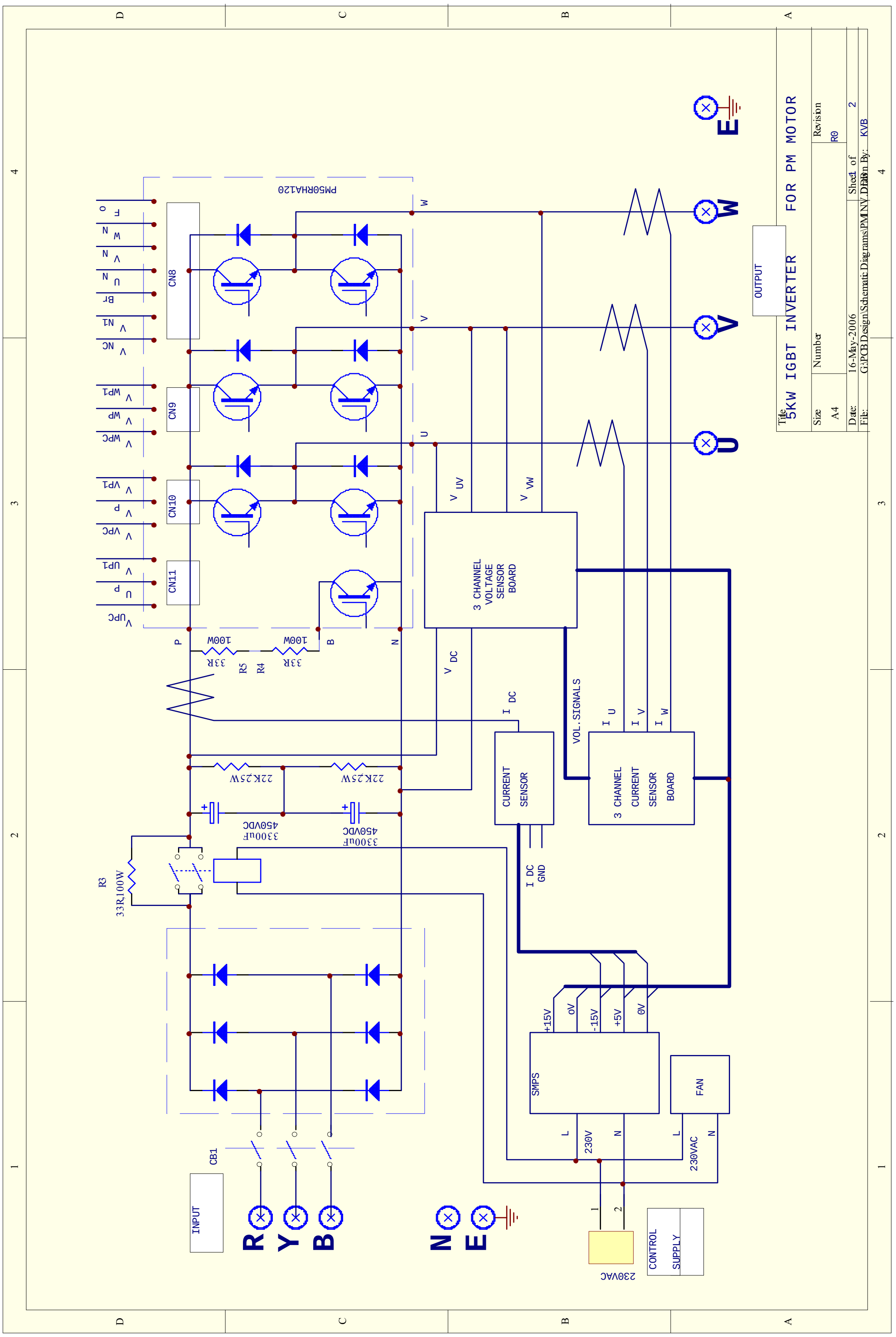

Fig. E.8 Circuit diagram of the IGBT inverter with their control boards

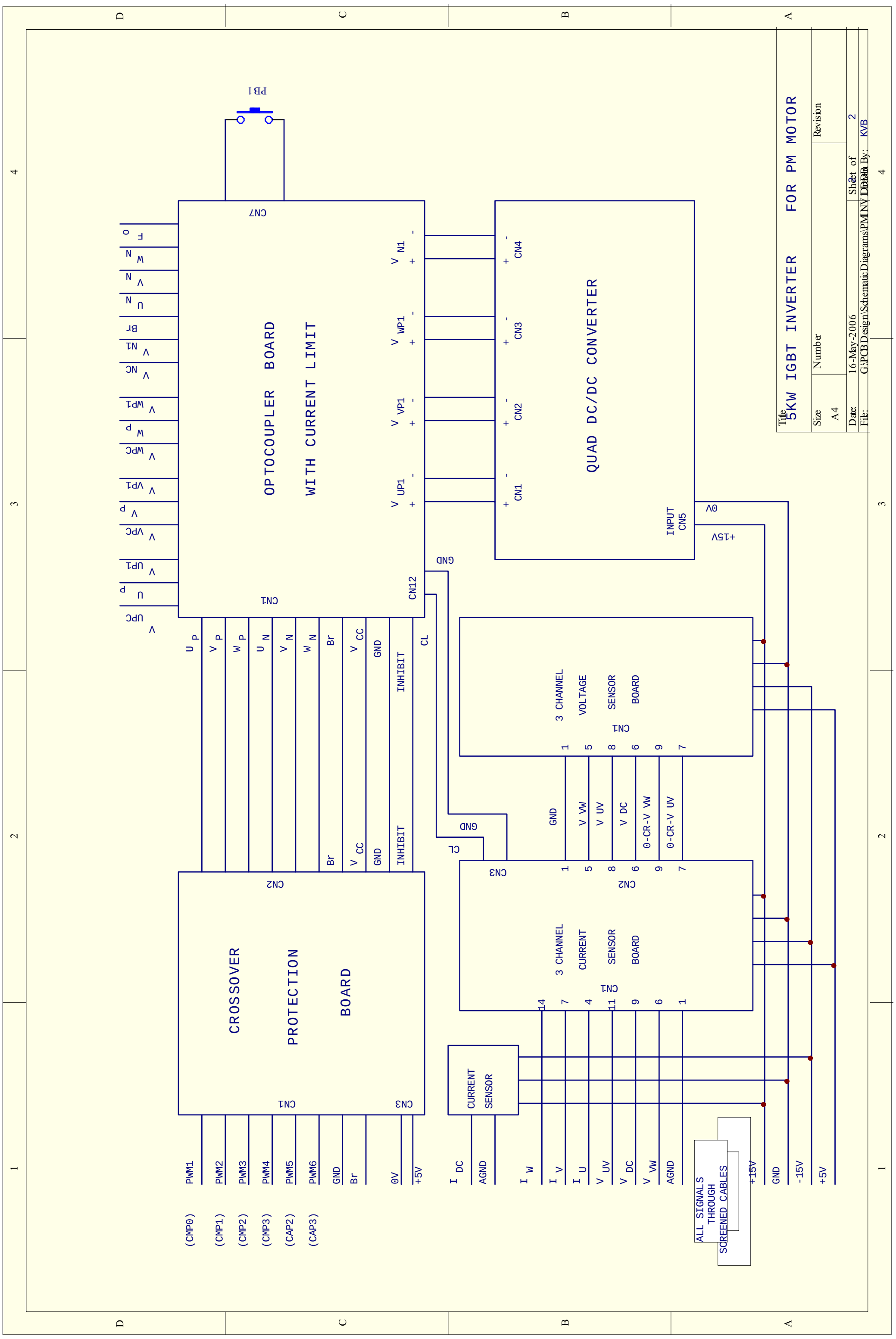

Fig. E.9 Interconnection between the IGBT inverter and control PCBs

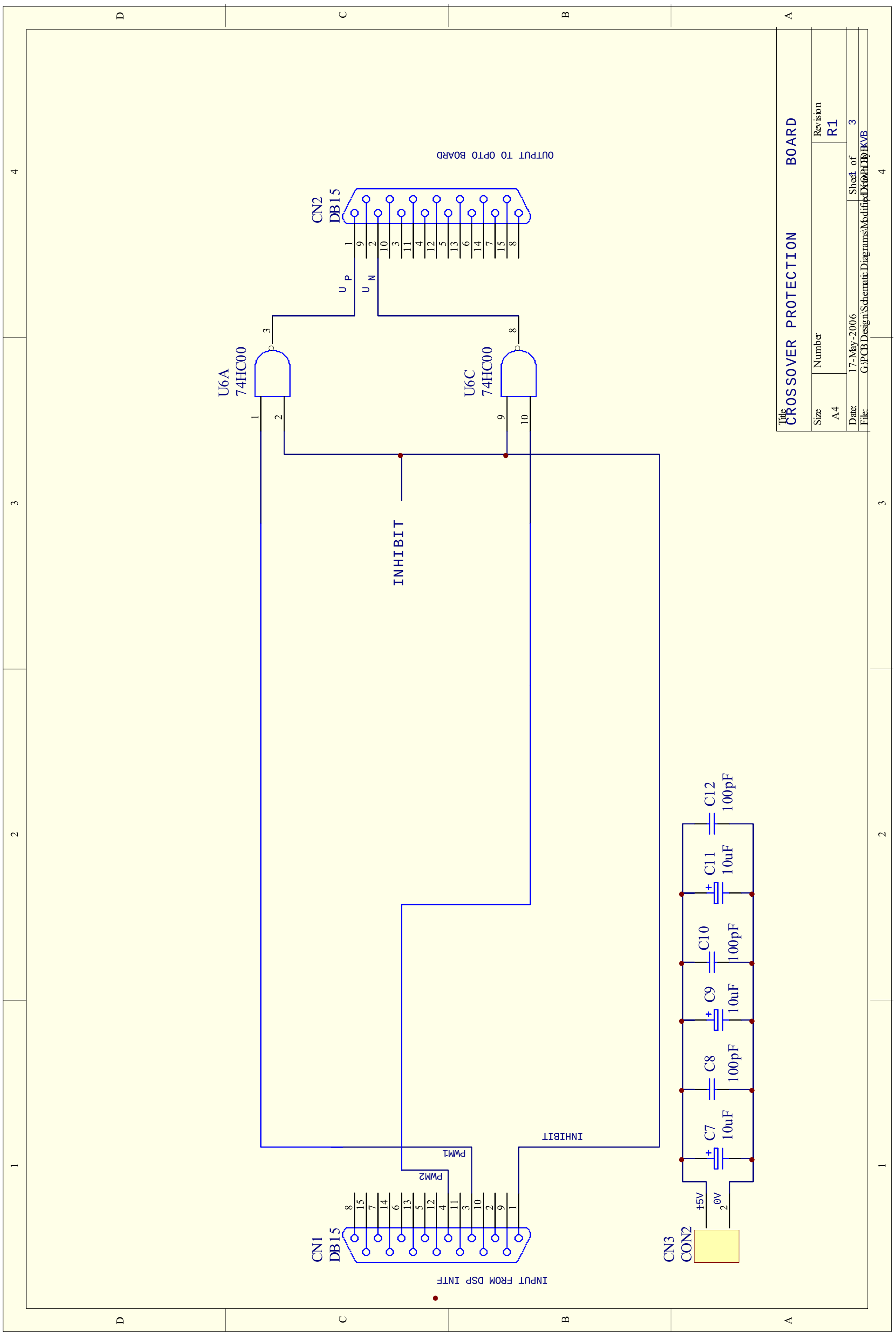

Fig.E.10 Cross-over protection board

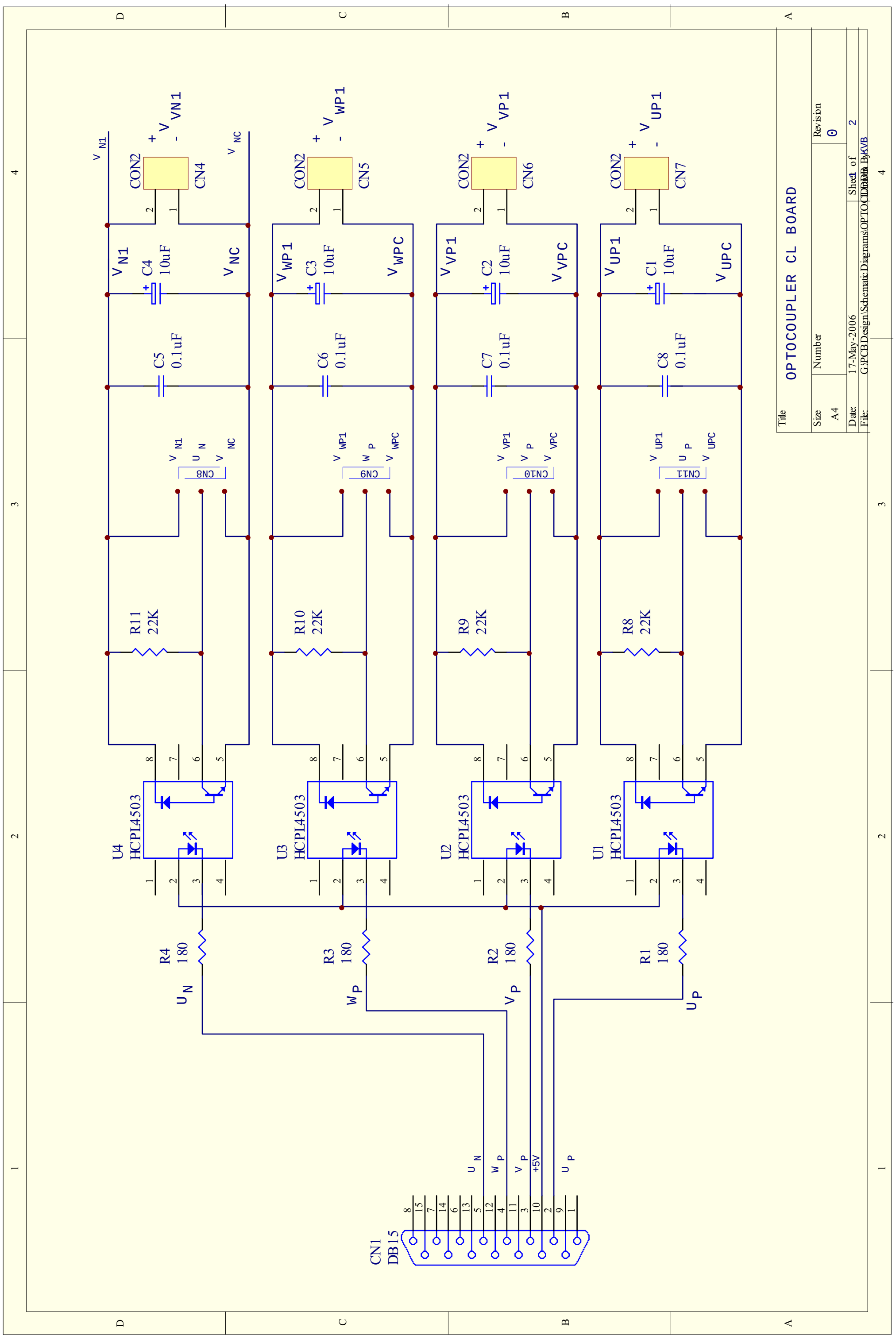

Fig. E.11 Opto-coupler board (part 1 of 2).

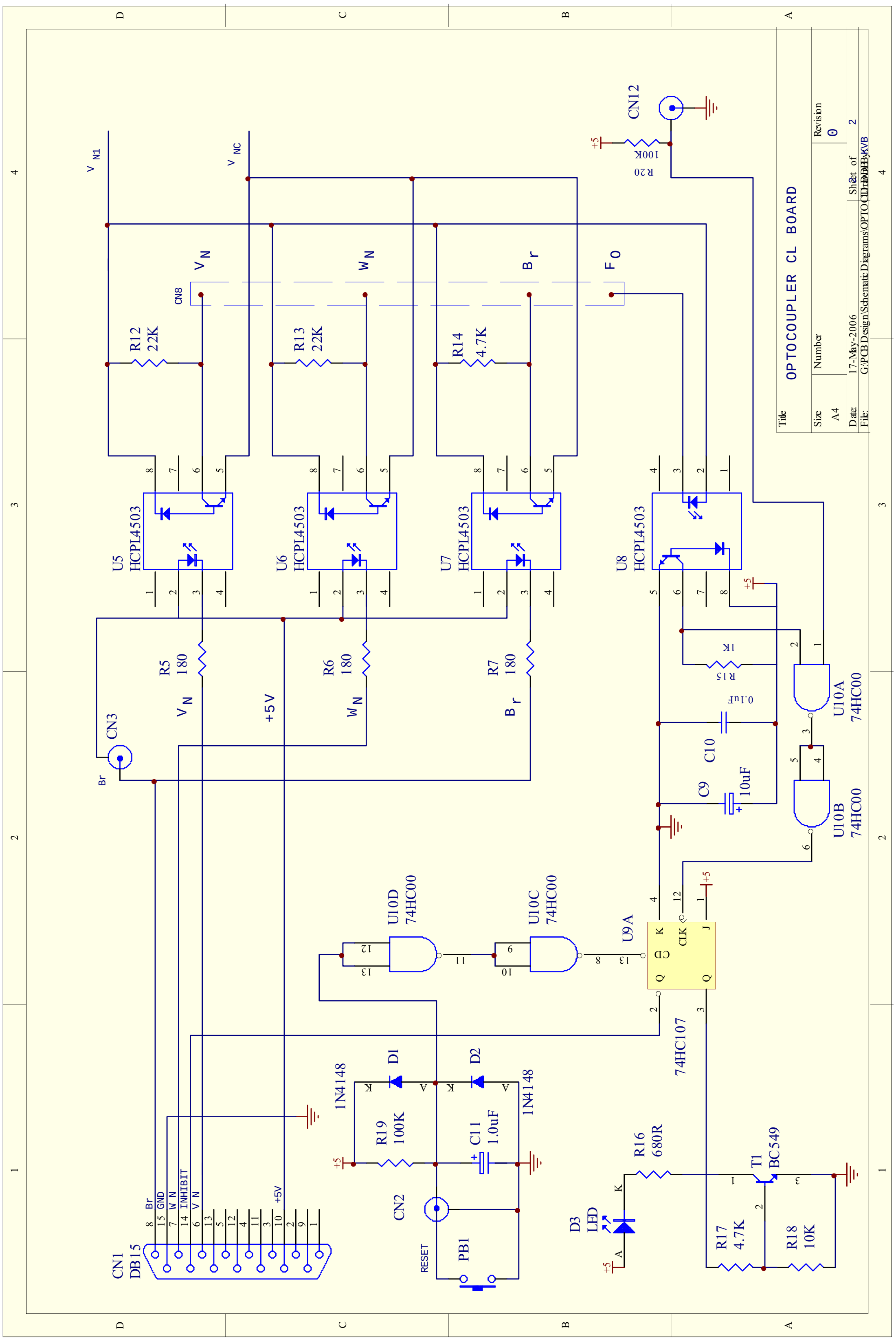

Fig. E.12 Opto-coupler board (part 2 of 2).

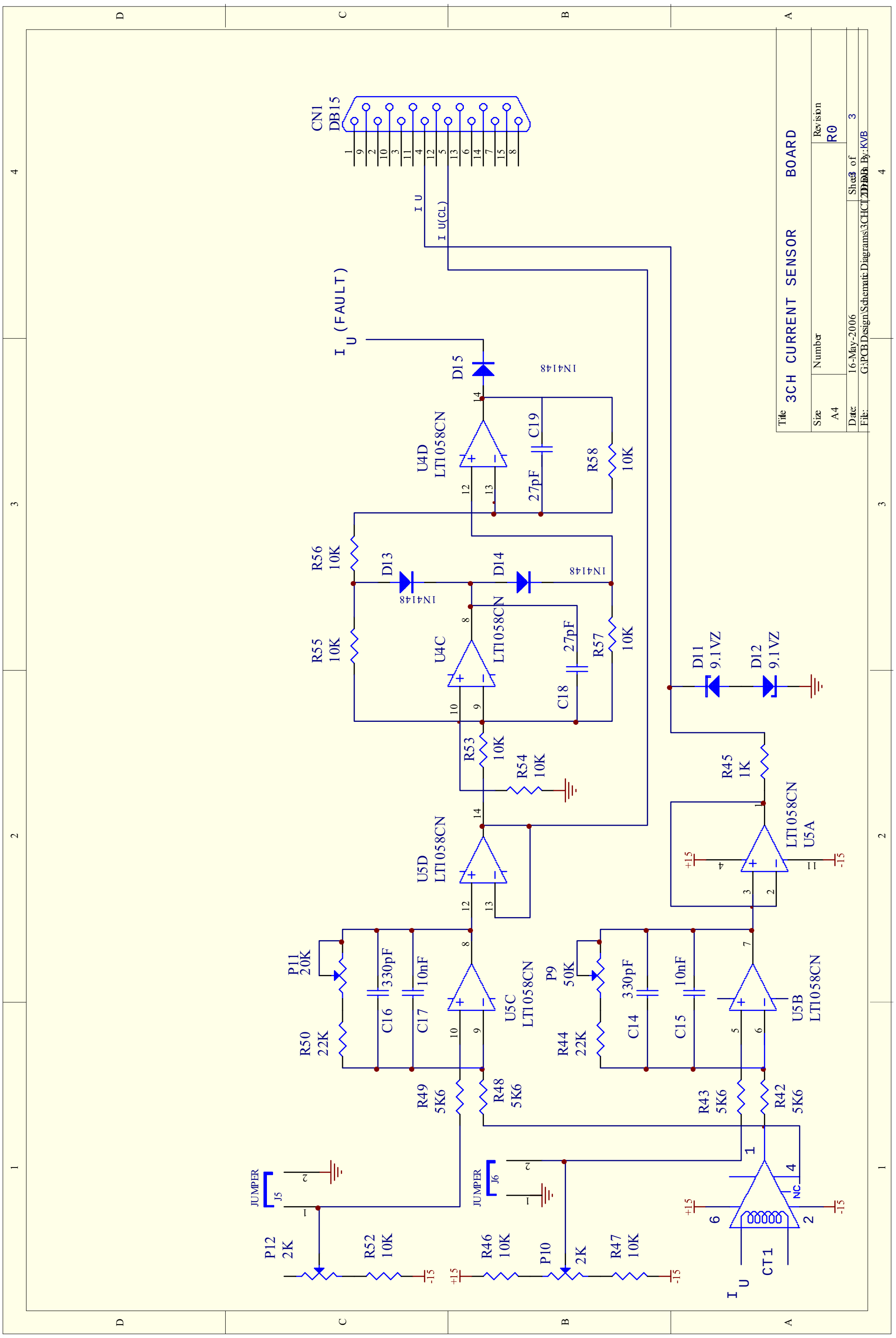

Fig. E.13 Three channel current sensor board

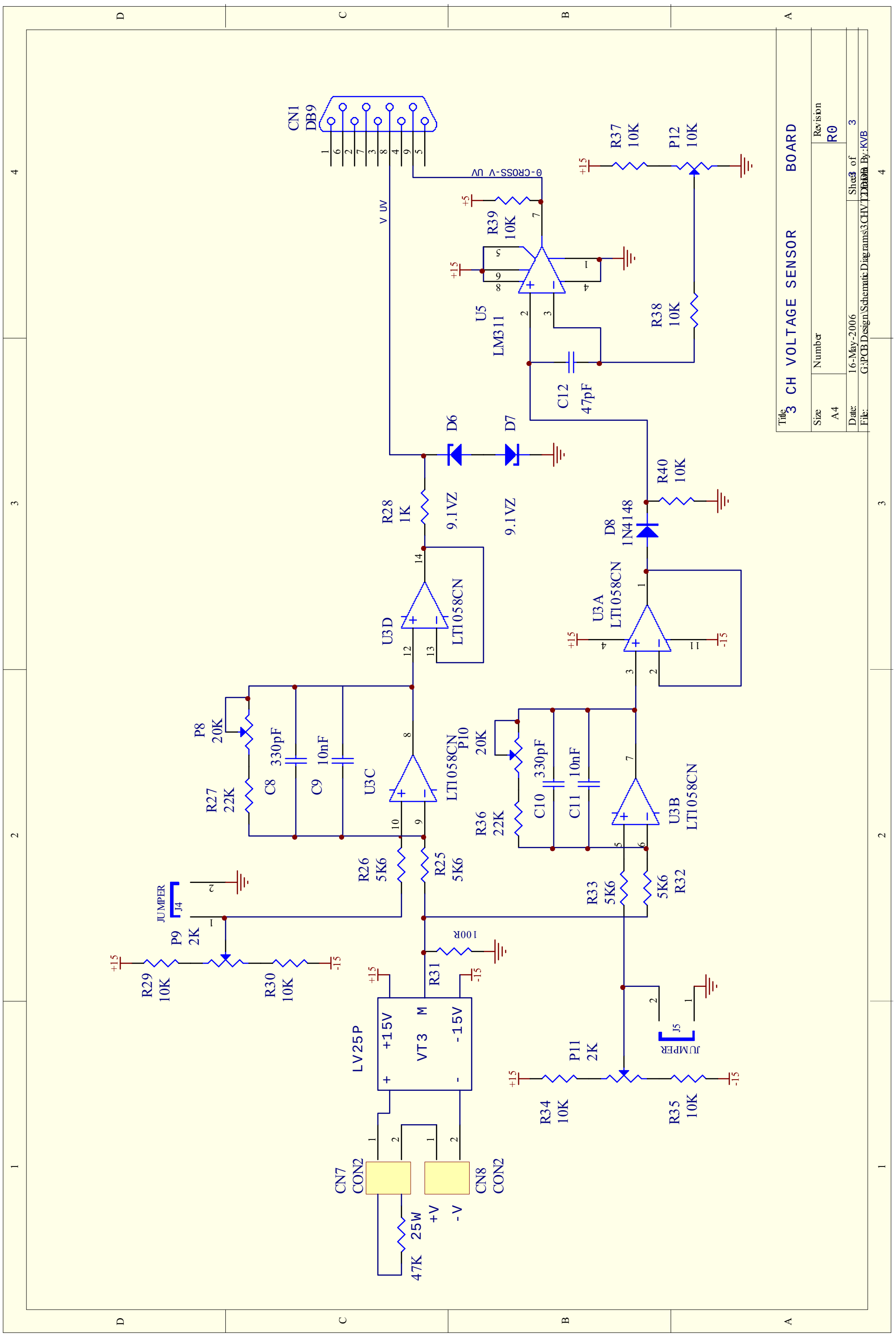

Fig. E.14 Three channel voltage sensor board

E.2.2. Incremental Encoder

For a vector current control IPM drive system, feedback of rotor position is crucial. The stability of speed and bandwidth of command response are also influence by the accurate detection of the rotor position. The most of the modern encoder uses optical scanning process which uses principle of photoelectric scanning. It is contact free and hence, the wear and tear is minimal. It can detect very fine lines and generates output signal with small periods. The measuring standards of periodic structure by optical scanning are known as graduations. These graduations are applied to a carrier substrate of glass or steel. In the incremental encoders, the graduation consists of the incremental track and a reference track. The position information is obtained by counting the individual increments from some point of reference. The reference mark is used after restarting the machine to find the last reference point selected.

The incremental encoder (ROD 426) from Heidenhain was employed in this work. The output signals of this type of encoder are two square wave pulse trains phase shifted by 90^0 (electrical) and number of pulse per revolution is 5000. The reference mark signal or the index consists of one reference pulse gated with the incremental signals. In addition, the integrated electronics produces inverse of all three pulse trains for noise-proof transmission. The specification of the encoder is provided in the Table E-1.

Table E-1 Specification of Incremental Encoder (Heidenhain ROD 426)

Incremental signal	Square wave TTL
Line counts	5000
System accuracy	1/20 of grating period
Power supply	5V+/-10%, 120mA
Mechanical permissible speed	<=16000r/min
Starting torque	0.01Nm(at 20^0 C)
Moment of inertia of rotor	$2.7.10^{-6}$kgm^2

E.2.3. DS1104 board

The DS1104 controller board is specifically designed for development of high speed multilevel digital controllers and real-time simulations in various fields. It is a complete real-time control system based on a 603 Power PC floating point processor of 250MHz. For advance I/O purposes, the board includes a slave DSP subsystem which performs digital input and output along with generation of PWM signals. The heart of this subsystem is a TMS320F240 digital signal processor from Texas Instruments. The controller board can be directly programmed using MATLAB/SIMULINK or hand coded C program. The DS1104 control board generated PWM signals were applied to the VSI. A connector panels give easy access to all input and output signals of the board through BNC cables. The external devices can be connected, disconnected or interchange without soldering via the connector panel which simplifies system construction, testing and troubleshooting greatly. The controller board is normally inserted into the PCI slot of the host PC. An overview of the features provided by the DS1104 board is shown in Table E-2. The technical specifications of the board are given in the E-2.

Table E-2 Technical specification of the DS1104 board

Manufacturer	dSPACE GmbH Technologiepark 25, 33100Paderborn Germany
Processor	♦ MPC 8240 with PPC630e core and on chip peripherals ♦ 64-bit floating point processor ♦ 250 MHz CPU
Memory	♦ Global memory: 32MB SDRAM ♦ flash memory: 8MB
ADC	♦ 4 multiplexed channels 16bit resolution, 2 μs conversion time ♦ 4 A/D channels, 12 bit resolution and 800 ns conversion time
Incremental Encoder interface	♦ 2 channels ♦ Single ended TTL or differential RS422 input ♦ 4 fold subdivision ♦ Max 1.65MHz ♦ 24-bit loadable position counter ♦ Rest on index
Slave DSP	♦ Texas Instruments TMS320F240 DSP ♦ 20 MHz clock frequency ♦ 1X3-phase PWM output ♦ 4X1 phase PWM output

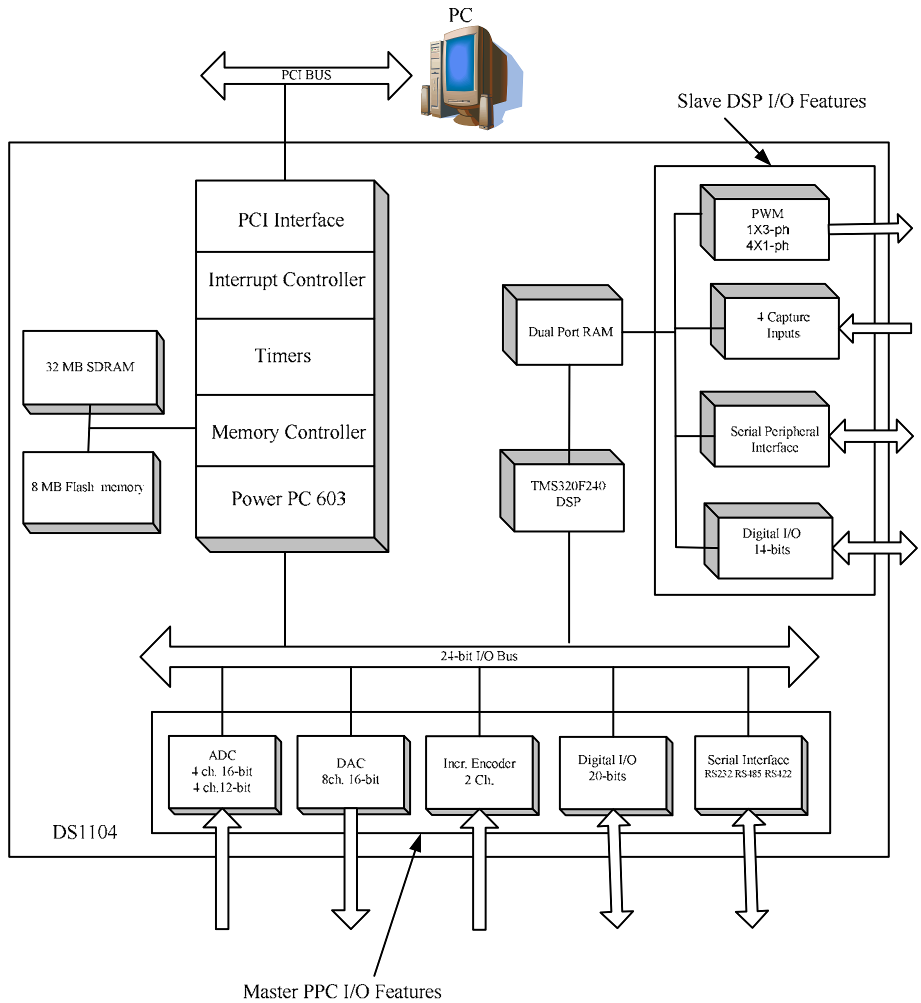

Fig. E.15 Overview of DS1104 controller board

The main processing unit MPC8240 of the DS1104 board consists of the PowerPC 603e microprocessor (with 250MHz CPU clock, 16kb L1 data cache and 16-kb L1 instruction cache), an interrupt controller, a synchronous DRAM controller, a number of timers and PCI interface. The master PPC controls the I/O features of analog to digital channels (ADC), digital to analog channels (DAC), bit I/O unit, incremental encoder interface and serial interface. The ADCs convert the analog feedback signals (up to 10V) to digital format so that the DSP can utilize them. In this work, the DC bus voltage and two line currents were feedback through ADC for use in the vector control algorithm. The DACs converts digital signals to analog so that they can be displayed on oscilloscope.

The 20-bits I/O unit can be used to transfer digital I/O to and from the controller board, if required.

The master PCC also provides an interface to the incremental encoder signal. It has two identical channels (Inc1 and Inc2) for this interface. Both channels are capable to support single ended TTL and differential signals. It has a maximum 1. 65MHz line count frequency. In other word, it can measure up to 1,650,000 encoder lines per second. The DS1104 performs internally a four fold subdivision of each encoder line. Hence, the board can actually handle count frequency up to 6.6MHz. The board is also equipped with a 24-bit position counter. Due to the fourfold subdivision, the counter can measure up to 2^{22} encoder line in the range of -2^{21} to $2^{21}-1$. The count direction is dictated by the direction of rotation of the encoder and the index pulse can reset the counter automatically. The both encoder channels also provide an index input which is connected to the interrupt control unit of DS1104. The index signal can be extracted and utilized to write the position information in the position counter. This feature was used in this work to detect the initial rotor position of the IPM machine. The speed of the machine can be calculated from the encoder interface.

The serial interface of the DS1104 contains universal asynchronous receiver and transmitter to communicate with external devices when necessary. The master PPC also provides synchronization of I/O for accurate control of analog input, output or encoder position readout. The various hardware-interrupts and timer devices of DS1104 can be manipulated to develop and manage complex control of the drive system efficiently.

1X3-ph PWM signal generation feature in slave DSP was used to switch the IGBTs of the VSI in this experimental work. The PWM signals are pulse trains of variable width with fixed frequency and magnitude. The width of the pulses varies from period to period according to a modulating signal. When a PWM signal is applied to the gate of an IGBT switch, it causes turn-on/turn-off intervals of the switch to change from one PWM period to another, according to the modulating signal. Since, the frequency of the PWM signal is much higher than the modulating signal, the energy delivered to the machine and its load depends primarily on the modulating signal. The 1X3-ph PWM generation is compatible with the space vector modulation (SVM) technique for control of electric drive. It can generate PWM signal in the frequency range of 1.2Hz to 5MHz and provides the signals for both the non-inverted and inverted phases. The space vector modulation technique discussed in section 2.4.2 shows that the information of sectors and the value of t_a and t_b which corresponds to right (t_a) and left(t_b) vectors of fig.2.11 can be determined from a space vector. The sectors which is in the range of 1 to 6 is determined by projecting the rotating space vector V_x on the plane defined by the basic space vectors V_1, V_2, V_3, V_4, V_5 and V_6. The value ta and tb are determined by the projection of the space vector on the two adjacent basic space vectors. For the slave DSP to generate PWM signal by the SVM technique the duty cycle ta/Ts , tb/Ts and sector information are taken as input. For a space vector in the first sector, the pulse pattern for the three non-inverted PWM signals SPWM1, SPWM3 and SPWM5 generated by the slave DSP is shown in Fig.E.16. The PWM switching signals are fed directly fro the slave processor to the inverter. The duty cycle are allowed to vary between 0 and 1. Consequently, over-modulation can not be facilitated directly.

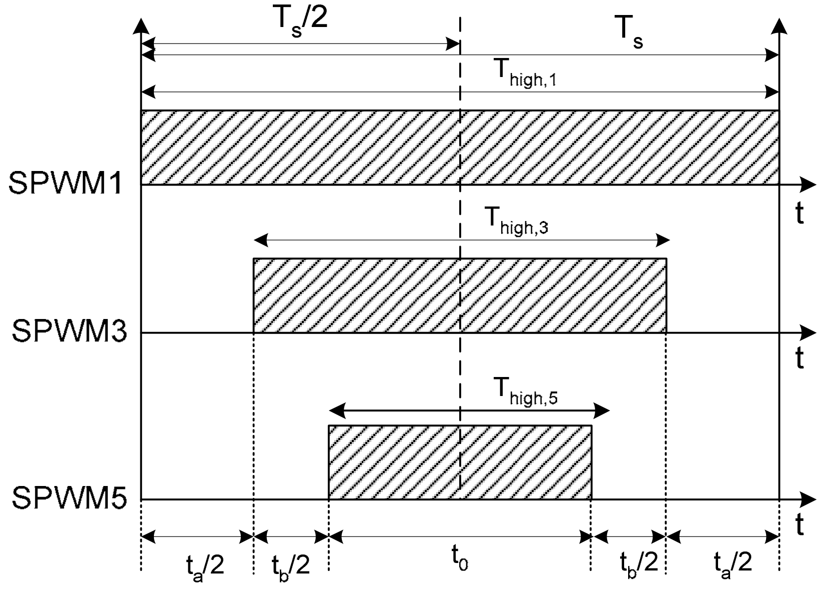

Fig. E.16 Generated PWM pulses of slave DSP with SVM technique

The resolution of the PWM signal used in this work was 100 ns for period of 0.1667ms. The dead time or dead band of the PWM signal generated can be specified. The dead band is the time gap between rising and falling edge of the non-inverted and inverted PWM signals. It introduces a time delay between complete turn off of one IGBT switch before turning on the other. Maximum allowable dead band is 100μs and should not be greater than $T_s/2$. In this work a 4μs dead band was specified for the safe operation of VSI.

E.2.4. Measurements of current and voltage

For high performance vector control of IPM machine, accurate measurement of phase current and DC bus voltage is essential. The phase current measurement accuracy and bandwidth influence directly the current control loop as well as the outer loop. Filtering a feedback signal additionally decreases the dynamic response time of the loop. The current is typically measured by one of the two methods: voltage drop across a resistor or magnetic transducer. Although resistive shunt sensing is less expensive, it is also a trade off between sensitivity and power dissipation on the resistor. Moreover, since resistor needs to be connected in series with the machine phase, it complicates the measurements because the signal of interest is very small differential value across the resistor compared to machine phase voltage. On the other hand, the magnetic transducer provides isolation to the measured signal by its very nature. It uses a ring type magnetic core with Hall-effect semiconductor element placed in an air-gap to measure the magnetic flux resulting from primary current through the center of the core. The overall bandwidth, accuracy and temperature independence of these type of current sensor are found to be sufficient for drive applications.

In this work, the machine currents were measured by LEM current sensors. The bandwidth of the used magnet sensor is 150kHz and response time is smaller than 1μs. The detailed circuit of the current sensor used in this work is given in the Fig.E.13. The output of the current transducer is passed through the filter and amplifier and finally limited to ± 9.1V by Zener diodes. The signal is fed to an anti- aliasing filter connected to the input of the ADC. The measured signal may be filtered by a digital low-pass filter subsequently.

In most of the high performance drive applications, the measurement of the DC bus voltage is required for the exact transformation of the reference voltage into the duty cycles for the inverter PWM. The measurement of DC bus voltage is not as crucial as the current measurements since the DC voltage is filtered a smoothed by the capacitors of appreciable size present in the DC bus. Usually one side of the DC bus is grounded. In this work LEM voltage sensor based on Hall Effect transducer was used to measure the DC bus voltage. The transducer provides galvanic isolation between primary and secondary circuit. Similar to current sensors, the output is limited to 9.1V by Zenner diode. The detailed circuit of the voltage sensor board is given in the Fig.E.14.

In the vector current controlled IPM drive system, measurement of phase voltage is not needed for control purpose. However, for performance analysis and recording purpose, measurement of phase voltage through LEM voltage sensor was provided in this work. The working principles of these voltage sensors are very similar to that of the DC bus voltage sensor.

E.2.5. Over current protection

An over-current protection is crucial in IPM motor drive since a very high demagnetizing current caused by some fault can permanently demagnetize the rotor magnets. A current comparator circuit is provided in the current sensor boards. The phase current is rectified with a precision rectifier in the current sensor board which is then compared with a preset value in the comparator. If the amplitude of the phase current is greater than the preset value, the output of the comparator becomes low which is wired to the inhibit signal of the VSI. Thus, for a current higher than the preset value, the switching of inverter is stopped. Once, the over-current fault is cleared, inhibit signal can be reset by push button operation.

E.3. Software Implementation

Traditionally, the machine and drive control was designed with analog components because they are easy to implement with relatively inexpensive components. However, such a system suffers easily by wear and tear with age, temperature drift and EMC interference. Additionally, any upgrade is difficult as design is hardwired. The recent development in the field of digital signal processing (DSP) makes it possible to implement drive control in digital system. The controls implemented in digital system are free from most of the drawbacks of analog system. The DSP technology offers both high performance and cost reduction and upgrade can be made very easily in the software. The DSP also have the capabilities to concurrently control and monitor a system. Furthermore, the complex control algorithm can be implemented without compromising reliability. In the digital environment, a dynamic control algorithm can adapt itself in real time to the variation in system behaviour.

This section presents the mutual interactions between control design and real time implementation. The experiment management and code generation real time implementation of SVM technique are explained.

E.3.1. Programming and Experiment management

As mentioned earlier, the drive control was implemented using a DSP based controller board DS1104 with I/O features and encoder interface. The main DSP of the controller board can be directly programmed using MATLAB-SIMULINK by MathWorks. This application software is effectively standards in the control community and requires no further explanations. SIMULINK is a graphic user interface integrated in MATLAB for modeling and constructing block diagram via drag and drop operations. Its large block library is further enhanced by the specific dSPACE and user-defined blocks libraries. The application of SIMULINK blocks along with dSPACE and user defined blocks simplify the automatic code generation and experiment setup including initialization of the I/O subsystems and PWM generation. The Real-time workshop is the extension of code-generation provided by the MathWorks. It generates C-code automatically from block diagrams and stat-flow systems. For flexibility, user can introduce own C-code into block diagram by special computation tool *S functions* or alternately by special user-codes with data transferring interface between SIMULINK and C. The own C-code should be preferred whenever the part of the control algorithm contains many if-loops (e.g. space vector modulation) or very extensive complex programs such as sensor-less speed control with Kalman filtering etc. The compiling and automatic download to the DSP is done via the Real-Time Interface (RTI).

The development environment of the dSPACE combines a set of tools that support seamless transition from theory to simulation and then to real time implementation of control algorithms. The software tools such as CONTROLDESK allow tuning of parameters and recording of data during the experiment in real-time mode. The CONTROLDESK is comprehensive experimental environment software that provides management, control and automation of experiments. This user interface enables access to every variable of the original block diagram. The parameters of controller such as reference signal of speed controller can be changed on-line and the response can be observed and recorded simultaneously. The Fig.E.17 shows a close up view of the ControlDesk screen during experimentation.

Fig. E.17 A close up view of ControlDesk screen

E.3.2. Real time Implementation of the SVM

In this work, the current vector control algorithm was implemented through SIMULINK blocks which generate the reference voltage signal for the S-function of SVM. The output of SVM S-function was used to generate the required PWM for the VSI.

This section describes real time implementation of Space Vector Modulation (SVM) technique for PWM generation in DS1104. The three phase reference voltage V_a^*, $V_b^*$and V_c^* can be represented in the stator reference frame as V_α^* and V_β^*.

For appropriate state of the space vector, the sector of the reference vector needs to be identified first. A comparison of α and β component of voltage specifies the position of the space vector in the αβ plane. For instance, if the reference voltage V_β^* is positive, the space vector will lie in the upper half of the Fig.E.18 (sector1, 2 and 3).

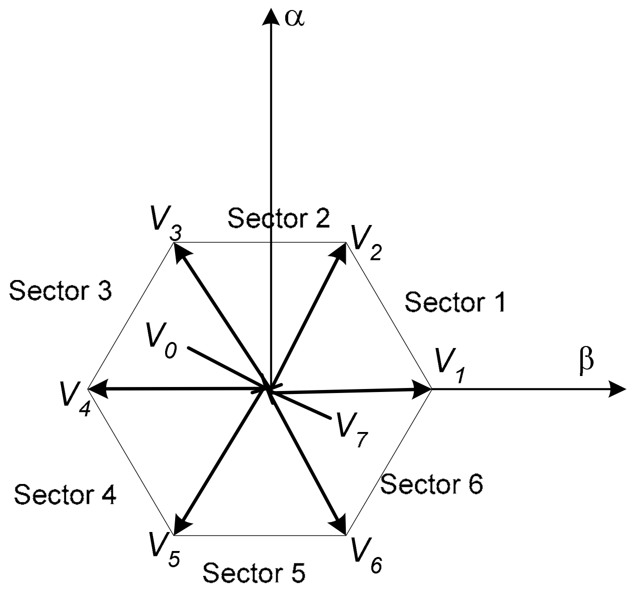

Fig.E.18 Sectors and basic vectors of SVM in *αβ*-plane

The flow chart of Fig.E.19 shows the process of sector selection and calculation of $d_1 = \frac{t_a}{T_s}$ d and $d_2 = \frac{t_b}{T_s}$ required by slave DSP of DS1104 for PWM generation. The normalization applied in the beginning of the process eliminates dependence of DC bus voltage. The algorithm discussed here was implemented by S-function block. The duty ratio d1, d2 and sectors were mapped by the slave DSP of the DS1104 into PWM signals for the VSI switching logics. In order to overflow of the slave DSP, usually duty ratios are limited between 0 and 1.

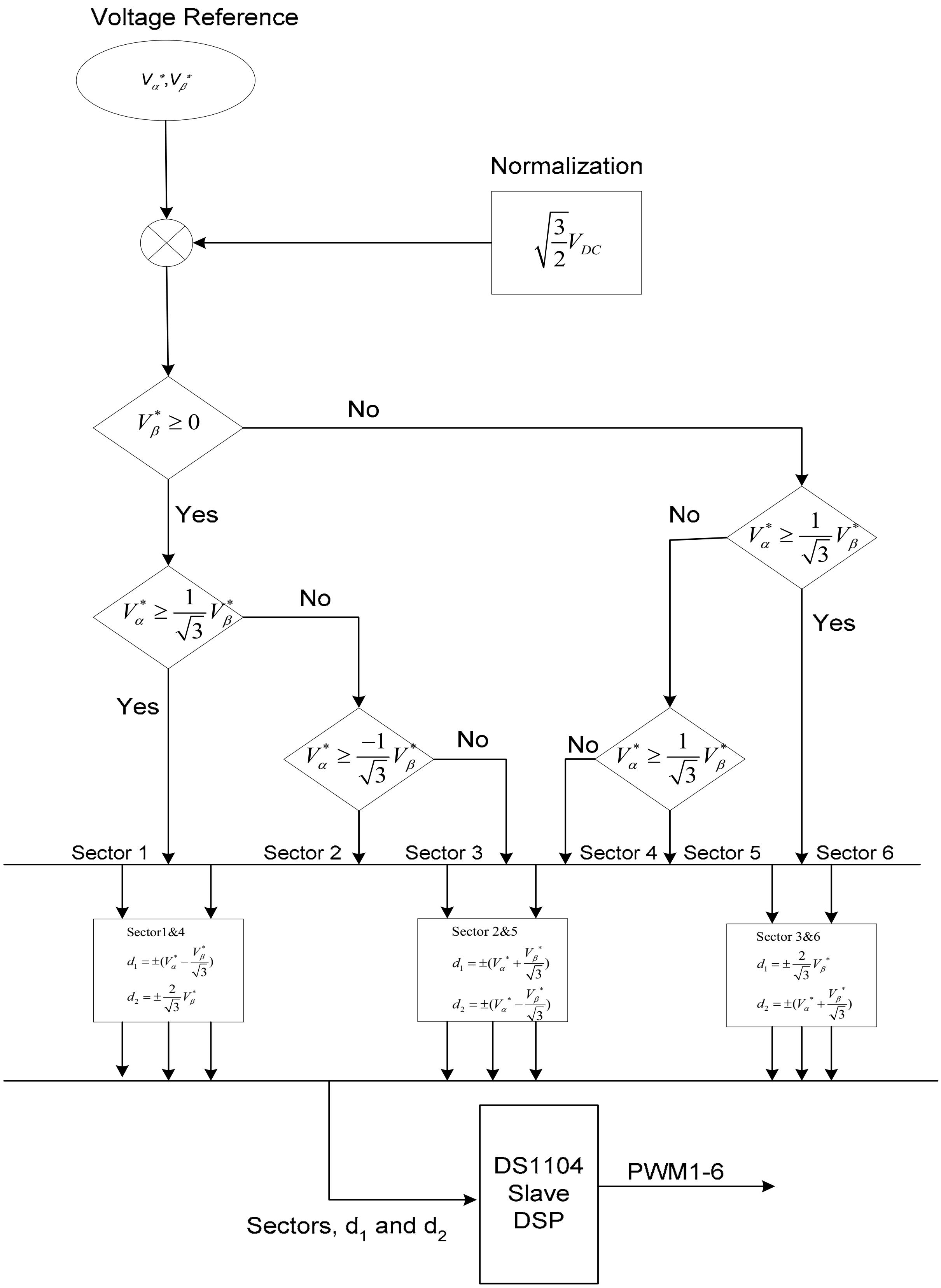

Fig. E.19 Flow chart of SVM and data transmission to Slave DSP

APPENDIX F

F. Publication List

International Journal

[1] R. Dutta and M. F Rahman, "*Design and Analysis of an Interior Permanent Magnet (IPM) Machine with Very Wide Constant Power Operation Rang*e" accepted for publication in **Transaction on Energy Conversion.**

[2] R. Dutta and M. F. Rahman, "A Comparative Analysis of Two Test Methods of Measuring d- and q- Axes Inductances of Interior Permanent-Magnet Machine," *Magnetics, IEEE Transactions on*, Vol. 42, No. 11, pp. 3712, 2006.

[3] R. Dutta and M. F Rahman, "*Analysis and Comparison of Methods for determining d- and q-axes Inductances of IPM Machines*" accepted for publication in **Journal of Electrical and Electronics Engineering Australia**.

[4] R. Dutta and M. F. Rahman, "Interior Permanent magnet Generator: Generator of New Millennium", **The Special Issue of International Energy Journal,** Volume 6, Number 1, Part 1, pp 1-51 to 1-58, June 2005, ISSN:1513-718 X

Pear reviewed Conference Papers

[5] R. Dutta, S. Sayeef and M. F Rahman, "Cogging Torque analysis of the Segmented Interior Permanent Magnet IPM machine" accepted for publication in the proceeding of the International Electrical Machine and Drive Conference (IEMDC, 07), Turkey.

[6] R. Dutta, S. Sayeef and M. F. Rahman, "Cogging torque analysis and its effect on Direct Torque control in the Segmented Interior Permanent Magnet Machine", accepted for publication in the proceeding of the Power Electronics Specialist Conference (PESC, 07). USA.

[7] R. Dutta and M. F Rahman, "Experimental Verification of a Segmented Magnet Interior Permanent Magnet Machine (IPM) with Wide Constant Power Speed Range (CPSR)" Proceeding of Australian Power Engineers Conference, 2006 (AUPEC,06),Melbourne, Australia.

[8] R. Dutta and M. F Rahman, "Design of an Interior Permanent Magnet (IPM) Machine with Very Wide Constant Power Operation Range" proceeding of the Industrial Electronics Conference,2006 (IECON'06), Paris, France.

[9] R. Dutta, M.F. Rahman, "Analysis and Comparison of Methods for Determining d- and q-axes Inductances of IPM Machines", proceeding of International Electric Machines and Drives Conference (IEMDC) in San Antonio, Texas, USA (May 14 – 18, 2005), IEEE catalogue no: 05EX1023C and ISBN : 0-7803-8988-3(CD ROM).

[10] R. Dutta and M. F. Rahman, "A Segmented Magnet Interior Permanent Magnet Machine with Wide Constant Power Range for Traction Application in Hybrid Vehicles" proceeding of IEEE Vehicle Power and Propulsion(VPP) Conference in Illinois, Chicago, USA (September 7-9, 2005), IEEE catalogue no:05EX1117C and ISBN : 0-7803-9281-7(CD ROM).

[11] R. Dutta and M. F. Rahman, "Effect of Iron Loss on the Performance of Interior Permanent Magnet Machines", Proceeding of Australian Power Engineers Conference (AUPEC 2005), Hobart, Australia, 25th -28th Sept, 2005. ISBN:

[12] R. Dutta and M. F. Rahman "Comparison of Core Loss Prediction Methods for the Interior Permanent Magnet Machine" proceeding of 6th International conference on Power Electronics and Drive System (PEDS 2005), 28th Nov- 1st Dec , KualaLampur, Malaysia, ISBN: 0-7830-9297-3, IEEE Catalog Number: 05TH8824C (CD ROM).

[13] R. Dutta and M.F. Rahman "A Segmented Magnet Interior Permanent Magnet Machine and Its Control" Proceeding of Second National Power Electronics Conference (NPEC 2005), Dec 22 - 24, IIT, Kharagpur, India.

[14] R. Dutta and M. F. Rahman, "Interior Permanent magnet Generator: Generator of New Millennium", proc. International conference on Electrical Supply Industry in Transition: Issues and Prospects for Asia, AIT, Thailand, 14-16 January, 2004, pp 1-26 to 1-34, Vol. 1,(CD-ROM), (also accepted for publication in special issue of International Energy Journal (IEJ-AIT)).

[15] R. Dutta and M. F. Rahman, "A Novel IPM Machine for Integrated Starter Alternator Application", Proc. AUPEC 2004, Brisbane, Australia, 26th -29th Sept, 2004. ISBN: 1-864-99775-3 (CD ROM).

[16] R. Dutta and M. F. Rahman, "Vector Control Techniques for Low Voltage IPM Machine in 42v System", Proc. AUPEC 2004, Brisbane, Australia, 26th -29th Sept, 2004. ISBN: 1-864-99775-3 (CD ROM).

[17] R. Dutta and M. F. Rahman, "Investigation of Suitable Vector Control Techniques for Low Voltage IPM Machine in 42V System", Proc. The 30th Annual Conference of the IEEE Industrial Electronics Society (IECON 2004),Busan,Korea, Nov 2-6,2004, IEEE catalog No: 04CH37609C, ISBN: 0-7803-9731-7 (CD ROM).

[18] R. Dutta and M.F. Rahman, "An IPM Machine with Segmented Magnet Rotor for Integrated Starter Alternator", Proc.3rd International Conference on Electrical &Computer Engineering, 2004 (December 28-30, 2004),Dhaka, Bangladesh.

[19] R. Dutta and M. F. Rahman, "A New Rotor Design of IPM machine suitable for wide speed range", Proc. AUPEC 2003, Christchurch , New Zealand, 28th Sept-2nd , 2003. ISBN: 0-473-09867-9 (CD ROM).

[20] R. Dutta and M. F. Rahman, "A New Rotor Design for IPM machine", Proc. The 29th Annual Conference of the IEEE Industrial Electronics Society (IECON 2003),Roanoke, Virginia, USA, Nov 2-6,2003, IEEE catalog No: 0-3CH37468C, ISBN: 07803-7907-1 (CD ROM).

[21] R. Dutta and M.F. Rahman, "An Investigation of A Segmented Rotor Interior Permanent Magnet (IPM) Machine for Field Weakening", Proc. The 5th International conference on Power Electronics and Drive systems (PEDS 2003), Singapore, 17-20 Nov, 2003. ISBN: 0-7803-7886-5 (CD ROM).